THE UNIVERSITY *of* EDINBURGH

Industrially Challenging Separations Via Adsorption in Metal-Organic Frameworks: A Computational Exploration

Matthew J Lennox

PhD

The University of Edinburgh

2014

Declaration

I, Matthew Lennox, hereby declare that the work presented in this thesis was undertaken in the School of Engineering at The University of Edinburgh between July 2010 and August 2014. The work presented herein is the original work of the author except where indicated otherwise and has not been submitted for any other degree or professional qualification, either at The University of Edinburgh or elsewhere.

Signed:

Matthew James Lennox

Tuesday, 25 November 2014

Lay Summary

One of the major challenges facing scientists in the development of new materials for industrial use is ensuring that the material is (a) capable of doing the job it is supposed to do and (b) is one of the best materials for that particular job. In practice, this means that new materials must be thoroughly investigated in the laboratory using a wide range of techniques, all of which require time, money and manpower to carry out. The goal of the work presented in this thesis is to relieve some of the workload of our experimental colleagues by developing computational methods by which promising materials for use in two important industrial processes may be identified. The processes in question were a) the separation of propane from propylene, and b) the separation of mixtures of xylene isomers.

The materials studied in this work are all metal-organic frameworks (MOFs) – a relatively novel class of crystalline materials. Many MOFs are porous – i.e. they contain space into which certain chemicals may be soaked up (or 'adsorbed'), much like a sponge soaks up water. The computer experiments presented in this thesis use a variety of techniques, including Monte Carlo and molecular dynamics simulations, to explain why some MOFs are better than others at adsorbing certain chemicals. More importantly, the work tries to understand why some MOFs, if given the choice, prefer to adsorb one chemical over another and recommend means by which this innate preference may be enhanced.

As a result of this work, a number of highly promising MOFs for the separation of propane from propylene and the separation of xylene isomers have been identified for future experimental investigation. In addition, many of the key structural elements of the MOF – which define the performance of the material in these separations – have been identified. Based on these structural features, protocols have been developed which allow for the design and rapid evaluation of new materials for these separations.

Abstract

In recent years, metal-organic frameworks (MOFs) have been identified as promising adsorbents in a number of industrially relevant, yet challenging, separations, including the removal of propane from propane/propylene mixtures and the separation of mixtures of xylene isomers. The highly tuneable nature of MOFs - wherein structures may be constructed from a variety of diverse building blocks – has resulted in the publication of a staggering number of frameworks incorporating a wide range of network topologies, pore shapes and pore diameters. As a result, there are a huge number of candidate adsorbents to consider for a given separation. Molecular simulation techniques allow the identification of those structural features and characteristics of a MOF which exert the greatest influence on the adsorption and separation of the compounds of interest, providing insights which can both guide the selection and accelerate the development of adsorbents for a specific application.

The separation of propane/propylene mixtures via adsorption has typically focused on selective adsorption of the olefin, propylene, via specific olefin-adsorbent interactions. These propylene-selective MOFs result in processes which selectively remove the most abundant species in the process stream and are typically characterised by high heats of adsorption, resulting in large adsorption units and adsorbents which are difficult to regenerate. In this work, the capability of MOFs to selectively adsorb propane over propylene is explored, potentially allowing for the design of smaller and more energy-efficient adsorption units. By studying a range of different MOFs as well as carbon-based model pores, it was found that the low-pressure selectivity of the structure is determined by the strength of the electrostatic interaction between propylene and the framework, while the adsorptive preference at industrially-relevant pressures is dominated by the enhanced packing efficiency of propylene over propane. The confinement of C3 molecules, however, may be employed to negate this entropic advantage and guide the development of materials which selectively adsorb propane over propylene.

It has recently been reported that the adsorptive preference of a MOF for one xylene isomer over another may be predicted based solely on the pore size distribution of the structure. In this work, the impact of pore size on selectivity was studied systematically in both one-dimensional model pore systems of varying geometries and analogous published MOF structures. The ability of the framework to discriminate between xylene molecules in these systems was found to be determined primarily by the different packing arrangements available to the different isomers – while small pores were found to favour the slimmest of the isomers, larger pores were found to favour the more compact *ortho*- isomer.

Finally, the adsorption and diffusion of xylene isomers in a more complex MOF, UiO-66(Zr), was studied in depth. Simulations were able to correctly predict the previously-reported preference of the MOF for *ortho*-xylene (oX). The smaller volume of the oX molecule compared to the other isomers was found to be responsible both for an enhanced entropic contribution and higher guest-host interaction energies. The importance of framework flexibility in the diffusion of xylene isomers in UiO-66(Zr) was also explored, with distortion of the structure in response to interaction with adsorbed molecules found to be essential in allowing xylenes to diffuse through the pore space.

Acknowledgements

When I started writing this thesis, I did not realise that starting this particular section would be so challenging, but then I did not fully appreciate just how many people had contributed to my life and work over these past four years until I sat and thought about it. Certainly there are more people who deserve my thanks than have actually received any to date so, with some trepidation in case I omit someone, let us try to put that right…

First and foremost I would like to thank my supervisors Dr. Tina Düren and Dr. Lev Sarkisov for their friendship and support, during both my PhD and undergraduate studies at The University of Edinburgh. To Tina – thank you for your patience, encouragement and advice over the past nine years, without which my journey from failed undergraduate chemistry exams to a finished thesis would not have been possible. To Lev – thank you for taking me under your wing and giving me a taste of computational research as an undergraduate and, of course, for your continuing help during my PhD.

My research would not have been possible without funding from the EU FP7 MACADEMIA project, which I am extremely grateful to have been a part of. The past four years would not have been nearly as fruitful or enjoyable without the input of my MACADEMIA colleagues - thank you all for making my introduction to academia a welcoming and rewarding experience. In particular, I would like to extend my gratitude to: Prof. Dirk de Vos, Drs. Michael Maes and Frederik Vermoortele and Ben van der Voorde of KU Leuven for their assistance and contribution to our work on xylene adsorption; Prof. Guillaume Maurin and Dr. Naseem Ramsaheye (Université Montpellier II) and Dr. Qingyuan Yang (Beijing University of Chemical Technology) both for the determination of partial charges, the optimised MOF structures used throughout this thesis and their support and training in the use of DL_Poly and flexible force fields for xylene diffusion studies in UiO-66(Zr); Drs. Philip Llewellyn, Isabelle Beurroies, Mohammed Boulhout and Andrew Wiersum (Université Aix-Marseille/CNRS) for their contribution to our

studies of xylene adsorption and propylene/propane separations; Dr. Alexandre Ferreira (University of Porto) for fruitful discussion of xylene separations; and Prof. Richard Walton and Dr. Alexis Munn (University of Warwick), Prof. Christian Serre and Drs. Thomas Devic, Patricia Horcajada and Hubert Chevreau (Institut Lavoisier), Prof. Norbert Stock and Dr. Helge Reinsch (Christian-Albrechts-Universitaet Kiel) and Prof. Jong-San Chang (Korea Research Institute of Chemical Technology) for all of their MOF structures (new and old), collaboration and advice.

Away from the MACADEMIA project, I would like to thank Dr. Carole Morrison and Claire Hobday of the University of Edinburgh's School of Chemistry for their *ab initio* simulations of linker rotation in UiO-66(Zr) and Dr. Stephen Moggach (also of the UoE School of Chemistry) for his contribution to our studies on the computational screening of MOFs for xylene separations. Thanks too to the UoE Chemical Engineering undergraduate students whom I co-supervised (Alistair Gellan, David Birchett and Thomas Alexander) for their hard work on simulations of xylene adsorption, propylene/propane separations and propylene/nitrogen separations and subsequent contributions to a number of conference presentations.

Thank you to all my colleagues and friends in the now-dispersed Düren research group – in particular Drs. David Fairen-Jimenez, Jenny Williams, Peyman Moghadam, Linjiang Chen and Ana-Maria Banu – for your help and advice and for making our office such an enjoyable working environment.

I would also like to acknowledge the contribution of the IT and support staff of the School of Engineering and the Edinburgh Compute and Data Facility, who maintain and operate the CLX, VLX and Eddie computer clusters on which my research was carried out.

Finally, I would like to thank my friends and family – both present and absent – for their faith, understanding and support.

Table of Contents

Declaration i
Lay Summary ii
Abstract iii
Acknowledgements v
1 Introduction 1
1.1 Outline of Thesis 2
1.2 Publications and Presentations Arising From This Work 4
1.2.1 Publications 4
1.2.2 Presentations 4
2 Materials and Simulation Methods 6
2.1 Materials 6
2.1.1 Metal-Organic Frameworks 6
2.1.2 Model Pore Systems 9
2.2 Simulation Methods 10
2.2.1 Statistical Mechanics 11
2.2.2 Stochastic (Monte Carlo) Methods 12
2.2.3 Molecular Dynamics 20
2.2.4 Potentials and Periodic Boundary Conditions 22
2.2.5 Characterisation Tools 28
3 Molecular Simulation Studies of Propylene/Propane Separations in Metal-Organic Frameworks 31
3.1 Background 31
3.2 Method 37
3.2.1 Structures of Interest: MOFs and Model Pores 38
3.2.2 Force field Parameters 39
3.2.3 Simulation Details 41
3.3 Competitive C_3 Adsorption in MOFs in Low Loading Regimes 42
3.3.1 Overview 43
3.3.2 Influence of van der Waals Interactions 46
3.3.3 Influence of Electrostatic Interactions 55
3.4 Competitive C_3 Adsorption in MOFs in High Loading Regimes 64

3.4.1 Overview 64
3.4.2 Propylene-Selective MOFs 65
3.4.3 Propane-Selective MOFs: The MIL-140 Series 70
3.5 Conclusions 74
4 Pore-Size Effects in Competitive Adsorption of Xylene Isomers 76
4.1 Background 76
4.2 Method 79
4.2.1 Force Field Details 80
4.2.2 Simulation Parameters 81
4.3 Competitive Adsorption in 1D Rhombic Pore Systems 82
4.3.1 Adsorption of pX-oX Mixtures in Model Pores 82
4.3.2 Adsorption of Mixtures Containing mX in Model Pores 94
4.3.3 Comparison of Model Pore Systems with MOFs 99
4.4 Xylene Adsorption in the MIL-140 Series 104
4.5 Conclusions 115
5 Molecular Simulation Studies of Xylene Adsorption and Diffusion in UiO-66(Zr) 118
5.1 Introduction 118
5.2 Method 122
5.2.1 Force Field Details 122
5.2.2 Monte Carlo Simulations 122
5.2.3 Molecular Dynamics Simulations 123
5.3 Single-Component Xylene Adsorption 124
5.4 Competitive Adsorption 135
5.4.1 Selectivity Towards ortho-xylene 136
5.4.2 Competitive Adsorption of pX/mX Mixtures 139
5.5 Diffusion of Xylene Isomers in UiO-66(Zr) 142
5.6 Conclusions 149
6 Summary and Outlook 151
Nomenclature and Acronyms 157
References 160
Appendix A : MOFs Studied in the Present Work 173
Appendix B : Force Field Parameters Used to Describe Flexible UiO-66(Zr) 175
Appendix C : Framework Atom van der Waals Parameters 178

Appendix D : Sources of MOF Partial Charges 179

Appendix E : MOF Structural Characteristics 180

Appendix F : Pressure Dependence of Propylene-MOF Electrostatic Interactions in 1D MOFs 181

Appendix G : Effect of Mixture Composition on Propylene Selectivity 183

Appendix H : C_3 Single-Component Isotherms 184

Appendix I : V_d as a Function of Wall Intersection Angle for Rhombic Model Pore Systems 195

Appendix J : Selectivity at 2 kPa for Xylene Adsorption in Model Rhombic Pores 197

Appendix K : Xylene-Framework and Xylene-Xylene Interactions in Rhombic Model Pores for oX-mX and pX-mX Mixtures 200

Appendix L : Single-Component Xylene Isotherms in the MIL-140 Series 202

Appendix M : Xylene-Framework Interaction Energies in the Intermediate Tetrahedral Pore of Hydroxylated UiO-66(Zr) 204

1 Introduction

In recent years, economic and environmental driving forces have seen the chemical industry move towards more energy-efficient separation processes either through the replacement or enhancement of existing technologies. Separation of a gas or liquid mixture by the preferential adsorption of one or more components into a porous solid represents one such energy-efficient alternative (Yang, 1997). In order for any adsorption process to effectively separate a multi-component mixture, a suitable adsorbent is required – a role traditionally filled by zeolites, activated carbons, silica or activated alumina. More recently, metal-organic frameworks (MOFs) have emerged as promising adsorbents for a wide range of adsorptive gas- (Li *et al.*, 2009a) and liquid-phase (Alaerts *et al.*, 2008; Moreira *et al.*, 2012b) separations and gas storage (Farrusseng, 2011) applications.

MOFs are constructed from metal nodes which are connected together via organic moieties, creating scaffold-like, crystalline solids. One of the attractions in working with MOFs is their highly tuneable nature, wherein, for example, the surface area and pore volume available for adsorption, the composition, functional groups, pore topology and pore diameter may be tailored towards a specific application through the judicious choice of synthesis materials and conditions (Rowsell and Yaghi, 2004). The wide range of available starting materials has resulted in a rapid increase in the number of known MOF structures and upwards of 38,000 MOFs have been published to date (Wood, 2013). Selecting the most appropriate MOF for a given application is therefore a daunting prospect given the sheer number of candidates which must be evaluated. The need to consider a high number of structures coupled with increasing access to high-performance computing facilities has seen molecular simulation play a more prominent role in the evaluation of MOFs for industrial applications in recent years (Yang *et al.*, 2013).

The work presented in this thesis focuses on the computational evaluation of MOFs as suitable adsorbents for two key industrial separations – the separation of propane

from propylene and the separation of *para*-, *meta*- and *ortho*-xylene. Both separations are industrially relevant due to the high demand for high-purity streams of the compounds involved and are particularly challenging due to the similarity in the compounds physical properties. The separation of propane from propylene represents one of the most widely implemented separations in the chemical industry and remains one of the most energy-intensive, utilising cryogenic distillation processes under high reflux and with a high number of stages (Ren *et al.*, 2006). In this case, the development of replacement adsorption processes has been hindered by a lack of suitable adsorbents, a challenge which MOFs may help to overcome. The separation of xylene isomers is primarily carried out using a complex simulated moving bed (SMB) liquid-phase adsorption process using a *para*-xylene-selective zeolite as the adsorbent. Here, the desire is to enhance the existing process through the development of structures which are more selective towards *para*-xylene. The aim of this work, therefore, is to evaluate the competitive adsorption of propane/propylene and xylene mixtures in variety of MOFs using a range of computational tools and to identify the structural properties which are of most importance in determining the selectivity of the MOF for one component or the other, with the ultimate goal of developing an effective set of design heuristics to guide the development and selection of new MOF adsorbents for these separations.

1.1 Outline of Thesis

An introduction to the materials examined in this thesis, which includes metal-organic frameworks as well as carbon-based model pore systems, and the computational techniques employed in this work is provided in Chapter 2.

Chapter 3 concerns the evaluation of MOFs for propane/propylene separations and provides an overview of the current state-of-the-art process and competing technologies before discussing the competitive adsorption of propane/propylene mixtures at low and high loading. Particular emphasis is placed on the influence of structural characteristics such as pore size, geometry and composition on the

interaction between propane/propylene and the framework and on the identification of MOFs which selectively adsorb propane over propylene. A number of industrially-relevant, propane-selective structures are discussed and a screening protocol based on pore diameter which allows the identification of structures in which the enthalpy of adsorption of propane is expected to be higher than that of propylene is presented.

In Chapter 4, the influence of pore diameter and geometry on competitive xylene adsorption in one-dimensional channel systems is explored. The validity of a previously developed screening protocol based solely on pore diameter (Moghadam, 2013) in both model pore systems and analogous MOF structures is considered and the protocol extended to include both the influence of meta-xylene and pore geometry on the separation.

The adsorption kinetics and adsorption equilibria of xylene isomers in UiO-66(Zr) are investigated in Chapter 5. The mechanism behind the experimentally-observed preference of the MOF for *ortho*-xylene (Barcia *et al.*, 2011; Chang and Yan, 2012; Moreira *et al.*, 2012a; Duerinck *et al.*, 2013) is identified and the complex interplay between entropic and enthalpic effects during adsorption is discussed. The impact of framework flexibility on the diffusion of xylene isomers is explored and the different kinetic behaviours of the three isomers observed in experiment (Moreira *et al.*, 2012a) is explained.

A summary of the key outcomes of this work and recommendations for future studies are provided in Chapter 6.

1.2 Publications and Presentations Arising From This Work

1.2.1 Publications

"*Polymorphism of metal-organic frameworks: direct comparison of structures and theoretical N-2-uptake of topological pto- and tbo-isomers*.", **2014**, N.-Y. Zhu, M.J. Lennox, T. Düren, W. Schmitt, Chemical Communications, 50(32): 4207-4210.

"*Hetero- Epitaxial Approach by Using Labile Coordination Sites to Prepare Catenated Metal- Organic Frameworks with High Surface Areas.",* **2014**, N.-Y. Zhu, M.J. Lennox, G. Tobin, L. Goodman, T. Düren, W. Schmitt, Chemistry-a European Journal, 20(13): 3595-3599.

"*p-Xylene-Selective Metal-Organic Frameworks: A Case of Topology-Directed Selectivity.*", **2011**, F. Vermoortele, M. Maes, P.Z. Moghadam, M.J. Lennox, F. Ragon, M. Boulhout, S. Biswas, K.G.M Laurier, I. Beurroies, R. Denoyel, M. Roeffaers, N. Stock, T. Düren, C. Serre, D.E. De Vos, Journal of the American Chemical Society, 133(46): 18526-18529.

1.2.2 Presentations

"*Understanding the selective adsorption of propane over propylene in MOFs through molecular simulation*"
37th Annual British Zeolite Association Meeting, Glasgow, **2014** (Oral Presentation)
M.J. Lennox, T. Düren

"*A computational MOF screening protocol for xylene separation*"
17th International Zeolite Conference, Moscow, **2013** (Oral Presentation)
M.J. Lennox, P.Z. Moghadam, A.D. Gellan, T. Düren

"*Computational screening of MOFs for adsorption applications*"
The Future Potential of MOFs Workshop, Brussels, **2013** (Oral Presentation)
M.J. Lennox, P.Z. Moghadam, A.D. Gellan, T.C. Alexander, T. Düren

"*Towards the computational screening of MOFs for xylene separation*"
36th Annual British Zeolite Association Meeting, Keele, **2013** (Oral Presentation)
M.J. Lennox, P.Z. Moghadam, A.D. Gellan, T. Düren

"*What makes a good MOF for propene/nitrogen separations?*"
36th Annual British Zeolite Association Meeting, Keele, **2013** (Oral Presentation)
T.C. Alexander, M.J. Lennox, T. Düren

"*Towards the computational screening of MOFs for xylene separation*"
11th International Conference on the Fundamentals of Adsorption, Baltimore, **2013** (Poster Presentation)
M.J. Lennox, P.Z. Moghadam, A.D. Gellan, T. Düren

"*Exploring xylene separations in MOFs through molecular simulation*"
Université Montpellier II, **2012** (Invited Lecture)
M.J. Lennox, P.Z. Moghadam, A.D. Gellan, T. Düren

"*Xylene adsorption in UiO-66(Zr): a molecular perspective*"
35th Annual British Zeolite Association Meeting, Chester, **2012** (Poster Presentation)
M.J. Lennox, T. Düren

"*Towards the computational screening of MOFs for xylene separation*"
3rd International Conference on Metal-Organic Frameworks and Open Framework Compounds, Edinburgh, **2012** (Poster Presentation)
M.J. Lennox, P.Z. Moghadam, A.D. Gellan, T. Düren

2 Materials and Simulation Methods

This chapter serves as an introduction to the materials and computational methods which underpin the work presented in this thesis. Section 2.1.1 provides an introduction to the realm of metal-organic frameworks (MOFs), outlining their underlying chemistry and potential applications. Adsorption in artificial model pore systems plays an important role in the further rationalisation of the observations of adsorption in MOFs in the present work and these model pores are discussed in Section 2.1.2. The contents of the computational toolbox brought to bear in this thesis are reviewed in Section 2.2, covering classical simulation techniques such as Monte Carlo and molecular dynamics simulations, methods used in the characterisation of porous solids and the potentials and force fields used to describe the systems of interest.

2.1 Materials

2.1.1 Metal-Organic Frameworks

Metal-organic frameworks (MOFs) are a relatively new class of materials which have emerged from coordination polymer chemistry over the past few decades (Batten *et al.*, 2013). MOFs are constructed from metal nodes which are connected together using organic linkers, typically creating a periodic, crystalline structure (Rowsell and Yaghi, 2004). Following the work of Yaghi and co-workers in the mid-1990s (Yaghi *et al.*, 1995; Yaghi and Li, 1995), scientific interest in metal-organic frameworks has flourished and the Cambridge Structural Database now contains over 38,000 such structures (Wood, 2013), while a further 137,000 hypothetical MOF structures have been postulated (Wilmer *et al.*, 2012b).

A wide range of different metals and organic ligands can be used in the synthesis of MOFs and a diverse array of crystal structures may be achieved through alteration of either the metal or, more frequently, the organic linker (Yaghi *et al.*, 2003). The

well-known IRMOF-1 structure ((Eddaoudi *et al.*, 2002); Figure 2.1 (centre)), for example, is built up from Zn_4O clusters and benzene di-carboxylate (BDC) linkers. The linker may be replaced with a longer moiety such as bi-phenyl-di-carboxylate (BPDC) to produce a more open framework, IRMOF-10, which retains the same topology as IRMOF-1 ((Eddaoudi *et al.*, 2002); Figure 2.1 (left)). In the case of MIL-47(V) (Barthelet *et al.*, 2002), the BDC linker is combined with vanadium rather than zinc, resulting in a completely different, one-dimensional structure (Figure 2.1 (right)). This 'building block' approach represents one of the major attractions of MOF chemistry, wherein structural features such as topology, local chemical environment, pore size and surface area may be tailored to a specific application through judicious choice of starting materials (Li *et al.*, 2009a). As such, MOFs with pores ranging from only a few Ångstrom (Serre *et al.*, 2006) to upwards of 25 Å in diameter (Ferey *et al.*, 2004) and BET surface areas as high as 7,000 m^2/g (Farha *et al.*, 2012) have been reported. A complete list of the MOF structures investigated in this work may be found in Appendix A.

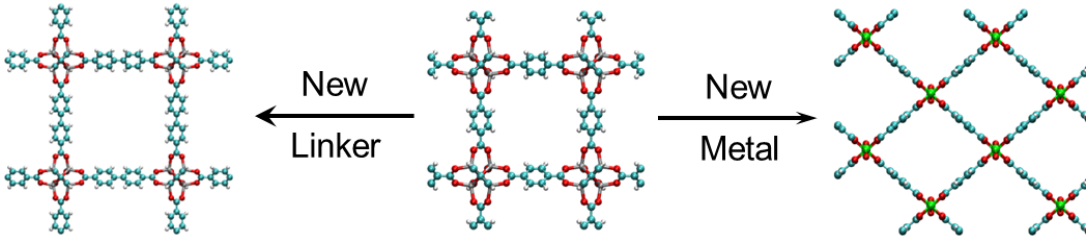

Figure 2.1 – The building block approach to MOFs: IRMOF-1 (centre) uses Zn + benzene dicarboxylate (BDC), IRMOF-10 (right) uses Zn + bi-phenyl-di-carboxylate (BPDC), MIL-47(V) uses V + BDC. Colour scheme: C – cyan; H – white; O – red; Zn – grey; V – green.

The organic-inorganic coordination bonds found in MOFs result in structures which are generally less robust in nature than other microporous materials such as zeolites and activated carbons. Early MOFs were often characterised by low hydrothermal stability (Rowsell and Yaghi, 2004), although more recently MOFs which are hydro- and solvothermally resilient have been reported (Cavka *et al.*, 2008; Low *et al.*, 2009). Additionally, the organic-inorganic nature of MOFs can give rise to a significantly higher degree of structural flexibility than in zeolites. In many cases,

this flexibility is limited to low-impact rotation or bending of the organic linker, which has minimal effect on the overall structure. MOFs which exhibit high levels of flexibility, however, have been reported including pore expansion through gate-opening (Serre *et al.*, 2002) or swelling (Serre *et al.*, 2004a) and alteration of pore window size via linker rotation (Fairen-Jimenez *et al.*, 2012).

The inclusion of organic – often aromatic – ligands in the structure also allows MOFs to be further adapted by functionalising the linker, either directly during the synthesis or via post-synthetic modification of the framework (Cohen, 2012). The addition of polar substituents to the ligand can, for example, enhance the adsorption of polar species via specific interactions (Torrisi *et al.*, 2010), alter the size and shape of the pore system (Devic *et al.*, 2009), the topology of the MOF (Dau *et al.*, 2012) or even optimise the pore size for a given sorbate (Yang *et al.*, 2011c). The metal centre may also be altered via post-synthetic modification, allowing the incorporation of a second metal either directly into the framework (Kim *et al.*, 2012b) or as an extra-framework cation (Ferey *et al.*, 2007) and the further tuning of magnetic, luminescent or conductive properties.

The diversity of available structures has meant that the suitability of MOFs for a wide range of applications has been investigated, including catalysis (Lee *et al.*, 2009), gas storage (Farrusseng, 2011), CO_2 capture, vapour (Li *et al.*, 2009a) and liquid-phase separations (De Malsche *et al.*, 2012; Duerinck *et al.*, 2013), chiral separations (Xie *et al.*, 2011), photoluminescence (Serre *et al.*, 2004b; Wang *et al.*, 2009), sensing (Greathouse *et al.*, 2010) and drug delivery (Hinks *et al.*, 2010; Ke *et al.*, 2011). The huge number of MOF structures remains a double-edged sword, however, as for any given application there are a significant number of candidate MOFs which must be evaluated. To this end, a number of computational approaches have been implemented in order to streamline both the evaluation of candidate MOFs and the design and development of new structures, ranging from large-scale screening of structures via grand canonical Monte Carlo (GCMC) simulations (Greathouse *et al.*, 2010; Wilmer *et al.*, 2012b) to the characterisation of MOFs for adsorption applications using a combination of GCMC and other computational tools

(Duren *et al.*, 2009; Sarkisov and Harrison, 2011) and the theoretical exploration of linker functionalization (Yang *et al.*, 2011c).

2.1.2 Model Pore Systems

The isoreticular nature of many MOFs enables the creation of a range of structures with identical topologies but varying pore diameter through the modification or replacement of the organic linker. The use of different linkers, however, also results in changes in the composition of the MOF and, potentially, variations in the geometry of the resultant pore system. The impact of the new linker on an adsorption process, therefore, can be quite complex. The study of model pore systems allows the effect of, for example, pore size on adsorption to be evaluated in the absence of variations in the composition of the material or the shape of the pore. In this work, the study of adsorption in model pore systems serves to decouple the influence of the basic structural features of a MOF (i.e. pore diameter and geometry) on adsorption from other factors such as composition or linker orientation and, ultimately, helps to evaluate which aspects of a MOF structure are most important in the separation of propane/propylene and xylene mixtures.

In a typical model pore system, the underlying shape and composition of the pore wall is fixed while a single parameter – e.g. the radius of a cylindrical pore – is varied. The earliest implementations of this approach studied the interaction of simple species with infinite, carbon-based cylindrical or slit like pores (Everett and Powl, 1976). More recently, model pores have been used to evaluate the impact of surface heterogeneity on the adsorption of simple molecules (Bojan *et al.*, 1992b), the effect of pore diameter on the competitive adsorption of ethane/ethylene mixtures (Curbelo and Muller, 2005; Do and Do, 2005) as well as the adsorption of aromatic molecules in slit pores of varying widths (Klomkliang *et al.*, 2012), to give just a few examples.

In the present work, two different one-dimensional topologies of model pore were constructed: rhombic and triangular (Figure 2.2). These systems were selected as

they represent common MOF topologies. The rhombic channel is observed in a number of MOFs including MIL-47(V) and the MIL-53 systems, while more recently, a series of small-pore, isoreticular triangular channel MOFs have been described (Guillerm *et al.*, 2012). Both model pore systems were comprised of intersecting graphitic sheets which are in turn created from carbon atoms placed on a hexagonal grid (Figure 2.2; right). In the case of rhombic systems, four sheets were used and the angle of intersection of the sheets could be varied from 0° to 90°. In the triangular system, an additional vertical graphite sheet was introduced and the intersection angle was set to 60°, resulting in an array of equilateral triangular channels. The channel size was adjusted by increasing the edge length of the pore (i.e. the separation distance between intersecting sheets) by an integer number of hexagonal 'aromatic' units (2.8 Å in total length).

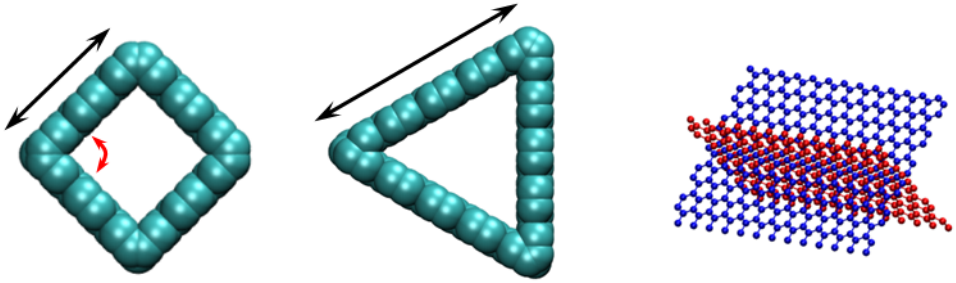

Figure 2.2 – Rhombic (left) and triangular (centre) carbon model pores used in this work. The pores are created from intersecting graphitic sheets (red and blue atoms in the right-most picture). The pore may be modified via adjustment of the edge length (black arrows) and, in the case of rhombic pores, the intersection angle (red arrow).

2.2 Simulation Methods

The work presented in this thesis was undertaken using a wide range of classical simulation methods, the underlying principles of which are described in this chapter. A brief introduction to statistical mechanics is provided in Section 2.2.1, followed by an outline of the Monte Carlo approach (Section 2.2.2). Molecular dynamics, which allows the evolution of systems with time to be explored through integration of Newton's equations of motion, is described in Section 2.2.3. The force fields and

potentials which form the basis of these classical simulations are listed in Section 2.2.4. Finally, the computational tools used to characterise the structures examined in this work are described in Section 2.2.5.

2.2.1 Statistical Mechanics

Statistical mechanics is a branch of thermodynamics which describes the calculation of macroscopic properties – i.e. the properties of the bulk system – through the measurement of microscopic quantities. Thus, macroscale properties such as fluid density or enthalpy of adsorption may be calculated from the study of interactions on a molecular scale. The key concepts in this approach are the microstate, macrostate and the statistical ensemble. A microstate describes a single, instantaneous snapshot of a system – each atom has a specific position, energy and velocity associated with it. A system at equilibrium – the macrostate – passes through many millions of such microstates over time. In order to link micro and macroscopic properties, a set of thermodynamic constraints is placed on the microscopic system through the choice of the statistical ensemble. The ensemble is chosen to describe the macroscopic system of interest:

- The canonical (NVT) ensemble keeps the number of molecules (N), the volume (V) and temperature (T) of the system fixed, mimicking a closed system at thermal equilibrium with its surroundings.
- The isothermal-isobaric (NPT) ensemble is a closed system at thermal and mechanical equilibrium with its surroundings, keeping the number of molecules, pressure (P) and temperature fixed.
- The grand canonical (μVT) ensemble fixes the chemical potential (μ), volume and temperature of the system, while the number of molecules is allowed to fluctuate. This mimics a system in material and thermal equilibrium, such as that observed during adsorption experiments.

The above is not an exhaustive list of the available ensembles but rather represents the most commonly implemented ones (Hill, 1956). Having selected an appropriate ensemble, a macroscopic property, *M*, of the system may be determined by averaging the same property over all microstates.

In molecular dynamics (MD), which is discussed in detail in Section 2.2.3, the positions and velocities of all particles in each microstate are determined from their positions and velocities in the previous microstate through equations of motion. The simulation thus follows the evolution of the system in time and the time-averaged properties of the system are determined. In stochastic simulations, the goal is to sample all possible microstates but not necessarily in chronological order and an ensemble-averaged rather than time-averaged value is determined. It is assumed that the time and ensemble average value are equivalent (i.e. the system is ergodic and that macroscopic average is not dependent on either the order in which the microstates are visited or the initial configuration (Frenkel, 1996)). While this is generally a valid assumption in the case of adsorption simulations, there do exist systems – for example metastable or glass-like systems – which are non-ergodic and for which standard stochastic approaches are not well-suited.

2.2.2 Stochastic (Monte Carlo) Methods

For an ergodic system – i.e. one in which the time-average and ensemble-average behaviours are identical – the macroscopic property, *M*, may be linked to the property in the microstate as follows:

$$M_{Macroscopic} = \langle M \rangle = \sum_i M_i \eta_i \qquad \textbf{Equation 2.1}$$

Where $M_{Macroscopic}$ is measured at the macroscopic level, <*M*> is the ensemble average value of the property, M_i is the measured value of the property in a particular microstate, i, and η_i is the probability of observing said microstate. Thus, the

ensemble average value may be determined if both the instantaneous values of M_i and the probability of observing each microstate are known.

In order to describe the probability of observing a specific microstate, an additional term – the partition function (Z) – must be introduced. The partition function represents the sum of all possible accessible states of a thermodynamic system and its form is dependent on the chosen thermodynamic ensemble (Dill and Bromberg, 2003). For the purposes of demonstrating the underlying principle, the remainder of this section shall consider the grand canonical ensemble, in which the majority of the work in this thesis was undertaken.

In a grand canonical ensemble, all microstates share the same chemical potential, volume and temperature, mimicking equilibrium adsorption experiments wherein a system of fixed volume is allowed to exchange mass with an external bulk fluid at a fixed temperature until a chemical equilibrium is reached. The total energy of the system (E_i) and the total number of molecules within the simulation volume (N_i) are allowed to fluctuate between microstates. Both E_i and N_i follow a Boltzmann distribution and the partition function, $Z_{\mu VT}$, must represent the sum of all possible combinations of these two variables:

$$Z_{\mu VT} = \sum_{k} (e^{-\beta E_i}) \cdot (e^{\beta \mu N_i}) \qquad \textbf{Equation 2.2}$$

Where

$$\beta = \frac{1}{k_B T} \qquad \textbf{Equation 2.3}$$

In which k_B is the Boltzmann constant and T represents the temperature of the system.

Since the partition function describes all possible microstates, the probability of observing one particular microstate, which has energy E_i and number of molecules N from that collection is simply:

$$\eta_i = \frac{1}{Z_{\mu VT}} \cdot \left(e^{-\beta E_i}\right) \cdot \left(e^{\beta \mu N}\right) \qquad \textbf{Equation 2.4}$$

Having developed an expression for the probability of observing microstate *i*, Equation 2.1 may be re-written for the grand canonical ensemble:

$$\langle M \rangle_{\mu VT} = \sum_{i,N} M_i \eta_i = \frac{1}{Z_{\mu VT}} \cdot \sum_{i,N} M_i \cdot \left(e^{-\beta E_i}\right) \cdot \left(e^{\beta \mu N}\right) \qquad \textbf{Equation 2.5}$$

Here, M_i represents the average value of the property in microstate *i* over the entirety of the microstate volume. The solution of Equation 2.5 would involve a summation over all possible microstates – an intractable problem due to the extremely high number of microstates involved. In order to make Equation 2.5 more amenable to computation, it is useful to assume classical behaviour in the system. In this case, a microstate – wherein the positions and momenta of all particles is known – may be considered a single point in phase space and *M* may be considered a function of particle momentum, particle position and the probability of observing a particular configuration. The macroscopic property, *M*, is thus the integral over all momenta ($\boldsymbol{v}$) and positions ($\boldsymbol{s}$) of the particles:

$$M = \iint M(\boldsymbol{v}, \boldsymbol{s}) \cdot \rho(\boldsymbol{v}, \boldsymbol{s})\, d\boldsymbol{v}\, d\boldsymbol{s} \qquad \textbf{Equation 2.6}$$

Where ρ is the probability distribution of accessible configurations. This expression may be further simplified by de-coupling the energy of the system into a kinetic portion, which depends solely on momentum, and a potential term which is dependent solely on position. The potential energy of the system, $U(\boldsymbol{s})$, is calculated from the positions of the particles and is based on intermolecular interactions, which

may be calculated from force fields (Section 2.2.4). The kinetic term for a single particle may be expressed using ideal gas theory as:

$$\frac{V}{\Lambda} \qquad \text{in which} \qquad \Lambda = \hbar\sqrt{\frac{\beta}{2\pi m}} \qquad \textbf{Equation 2.7}$$

In which Λ is the de Broglie wavelength of the particle, $\hbar$ is Planck's constant and m is the mass of the particle. Analogous to Equation 2.4, the probability of observing a particular configuration, $\rho(\mathbf{s})$, may be defined as:

$$\rho(\boldsymbol{s}) = \frac{1}{Z_{\mu VT}} \cdot \frac{V^N}{N!\,\Lambda^{3N}} \cdot (e^{-\beta U(\boldsymbol{s})}) \cdot (e^{\beta \mu N}) \qquad \textbf{Equation 2.8}$$

The ensemble average value of M may therefore be expressed in a classical form equivalent to Equation 2.5:

$$\langle M \rangle_{\mu VT} = \frac{1}{Z_{\mu VT}} \cdot \sum_N \frac{V^N}{N!\,\Lambda^{3N}} \cdot \int M(\boldsymbol{s}) \cdot (e^{-\beta U(\boldsymbol{s})}) \cdot \left(e^{\beta \mu N}\right) d\boldsymbol{s} \qquad \textbf{Equation 2.9}$$

In the most basic of Monte Carlo (MC) techniques, $<M>$ is determined by sampling a huge number of random configurations (points in phase space) and evaluating the integral in Equation 2.9 for each point. It is clear that this approach is still limited in practice by the extremely large number of configuration which must be sampled. In order to circumvent this limitation, Metropolis *et al* (1953) introduced the concept of *importance sampling* to MC calculations. Many of the points in phase space are statistically unlikely to occur (i.e. their Boltzmann factors are negligible) and their contribution to the ensemble average is therefore minimal. In importance sampling, those configurations with a high Boltzmann factor and large contribution to the integral in Equation 2.9 are sampled preferentially. The contribution of these points to the ensemble average is subsequently corrected to account for the statistical bias which is introduced through this method.

The general MC algorithm follows a random walk through phase space in which each successive step on the walk attempts to introduce a small, random perturbation to the system. Each configuration is therefore affected only by the immediately preceding configuration, generating a Markov chain (Allen and Tildesley, 1987). The probability of moving from the old configuration (*o*) to a new configuration (*n*) is denoted by the transition probability, $\pi(o \rightarrow n)$. For a system in equilibrium, the number of moves from (*o*) to (*n*) will be approximately equal to the number of moves from (*n*) to (*o*). In MC simulations, a stricter condition is implemented: the number of moves from (*o*) to (*n*) must be exactly the same as the number of moves from (*n*) to (*o*) (Frenkel, 1996):

$$\pi(o \rightarrow n) \cdot \rho(o) = \pi(n \rightarrow o) \cdot \rho(n) \qquad \textbf{Equation 2.10}$$

Where $\rho(o)$ and $\rho(n)$ are the probabilities of observing the old and new configurations. The overall transition probability is the product of two terms: the probability of attempting such a move, *att()*, and the probability of accepting the move, *acc*(). In the Metropolis scheme, *att()* is symmetric and the chance of attempting a move from (*o*) to (*n*) is equal to the chance of attempting to move from (*n*) to (*o*). Equation 2.10 thus becomes:

$$acc(o \rightarrow n) \cdot \rho(o) = acc(n \rightarrow o) \cdot \rho(n) \qquad \textbf{Equation 2.11}$$

In an unbiased MC scheme, $acc(o \rightarrow n)$ and $acc(n \rightarrow o)$ are equal to unity, resulting in the acceptance of every perturbation and the entirety of phase space is thus explored. Metropolis *et al* (1953) introduced alternative acceptance criteria which still satisfy the detailed balances presented above (Equation 2.10 and Equation 2.11). In the Metropolis scheme, the acceptance probability is related to the relative probability of observing the old and new configurations. If $\rho(n)$ is greater than $\rho(o)$ then the move $(o \rightarrow n)$ is accepted (i.e. $acc(o \rightarrow n) \equiv 1$). If the absolute likelihood of observing configuration (*n*) is lower than that of observing configuration (*o*) then the acceptance probability is inversely proportional to the difference (i.e. if configuration

(*o*) is much more likely than configuration (*n*), the move will not be accepted). These criteria may be expressed for a transition from (*o*) to (*n*) as follows:

$$acc(o \rightarrow n) = \min\left(1, \frac{\rho(o)}{\rho(n)}\right) \qquad \textbf{Equation 2.12}$$

Except for extremely simple systems, ρ(*o*) and ρ(*n*) may not be calculated directly due to the complicated nature of the partition function (see, for example, Equation 2.8). By considering the ratio of the two, however, the partition function may be eliminated from the calculation. The exact form of the acceptance criteria in Equation 2.12 depends on the type of perturbation being attempted on the system. For MC simulations in the grand canonical ensemble (GCMC), the following perturbations are always considered:

- Insertion of a new molecule into the system (insertion)
- Removal of an existing molecule from the system (deletion)
- Movement of an existing molecule by a small amount (displacement)

For molecules with more than one atom, an additional move (rotation) is included in which an existing molecule is subjected to a random rotation around its centre of mass. In the case of multi-component simulations, a further move is considered (identity swap) in which an attempt is made to replace an existing molecule of one species with a molecule of another species, while retaining the position and orientation of the original molecule (Cracknell *et al.*, 1993).

For rotation and translation moves, the total number of molecules remains the same and the acceptance probability for the move is dependent solely on the total energy of the system:

$$acc(o \rightarrow n) = min\left(1, e^{\left(-\beta\left(U(n)-U(o)\right)\right)}\right) \qquad \textbf{Equation 2.13}$$

Conversely, for a move from configuration (*n*) to configuration (*o*):

$$acc(n \to o) = min\left(1, e^{\left(-\beta\left(U(o)-U(n)\right)\right)}\right) \qquad \textbf{Equation } 2.14$$

In both insertion and deletion moves, wherein both the potential energy of the system and the number of molecules change, the acceptance probability depends upon the chemical potential, the system energy and the number density of particles in the simulation volume. For the insertion of a new molecule:

$$acc(o \to n) = min\left(1, \frac{V}{\Lambda^3(N+1)} e^{\left(\beta\left(\mu-U(N+1)+U(N)\right)\right)}\right) \qquad \textbf{Equation 2.15}$$

It is often simpler to express the chemical potential of the system in terms of the fugacity, *f*, of the bulk fluid:

$$\mu = \frac{\ln(f\beta\Lambda^3)}{\beta} \qquad \textbf{Equation 2.16}$$

The fugacity of the bulk fluid may be readily determined from the composition, temperature and pressure of the system using an equation of state – the Peng-Robinson equation of state in this work (Peng and Robinson, 1976). The acceptance probability for the insertion of a new molecule thus becomes:

$$acc(o \to n) = min\left(1, \frac{\beta f V}{(N+1)} e^{\left(-\beta\left(U(N+1)-U(N)\right)\right)}\right) \qquad \textbf{Equation 2.17}$$

And for the deletion move:

$$acc(o \to n) = min\left(1, \frac{N}{\beta f V} e^{\left(-\beta\left(U(N)-U(N+1)\right)\right)}\right) \qquad \textbf{Equation 2.18}$$

These acceptance criteria must be further modified in the case of gas mixtures to take into account the different fugacities and number of molecules of each species

(Frenkel, 1996). In this work, insertion and deletion moves are further altered through the introduction of energy biasing. In an un-biased insertion move, a new molecule is created at a random point in the simulation cell. In the case of adsorption, where the simulation cell contains a large number of framework atoms at fixed locations, many of these random insertions are rejected due to an overlap between the inserted molecule and the framework. In an energy-biased insertion, new molecules are preferentially inserted into regions where the interaction energy between the sorbate and the framework is not positive (i.e. there are no overlaps with framework atoms), thus reducing the number of rejected insertions and the required simulation time (Snurr *et al.*, 1993).

Finally, the acceptance criteria for the identity swap move, which may be considered to be the deletion of a molecule of species *a* coupled with the simultaneous insertion of a molecule of species *b* at the same point, may be expressed as:

$$acc(o \rightarrow n) = min\left(1, \frac{f_b N_a}{f_a (N_b + 1)} e^{\left(-\beta\left(U(N+1)-U(N)\right)\right)}\right) \qquad \textbf{Equation 2.19}$$

It should be noted that the acceptance criteria for these MC moves only consider the energy difference between the old and new configurations and do not consider any energy barriers which may be associated with the movement from the old to the new state. As such, these methods cannot be used to evaluate phenomena in which the energy pathway is as important as the initial and final values of the system energy, such as transport phenomena. Similarly, care must be taken in adsorption simulations that the GCMC technique does not introduce artificial or non-realistic effects such as the inclusion of physically inaccessible regions of the pore space in calculations of pore volume, for example.

The simulation of adsorption in a porous solid via GCMC thus consists of several steps. First, a simulation cell containing a porous, crystalline solid free of adsorbed molecules is created. The temperature, total vapour pressure and composition (which fix the fugacity of the species involved) are then chosen. From this originally empty solid, a Markov chain of configurations is generated by first attempting to alter the

system using one of the moves outlined previously and then deciding whether to accept the move based on the appropriate acceptance criteria. As the simulation progresses, the total potential energy of the system will decrease towards a minimum, at which point the system is said to be in equilibrium around which successive microstates will fluctuate. This equilibration process may take anything from 10^6 Monte Carlo steps for relatively low density systems to upwards of 10^8 MC steps for dense systems. Once equilibrium is achieved, sampling of the properties of interest of the system (e.g. the number of adsorbed molecules, the energy of interaction of the sorbate molecules with the framework, etc.) may commence – these are typically sampled and averaged over a further 10^7 to 10^8 MC steps. The entire process is repeated over a wide range of external pressures in order to generate a complete adsorption isotherm.

2.2.3 Molecular Dynamics

In contrast to MC, where the ensemble average of a property is determined, Molecular Dynamics (MD) simulations consider the evolution of a system in time, allowing the dynamics of a system to be examined. The starting point for any MD simulation is an initial configuration in which the atomic positions and velocities of all molecules at time $t = 0$ are known. From this, the positions and velocities a short time in the future ($t+\Delta t$) are determined by integrating Newton's equations of motion for each molecule. Each successive microstate is thus connected to the initial configuration. The timescale which may be investigated using MD techniques depends upon the size and complexity of the system but the upper limit for MOF systems is on the order of tens of nanoseconds (Yang *et al.*, 2011a). While MD may be used to evaluate the diffusion of light gases or fast-moving species, the timescale accessible to MD simulations limits their usefulness in examining the movement of slower-moving compounds with small self-diffusion coefficients (Maginn *et al.*, 1996).

The interaction of a particular molecule, *i*, with a nearby atom, *j*, separated by distance $\mathbf{r_{ij}}$ may be calculated using any one of a number of force fields, which are discussed in more detail in Section 2.2.4. Once the intermolecular interaction energy,

$\boldsymbol{U_{ij}}$, has been calculated, the force acting on the molecule, $\boldsymbol{F_i}$, is simply the partial derivative of the interaction energy with respect to distance:

$$F_i = \frac{\partial U(\boldsymbol{r_{ij}})}{\partial r} \qquad \textbf{Equation 2.20}$$

This procedure must be repeated for the interaction of molecule *i* with all other molecules to determine the overall force acting on molecule *i* at time *t*. The force acting on a body, its mass (*m*) and the acceleration subsequently experienced by the body are related through Newton's second law. The acceleration of the molecule (i.e. the second derivative of position with respect to time) may therefore be determined if the force acting on a molecule is known:

$$F_i = \frac{\partial U(\boldsymbol{r_{ij}})}{\partial r} = m\frac{d^2r}{dt^2} \qquad \textbf{Equation 2.21}$$

The integration of Equation 2.21 may be achieved using a number of different algorithms, generally based around a Taylor series expansion of the particle coordinates in time. In this work, the Velocity Verlet algorithm (Frenkel, 1996) was used. Solving Equation 2.21 yields the new position and velocity of molecule *i* at time (t+Δt). This process must be repeated for every molecule in the system, allowing a new configuration to be generated. The accuracy of the calculated positions and velocities is dependent upon the size of the timestep (Δt) – typically this is on the order of femtoseconds.

As in MC simulations, MD simulations may be carried out in different ensembles depending upon the type of system being investigated. In this work, the NVT ensemble was used to emulate the diffusion of a fixed number of molecules in a fixed volume of space at a specific temperature. In order to keep the temperature of the system – which is influenced by the velocity and kinetic energy of the particles contained within the simulation volume – near to the desired value, a thermostat algorithm is applied to the simulation. In this work, the Berendsen thermostat is used

(Berendsen *et al.*, 1984), in which the velocities of particles within the system are scaled following a weak coupling scheme with an external heat bath.

2.2.4 Potentials and Periodic Boundary Conditions

Both MC and MD simulations require the calculation of the potential energy of the system, which is dependent both on the interaction between molecules (intermolecular interactions) and between atoms contained within the same molecule (intramolecular interactions). The total energy of the system, U_{tot}, is thus the sum of all interactions between pairs of atoms which are not bonded together, $U_{non\text{-}bonded}$, and groups of atoms which are connected by chemical bonds, U_{bonded}:

$$U_{tot} = U_{bonded} + U_{non-bonded} \qquad \textbf{Equation 2.22}$$

Bonded potentials include bond stretching, bond bending and proper and improper torsional bending, while non-bonded potentials include dispersion (van der Waals) and electrostatic (Coulombic) interactions:

$$U_{bonded} = \sum U_{stretch} + \sum U_{bend} + \sum U_{torsion} \qquad \textbf{Equation 2.23}$$

$$U_{non-bonded} = \sum U_{vdW} + \sum U_{Coul} \qquad \textbf{Equation 2.24}$$

Although these energies may be calculated exactly via first principles methods, this approach is limited both by a relatively poor description of dispersion interaction and by the high computational cost associated with such a calculation. The system size which may be considered is generally on the order of a few hundred atoms and, as a result, classical simulations, which operate over a larger number of atoms, rely on semi-empirical functions to approximate the bonded interaction energies.

Both bond stretching and bond bending are generally described using a harmonic function (Figure 2.3), where the variation of bond length (L) or angle (θ) around an equilibrium length (L_{eq}) or angle (θ_{eq}) is constrained by some harmonic spring constant (k_L or k_θ).

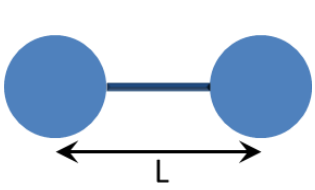

$$U_{stretch} = \frac{k_L}{2}\left(L - L_{eq}\right)^2$$

Equation 2.25

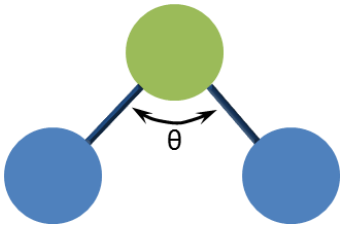

$$U_{bend} = \frac{k_\theta}{2}\left(\theta - \theta_{eq}\right)^2$$

Equation 2.26

Figure 2.3 – Schematic representation of the harmonic potential describing bond stretching (left) and bond bending (right). The bond length (L) and bond angle (θ) are defined between the blue atoms.

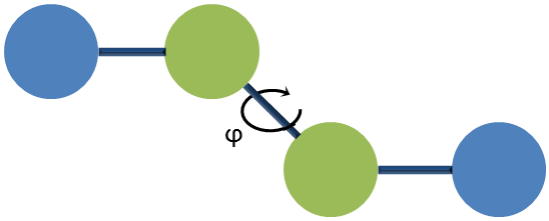

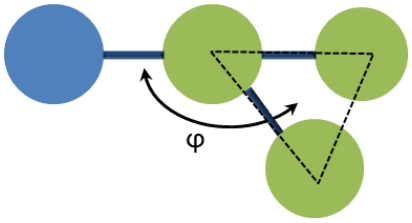

$$U_{torsion} = k_\varphi\left[1 + \cos\left(n_p\varphi - \varphi_{eq}\right)\right]$$

Equation 2.27

Figure 2.4 – Schematic representation of proper (left) and improper (right) torsion angles, both of which may be described using a periodic cosine potential (Equation 2.27). The dihedral angle (φ) is defined between the two blue atoms in the case of proper torsional bonds and between the blue atom and the plane formed by the remaining three green atoms for improper torsional bonds.

Proper and improper torsions may both be described using a periodic cosine potential (Figure 2.4) based on the variation of a dihedral angle, φ, around an equilibrium

dihedral angle, φ_{eq}, constrained by some dihedral force constant, k_φ. Following the work of Yang *et al* (2011a; 2011b), the periodicity, n_p in Equation 2.27, was set to equal two in the present work.

In this work, all sorbate and framework molecules were treated as rigid (i.e. the bonded potential terms were neglected and all bond lengths and angles were kept fixed) with the exception of some MD simulations of the MOF UiO-66(Zr) (Cavka *et al.*, 2008), in which the MOF was treated as flexible following the work of Yang *et al* (2011a; 2011b). The bonded parameters used to describe the MOF in those simulations may be found in Appendix B.

The relatively short-range van der Waals (vdW) interactions between non-bonded atoms are well described using the 12-6 Lennard-Jones (LJ) potential, in which the interaction between two atoms, *i* and *j*, varies with separation distance, r_{ij}:

$$U_{vdW,ij} = 4\epsilon_{ij}\left[\left(\frac{\sigma_{ij}}{\boldsymbol{r_{ij}}}\right)^{12} - \left(\frac{\sigma_{ij}}{\boldsymbol{r_{ij}}}\right)^{6}\right] \qquad \textbf{Equation 2.28}$$

Each atomic type is also described by a potential well depth (ε) – which indicates the maximum strength of interaction between *i* and *j* – and an LJ diameter (σ), which is conceptually related to the size of the atoms. For interactions between atoms of different types, the LJ cross-terms are calculated following Lorentz-Berthelot mixing rules:

$$\epsilon_{ij} = \sqrt{\epsilon_i \cdot \epsilon_j} \qquad \textbf{Equation 2.29}$$

$$\sigma_{ij} = \frac{\sigma_i + \sigma_j}{2} \qquad \textbf{Equation 2.30}$$

The short-range nature of the LJ potential means that the interaction energy tends towards zero quite quickly and the total contribution to the system energy of two atoms with a large separation distance is close to zero. For this reason, the LJ

potential is generally truncated at a specified cut-off distance, beyond which the LJ interaction energy is assumed to be zero. In this work, a cut-off distance of 15 Å is used.

As is common in simulations of MOFs, the LJ parameters used to describe framework atoms in this work were taken either from the DREIDING force field (Mayo *et al.*, 1990) or, for those elements not included in the DREIDING force field, the Universal Force Field (UFF; (Rappe *et al.*, 1992)). These parameters are summarised in Appendix C. The wall atoms of the carbon-based model pore systems were described using standard parameters (σ = 3.4 Å, ε/k_B = 28 K; (Bojan *et al.*, 1992a)). LJ parameters for the sorbate molecules (propylene, propane, *para*-xylene, *meta*-xylene and *ortho*-xylene) were described using force fields developed to describe the vapour-liquid equilibria of the pure components. In the case of the C_3 molecules, the modified TraPPE potentials of Bae *et al* (2012) were used, while the OPLS force field (Jorgensen *et al.*, 1993) was used to describe the xylene isomers. A list of the LJ parameters for the C_3 and xylene molecules may be found in Sections 3.2.2 and 4.2.1 respectively.

In the case of species with a non-uniform distribution of charge (e.g. polar or quadrupolar species), the electrostatic interactions between charged atoms must be taken into account. This is generally accomplished by assigning a partial point charge (q) to each LJ interaction centre and calculating the interaction between partial charges *i* and *j* via a Coulombic potential:

$$U_{Coulombic,ij} = \frac{q_i q_j}{4\pi\epsilon_0 \boldsymbol{r_{ij}}} \qquad \textbf{Equation 2.31}$$

Where ε_0 is the permittivity of free space. As the influence of electrostatic interactions may be experienced over a much larger separation distance than VdW, these interactions may not be truncated in the same manner as the LJ potential and a long-range summation technique must be employed to correctly evaluate the Coulombic contribution. In this work, the Ewald summation technique (Ewald, 1921) was employed for interactions between sorbate molecules and the framework, while

the faster Wolf method (Wolf *et al.*, 1999) was used to calculate Coulombic interactions between sorbate molecules.

The partial charges used in the work were derived from one of three sources. Where available – either from literature or supplied by project partners – accurate charges determined via Density Functional Theory (DFT) calculations were used for framework atoms. Where DFT charges were not available, partial charges for framework atoms were determined using the Extended Charge Equilibration (EQeq) method (Wilmer *et al.*, 2012a), which has been demonstrated to produce charges which are in good agreement with those derived from DFT techniques. A full list the sources of the partial charges used for the various frameworks studied in this work may be found in Appendix D. Partial charges for polar sorbate molecules (propylene and the xylene isomers) were taken from the modified TraPPE force field of Bae *et al* (2012) and the OPLS force field (Jorgensen *et al.*, 1993) respectively.

As the system size even for classical simulations is limited to only 10^3-10^4 atoms, the simulation of the bulk properties of the system requires careful choice of boundary conditions at the edges of the simulation volume. In an isolated box containing 10^3 atoms, for example, a significant portion of the atoms (at least 40%) are likely to be found near the edges of the system and such a simulation is thus not representative of the bulk phase (Frenkel, 1996). In order to overcome this limitation, periodic boundary conditions are used, in which a central, primary simulation volume is replicated an infinite number of times in each direction (Figure 2.5).

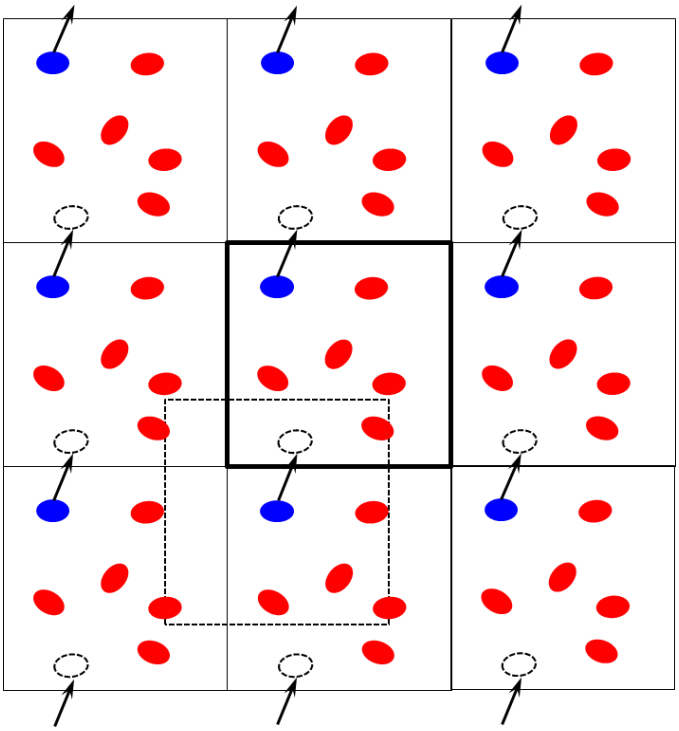

Figure 2.5 – Periodic boundary conditions for a two-dimensional system. The primary simulation cell (outlined in bold black lines) is replicated in each direction *ad infinitum*. When an atom leaves a simulation cell, it is replaced by its periodic image from a neighbouring cell (here the blue atom moves to a new position indicated by the arrows). Atoms only interact with the nearest periodic image of any other atom – for the blue atom these fall within the box marked in dashed black lines.

The movement of particle *i* through the primary simulation cell is replicated in all other images of the cell and particles which attempt to exit the simulation box via one side will re-enter the same box on the opposite side. During the evaluation of interatomic interaction energies, particle *i* is only allowed to interact with the nearest periodic image of any atom in the primary simulation cell. Using periodic boundary conditions thus allows the properties of a bulk system to be sampled effectively. Care must be taken, however, to choose an appropriately sized primary simulation cell. In order to prevent a particle interacting with the periodic image of itself and introducing artificial long-range ordering to the system, the smallest dimension of the primary simulation cell must be at least twice the cut-off radius chosen for the truncation of LJ interactions.

2.2.5 Characterisation Tools

In order to successfully evaluate the impact of the structural properties of a porous solid on its adsorption properties and ultimately determine whether a relationship between a particular structural property and a particular adsorption property exists, it is necessary to be able to assess the structural characteristics of the structure in an accurate and consistent manner. Porous solids are typically characterised by their surface area, available pore volume and the size, or distribution of sizes, of accessible void spaces (Rouquerol *et al.*, 1999). Experimentally, a number of standard techniques are recommended for the evaluation of these structural properties (Sing *et al.*, 1985) and by following these recommendations, new structures may be compared to existing frameworks fairly. More recently, several computational strategies have been developed which enable framework characteristics to be determined directly from the crystal structure of the framework – i.e. the equilibrium positions of atoms within the MOF after the removal or all extra-framework species as determined via X-ray diffraction (XRD).

The surface area available for adsorption is typically expressed experimentally as the surface area per gram of adsorbent which is accessible to nitrogen molecules during adsorption at 77 K (although for polar surfaces, argon is often used) (Sing *et al.*, 1985). This surface area is generally determined by applying the Brunauer-Emmett-Teller (BET) formulation to a nitrogen adsorption isotherm, from which the total number of nitrogen molecules which form a single, well-defined adsorbed layer (a monolayer) may be determined. Knowing both the number of molecules and the projected area of a single nitrogen molecule allows the calculation of the total area of the monolayer which, when divided by the adsorbent sample mass, gives the nitrogen BET surface area (SA_{BET}) (Rouquerol *et al.*, 2006). In the computational evaluation of a framework structure, the same method may be employed to determine the BET surface area based on a simulated nitrogen adsorption isotherm (Walton and Snurr, 2007). This simulated surface area (SA_{GCMC}) may not be identical to the experimentally determined surface area for the same MOF, which depends on the quality of the experimental sample. The same structure synthesised under different

conditions may, for example, exhibit different structural characteristics as a result in defects within the crystal structure (e.g. partially collapsed sections of framework or inaccessible voids) or less effective activation (e.g. some unreacted synthesis material remains in the framework, reducing the space available for adsorption). The GCMC BET surface area may therefore be considered the theoretical surface area of the ideal structure under perfect synthesis and activation conditions, providing both a benchmark figure for experimental groups and a way of eliminating the effect of synthesis/activation procedures from the comparison of different MOFs (Duren *et al.*, 2009).

A computational alternative to the BET surface area is the accessible surface area (SA_{acc}) of the MOF (Duren *et al.*, 2007), which is determined from MC simulations in which a spherical probe is randomly inserted near each of the framework atoms in a structure. The accessible surface area is calculated from the percentage of insertions which do not result in an overlap with other framework atoms. This method is generally less computationally expensive than simulating a nitrogen adsorption isotherm and, in most cases, provides a surface area comparable to the simulated BET surface area when a nitrogen-sized probe is used (Duren *et al.*, 2007). In this work, the surface area of all MOFs was determined via the accessible surface area method using the code of Düren *et al*, a probe radius of 1.84 Å and a grid spacing of 0.25 Å.

The pore volume of a MOF may be determined using a similar MC scheme. In this case, a spherical probe is inserted into the simulation cell and the total pore volume is evaluated based either on the fraction of the insertions which do not result in an overlap with a framework atom (the geometric pore volume) or on the total probe-framework interaction energy per unit mass of framework. Where the LJ parameters for the probe are chosen to match those of a helium atom, the second method has been shown to be analogous to the experimentally determined Helium pore volume (Myers and Monson, 2002). In this work, the Helium pore volume (PV_{He}) at 298 K was determined using the Poreblazer tool kit of Sarkisov and Harrison (2011) using a

grid spacing of 0.25 Å. The LJ parameters for helium (σ = 2.58 Å, ε/k_B = 10.22 K) were taken from Hirschfelder *et al* (1954).

The pore size distribution (PSD) of a structure is used to describe the range of pore diameters (d) which are present in a structure. The pore size plays a key role in adsorption, where the strength of interaction with the framework walls and the packing structure and density of adsorbed molecules depends strongly on the cavity diameter. These pores may be classified as either micropores (d < 20 Å), mesopores (20 Å < d < 500 Å) or macropores (d > 500 Å) (Rouquerol *et al.*, 1999). In MOFs, whose pores are typically less than 30 Å in diameter, the determination of the PSD focuses on the micro- and mesoporosity of the system. Experimentally, this may be accomplished via the examination of the adsorption isotherms of nitrogen and other species or immersion microcalorimetry. Computationally, the determination of the PSD of a structure is typically achieved following the method of Gelb and Gubbins (1998), in which MC simulations are employed to determine the largest sphere which may be inserted into a cavity without overlapping with any framework atoms and it is this method which is employed in the present work.

All of the MOFs investigated as part of this thesis were first characterised using the above methods and the nitrogen-accessible surface area, helium pore volume and the diameters of all cavities within each structure are listed in Appendix E. In all cases, consistent LJ parameters were used and were taken from either the DREIDING (Mayo *et al.*, 1990) or UFF (Rappe *et al.*, 1992) force fields (Appendix C).

3 Molecular Simulation Studies of Propylene/Propane Separations in Metal-Organic Frameworks

In this chapter, the suitability of MOFs for the selective removal of propane from propane/propylene mixtures via adsorption is assessed. After the industrial relevance of the separation and competing technologies are outlined in Section 3.1, the simulation and force field parameters are described in Section 3.2. The adsorption of propane, propylene and mixtures thereof in the low loading regime is explored in Section 3.3, while adsorption at high pressure is considered in Section 3.4. Particular emphasis is placed on the identification of the characteristics and structural features of the MOF which determine whether the structure will selectively adsorb propane or propylene and these are summarised in Section 3.5.

3.1 Background

Propylene (C_3H_6) is one of the most important precursors in the petrochemicals industry, with upwards of 50 million tonnes produced annually (Zimmermann, 2011). The polymerisation of propylene to polypropylene forms the largest market for the compound and accounts for approximately two-thirds of annual consumption. In addition, propylene is a feedstock to a range of other processes including the production of acrylonitrile, propylene oxide and cumene (Kirk *et al.*, 1991). Industrial production of propylene is primarily through the catalytic or steam cracking of longer chain hydrocarbons, a reaction which produces a product stream typically containing, in addition to the olefin, between 0.1 - 0.3 mole fraction of the paraffin, propane (C_3H_8) (Zimmermann, 2011). Thus, the separation of this propylene/propane mixture to produce a polymer-grade propylene product represents one of the most widely implemented separations in the refining industry. Due to the close boiling points of the two components (Propylene: 225.6 K, Propane: 231.1 K), the propane/propylene (C_3) separation is typically carried out through a cryogenic distillation process. The low relative volatility of the mixture results in an expensive

and energy-intensive process requiring high reflux ratios combined with over one hundred theoretical stages (Ren *et al.*, 2006). This high level of energy consumption has fuelled research into alternative approaches to the separation of C_3 mixtures over the past fifty years and extractive distillation (Kumar *et al.*, 1972), absorption into some form of metal salt (Blytas, 1992; Keller *et al.*, 1992), membrane permeation (Tanaka *et al.*, 1996) and adsorption into porous media (Da Silva and Rodrigues, 2001; Lamia *et al.*, 2009; Huang and Cao, 2013) have all been suggested as potential replacements for the existing distillation process.

The separation of olefin/paraffin mixtures through absorption traditionally focuses on the selective binding of the olefin to an available solvated metal ion through a process referred to as π-complexation (Eldridge, 1993). While metal-olefin complexes were first reported in the early 1800s (Hunt, 1984)[1], the currently-accepted mechanism of their formation was not described until the second half of the 20th century (Dewar, 1951; Chatt and Duncanson, 1953). π-complexation is a specific interaction between the π electron orbital of the carbon-carbon double bond within the olefin and the *d*- and *s*-orbitals of the metal ion. This interaction is short-range and of relatively high strength and, as a result, complexes formed between olefins and metal ions such as Hg(II), Pd(II) and Pt(II) are often difficult to reverse without decomposition or conversion of the olefin to another product. Complexes with copper or silver ions, however, are generally reversible through the adjustment of either temperature or pressure (Keller *et al.*, 1992). π-complexation may also be introduced to both adsorption and membrane separation processes as a means to achieve higher selectivity towards the olefin, as shall be discussed shortly. While absorption via π-complexation provides a highly olefin-selective separation, industrial implementation of such processes has been limited by the high sensitivity of the complexation process to air, water, sulphides and acid gas contaminants (Blytas, 1992; Eldridge, 1993). More recently, silver- and copper-based ionic liquids have been shown to be highly selective towards the olefin and may be less

[1] While Hunt provides a fascinating account of the discovery and subsequent controversy over the composition of these platinum-ethylene complexes, it is interesting to note that these compounds also represent the first forays into organometallic chemistry – a field from which metal-organic frameworks will eventually emerge.

susceptible to feed contamination while providing the additional benefit of exhibiting extremely low volatilities, allowing for easier downstream solvent recovery (Sanchez *et al.*, 2009; Chen *et al.*, 2013b).

In the separation of gas mixtures via membrane operations, one (or more) of the compounds is able to quickly permeate through the membrane while the progress of the other species in the mixture is retarded by a combination of the chemical affinity of the species for the membrane material and the kinetic barriers to movement through the medium (Porter, 1990). In addition, it is possible to carry out the separation in the presence of a solvent into which one species is more soluble than the other, allowing an increased rate of absorption into the membrane and a greater concentration differential across the medium (Bryan, 2004). Frequently, the presence of Ag(I) metal ions within the membrane or the solvent is used to enhance the solubility of the olefin, based on π-complexation (Rabago *et al.*, 1996; Kwasniewski *et al.*, 1999; Ravanchi *et al.*, 2010). In many cases, however, the relatively low number of available silver sites leads to swift deactivation of the membrane in the presence of even trace impurities (Bryan, 2004). More recently, hollow-fibre (Faiz *et al.*, 2013), carbonized (Hayashi *et al.*, 1996), ionic liquid (Faiz and Li, 2012) carbonaceous (Xu *et al.*, 2012; Ma *et al.*, 2013) and MOF-based (Hara *et al.*, 2014; Liu *et al.*, 2014) membranes have all been demonstrated to exhibit high levels of selectivity towards the olefin in ethylene/ethane or propylene/propane mixtures. While membrane operations offer high separation factors for olefin/paraffin mixtures, problems with solvent recovery, membrane degradation, thermal stability and deactivation have thus far limited their uptake by industry (Freeman and Yampolskii, 2010).

The adsorptive separation of olefin/paraffin mixtures on porous materials may be broadly split into two categories - those accomplished with the aid of π-complexation agents and those without (Eldridge, 1993). One of the earliest examples of the former can be found in the work of Hirai and co-workers (1985), wherein ethylene is selectively adsorbed on silver chloride-doped polystyrene resin. The post-synthetic dispersal of silver or copper sites on a range of traditional adsorbent materials was

re-visited by Yang and co-workers in the late 1990s (Cheng and Yang, 1995; Yang and Kikkinides, 1995; Rege *et al.*, 1998; Padin and Yang, 2000), resulting in a variety of olefin-selective, silver- and copper-impregnated adsorbents encompassing zeolites, clays, silicas and polymeric resins. It has been noted, however, that the incorporation of metal sites during, rather than after, the synthesis of the adsorbent may result in a more homogeneous distribution of complexation sites and eliminate the potential problems of aggregation or leaching of the metal species (Chen *et al.*, 1997; Tuel, 1999). The direct incorporation of a range of transition metals at the synthesis step, and the potential for these to be subsequently under-coordinated, leaves MOFs ideally placed to utilise π-complexation in order to selectively remove propylene from C_3 mixtures. Several MOFs which take advantage of the presence of open metal sites have been demonstrated to selectively adsorb olefins over paraffins, of which HKUST-1 (Hartmann *et al.*, 2008; Lamia *et al.*, 2009; Ferreira *et al.*, 2011), MIL-100 (Yoon *et al.*, 2010) and CPO-27 (Bao *et al.*, 2011; Bae *et al.*, 2012; Bloch *et al.*, 2012; Bohme *et al.*, 2013) have been the most extensively studied. While the inclusion of open metal sites within the structure is clearly beneficial with regards to the adsorption of propylene, these sites are inherently difficult to model in classical molecular simulations due to the short-range, specific nature of the double-bond – metal interaction (Jorge *et al.*, 2010; Bae *et al.*, 2012). Despite recent advances in the modelling of these types of interactions (Chen *et al.*, 2011; Fischer *et al.*, 2012) which allow specific C_3-MOF systems to be explored, the investigation of the impact of open metal sites on propylene/propane separation on a larger scale, over a range of systems, remains currently impractical. As such, this work focuses on MOFs which do not rely on π-complexation to achieve the desired separation i.e. MOFs without open metal sites.

Such MOFs, which rely on non-specific (i.e. solely dispersion and electrostatic) interactions between the hydrocarbons and the adsorbent, are capable of selectively adsorbing either the olefin or the paraffin. Additionally, in the absence of π-bonding between the olefin and metal site, lower heats of adsorption – and easier regeneration of the adsorbent – can be expected (Grande *et al.*, 2004).

Given their extensive utilisation in industry, it is not surprising that much of the scientific literature has focused upon the potential of zeolites for olefin/paraffin separations by adsorption. The adsorptive separation of propylene/propane mixtures using zeolite 13X was demonstrated to be a viable process by Shu and co-workers in 1990 (Shu *et al.*, 1990) and since then a range of viable separation processes using zeolites 13X (Jarvelin and Fair, 1993; Gomes *et al.*, 2009; Grande *et al.*, 2010), 5A (Jarvelin and Fair, 1993) or 4A (Da Silva and Rodrigues, 2001; Grande *et al.*, 2006) have been reported. In each case, the zeolite selectively adsorbs propylene over propane. In addition, a number of zeolites have been shown to selectively adsorb the olefin at low loadings on a laboratory-scale, including NaX (Choudhary *et al.*, 1995; van Miltenburg *et al.*, 2008), NaA (Gladden *et al.*, 1997), NaY (Hampson and Rees, 1994; Choudhary *et al.*, 1995), Na-MOR (Choudhary *et al.*, 1995), H-FAU (Pantu *et al.*, 2007) and H-MOR (Pantu *et al.*, 2007). None of the zeolites mentioned thus far are purely siliceous in nature - each one contains framework aluminium species and, with the exception of the work of Pantu *et al*, extra-framework cations. In contrast, the Henry's constant of the paraffin has been shown to be greater than that of the corresponding olefin on purely siliceous zeolitic materials such as Si-chabazite (Olson *et al.*, 2004), Theta-1 (Hampson and Rees, 1994), DD3R (Zhu *et al.*, 2000) and silicalite-1 (Jakobtorweihen *et al.*, 2005). In each case, enhanced low pressure uptake of the paraffin was reported for C_2 and/or C_3 systems. More recently, Kim *et al* (2012a) used GCMC simulations to evaluate 171 real and 30,000 hypothetical pure silica zeolites for the separation of ethane and ethylene. None of the structures were found to be selective towards ethylene, indicating that olefin selectivity in zeolites is a consequence of the interaction of the carbon-carbon double bond with extra-framework metallic species. While strong π-complexes tend to form via olefin-transition metal interactions (Faiz and Li, 2012), the alkali metal ions present in the majority of reported olefin-selective zeolites (Na^+ in most cases) still provide additional olefin-specific interaction sites (Engerer and Hanusa, 2011).

In the last decade, the focus of the scientific community has shifted somewhat to include olefin/paraffin physisorption on non-zeolitic materials such as carbon- or alumino-phosphate-based porous solids. One of the first of these less traditional

materials shown to be paraffin selective was aluminium methylphosphonate polymorph alpha (AlMePO-α). Herdes and coworkers (2007) demonstrated that AlMePO-α selectively adsorbs the paraffin ethyl chloride from an ethyl chloride/vinyl chloride mixture through a combination of experimental and computational adsorption studies. The same simulation force fields and techniques were later applied to ethylene/ethane mixtures (Kroon and Vega, 2009), where the material was again found to preferentially adsorb the paraffin.

Purely carbonaceous materials have provided a rich source of paraffin selective materials. A range of computational studies have shown that, in the absence of surface impurities, the enthalpies of adsorption of paraffins are higher than those of the corresponding olefin in carbon-based adsorbents (Curbelo and Muller, 2005; Do and Do, 2005; Cruz *et al.*, 2010; Albesa *et al.*, 2012; Huang and Cao, 2013), a finding supported by the experimental work of Rawat et al (2011). With the exception of diamondyne (Huang and Cao, 2013), whose structure includes a small number of high energy sites which are only accessible to the smaller olefinic molecules, these materials were found to be paraffin-selective in competitive adsorption simulations.

To date, only two MOFs have been shown experimentally to be paraffin-selective – ZIF-7 (Gucuyener *et al.*, 2010; van den Bergh *et al.*, 2011) and ZIF-8 (Bohme *et al.*, 2013; Hara *et al.*, 2014; Liu *et al.*, 2014). While the different responses of the so-called ‘gating’ effect (Fairen-Jimenez *et al.*, 2012) in these structures to the paraffin and the olefin ensures that there is a significant kinetic contribution to the observed alkane/alkene separation factors, the alkane appears to be the more strongly adsorbed species, evidenced by the presence of the roll-up phenomena in the breakthrough experiments of Gucuyener *et al* (2010) and Böhme *et al* (2013) on ZIF-7 and ZIF-8 respectively, as well as the enhanced propane uptake at low pressure in the single component adsorption isotherms presented by Böhme *et al* (2013) on ZIF-8.

From a design perspective, it is preferred to seek a process which minimises the required quantity of separation medium and so minimise the size and thus capital and

operating cost of the unit. Given the propylene-rich nature of the feed stream, this suggests that a material which selectively removes propane from the mixture is most desirable in the case of absorption or adsorption, while for a membrane process it is advantageous for propane to be the faster permeating component. It is clear that adsorption is the only process of the three for which this criterion has been demonstrably met, with enhanced or preferred uptake of the paraffin being reported on a number of zeolites, carbon-based adsorbents and on the MOFs ZIF-7 (Gucuyener *et al.*, 2010) and ZIF-8 (Li *et al.*, 2009b). It is interesting to note that despite the seemingly limitless combinations of physical characteristics, topologies and chemical compositions accessible to MOFs, only two have been shown to be selective towards propane thus far. It is unlikely that ZIF-7 and ZIF-8 will ultimately prove to be unique amongst MOFs in this respect, an observation from which the central theme of this chapter emerges - how can we design a MOF which will selectively adsorb propane? Using insights gained from the simulation of both single- and multi-component adsorption of propane and propylene in a range of MOFs, the remainder of this chapter sets out to identify the structural features which are most desirable for selective propane adsorption.

3.2 Method

In the present work, the adsorption of propylene, propane and mixtures thereof was studied through GCMC simulations in a range of MOF structures as well as nine carbon-based, one-dimensional, triangular model pore systems. The MOFs and model pores which were selected for study are outlined in Section 3.2.1 alongside a summary of their structural characteristics. Details of the force field parameters used in this work and the various input parameters and details of the simulation setup may be found in Sections 3.2.2 and 3.2.3.

3.2.1 Structures of Interest: MOFs and Model Pores

In total, 21 metal-organic frameworks were selected for study. While many of these structures were chosen as they represent MOFs which were under active development as part of the MACADEMIA project, additional frameworks were included to ensure that the study encompassed a wide range of pore sizes, chemical compositions, surface areas and degrees of linker functionalisation. The MOFs included in the study, their composition and the dimensionality of their respective pore networks are listed in Appendix E.

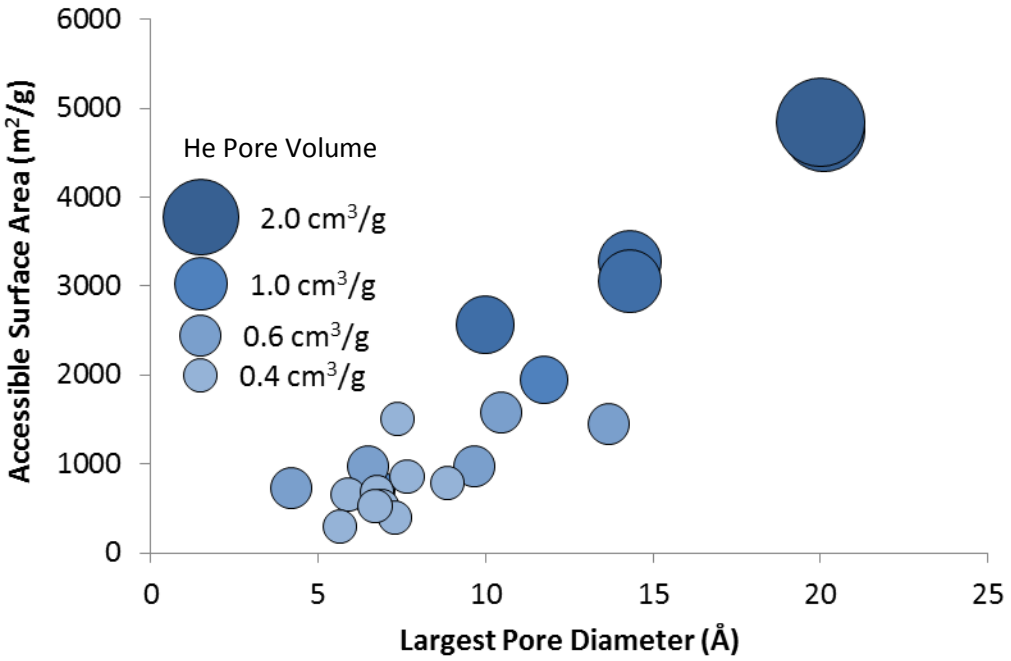

Figure 3.1 – Summary of the key structural characteristics of the investigated MOFs (blue circles). Larger helium pore volumes are indicated by larger circles and darker colours. Circles corresponding to pore volumes ranging from 0.4 – 2.0 cm^3/g are provided for comparison.

The key structural characteristics – helium pore volume, accessible surface area and pore size distribution of each of the MOFs studied were determined following the geometric methods outlined in Section 2.2.5. The results of this characterisation are listed in full in 0 and are summarised in Figure 3.1. These results confirm that the

selected frameworks cover a suitable range of pore volumes (ranging from 0.21 – 2.72 cm^3/g), surface areas (113 – 4840 m^2/g) and pore diameters (4.2 – 20.1 Å).

In order to decouple the effects of pore diameter from other linker-dependant variables such as composition and pore shape in one-dimensional structures, a system consisting of an array of identical, carbon-based, one-dimensional, equilateral triangular channels was chosen for study. The diameter of these channels was adjusted by altering the number of carbon atoms on each side of the triangle and, based on the calculated PSD of the various pore systems, was found to range from 2.9 – 22.1 Å. The creation of these model pore systems is discussed in detail in Section 2.1.2.

3.2.2 Force field Parameters

All MOF and model pore frameworks were assumed to be rigid during adsorption simulations. In the case of MOFs, atoms were kept fixed at their crystallographic positions, with the exception of the four UiO-66 frameworks, where the geometry optimised structures of Yang *et al* were used (Yang *et al.*, 2011b; Yang *et al.*, 2011c). The Lennard-Jones parameters for MOF atoms were taken from the DREIDING (Mayo *et al.*, 1990) or, for atoms for which DREIDING potentials were not available, UFF (Rappe *et al.*, 1992) force fields. These parameters are summarised in Appendix C. In order to incorporate propylene-MOF Coulombic interactions in the simulations, partial charges were included in each of the MOFs studied. Where available, charges derived from density functional theory (DFT) were taken from literature. For MOFs where literature charges were not available, charges were provided either by project partners (Yang and Maurin, 2010) or calculated using the extended charge equilibration (EQeq) method (Wilmer *et al.*, 2012a). The sources of partial charges used in this work are listed in Appendix D. As is common in simulations of carbon model pores (Bojan *et al.*, 1992a), the model pore systems were modelled as consisting solely of non-charged carbon atoms (σ = 3.4 Å, ε/k_B = 28 K).

Propylene and propane were modelled using united-atom models wherein the carbon and hydrogen atoms of each CH_x group within the C_3 molecule are combined into a single interaction site. Both molecules were treated as rigid – i.e. all bond angles and bond lengths were kept fixed at their equilibrium values[2]. In the case of propane, the TraPPE-UA model was used (Potoff and Siepmann, 2001), which contains two $CH_3\_sp^3$ sites and one $CH_2\_sp^3$ site, all of which are assumed to be charge neutral (q = 0.0 e). Following the work of Bae *et al* (2012), propylene was described using the TraPPE-UA model with additional point charges developed to reproduce the experimentally-observed dipole moment of the molecule (Gutierrez-Sevillano *et al.*, 2010) and thus includes non-zero charges on some sites. In this model, a 'dummy', negatively charged (q = -1.74 e) site is placed on the carbon-carbon double-bond and, to maintain overall charge neutrality, compensating positive charges (q = +0.87 e) are added to the $CH_2\_sp^2$ and CH_sp^2 interaction sites. The resulting C_3 molecules are depicted in Figure 3.2, while the corresponding Lennard-Jones and Coulombic parameters, along with the bond angles and lengths for the two models are summarised in Table 3.1.

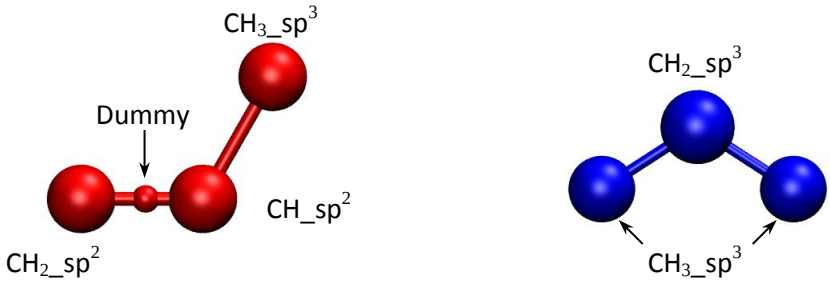

Figure 3.2 – Models of propylene and propane molecules used in this work.

All dispersion interactions were modelled using a truncated Lennard-Jones potential and a 15 Å radial cut-off. Electrostatic interactions between propylene and the MOF

[2] The validity of this assumption was investigated by comparing GCMC simulations with rigid sorbate molecules to simulations in which the C3 molecules were described using the appropriate TraPPE bond bending parameters in the MOFs MIL-47(V) and MIL-125(Ti). The inclusion of flexibility was not found to influence either single- or multi-component C_3 adsorption in these systems.

were calculated using the Ewald summation method (Ewald, 1921) with Ewald parameters optimised appropriately for each system (Frenkel, 1996), while propylene-propylene electrostatic interactions were calculated using the method of Wolf *et al* (1999).

Table 3.1– Bond lengths, angles and non-bonded parameters used for propylene and propane in this work.

Lennard-Jones and Coulombic Parameters			
Pseudo-atom	σ (Å)	ε/k_B (K)	q (e)
CH_sp^2	3.740	53.0	+0.87
$CH_2\_sp^2$	3.685	93.0	+0.87
Dummy	-	-	-1.74
$CH_3\_sp^3$	3.750	98.0	-
$CH_2\_sp^3$	3.950	46.0	-
Bond Lengths (Å)			
$CH_3\_sp^3$ - CH_sp^2	1.540		
CH_sp^2 – Dummy	0.626		
Dummy – $CH_2\_sp^2$	0.704		
$CH_3\_sp^3$ – $CH_2\_sp^3$	1.540		
Bond Angles (°)			
$CH_3\_sp^3$ - CH_sp^2 - $CH_2\_sp^2$	119.7		
$CH_3\_sp^3$ – $CH_3\_sp^3$ – $CH_3\_sp^3$	114.0		

3.2.3 Simulation Details

Pure component isotherms of propylene and propane, as well as multi-component isotherms of two different binary C_3 mixtures at 303 K were generated through GCMC simulations implemented in the MuSiC software package (Gupta *et al.*, 2003) as described in Section 2.2.2. Competitive adsorption simulations were undertaken for both an equimolar binary C_3 mixture (0.5 mole fraction propylene) and a

representative industrial binary mixture of 0.7 mole fraction propylene. The pressure for both single- and multi-component isotherms was from $1x10^{-7}$ – 10.7 bar, just below the saturation vapour pressure of the two components at 303 K (Lemmon *et al.*, 2014). Based on these pressure ranges, input fugacities for the GCMC simulations were calculated using the Peng-Robinson equation of state (Reid *et al.*, 1977). All simulations included at least $8x10^6$ initialisation steps followed by $12x10^6$ sampling steps and care was taken to ensure that simulations had reached equilibrium before sampling commenced.

In the analysis of binary adsorption isotherms, the selectivity (*S*) of the MOF is defined as follows:

$$S = \frac{x_{propylene}/x_{propane}}{y_{propylene}/y_{propane}} \qquad \textbf{Equation 3.1}$$

Wherein *x* and *y* represent mole fractions in the adsorbed and bulk phases respectively. In this construction, a selectivity of greater than unity indicates that the MOF selectively adsorbs propylene over propane, while a number less than unity indicates the reverse. Unless stated otherwise, reported selectivities are towards propylene.

3.3 Competitive C_3 Adsorption in MOFs in Low Loading Regimes

In this section, the adsorption of propylene and propane in MOFs at low loading where adsorption is dominated by the interaction between the adsorbed phase and the solid (Rouquerol *et al.*, 1999) is explored. In particular, the influence of pore size and linker functionalisation on the strength of C_3-MOF interactions and, ultimately, the selectivity of the structure will be evaluated.

3.3.1 Overview

Despite the relatively limited number of propane selective MOFs described in the literature, approximately half of the MOFs included in this study were found to preferentially adsorb propane at low C_3 loadings (Figure 3.3). In total, ten MOFs were found to be propane selective (a selectivity of less than 0.9) and nine were found to be propylene selective (a selectivity of greater than 1.1), while the remaining two (CAU-10 and IRMOF-3) exhibited selectivities between 0.9-1.1 and are essentially unable to discriminate between propylene and propane. Selectivities for adsorption of equimolar mixtures were found to range from 0.3 (MIL-140C) to 3.3 (MIL-68) and these values did not vary significantly when the bulk propylene concentration was increased to 0.7 mole fraction. The negligible influence of concentration on selectivity at low loadings is not unexpected. In this regime the selectivity of the material can be approximated as the ratio of the Henry's constants of the two species (Sarkisov, 2012), quantities which are not dependant on the bulk concentration of the species. In light of this, unless stated otherwise, further discussion of selectivity in this chapter will refer to adsorption of the equimolar mixture.

While MIL-68 and MIL-125(NH_2) were found to exhibit the highest selectivity towards propylene (S = 3.26 and 2.18 respectively), these are considerably lower than those reported on MOFs incorporating open metal sites e.g. CPO-27 (S = 24-46 (Bae *et al.*, 2012)), MIL-100(Fe) (S = 29 (Yoon *et al.*, 2010)) and it is clear that the inclusion of under-coordinated metal centres in the structure is the most effective way to enhance propylene selectivity in MOFs.

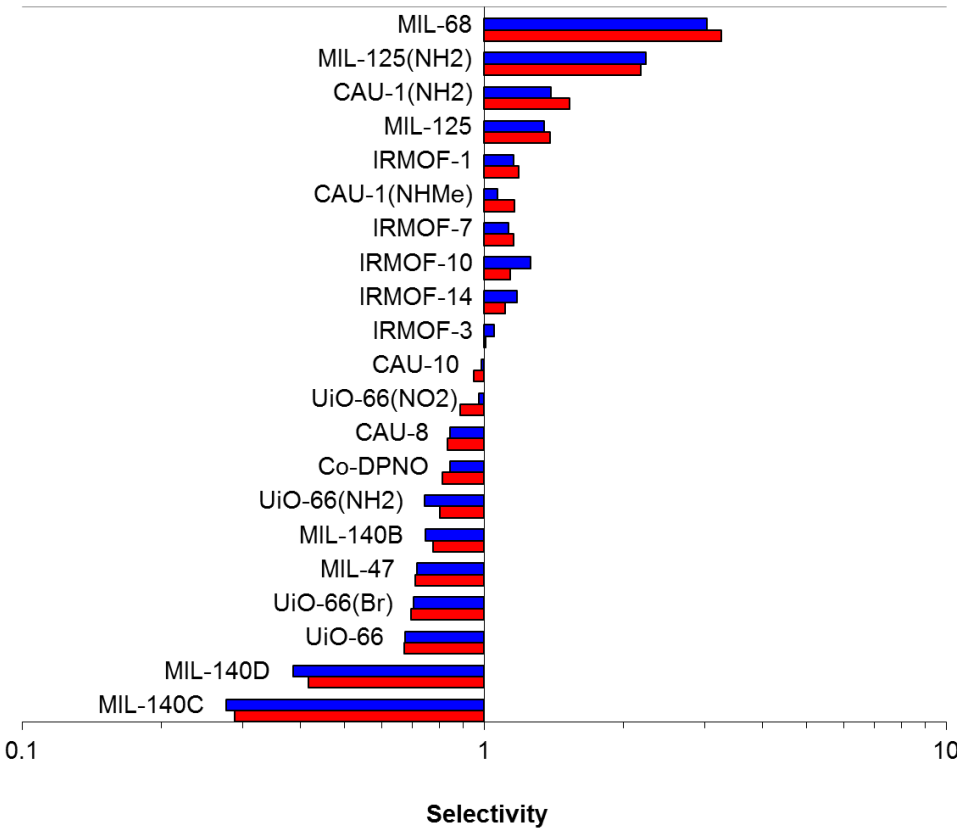

Figure 3.3 – Selectivity towards propylene from binary mixtures of 0.5 (red) and 0.7 (blue) bulk propylene mole fraction. The MOFs are ordered by equimolar selectivity and selectivities are displayed on a log scale.

Although the majority of the propane-selective MOFs exhibit relatively low selectivity (1.1 – 1.5 towards propane), both MIL-140C and MIL-140D demonstrate a strong preference for propane (S = 3.4 and 2.4 towards the paraffin respectively) and compare favourably to previously reported propane-selective materials, which range in selectivity from 1.3 in purely siliceous zeolites (Jakobtorweihen *et al.*, 2005) to 3.4 in carbon-based porous frameworks (Huang and Cao, 2013).

At low loading, multi-component adsorption is dominated by the competition between molecules of different species for the adsorption sites which provide the strongest interaction between the sorbate molecule and the adsorbent (Do, 1998), with the species which interacts more strongly with the framework generally being preferentially adsorbed. The behaviours observed in simulation (Figure 3.3) indicate

that these MOFs may be split into three categories: those in which propane interacts more strongly with the framework; those in which propylene interacts more strongly; and MOFs in which the sorbate-framework interactions of the two species are approximately equal. The sorbate-framework interaction energies of the two species may be easily compared by examining the ratio of these quantities to each other:

$$\alpha = \frac{E_{propylene-MOF}}{E_{propane-MOF}} \qquad \textbf{Equation 3.2}$$

Where E represents the average energy of interaction (kJ/mol) calculated from simulation data for the species pair indicated. Thus, a value of α which is greater than one indicates that propylene interacts more strongly with the framework. The close correlation between α and selectivity at low loading for the investigated MOFs is illustrated in Figure 3.4.

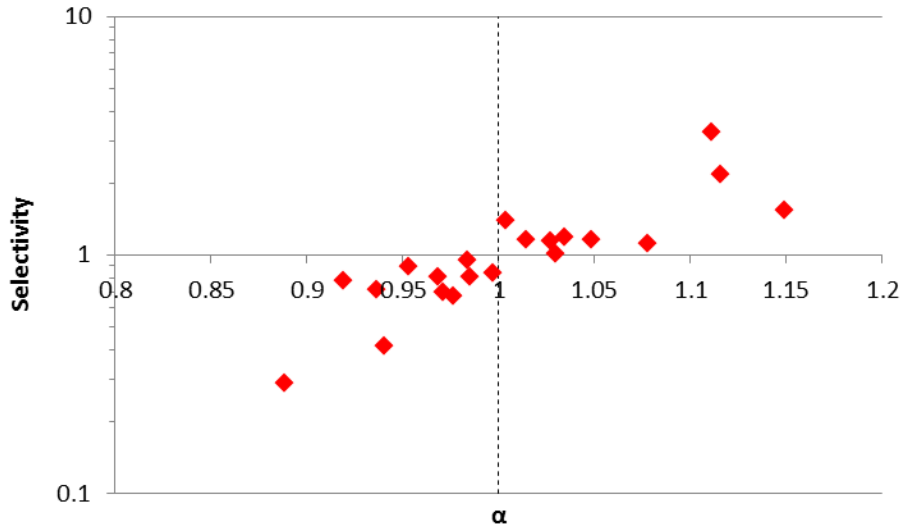

Figure 3.4 – Dependence of selectivity towards propylene at low loading on the ratio of C_3 sorbate-framework interaction energies, including electrostatic interactions for propylene, for the MOFs studied. The dashed line indicates a value of α = 1.

It is clear that the first step in designing a propane-selective MOF is to ensure that α is less than one and, for more strongly selective MOFs, preferably less than 0.95. Based on the molecular models used, there are two primary factors which determine

α: (1) the relative strength of the van der Waals interaction between molecule and framework for propylene and propane and (2) the magnitude of the electrostatic interaction between the MOF and the propylene dipole. In the vast majority of the MOFs in this study, the van der Waals contribution favours propane as shown in Figure 3.5. The same figure demonstrates that while the electrostatic contribution is always attractive in nature, leading to an increase in α, there is considerable variation in the magnitude of this increase. In order to ensure that α is less than unity, it is therefore necessary to understand how to both maximise the van der Waals discrimination towards propane and minimise the electrostatic interaction of propylene with the framework.

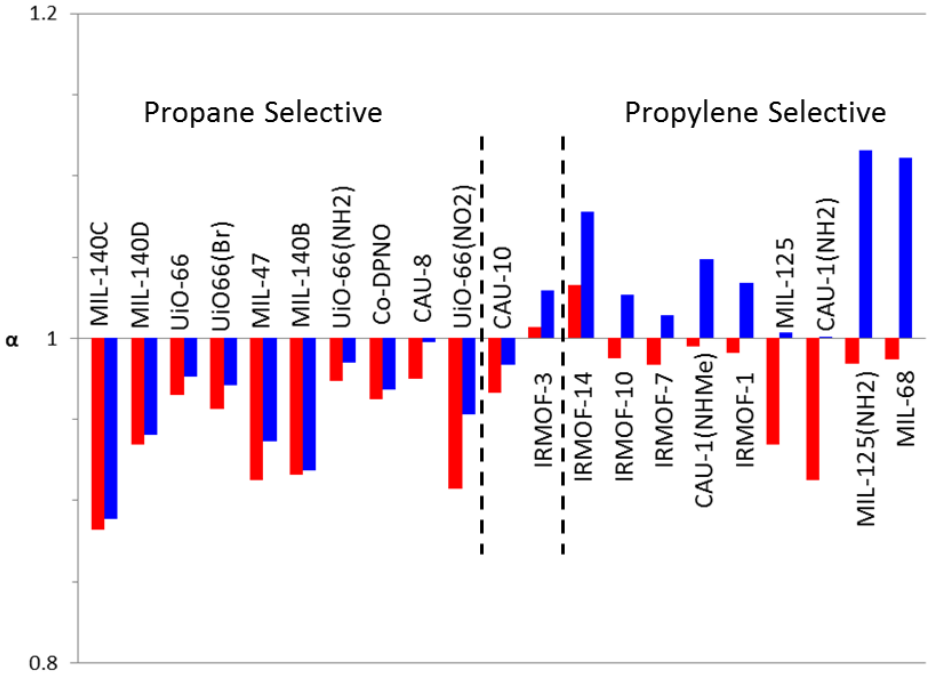

Figure 3.5 – Ratio of C_3-MOF interaction energy (α) with propylene dipole-MOF interactions excluded (i.e. solely van der Waals interactions - red) and included (blue). The MOFs are ordered by selectivity, with the most propylene selective on the right.

3.3.2 Influence of van der Waals Interactions

In all but two MOFs, propane was observed to exhibit a stronger van der Waals interaction with the framework than propylene in both single-component and mixture

simulations, with C_3-MOF van der Waals interactions for the paraffin found to be an average of 5.2% greater than those for the olefin. This relative enhancement in propane-MOF van der Waals interactions differs noticeably between MOFs, ranging from essentially negligible in IRMOFs 1, 3 and 14 to 13.4% in MIL-140C.

When only van der Waals interactions are considered, the lowest C_3-framework interaction ratios (α_{VdW}) are observed in systems which contain comparatively small pores - less than 8 Å in diameter. As the pore diameter increases, the MOF is less able to discriminate between the two molecules from an energetic perspective and α_{VdW} tends towards unity, a pattern which is replicated in competitive adsorption simulations carried out in triangular model pores (Figure 3.6).

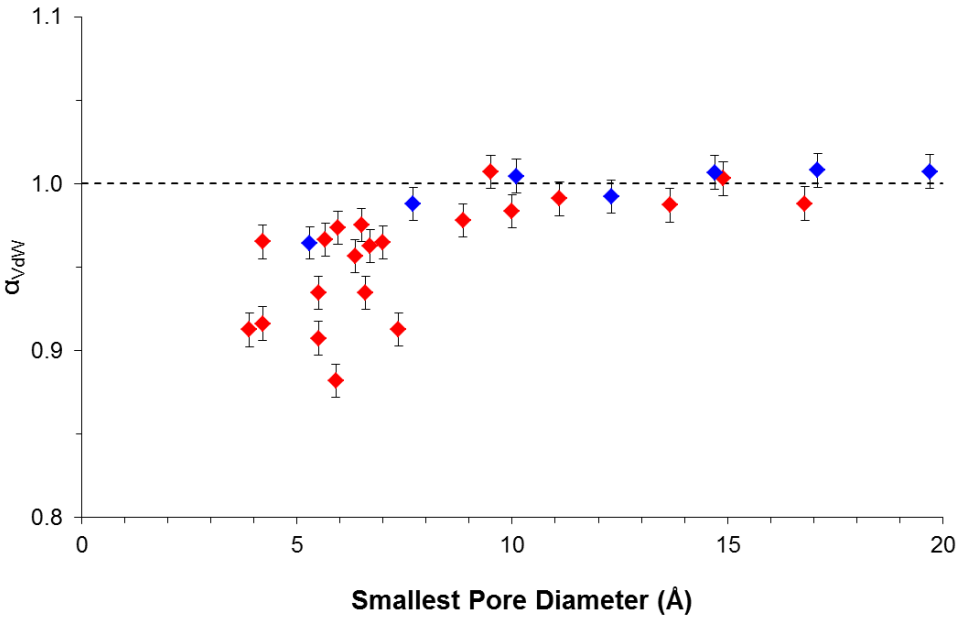

Figure 3.6 – Variation of C_3-MOF interaction energy ratio (α_{vdw}) with pore diameter based solely on van der Waals interactions in MOFs (red) and triangular model pores (blue). In the case of MOFs which contain two or more types of cavity, the smallest accessible pore diameter (i.e. the pore into which C_3 molecules are adsorbed at low loading) is used.

The reduction in pore diameter ensures that adsorbed C_3 molecules are able to interact strongly with a higher number of framework atoms, resulting in a higher

enthalpy of adsorption. To illustrate this concept, consider the adsorption of a single $CH_3\_sp^3$ pseudo-atom in model, triangular channels. The total interaction energy of this atom with the carbon framework as it is moved from one corner of the pore to the opposite wall is shown in Figure 3.7 for channels of increasing diameter.

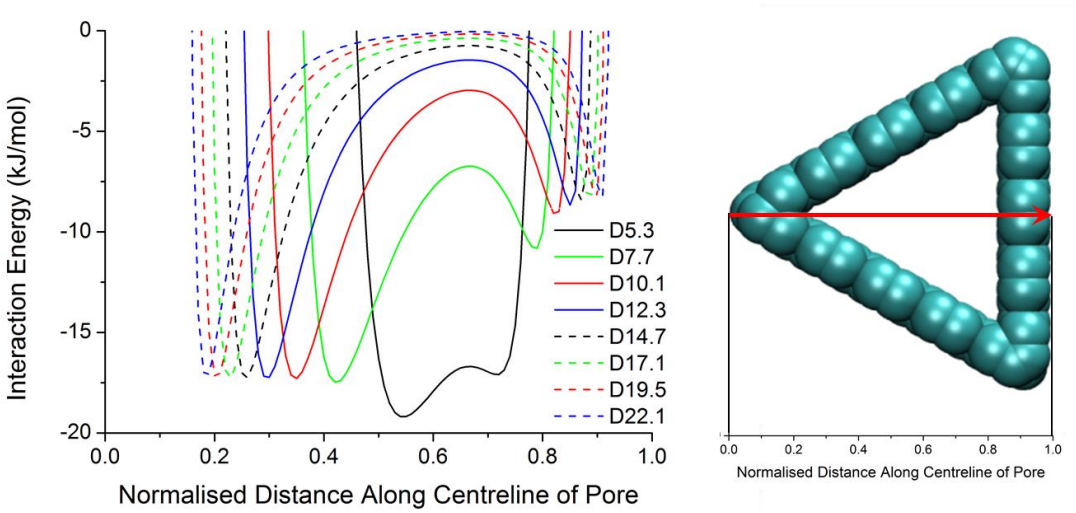

Figure 3.7 - Path used in determining the total interaction energy profile of a $CH_3\_sp^3$ atom with the framework (right – red arrow) and total interaction energy with the framework for a $CH_3\_sp^3$ atom as a function of distance along the triangular pore for increasing channel diameter (left). The channel diameters determined from the PSD are indicated to the nearest 0.1 Å.

The observed asymmetric profile is indicative of the different adsorption environments near the corner (normalised distance → 0) and near the wall of the pore (normalised distance → 1). Near the corner of the pore, the $CH_3\_sp^3$ atom strongly interacts with two pore walls, rather than the single wall available when adsorbed on the opposite side of the pore, resulting in an appreciable enhancement in total interaction energy. Similarly, as the pore size is decreased, the adsorbed atom is able to interact more strongly with all three pore walls, resulting in the interaction energy becoming non-negligible in the centre of the pore. For the smallest pore studied (d = 5.3 Å), the pore walls are sufficiently close to one another that the $CH_3\_sp^3$-framework interaction energy profile begins to converge towards a single, much deeper energy minimum.

In addition to generating a much stronger C_3-framework interaction, the increased overlap of potentials present in the 5.3 Å and 7.7 Å diameter model pores is fundamental to the ability of these structures to differentiate between propylene and propane based on their interaction energies. The energy minima observed in Figure 3.7 represent the optimum position for $CH_3\_sp^3$ atoms to be located during adsorption at low loading, ensuring the maximum interaction with the framework. Assuming that each CH_x pseudo-atom is located close to their optimum positions, the theoretical maximum C_3-framework interaction energy may be approximated as being the sum of the maximum individual CH_x-framework interaction energies and, from these C_3 interaction energies, a theoretical value of α_{VdW} may be determined. Thus, evaluation of the sorbate-framework interaction energy profiles for each of the four CH_x pseudo-atoms (Figure 3.8) allows the enhancement in α_{VdW} at reduced pore diameters to be explored.

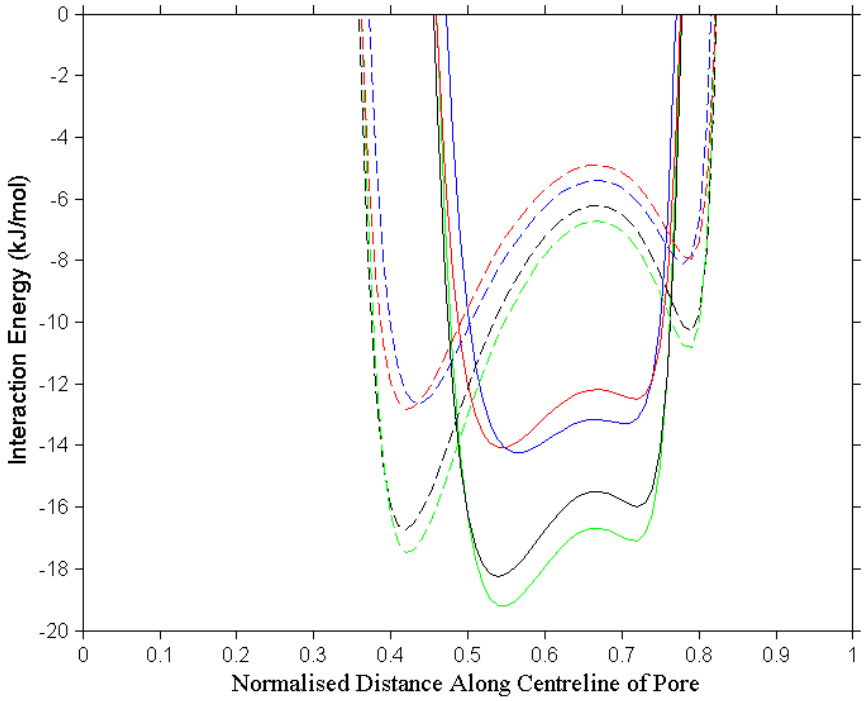

Figure 3.8 – Interaction energy profiles for the four CH_x pseudo-atoms in 5.3 Å (solid lines) and 7.7 Å (dashed lines) diameter model pores: $CH_3\_sp^3$ (green), $CH_2\_sp^3$ (blue), $CH_2\_sp^2$ (black) and CH_sp^2 (red).

On comparison of the energy profiles in these two pores, it is clear that the overlap of potentials observed on reduction of the pore diameter introduces a scaling factor to

the minima observed in the potential profiles, which has the effect of amplifying any existing difference in CH_x-framework interactions. Consider, for example, one end of the C_3 molecules, where the $CH_2\_sp^2$ group of propylene is replaced with a $CH_3\_sp^3$ group in propane. In the 7.7 Å diameter pore, this replacement results in a 0.73 kJ/mol enhancement in interaction energy, compared to 0.92 kJ/mol in the smaller pore. Although this increases the absolute difference between $CH_3\_sp^3$- and $CH_2\_sp^2$-framework interaction energies, it does not affect the ratio of these energies to one another as the maximum interaction energies for the two groups are increased by a similar factor.

The overlapping wall potentials have a greater influence on the central atoms of the C_3 molecules. In the larger pore, the central pseudo-atoms (CH_sp^2 in propylene and $CH_2\_sp^3$ in propane) interact primarily with the corner atoms of the pore. The CH_sp^2 group thus has a lower energy minimum than $CH_2\_sp^3$ as a result of it having a higher value of LJ epsilon. In contrast, in the smaller pore, the $CH_2\_sp^3$ group – having the largest value of LJ sigma – feels the presence of the opposite wall more strongly and thus has a lower energy minimum than CH_sp^2.

When all CH_x groups are assumed to be located in their energetically optimal positions, α_{VdW} can be seen to decrease slightly from 0.99 to 0.98 in, respectively, the 7.7 Å and 5.3 Å pores. This decrease is a result of the switch in the order of maximum interaction energies of the central CH_x groups – in the absence of this reversal, the theoretical value of α_{VdW} for ideally positioned C_3 molecules would remain unchanged. The non-linear nature of the C_3 molecules, however, ensures that not all CH_x groups can be located in their optimum positions and it is this departure from ideality which is responsible for the decrease in α_{VdW} in smaller pores which is observed in adsorption simulations (Figure 3.6). The sub-optimal positioning of CH_x groups manifests itself in a noticeable difference between the theoretical maximum interaction energy and the observed interaction energy during GCMC simulations. In the 5.3 Å pore, for example, the observed propane-framework interaction energy (-48.0 kJ/mol) is only 90% of the calculated theoretical maximum interaction energy (-52.6 kJ/mol). Furthermore, due to the different bond angle and CH_x bond lengths

present in propane and propylene, the impact of this sub-optimal atomic positioning need not be the same for each C_3 molecule. In the 7.7 Å pore, while neither propane or propylene are able to position themselves so as their respective CHx groups are in the energetically optimal positions, they are both able to locate themselves equally close to the optimum and the observed and calculated values of α_{VdW} are therefore identical. In the smaller pore, the pore dimensions more closely match those of the slightly larger propane molecule, allowing the terminal CH_x groups to sit closer to their respective optimal positions (i.e. the corners of the pore) than in propylene. As the propylene CH_x groups are further from their optimal positions than those in propane, the observed α_{VdW} (0.96) is much lower than the calculated value (0.98). It is clear, therefore, that while a slight van der Waals preference for propane may be predicted based solely on the interaction potentials, the observed preference may be significantly enhanced through the alteration of pore shape.

The impact of pore shape becomes more apparent when the enhancement in van der Waals discrimination towards propane in MOFs is considered, as evidenced by the much wider distribution in α for similar pore diameters seen in Figure 3.6. Indeed, in the MIL-140 series of MOFs - the closest analogues of the triangular model pores previously investigated - the lowest value of α_{VdW} is observed not in the smallest pore but in an intermediately-sized channel.

The MIL-140 series of frameworks (Guillerm *et al.*, 2012) are based on infinite, 1D zirconium oxide chains connected to one another via one of four different organic linkers (Figure 3.9), creating a framework consisting of 1D triangular channels with pore diameters ranging from 3.3 Å (MIL-140A) to 6.6 Å (MIL-140D). C_3 adsorption simulations carried out in MIL-140A showed that the pore is too small to allow either propane or propylene to adsorb and hence this work shall focus on the three remaining structures.

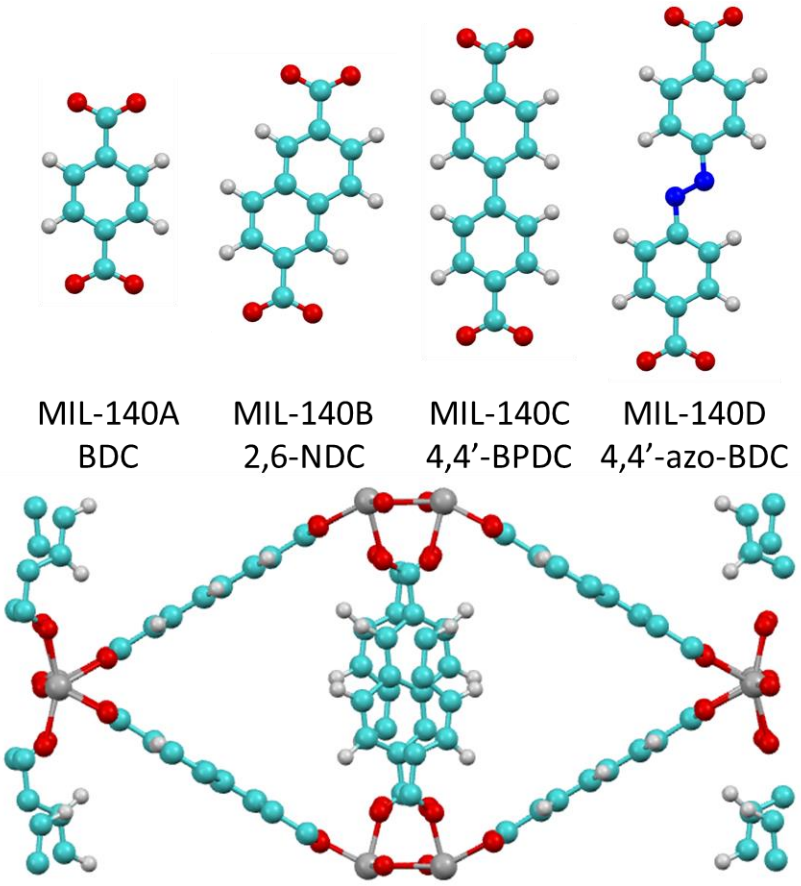

Figure 3.9 – The four linkers used in the MIL-140 series (top) and a single unit cell of MIL-140B (bottom) demonstrating the array of one-dimensional triangular channels common to all of the MOFs in this series. Colour scheme: C – cyan; H – white; O – red; N – blue; Zr – grey.

Although the pores in the MIL-140 series are less homogenous in composition and in geometry than the triangular model pores, the variation in total CH_3_sp^3-framework van der Waals interaction across the centrelines of the MIL-140 pores (Figure 3.10) follows a similar pattern to that observed in the model pores. A distinctly asymmetric energy profile is present in MIL-140C and D as the probe atom is moved from the corner of the pore, through the middle of the pore to the opposite wall. As observed in the triangular model pores, the two distinct energy minima in the profile begin to converge to a single minimum as the pore diameter is decreased from 6.6 Å (MIL 140D) to 5.9 Å (MIL-140C). A further reduction in pore diameter to 4.2 Å (MIL-140B) sees the completion of this convergence and the probe atom now interacts equally strongly with all three pore walls.

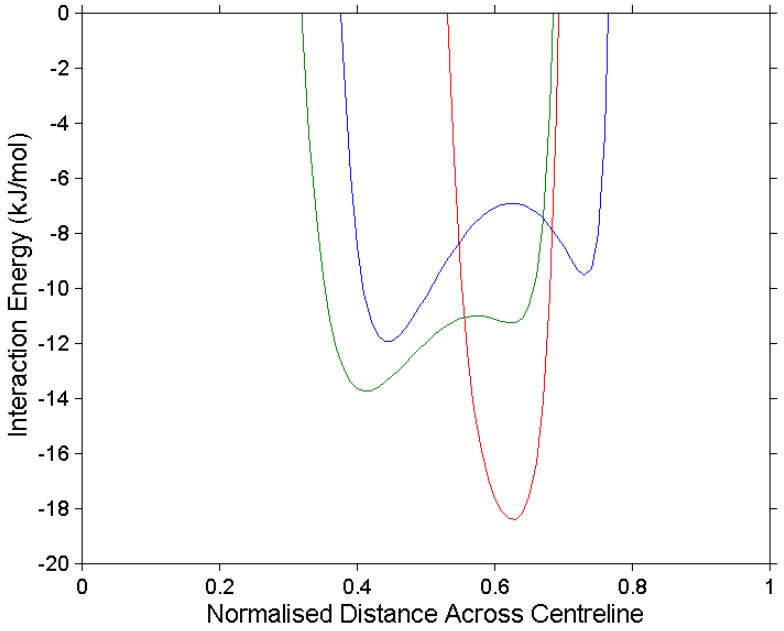

Figure 3.10 – CH_x-MOF van der Waals interaction energy profiles for the CH_3_sp^3 pseudo-atom in the pores of MIL-140B (red), MIL-140C (green) and MIL-140D (blue). The centreline was determined following the conventions outlined in Figure 3.7.

As described for the model pore systems, the theoretical maximum total C_3-MOF interaction energy - and associated values of α_{VdW} - in each of the three MIL-140 structures may be approximated using the determined energy minima for the individual CH_x pseudo-atoms. These values are compared with the actual values of van der Waals interaction energy and α_{VdW} observed in GCMC simulations in Table 3.2.

Table 3.2 - Summary of theoretical (i.e. calculated from minima in the energy landscape of the various CH_x groups) and observed values of C_3-MOF van der Waals interaction energies and α_{vdW}.

	$E_{VdW,propylene\text{-}MOF}$ (kJ/mol)		$E_{VdW,propane\text{-}MOF}$ (kJ/mol)		α_{VdW}	
MOF	Theoretical	Observed	Theoretical	Observed	Theoretical	Observed
MIL-140B	-46.6	-38.0	-51.2	-41.5	0.91	0.92
MIL-140C	-37.3	-29.3	-41.0	-33.2	0.91	0.88
MIL-140D	-33.3	-23.4	-36.6	-24.9	0.91	0.93

As was the case in the model pore systems, the C_3-framework van der Waals interactions observed in simulation are considerably lower than the calculated theoretical maxima, ranging from only 68% to 82% of the maximum value. The combination of pore and sorbate shape results in the various CH_x groups being positioned some distance away from their energetically optimum locations and, again, this effect can have a greater influence on one or other of the C_3 molecules. In contrast to the model pores, no reduction in the theoretical α_{VdW} was observed on reduction of the pore diameter. In the two smallest model pores, a reversal in interaction orders was found for the CH_sp2 and CH2_sp3 groups, which was responsible for the reduction in theoretical α_{VdW}. In all three MOF structures, the CH_2_sp3 group has a much lower energy minimum than the corresponding CH_sp2 pseudo-atom. In the absence of this reversal in interaction strengths, there is no change in theoretical α_{VdW}. The values of α_{VdW} observed in GCMC simulation, however, do show considerable variation. In the case of MIL-140B and MIL-140D, propylene is able to access more favourable configurations than propane. In MIL-140B, the optimum locations are in the centre of the channel, running along the length of the pore. Both C_3 molecules adsorb in the centre of the channel with their long axes aligned with the channel axis. The smaller kinetic diameter of propylene therefore ensures that the distance from channel centre to each of the CH_x groups is minimised compared to propane. The observed propylene-MOF interaction energy is thus closer to its theoretical maximum than propane and α_{VdW} is thus shifted slightly towards propylene. In MIL-140D, the optimum positions are in the corners of the pore and, as in MIL-140B, the smaller propylene molecule is able to minimise the distance between optimal and obtainable CH_x locations, resulting in a higher than predicted value of α_{VdW}. In MIL-140C, the observed value of α_{VdW} is much lower than predicted. In this case, the pore is better suited to the slightly larger propane molecule. As in the 5.5 Å model pore, the longer propane molecule is better able to locate its terminal CHx groups in opposite corners of the pore and more fully optimising its interaction energy as a result.

While we can predict that structures with pores of less than 8 Å in diameter will exhibit a preference for propane based on van der Waals interactions, the electrostatic interaction of propylene with the MOF is capable of reversing the overall energetic preference (Figure 3.5). We now turn our attention, therefore, to the impact of the structure and composition of the MOF on this electrostatic interaction.

3.3.3 Influence of Electrostatic Interactions

The electrostatic interaction between the propylene dipole and the framework was found to be an attractive contribution in all MOFs, ranging from -0.1 to -5.0 kJ/mol. Given that the difference between the C_3-MOF van der Waals contributions for the two species was typically around 2 kJ/mol, the strength of the propylene-MOF Coulombic contribution goes a long way towards determining the energetic selectivity of the material. In this section, the dependence of electrostatic contribution on pore diameter in one-dimensional MOFs is explored along with the influence of linker functionalization on the electrostatic contribution in UiO-66, MIL-125 and IRMOF-1.

In total, eight MOFs with 1D pore systems were included in the study: MIL-140B, MIL-140C, MIL-140D, CAU-8, CAU-10, Co-DPNO, MIL-47(V) and MIL-68(V). Of these, seven had channels less than 8 Å in diameter, while the channel in MIL-68(V) was much larger (13.7 Å). As such, additional simulations in CPO-27(Ni) were carried out in order to introduce an intermediately sized pore (11 Å) to the study and bridge the gap between MIL-68(V) and the other MOFs. As outlined in Section 3.1, CPO-27(Ni) contains a high density of open metal sites whose impact on propylene adsorption is not accounted for in the models used in this work. For this reason, while inclusion of CPO-27(Ni) in this study allows the link between pore diameter and C_3-MOF electrostatic interactions to be examined more fully on a purely theoretical basis, the simulation results on this MOF are not considered outwith of this section.

In these 1D MOFs, the magnitude of the electrostatic interaction between the carbon-carbon double bond (C=C) and the framework depends strongly on the diameter of the channel (Figure 3.11), with small pore MOFs generating only slightly attractive interactions (-0.1 to -0.8 kJ/mol) when compared to the larger CPO-27(Ni) and MIL-68(V) channels (-3.8 and -5.0 kJ/mol respectively).

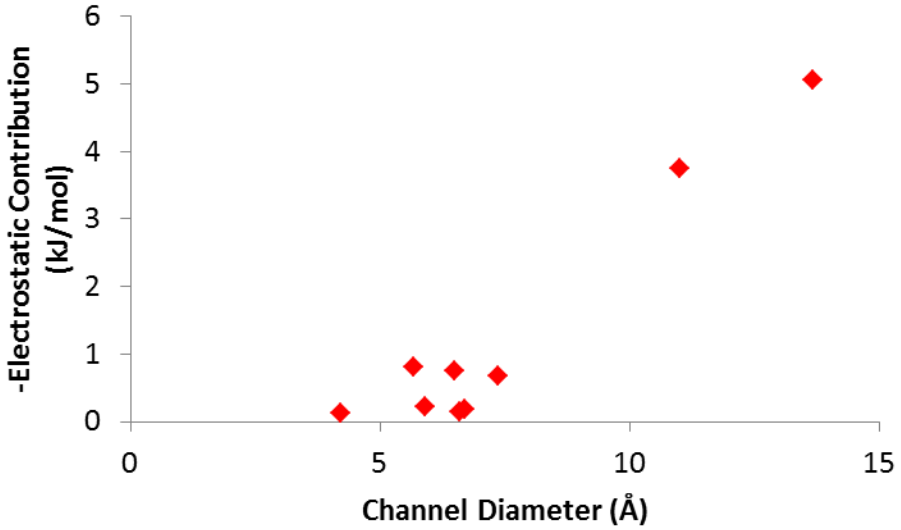

Figure 3.11 – Variation in total electrostatic interaction between the propylene quadrupole and the MOF for 1D channel systems at 303 K and low levels of propylene loading.

The increase in electrostatic interactions with increasing pore diameter is at first glance somewhat counter-intuitive, as a greater degree of overlap in the interaction potentials would normally be expected to occur in smaller pores, producing a stronger interaction. In order to explain this unexpected behaviour, it is necessary to first consider the hypothetical Coulombic interaction of the dipole with the framework in the absence of any competing van der Waals interactions. To this end, additional simulations were carried out using a version of the Kh_d toolset (Sarkisov, 2012) modified in-house. In these simulations, the MOF unit cell was discretised on a 0.25 Å grid and the interaction of a probe molecule with the framework at each point on the grid was evaluated and averaged over 1000 trial orientations. The interaction of two different versions of a propylene probe molecule in MIL-140C, MIL-47(V) and MIL-68(V) was studied. In the first instance, the propylene probe

was considered to interact with the framework solely via a Coloumbic interaction (i.e. the probe did not have a volume and could not physically overlap with framework atoms). This Coulombic interaction was determined using the method of Wolf *et al* (1999) with a cut-off radius of 15 Å. In the second case, the propylene probe interacted with the framework solely via van der Waals interactions.

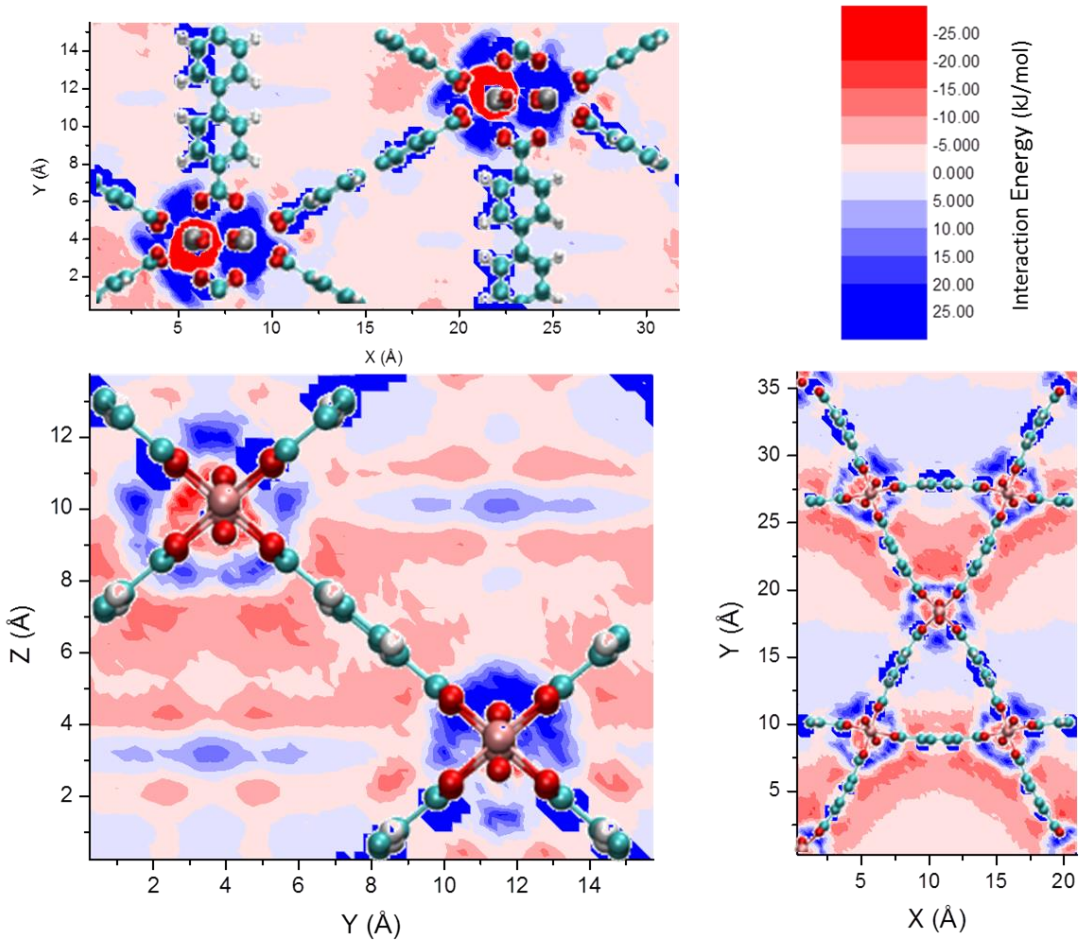

Figure 3.12 – Cross-section of C=C-MOF electrostatic interaction energy profile in a plane perpendicular to the channel axis for MIL-140C (top-left), MIL-47(V) (bottom-left) and MIL-68(V) (bottom-right). The positions of the framework atoms are indicated (ball-and-stick representation). Atom colour scheme: V – pink; Zr – grey; C – cyan; H – white; O – red.

Cross-sectional slices of the C=C-MOF electrostatic interaction profiles obtained from simulations in which only electrostatic interactions were considered are shown in Figure 3.12. In each case, the most repulsive electrostatic areas (dark blue) are

located near the oxygen atoms of the metal oxide cluster and the carbon atoms of the linker, while the most attractive areas (dark red) are near the metal atoms and near the hydrogen atoms of the linkers. The arrangement of the linkers within these channels is such that no linker is directly opposite another linker, which results in the asymmetric profiles observed in Figure 3.12. At the top of the image, the slice coincides with the hydrogen atoms of the linkers and represents a strongly attractive region (-5 to -15 kJ/mol), while at the opposite pore-wall (the bottom of the image) the slice coincides with the carbon atoms of the linker and is seen to be slightly repulsive (0 to +5 kJ/mol). The regions near the pore walls are thus composed of alternating strongly attractive and weakly repulsive regions as one moves along the length of the channel. The overall effect, therefore, is that the near-wall regions may be considered to be slightly attractive overall. In the centre of the pore, however, the two opposite wall potentials essentially cancel each other out, resulting in a neutral zone where the interaction energy is close to zero. Irrespective of channel diameter, adsorption near the pore wall can be seen to maximise the electrostatic interaction between quadrupole and MOF, while adsorption near the centre of the channel generates much lower Coulombic interaction energies. It should be noted that while the method employed in this work to calculate the C=C-MOF electrostatic interaction returns the *average* interaction energy at each grid point, it is possible that for areas in which the probe experiences overall slightly repulsive interactions there may be specific orientations of the quadrupole which generate attractive interactions. Given that the quadrupole is likely to align itself so as to maximise the attractive interaction, future work should investigate the existence of these orientations in more detail.

Having identified the ideal adsorption locations within MOF channels for the propylene dipole from an electrostatic perspective, we now consider how well these optimal electrostatic adsorption sites mesh with the optimal van der Waals adsorption sites in each of the three MOFs. Examination of propylene-MOF van der Waals interaction profiles obtained through simulations in which only vdW interactions were considered allows the inaccessible regions of the unit cell, along with the preferred van der Waals adsorption sites, to be identified. Cross-sectional slices

through these profiles, analogous to those presented in Figure 3.12, for MIL-47(V) and MIL-68(V) are shown in Figure 3.13. It is clear that in MIL-68(V), the preferred van der Waals adsorption sites are near the pore walls, which coincides with the preferred electrostatic interaction sites. In MIL-47(V), the overlap in van der Waals wall potentials due to the smaller pore size mean that the preferred adsorption sites are in the centre of the channel, coincident with the regions of near-zero electrostatic potential. The lower propylene-MOF electrostatic interaction energies observed in GCMC simulations in smaller channels sizes is thus a result of a mismatch in ideal electrostatic adsorption sites and ideal van der Waals adsorption sites.

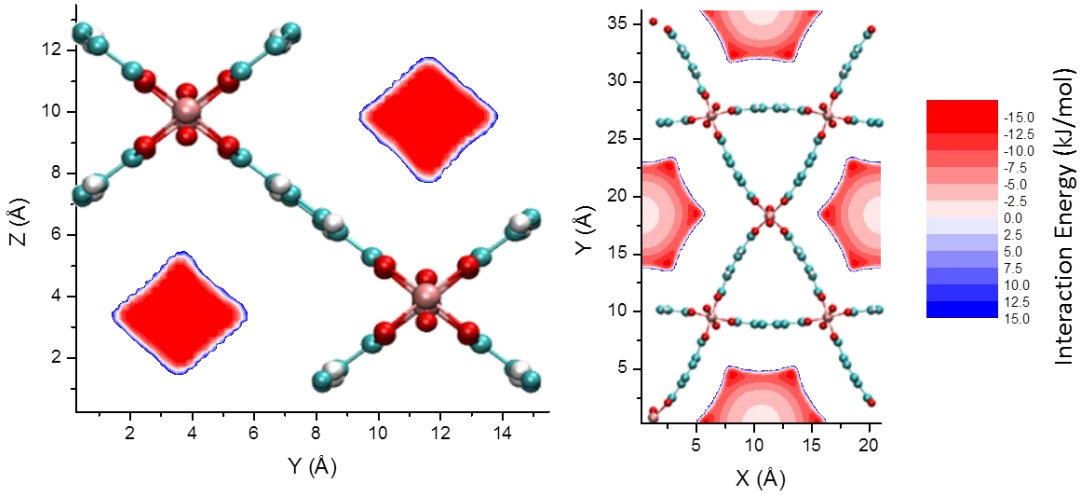

Figure 3.13 - Cross-section of propylene-MOF van der Waals interaction energy profile in a plane perpendicular to the channel axis for MIL-47(V) (left) and MIL-68(V) (right).

Further evidence for this may be seen when the propylene-MOF electrostatic interactions calculated from GCMC simulations at higher pressures are examined (Appendix F). In the case of MIL-140B, where steric restrictions mean that the ideal van der Waals adsorption sites are the *only* adsorption sites, the propylene-MOF electrostatic interaction is unchanged at higher pressure. In MIL-140D and MIL-47(V), an increase in average propylene-MOF electrostatic interaction strength is observed at increasing pressure as molecules begin to adsorb at the less van der Waals-favourable sites away from the centre of the channel, which correspond to the better electrostatic interaction sites. In MIL-68(V), where the less favourable van der

Waals sites correspond to less favourable electrostatic sites, weaker propylene-MOF electrostatic interactions are observed at higher pressures.

While this phenomenon is not restricted to 1D channels, it is more challenging to predict in 3D pore systems. IRMOF-1, for example, consists of two large pores (11.1 Å and 14.3 Å in diameter respectively) but exhibits comparatively low propylene-MOF electrostatic interactions (-0.8 kJ/mol) in GCMC simulations. As in the 1D MOFs, the areas near the carbon atoms of the linker were found to be slightly repulsive (0 to +5 kJ/mol) when explored using the dipole molecular probe, while the corners of the pore were slightly attractive (0 to -5 kJ/mol). Two preferred van der Waals adsorption sites in IRMOF-1 were identified – one in the corners of the pore and another aligned with the carbon atoms of the linker. The electrostatic contributions from these two sites thus cancel each other out when averaged over the course of the GCMC simulation, resulting in low overall propylene-MOF electrostatic interactions.

The adjustment of the pore diameter of the structure is not the only way in which the propylene-MOF electrostatic interaction may be altered, however. Functionalization of the organic linker allows the introduction of additional polar groups to the system, which will alter the charge distribution on the framework. In general, the introduction of additional polar groups has shown to be beneficial with regards the adsorption of polar molecules (Torrisi *et al.*, 2010; Yang *et al.*, 2011c). In this work, the impact of functionalization on propylene-MOF electrostatic interactions was examined in three frameworks: UiO-66 (with BDC, Br-BDC, NH_2-BDC or NO_2-BDC linkers), MIL-125 (BDC or NH_2-BDC) and IRMOF-1 (BDC or NH_2-BDC). The propylene-MOF Coulombic contribution calculated from GCMC simulations at low loading in each of these systems is summarised in Figure 3.14. In the MIL-125 and UiO-66 series, the introduction of functional groups results in stronger propylene-MOF electrostatic interactions. In IRMOF-1, however, the introduction of an NH_2 group to the linker produces the opposite effect – the average electrostatic interaction at low loading is weaker in IRMOF-3 (-0.42 kJ/mol) than in IRMOF-1 (-0.8 kJ/mol).

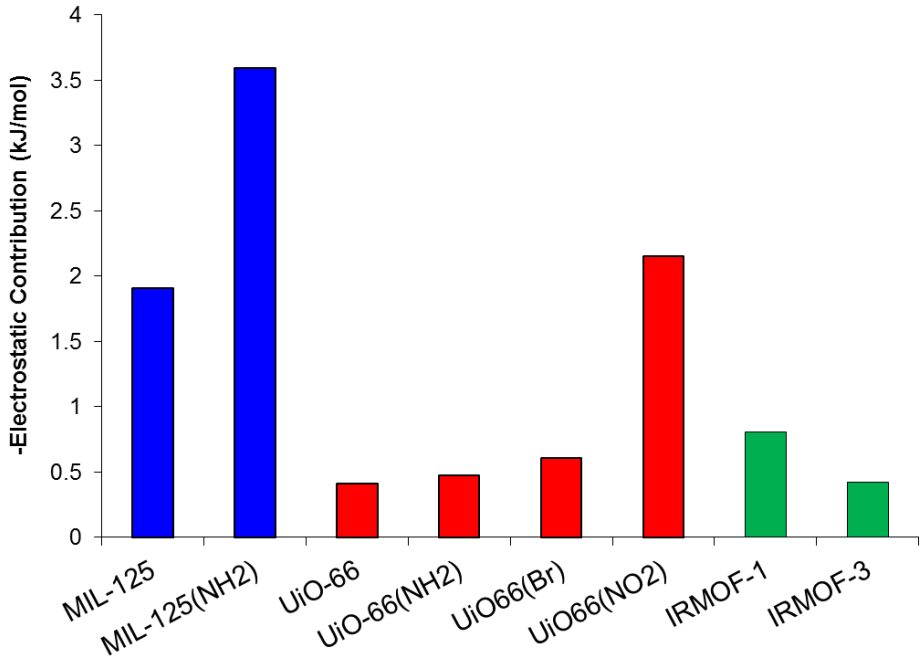

Figure 3.14 – Propylene-MOF electrostatic interaction in the various forms of the MIL-125 (blue), UiO-66 (red) and IRMOF-1 (green) structures. Note that IRMOF-3 is the NH_2-functionalised analogue of IRMOF-1.

This unexpected behaviour in the IRMOF-1 system is in fact an extension of the mechanism responsible for the overall low electrostatic interactions in the un-modified IRMOF-1 structure outlined previously. One of the two preferred van der Waals interaction sites in the IRMOF framework is near the aromatic carbon atoms of the linker. Each of these atoms carries a slightly negative charge (q_C = -0.14 e), and it is this slightly negative charge with results in an overall repulsive environment for the dipole. By functionalising the linker, one slightly positively charged hydrogen atom (q_H = +0.15 e) is replaced with an NH_2 group (q_N = -0.962 e, q_H = +0.425 e). The preferred van der Waals adsorption site remains near the benzene ring, but the introduction of the extremely negatively charged nitrogen atom means that the local electrostatic environment is now even more repulsive for the quadrupole. The electrostatic environment in the corner of the pore remains unchanged and attractive to the dipole and the two preferred van der Waals adsorption sites for IRMOF-3 thus average out to be much closer to zero than in IRMOF-1. In order to maintain overall

charge neutrality, the regions of pore space near the hydrogen atoms of the NH2 group of IRMOF-3 (near the centre of the pore) are considerably more attractive to the dipole than the same regions in IRMOF-1. As such, while the propylene-IRMOF-1 electrostatic interactions remain unchanged (-0.79 kJ/mol) at higher pressures, where propylene molecules begin to fill the centre of the pore, the total propylene-IRMOF-3 electrostatic interactions shows a considerable increase as molecules start to adsorb in this central region (-0.90 kJ/mol).

In the much more confined pores of MIL-125 (d = 5 Å) and UiO-66 (d = 6.5 Å), the positively charged atoms of the substituent groups – which represent attractive regions to the dipole – play a greater role at low loadings. MIL-125 consists of two pore types, one much smaller than the other (d = 5 Å and 11 Å respectively) and, at low loading, adsorption takes place primarily in the smaller of the two. This smaller pore is defined by the edges of the BDC linkers (Figure 3.15), so as the hydrogen atoms of the linkers protrude into the pore. The introduction of an NH_2 group onto the linker means that both hydrogen atoms of the amino group now protrude into the smaller pore and the total number of hydrogen atoms per small pore is increased. The presence of the adjacent nitrogen atom leaves the amino hydrogen atoms much more positively charged (q = +0.305 e) than the equivalent atom in the un-modified MOF (q = +0.145 e). These two factors combine to increase the electrostatic interaction considerably at low loading.

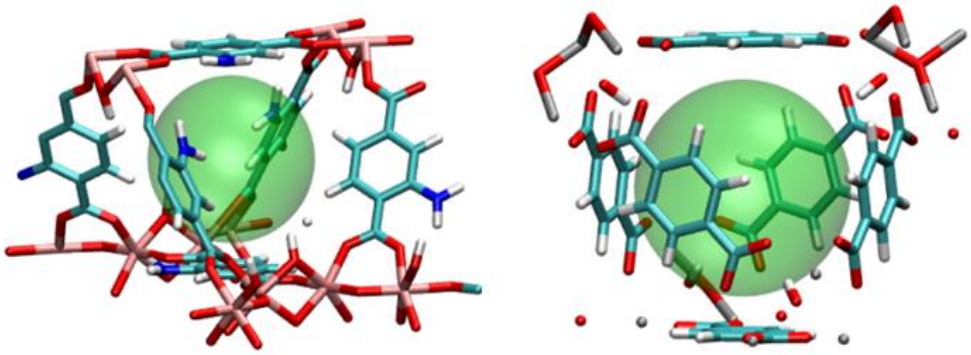

Figure 3.15 – The smaller pores of MIL-125(NH_2) (left) and UiO-66 (right). The transparent green spheres represent the pore diameters as determined from the PSD. Colour scheme: C – cyan; H – white; O – red; Ti – pink; N – blue; Zr – grey.

In UiO-66, the introduction of the bromo- and nitro- functional groups results in the largest increase in electrostatic contribution. Unlike the MIL-125 structures, C_3 adsorption at low loading in UiO-66 takes place primarily in pores which are defined by the flat surface – rather than the edges – of the BDC linker (Figure 3.15). Propylene is adsorbed in the centre of the pore and, as such, interacts equally strongly with both the positively charged hydrogen atoms and the negatively charged carbon atoms of the linker. The introduction of functional groups to the linker results in a much wider range of charges being present on the linker atoms and a stronger electric field gradient. While the location of energy extrema in the interaction profiles remains relatively unchanged, attractive areas become more attractive, while repulsive regions become more repulsive. As the most strongly repulsive regions are near the edges of the pore, away from adsorbed molecules, the overall attractive interaction experienced in the centre of the pore is increased. The introduction of functional groups also introduces additional steric constraints (particularly in the case of the bulky NO_2 group) and is likely to subtly alter the preferred van der Waals adsorption sites within the pore. It can be seen that further efforts are required to more fully understand the interplay between these factors in non-trivial pore geometries such as those found in many MOFs.

These results show that linker functionalization can provide an effective means of increasing the selectivity of the MOF towards propylene in structures with smaller

pores (less than ~ 10-12 Å in diameter). The impact of functionalization on propylene selectivity in larger pores appears to be limited and, depending on the geometry of the pore, may even be detrimental to propylene-MOF electrostatic interactions.

3.4 Competitive C_3 Adsorption in MOFs in High Loading Regimes

While the previous section focused on understanding selectivity in MOFs when operating near the zero loading regime, the majority of industrial adsorption processes operate outside this zone. In this section, the selectivity of MOFs at higher loading is explored where the packing of molecules within the pore system plays a major role. Unless stated otherwise, selectivity is reported for equimolar C_3 mixtures at 11 bar, slightly below the estimated saturation vapour pressure of the mixture (Lemmon *et al.*, 2014).

3.4.1 Overview

Although approximately half of the MOFs in this study were demonstrated to be propane selective at low pressure, all but three structures were found to be selective towards propylene at higher pressure (Figure 3.16), with typical selectivities ranging from 1.2 - 1.6. In the majority of cases where MOFs were initially propane selective, a reversal in selectivity was observed at an external pressure of approximately 0.1 – 0.5 bar. The exceptions to this trend were the three MIL-140 structures, which exhibit a remarkable selectivity towards propane even at saturation (red, blue and yellow diamonds in Figure 3.16). This unusual behaviour is explained in detail in Section 3.4.3.

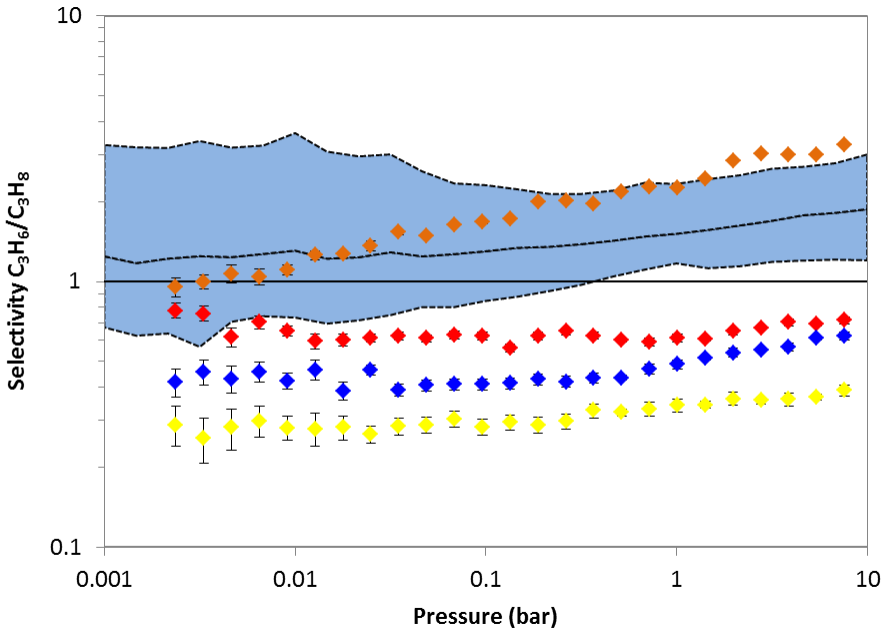

Figure 3.16 – Variation in selectivity with pressure for an equimolar C_3 mixture. For ease of viewing, only the data for those MOFs which are discussed in detail are marked explicitly (diamonds): MIL-140B (red), MIL-140C (yellow), MIL-140D (blue) and CAU-10 (orange). The other MOFs in the study fall in the range highlighted in light blue, for which the minimum, average and maximum values of selectivity are indicated by black dashed lines.

The composition of the bulk mixture was found to have little impact on the selectivity at high pressure (Appendix G) except in the case of CAU-10 (orange diamonds in Figure 3.16), where the selectivity towards propylene was found to be significantly enhanced for a propylene-rich feed (S = 4.3 versus only 3.3 in the equimolar case). The mechanisms at work in this special case are discussed in Section 3.4.2.

3.4.2 Propylene-Selective MOFs

Whereas selectivity at low loading is primarily determined by the relative C_3-MOF interaction energies of propane and propylene, as the total C_3 loading is increased, the multicomponent adsorption equilibrium is increasingly influenced by the ability of the two species to make efficient use of the available space and the interaction

between neighbouring C_3 molecules. Comparison of the bulk liquid densities of the two species (propylene: 11.8 mol/L, propane: 11.0 mol/L (Lemmon *et al.*, 2014)) as well as the van der Waals volume of the molecules based on the force fields used (propylene: 345 $Å^3$, propane: 364 $Å^3$), shows that propylene is the smaller molecule. Thus, propylene would be expected to achieve a higher packing density than propane and the selectivity of the MOF, irrespective of enthalpic preference, would be expected to shift towards propylene at higher loadings. As shown in Figure 3.16, this is the case in the majority of the structures studied. The enhanced packing density of propylene compared to propane in these propylene selective MOFs is clear to see in single-component adsorption data, where the adsorption capacity of the MOF for propylene is typically 15-20% higher than that of propane. The single component isotherms for propylene and propane in all of the MOFs studied in this work are presented in Appendix H.

The entropic advantage enjoyed by propylene over propane stemming from its increased packing density is not the only factor at work at high loadings. The adsorbed phase fluid-fluid interactions also favour the adsorption of propylene over propane. C_3-C_3 interactions for both species increased with increasing pore diameter, before reaching a plateau of -5 to -7 kJ/mol for propylene-propylene and -3 to -5 kJ/mol for propane-propane for pore sizes greater than ~ 10 Å (Figure 3.17). Propylene-propylene Coulombic interactions remained unchanged with respect to pore diameter, with an average value of -0.15 kJ/mol. Similar behaviour was observed during simulations carried out in the model pore systems (Figure 3.17). As the pore size is increased, a greater number of C_3 molecules are able to be accommodated within the cavity and so an adsorbed C_3 molecule is surrounded by a greater number of neighbouring molecules with which it can interact and the average C_3-C_3 interaction energy increases. Due to the short-range nature of van der Waals interactions, successive 'shells' of neighbouring adsorbed molecules bring a diminishing return on interaction energy, resulting in the plateaux observed in Figure 3.17. While the behaviour with respect to pore size is similar for both species, the higher packing density of propylene ensures that neighbouring propylene molecules are closer together, generating stronger interaction energies.

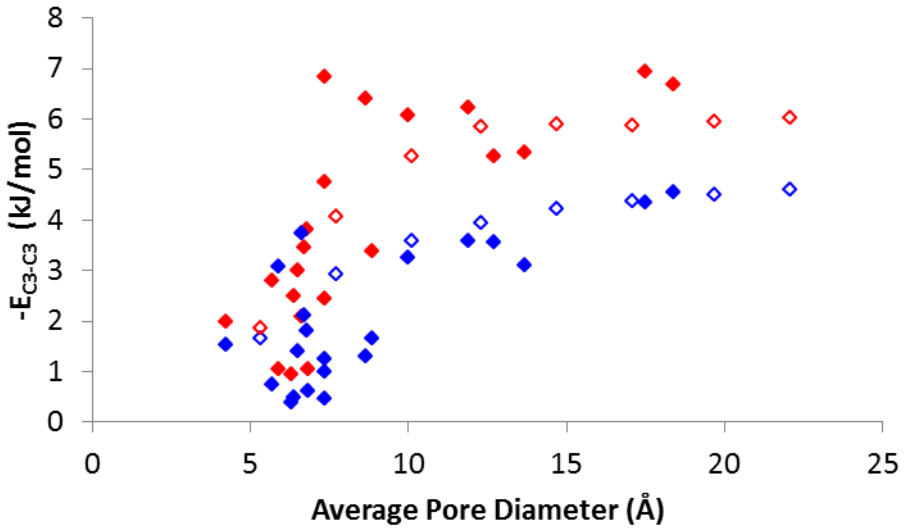

Figure 3.17 – Average fluid-fluid interaction energies at saturation loading as a function of average pore diameter for propylene (red) and propane (blue) in MOFs (filled symbols) and model triangular pores (open symbols).

The highest selectivity towards propylene was observed in CAU-10 (S = 3.3), a small-pore (d = 5.7 Å) MOF consisting of 1D channels of a roughly cubic nature. In this case, the selectivity towards propylene is primarily entropic in nature and is best understood through examination of single-component adsorption data. In pure-component simulations, both species exhibit complex isotherms with a number of identifiable inflection points (Figure 3.18).

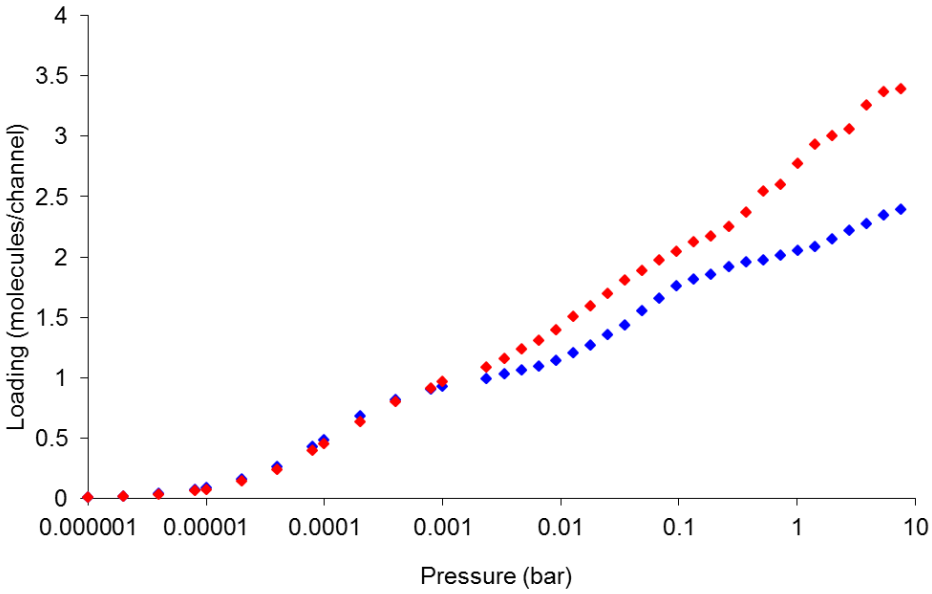

Figure 3.18 – Single-component adsorption isotherms of propylene (red) and propane (blue) in CAU-10 at 303 K.

For propane, two distinct inflection points are observed, corresponding to transitions in the adsorbed phase packing arrangement from one molecule per channel per unit cell to two and eventually three molecules/channel/UC (Figure 3.19(a)-(c)). The transition from two to three molecules/channel/UC is not completed however, and an average of only 2.5 propane molecules/channel/UC are observed at saturation. In the case of the smaller propylene molecule, a maximum of four molecules may be accommodated per cavity (Figure 3.19(d)), although the observed loading at saturation is somewhat lower (3.5 molecules/channel/UC). During these transitions, adsorbed C_3 molecules must relocate to less energetically favourable positions with respect to C_3-MOF interaction energies, and this loss in energy must be overcome by a combination of gains in system entropy and fluid-fluid interaction energy. In addition to the enhanced fluid-fluid interactions outlined above, the smaller propylene molecule is also less sterically hindered than propane in these sites (i.e. experiences a lower loss in entropy) and, consequentially, is able to overcome this transition energy penalty more easily than propane. As a result, the phase transitions for propylene occur at lower pressures and are less distinct than for propane.

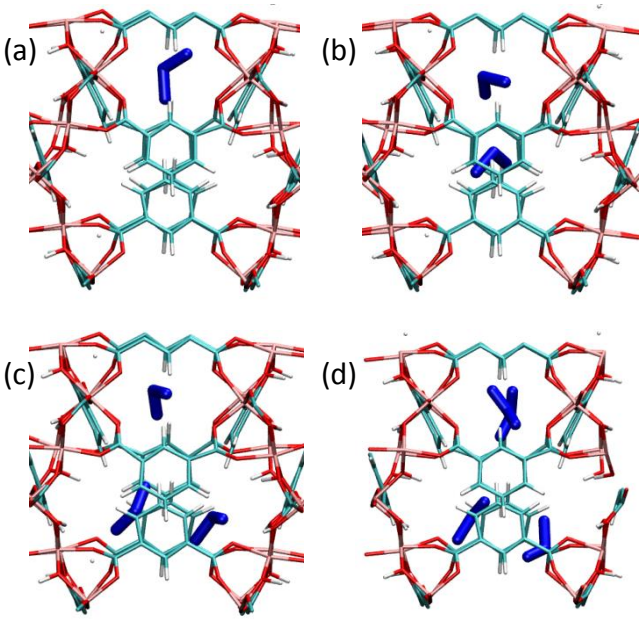

Figure 3.19 – Top-down view of C_3 molecules (blue) within the CAU-10 channel (channel runs from top to bottom of page). Images (a)-(d) correspond to loadings of 1, 2, 3 and 4 molecules per channel per unit cell respectively.

Similar behaviour is observed in competitive adsorption. Propylene begins to occupy the higher packing density sites at lower pressures than propane, resulting in an increase in selectivity. Even at higher pressure, when these sites become more easily accessible to propane, the higher fluid-fluid interactions generated by propylene mean that propylene molecules are unlikely to be displaced and the propylene selectivity remains high. As the system approaches saturation, a further increase in selectivity is observed as the tetra-molecular arrangement of propylene molecules becomes increasingly prevalent. This final phase transition, which is only accessible to propylene, explains why an increase in propylene concentration of the bulk mixture results in a significant increase in propylene selectivity. In both single- and multi-component simulation, little change in total interaction energy was observed during this final phase transition (-45.4 ± 0.2 kJ/mol at 3 molecules/channel; -45.3 ±0.2 kJ/mol at 4 molecules/channel), suggesting that the total change in system energy for the insertion of an individual molecule is close to zero. Examination of the acceptance criteria for an insertion move (Equation 2.15) indicates that the probability of accepting this insertion will depend strongly upon the fugacity of the species. Even for pure propylene, the saturation loading is only

3.5 molecules/channel/UC, or approximately a 50% probability of the tetra-molecular arrangement being observed compared to the tri-molecular arrangement. The relative increase in propylene fugacity in the 0.7 mole fraction propylene C_3 mixture compared to the equimolar mixture makes the transition to 4 molecules/channel/UC more likely to occur and accounts for the observed increase in selectivity towards propylene.

3.4.3 Propane-Selective MOFs: The MIL-140 Series

In stark contrast to the other MOFs studied, the MIL-140 structures (MIL-140B, C and D) were found to selectively adsorb propane over propylene even at high pressure Figure 3.16. The selectivity in MIL-140B remains steady across all pressures studied and both MIL-140C and MIL-140D exhibit only a slight increase in selectivity towards propylene as the pressure is increased, indicating that the entropic effects discussed in Section 3.4.2 are of limited influence in these structures. This unusual behaviour is not confined to competitive adsorption, manifesting itself in the single-component adsorption data as well.

The pure component isotherms of propylene and propane MIL-140B, C and D are shown in Figure 3.20. In all three structures, propane is adsorbed at much lower pressures than propylene, as outlined in Section 3.3. In MIL-140B and MIL-140C, the adsorption capacities for the two species are identical, while in MIL-140D the capacity for propylene is only 6% higher than propane. In those MOFs which were propylene-selective at high pressure – and in the model pore analogues of the MIL-140 series - a much higher adsorption capacity for propylene compared to propane was observed in single-component simulations, a result of the higher packing densities achievable by propylene (c.f. Section 3.4.2). The capacity of MIL-140B and MIL-140C, however, for the two species is identical, suggesting that propylene molecules are unable to pack more closely together than propane molecules. Comparison of competitive adsorption simulations in MIL-140B and its

model pore analogue allows the structural features responsible for this unusual behaviour to be identified.

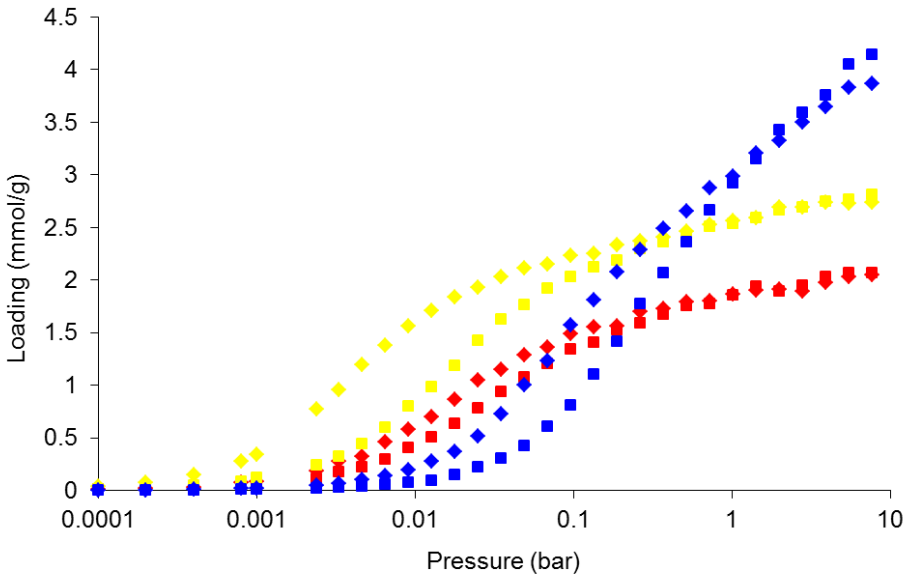

Figure 3.20 – Single-component adsorption isotherms for propylene (squares) and propane (diamonds) in MIL-140B (red), MIL-140C (yellow) and MIL-140D (blue) at 303 K.

Although both MIL-140B and the 5.3 Å model pore consist of similar one-dimensional, broadly triangular channels, the channel of MIL-140B is considerably more complex, as illustrated in Figure 3.21. The model pore is constructed from three essentially flat carbon surfaces, resulting in a regular triangular prism with no variation in the cross-sectional area of the triangle along the channel axis. While the channel of MIL-140B has two surfaces where the NDC linker is well-aligned with the channel, the third linker protrudes into the channel, introducing a periodic constriction to the pore. MIL-140B, therefore, may be more accurately considered as a series of roughly triangular pores connected by narrower triangular windows. This comparatively subtle difference in channel geometries between the MOF and model pore structures results in very different adsorption behaviour in multi-component simulations at high pressure.

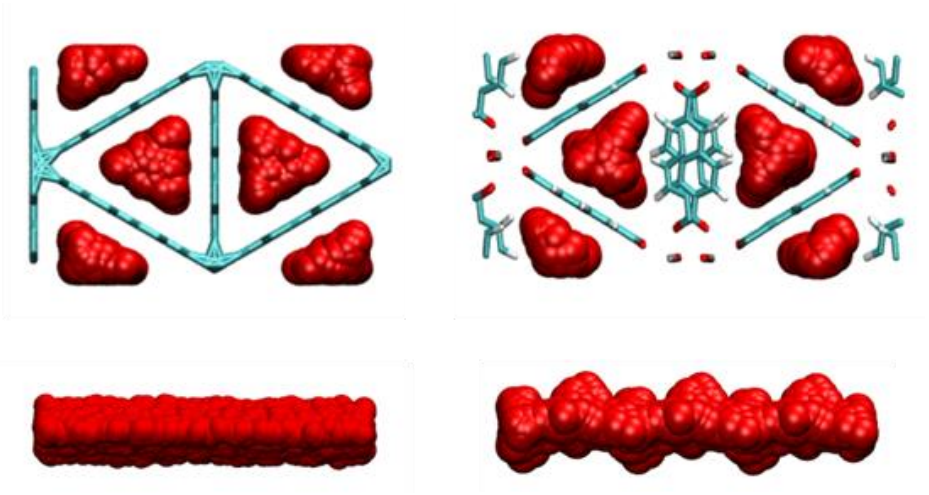

Figure 3.21 – Illustration of the helium accessible pore volumes (red) of a 5.3 Å model pore (left) and MIL-140B (right). The top images show variation in the channel cross-section, while the lower images show the variation in pore shape along the length of the channel.

Both structures behave very similarly at low loading, selectively adsorbing propane over propylene with C_3 molecules being adsorbed in a single-file arrangement along the centre of the pore. At high pressure, however, the model pore exhibits a reversal in selectivity, while MIL-140B remains propane-selective (Figure 3.22). In the model pore, although the pore walls restrict propane and propylene to the same packing density in two dimensions (i.e. one molecule per triangular slice), there is no such restriction along the channel axis and propylene is able to achieve a smaller average separation distance (4.07 Å vs 4.3 Å) at saturation as a result. In MIL-140B, C_3 molecules are prevented from packing as closely together by the protrusion of the central linker into the channel and so the average separation distance of the two species is identical. In addition to eliminating the packing advantage normally enjoyed by propylene, the enforced increase in separation distance also means that the fluid-fluid interactions for the two species are very similar. Competitive adsorption in MIL-140B, therefore, is governed primarily by the C_3-MOF interaction energy which, as discussed previously, strongly favours the adsorption of propane over propylene and the selectivity remains relatively constant across the full range of investigated pressures.

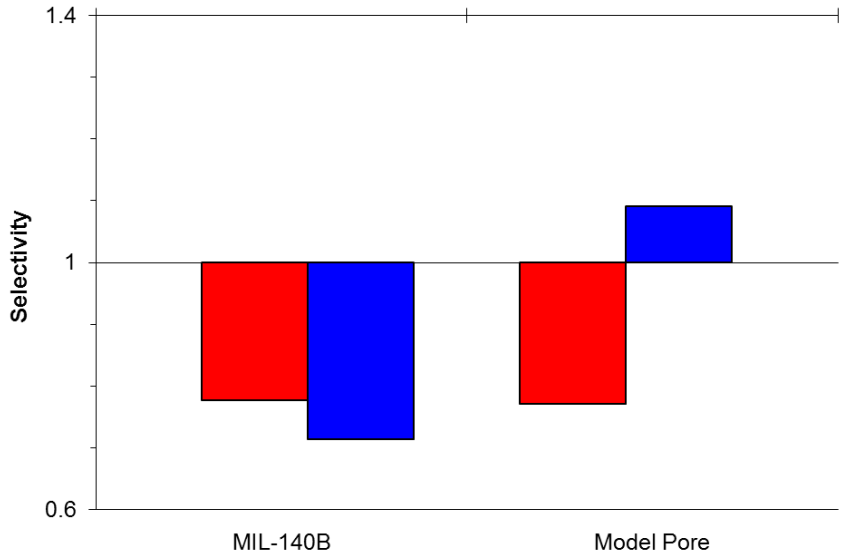

Figure 3.22 – Selectivity towards propylene in MIL-140B and equivalent 5.3 Å triangular model pore at low pressure (1 x 10^{-5} bar, red) and high pressure (11 bar, blue).

Similarly, the rotation of the central pillaring linker in MIL-140C and MIL-140D restricts the packing of C_3 molecules along the direction of the channel axis. In MIL-140C, as in MIL-140B, the MOF may be considered as a series of localised adsorption sites with limited scope for increased C_3 packing density, even at high pressure and the MOF remains strongly selective towards propane. The largest of the three MOFs, MIL-140D, exhibits slightly different behaviour. The longer azo-benzene linker creates a pore which is large enough for C_3 molecules to adsorb in each of the corners of the triangle (Figure 3.23), resulting in a significant increase in total C_3 uptake. The larger pore, however, also means that the constriction introduced by the central linker is less significant than in MIL-140B and MIL-140C and there is some scope for increased propylene packing density along the channel axis, particularly in the adsorption sites in the opposite corner of the pore from the central linker. The fact that MIL-140D does not restrict C_3 packing as effectively as the other two structures accounts both for the slightly higher propylene adsorption capacity in single-component simulations and the shift in selectivity towards propylene at higher pressure (Figure 3.16).

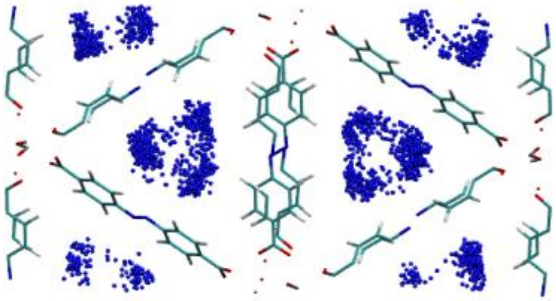

Figure 3.23 – C_3 adsorption sites in the corners of MIL-140D. The centres-of-mass of adsorbed C_3 molecules were recorded every 100,000 simulation steps and are indicated in blue.

3.5 Conclusions

In this chapter, the single-component and competitive adsorption of propane and propylene in a diverse selection of MOFs was explored. While, to date, experimental and computational studies have focused primarily on the development of MOFs which selectively adsorb propylene over propane, the simulation results presented herein show that it is possible for MOFs to preferentially adsorb propane over propylene under equilibrium conditions, potentially paving the way for the design of smaller and more cost- and energy-efficient separation C_3 units. In order to design such a MOF rationally, it is necessary for the structure to fulfil two criteria: first, the structure must exhibit an enthalpic preference for propane and, secondly, must be capable of restricting both species to the same, or similar, number of potential adsorption sites.

In order to achieve the first goal, the difference in C_3-MOF van der Waals interactions of the two species must be maximised, while simultaneously minimising the electrostatic interaction of propylene with the framework. MOFs with larger pores – greater than ~9 Å in diameter – were shown to be unable to differentiate between the two species based on their van der Waals interaction with the framework. In smaller pore MOFs, the overlap of C_3-framework interaction potentials resulted in a significant enhancement in the ability of the MOF to

discriminate between the two species. This behaviour was replicated in carbonaceous model pore systems, where the highest selectivity towards propane was found in the smallest pore. Comparison of the simulations carried out in these model pore systems to the analogous MIL-140 series also demonstrated that even small variations in pore shape can impact upon propane and propylene C_3-framework interaction energies to a different degree, suggesting that further exploration of the impact of pore shape on α_{VdW} for C_3 mixtures may lead to the further enhancement of propane-selectivity.

The use of small-pore MOFs was also shown to minimise the electrostatic interaction between propylene and propane for 1D channel systems, where steric restrictions and the overlap of van der Waals wall potentials forced molecules to adsorb in less desirable electrostatic environments. The reduction in MOF pore diameter thus kills two birds with one stone, a fact best demonstrated in the MIL-140 series of structures, which demonstrated some of the highest selectivities towards propane reported to date.

At high pressure, the majority of MOFs were shown to be selective towards the smaller propylene molecule, which makes better use of the available pore volume. It was demonstrated, however, that by selecting MOFs with appropriately sized and shaped pores, the entropic advantage normally enjoyed by propylene could be negated. In the case of the MIL-140 series, the disruption of C_3 packing along the length of the channel ensured that all three MOFs remained selective towards propane even at high pressure. In MIL-140C and D, this selectivity is combined with reasonably high capacity (3-4 mol/kg) to produce two promising adsorbents for the industrial separation of C_3 mixtures.

The case of CAU-10, however, demonstrates that it is not sufficient to select MOFs solely on pore diameter. Although the structure was propane selective at low loading as a result of its small pores and non-functionalised linkers, at high pressure, the pore shape was well suited to propylene adsorption, resulting in a propylene selective MOF at saturation. Further work, therefore, is needed to explore the influence of pore shape on adsorption at higher loading.

4 Pore-Size Effects in Competitive Adsorption of Xylene Isomers

In recent years, the suitability of a number of MOFs for the adsorptive separation of xylene isomers has been explored both experimentally (Alaerts *et al.*, 2008; Barcia *et al.*, 2011; Vermoortele *et al.*, 2011; Peralta *et al.*, 2012) and computationally (Castillo *et al.*, 2009; Granato *et al.*, 2014). In this chapter, the influence of pore diameter on the selectivity of the material in competitive xylene adsorption is investigated in one dimensional, model pore systems and analogous, real MOF structures. The industrial relevance and role of adsorption technologies in the separation of xylene isomers, along with the potential of MOFs for this separation, is outlined in Section 4.1. The simulation set-up and parameters are detailed in Section 4.2. The adsorption of xylenes in rhombic channel model pore systems is explored in Section 4.3, while Section 4.4 focuses on separations in the MIL-140 series of triangular channel systems. Finally, the key conclusions from this work are presented in Section 4.5.

4.1 Background

The xylenes (*para*-, *ortho*- and *meta*-xylene; Figure 4.1) are di-methyl-substituted aromatic compounds and are necessary precursors in a wide range of chemical processes. *para*-xylene (pX) remains the most commercially attractive of the isomers, used in the production of terephthalic acid – the basis for polyethylene terephthalate (PET) and its derived products. *ortho*- and *meta*-xylene (oX and mX) provide the building blocks for phthalic anhydride and isophthalic acid respectively (Cannella, 2000). Typically, these compounds are produced as a mixture containing all three xylene isomers plus a fourth isomer, ethylbenzene. As such, the efficient separation of mixtures of xylene isomers into their individual components is of great industrial relevance. Achieving such a separation through distillation, however, is

complicated by the close similarity of the compounds' boiling points (pX: 411.5 K; oX: 417.5 K; mX: 412.3 K) (Fabri *et al.*, 2000).

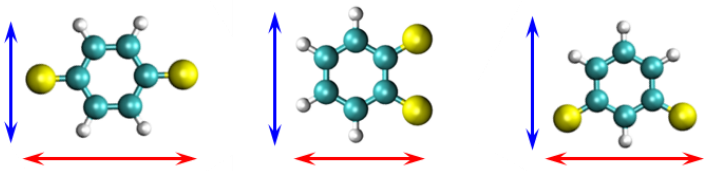

	pX	oX	mX
Waist Diameter (Å)	6.7	7.4	7.4
Length (Å)	9.6	7.8	8.8

Figure 4.1 – Images and key geometrical characteristics of *para*- (left), *ortho*- (centre), and *meta*-xylene (right). Colour scheme: waist diameter – blue arrows; length – red arrows; C – cyan; H – white; CH_3 group – yellow.

Until the mid-1970s, crystallisation represented the primary industrial separation method for producing pure *para*-xylene (Weissermel and Arpe, 2007). In this approach, the difference in the melting points of the isomers forms the basis of the separation process. The operation is limited, however, by comparatively low (~ 60%) pX recoveries (Fabri *et al.*, 2000).

The advent of adsorption-based simulated moving bed (SMB) technology allowed much higher levels of recovery to be achieved (upwards of 95%) and the majority of *para*-xylene is now produced through adsorption-based separation processes, e.g. UOP's PAREX process (Broughton *et al.*, 1970; Cannella, 2000). These processes are typically undertaken using a pX selective, ion-exchanged MFI or FAU zeolite as the adsorbent (Kurup *et al.*, 2005) and pX is removed in the extract along with the adsorbent. The separation mechanism relies heavily on the presence of extra-framework cations and, as a result, the operation is extremely sensitive to the water content of the stream (Minceva and Rodrigues, 2004; Silva *et al.*, 2012). The efficiency of an SMB xylene separation depends strongly upon the selectivity and

capacity of the adsorbent – the development of more highly *para*-selective materials would result in smaller SMB units and lower eluent consumption. Alternatively, a highly oX-selective material in which pX is the least preferred isomer would allow *para*-xylene to be removed as the raffinate. Recently, several MOFs have been identified which exhibit a strong adsorptive preference for either *ortho*- (Alaerts *et al.*, 2008; Gu *et al.*, 2009; Barcia *et al.*, 2011; Barcia *et al.*, 2012; El Osta *et al.*, 2012; Trens *et al.*, 2014) or *para*-xylene (Vermoortele *et al.*, 2011), providing a potential alternative to existing zeolite adsorbents.

Xylene separations in MOFs have been shown to rely on a number of different of adsorption mechanisms. In the one-dimensional, rhombic channels of MIL-47(V), all three xylene isomers exhibit similar enthalpies of adsorption and the experimentally reported *ortho*-selectivity (Alaerts *et al.*, 2008; Finsy *et al.*, 2009) is driven by the enhanced packing efficiency of oX molecules within the channels. The separation in other oX selective MOFs such as MIL-53(Al) and (Fe) (El Osta *et al.*, 2012; Duan *et al.*, 2013), UiO-66(Zr) (Barcia *et al.*, 2011; Chang and Yan, 2012) and MIL-101(Cr) (Trens *et al.*, 2014) is a result of higher enthalpies of adsorption for oX compared to the other isomers. In contrast, both the enthalpic preference and advantage in packing efficiency are in favour of *para*-xylene in MIL-125 and its amino-modified analogue (Vermoortele *et al.*, 2011; Moreira *et al.*, 2012b; Moreira *et al.*, 2012c) and both structures are selective towards pX as a result.

In the work of Vermoortele and co-workers (2011), potentially *para*-selective MOFs were selected on the basis of pore diameter, with smaller diameter pores (d < 6 Å) expected to preferentially adsorb the slimmest of the isomers – pX (Figure 4.1). This size-selectivity concept was further explored in computational studies of xylene adsorption in a range of MOFs by Moghadam and co-workers (Moghadam, 2013). It was reported that the preference of a material may be predicted based on its pore diameter: MOFs with pores less than 4 Å in diameter would be too small to allow xylene adsorption, MOFs with 4-6 Å pores are predicted to be pX-selective, while pore sizes ranging from 6-9 Å are expected to be oX-selective. Larger pore diameters are predicted to result in non- or only slightly selective materials as the pores are too

large to induce any difference in either molecular packing or sorbate-framework interactions between the three isomers.

It should be noted that the role of pX-mX selectivity in the separation was neglected in this screening protocol – i.e. it was assumed that the affinity of the MOF for mX always fell in between that for oX and pX and the order of selectivity was therefore either pX > mX > oX or oX > mX > pX. In addition, while the MOFs investigated by Moghadam had different pore diameters, the study did not include any MOFs with pore diameters in the 5.5-7.5 Å range, where it may be expected that a transition from pX-selective to oX-selective should occur. Finally, although the adsorptive preference was considered to be solely a function of pore diameter, the study also included a wide range of different pore shapes and topologies – features which also influence the selectivity of the material. The present work, therefore, seeks to address these points by first evaluating the impact of pore diameter on adsorptive preference in a series of one-dimensional model pore systems which, as discussed in Section 2.1.2, allows the effect of pore diameter to be decoupled from other MOF-dependant properties such as composition and pore shape. In particular the use of model pore systems allows greater control of the pore diameters to be included in the study, enabling the selectivity of channel systems in the 4-9 Å range to be examined in more detail and compared to analogous MOF structures. In the second case, competitive adsorption of xylene isomers is examined in the isoreticular MIL-140 series (Guillerm *et al.*, 2012), which provides an excellent opportunity to explore selectivity in small-pore 1D MOFs with diameters ranging from 3.3 Å to 6.6 Å, a region which was under-represented in the work of Moghadam. In both cases, the impact of mX on both selectivity and on any screening protocol is considered.

4.2 Method

In the present work, the competitive adsorption of equimolar binary mixtures of xylene isomers in a range of carbon-based model pore systems and analogous MOF structures was studied using GCMC simulations. In this chapter, one-dimensional

rhombic model pores with varying wall intersection angles (30°, 60° and 90°) were studied. One-dimensional rhombic channel systems are relatively common amongst MOFs (e.g. the CAU-8 (Reinsch *et al.*, 2013a), CAU-10 (Reinsch *et al.*, 2013b), MIL-53, DUT-8 (Klein *et al.*, 2010) and MIL-47(V) systems) and xylene adsorption in two such systems – MIL-47(V) (Alaerts *et al.*, 2008; Castillo *et al.*, 2009; Finsy *et al.*, 2009) and MIL-53 (Alaerts *et al.*, 2008; El Osta *et al.*, 2012; Duan *et al.*, 2013) – has been well-studied. The use of rhombic model pore systems thus allows both an exploration of the impact of pore diameter on adsorption and enables a direct comparison between MOFs and these model pores to be made. A wide range of pore diameters – typically between 3 Å and 20 Å – were studied for each intersection angle. In discussing individual model pore systems, the notation D*u*_A*v* will be followed, wherein *u* indicates the pore diameter (Å), determined from the PSD as outlined in Section 2.2.5, and *v* denotes the wall intersection angle in degrees.

Additionally, single- and multi-component xylene adsorption was studied in five one-dimensional channel-type MOFs: MIL-140A, MIL-140B, MIL-140C, MIL-140D and CAU-8. The MIL-140 series consists of equilateral triangular channels ranging in diameter from 3.3 Å to 6.6 Å (c.f. Section 3.4.3). The aluminium-based CAU-8 structure is comprised of 6.5 Å diameter rhombic channels with a wall intersection angle of 89°, which allows a good comparison to the 90° rhombic model pores as well as the extensively-studied MIL-47 and MIL-53 systems, which contain slightly larger pores (diameters of 7.4 and 8.5 Å respectively).

4.2.1 Force Field Details

The xylene molecules were considered to be completely rigid and modelled using the OPLS force field (Jorgensen *et al.*, 1993). The aromatic carbon and hydrogen atoms were defined explicitly while the methyl (CH_3) groups were treated as single interaction centres. As xylenes are slightly polar molecules, partial charges were

placed on all LJ interaction sites. The LJ interaction parameters, partial charges, bond lengths and angles for the xylene molecules are summarised in Table 4.1.

Table 4.1 - Bond lengths, angles and non-bonded parameters used for xylene isomers in this work (Jorgensen *et al.*, 1993).

Lennard-Jones and Coulombic Parameters			
Pseudo-atom	σ (Å)	ε/k_B (K)	q (e)
C	3.55	35.24	+0.115
H	2.42	12.03	+0.115
CH_3	3.80	85.51	-0.115
Bond Lengths (Å)			
C-C	1.400		
C-H	1.080		
C-CH_3	1.510		
Bond Angles (°)			
C-C-C	120.0		
C-C-H	120.0		
C-C-CH_3	120.0		

Both the model pore systems and MOFs were likewise considered to be rigid frameworks. The model pores were described solely via Lennard-Jones interactions (σ = 3.4 Å, ε/k_B = 28.0 K; (Bojan *et al.*, 1992a)). Lennard-Jones parameters for the MOFs were taken from the DREIDING force field (Mayo *et al.*, 1990) or the UFF (Rappe *et al.*, 1992) (see 0). Partial charges for the MOFs were calculated using the EQeq method (Wilmer *et al.*, 2012a).

4.2.2 Simulation Parameters

Competitive adsorption simulations of equimolar binary mixtures (pX-oX, pX-mX and oX-mX) were carried out in the model pore systems at 300 K and at two pressures (1 Pa and 2 kPa) corresponding to the pressures chosen for examination in

the work of Moghadam (2013). For the xylene-MOF systems, single-component isotherms were simulated at 300 K up to the saturation pressure of the isomers (~ 2 kPa), while binary adsorption simulations were carried out at pressures ranging from 1 Pa to 2 kPa. All simulations were implemented in the MuSiC software package (Gupta *et al.*, 2003) using the parameters and move types described in Section 2.2.2. All simulations included at least 100 x 10^6 initialisation steps followed by 150 x 10^6 sampling steps and care was taken to ensure that simulations had reached equilibrium before sampling commenced.

In the analysis of binary mixture simulations, the selectivity of the material ($S_{a\text{-}b}$) towards component *a* from a mixture of *a* and *b* is defined as follows:

$$S_{a-b} = \frac{x_a}{x_b} \cdot \frac{y_b}{y_a} \qquad \textbf{Equation 4.1}$$

Where *x* and *y* are mole fractions in the adsorbed phase and bulk phase respectively. A selectivity greater than 1.1 indicates a distinct preference for component *a*, while a selectivity of less than 0.9 indicates a distinct preference for component *b*. A selectivity between 0.9 and 1.1 may be considered to be non-selective.

4.3 Competitive Adsorption in 1D Rhombic Pore Systems

4.3.1 Adsorption of pX-oX Mixtures in Model Pores

The selectivity of each of the model pores towards pX at 1 Pa is summarised in Figure 4.2. The smallest pores investigated (D3.4_A90 and D3.9_A30) were too small to allow xylene adsorption and it can be seen that the next two smallest pores (D6.0_A60 and D6.1_A30) were the only channels to selectively adsorb pX over oX. Above this diameter, the pores are mainly oX-selective, with the highest selectivity towards oX ($S_{oX\text{-}pX}$ = 3.5) being observed in the D7.5_A90 pore.

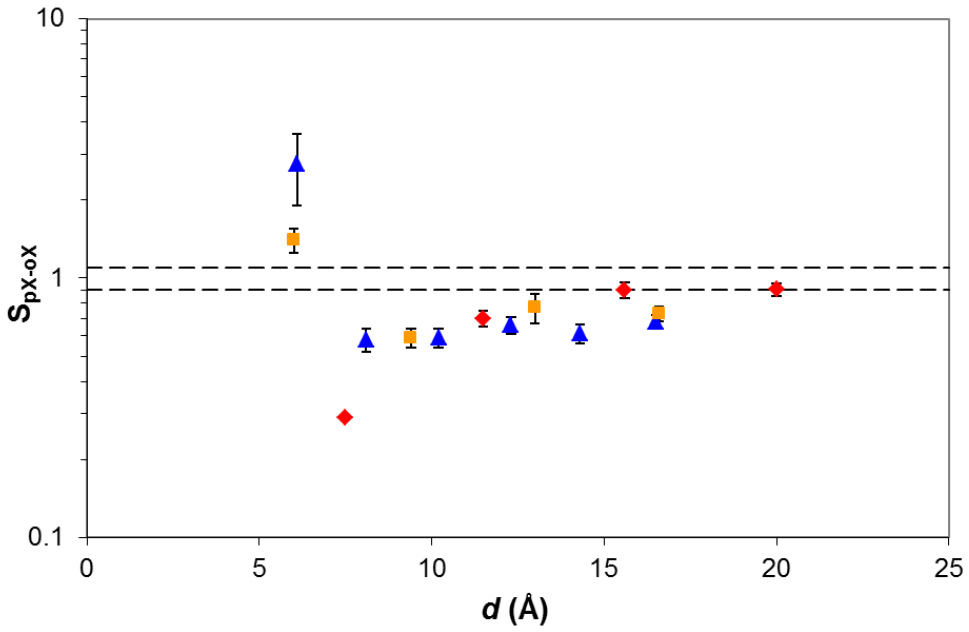

Figure 4.2 – Selectivity towards pX for equimolar pX-oX mixture at 1 Pa for rhombic model pores with wall intersection angles of 30° (blue triangles), 60° (orange squares) and 90° (red diamonds) as a function of the PSD channel diameter. Where error bars are not visible, the error is within the symbol size. The dashed lines indicate the non-selective region ($0.9 \leq S_{pX\text{-}oX} \leq 1.1$).

As the pore diameter is increased, the selectivity tends towards unity and the systems become less selective. For mixtures of pX-oX, the model pore systems are therefore in qualitative agreement with the observations of Moghadam. The range of pore diameters which remain selective towards oX is much wider for these model pore systems, however. While oX-selectivity in MOFs tends to tail off for diameters above ~9-12 Å, even the largest of the 30° and 60° model channel systems (D15.6_A30 and D16.5_A60) exhibit a low selectivity towards oX ($S_{oX\text{-}pX} \sim 1.4$). The 90° model pores, however, show closer agreement with the Moghadam protocol, becoming non-selective for diameters of greater than ~15 Å. The different behaviour of the 90° pores to the 30° and 60° pores as a function of the channel diameter is a result of the different geometries of the pores coupled with the limitations of the PSD method.

The MC PSD method (Gelb and Gubbins, 1998) determines the largest sphere which may be successfully inserted into the structure without overlap with wall atoms. For these simple channels, this corresponds to the largest diameter circle which may be placed on the centre of the channel cross-section (Figure 4.3).

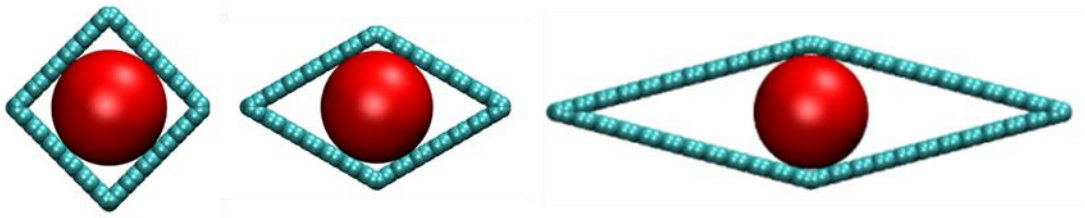

Figure 4.3 – Determination of the channel diameter using the largest sphere method (red) for the D20.0_A90 (left), D20.3_A60 (centre) and D20.8_A30 (right). Although all three systems exhibit very similar channel diameters, the volume fraction of the pores described by these diameters varies widely. Colour scheme: Largest sphere which may be inserted into the system – red; C – cyan.

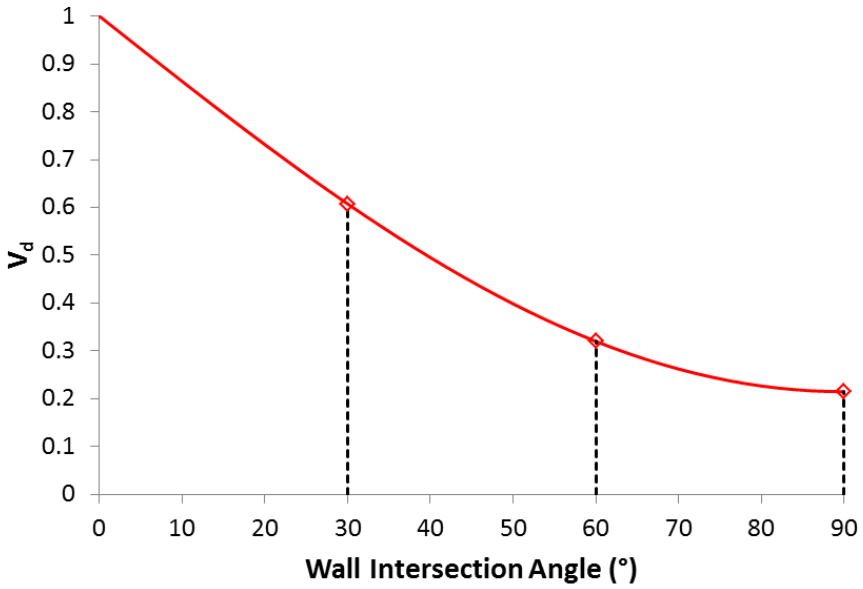

Figure 4.4 – Fraction of the channel volume not described by the channel diameter (as determined from the PSD method) as a function of the wall intersection angle (solid red line). The three diamonds and associated black dashed lines indicate the wall intersection angles of the model pores studied in this work.

It can be seen that as the wall intersection angle becomes more acute, the fraction of the channel cross-sectional area which falls outside this circle (V_d) becomes greater.

For regular rhombic channels, the evolution of V_d as a function of wall intersection angle may be solved analytically (Figure 4.4). The derivation of this relationship may be found in Appendix I.

The PSD channel diameter thus becomes a less accurate descriptor of the pore system for smaller intersection angles, for which the contribution of V_d becomes more significant. In the case of the 30° model pore systems, for example, V_d actually represents the majority of the pore volume (V_d = 0.61). While the largest of the 30° pores has a nominal channel diameter of 15.6 Å, the pore remains selective towards oX due to the contribution of the more confined regions of the pore volume found in the corners of the channel which, from the point of view of an adsorbed xylene molecule, are much less than 15.6 Å in size.

It is clear that while the PSD remains a useful tool for determining the diameter of any cavities present in a structure, care must be taken to consider the appropriateness of these values when comparing systems of different geometries. The development of a more extensive approach to the PSD which takes into account pore shape is outside the scope of the present work, however, and subsequent analyses will continue to rely upon the PSD channel diameter.

As previously stated, both the D6.0_A60 and D6.1_A30 pores selectively adsorbed pX over oX at 1 Pa. Interestingly, both isomers interact with the framework equally strongly, with pX and oX exhibiting near-identical xylene-framework interaction energies (pX: -134.5 kJ/mol; oX: -134.2 kJ/mol (D6.1_A30) and pX: -132.6 kJ/mol; oX -132.1 kJ/mol (D6.0_A60)). While the dependence of the xylene-pore interaction energy on pore diameter for the three model pore series will be discussed shortly, it is apparent that the observed pX-selectivity in these pores is not a result of an enthalpic preference of the structure for one isomer over the other. It should be noted that the fractional loading at 1 Pa is generally greater than 0.4 for all the model pore systems studied and so the influence of xylene-xylene interactions cannot be neglected. In fact, in these two pX-selective systems, the selectivity was found to be

driven by the xylene-xylene interactions, which were found to favour pX by 1.8 - 2.7 kJ/mol.

Although both pores have very similar channel diameters, different mechanisms are responsible for the enhanced pX-pX interactions in each of the two systems. In the case of the 60° system, *para*-xylene molecules tend to be arranged in a single-file arrangement with the long axes of the molecules perpendicular to the channel axis, the methyl groups in the corner of the pore and the faces of the aromatic rings at an angle of between 30° and 60° to the channel axis (Figure 4.5). The same arrangement is not as easily accessible for oX, whose neighbouring methyl groups are less well-suited to the corners of the pore. oX, therefore, tends to be found with its aromatic ring parallel to the channel axis, severely reducing its packing efficiency.

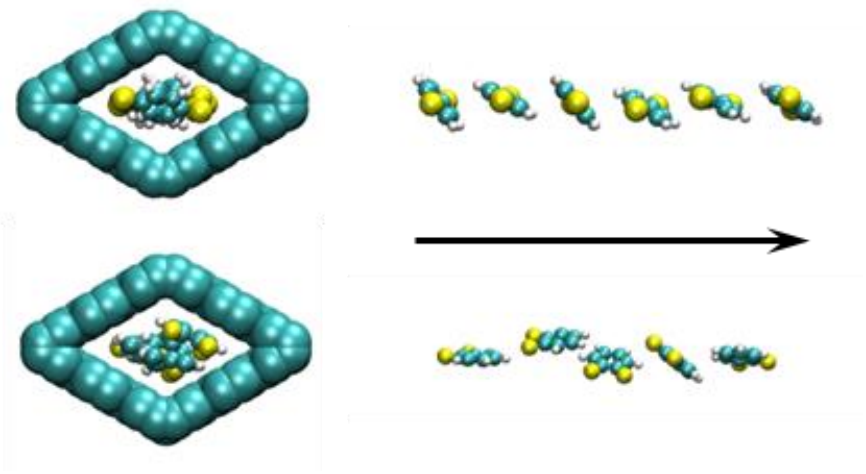

Figure 4.5 – Packing arrangements of pX (top) and oX (bottom) in the D6.0_A60 system looking along the channel (left) and a side-on view of the channel length (right). The framework atoms have been omitted for clarity in the right-hand image. The black arrow indicates the channel direction. Colour scheme: C – cyan; H – white; CH_3 – yellow.

While xylenes are restricted to a single file arrangement in the D6.0_A60 system, the pore volume in the acute corners of the D6.1_A30 system allow for a more complex packing arrangement wherein a line of vertical pX molecules (i.e. with their aromatic rings perpendicular to the axis running through the acute pore corners) is sandwiched between two lines of horizontal pX molecules (Figure 4.6). In this case, xylene

molecules are aligned with their long axes parallel to the channel axis and this arrangement allows the methyl groups of neighbouring pX molecules to interact strongly with one another. As both methyl groups are on the same side of the oX molecule, neighbouring oX molecules experience less favourable interactions between the methyl groups and the carbon and hydrogen atoms of the aromatic ring. In addition, as there is less space available between the lines of horizontal oX molecules compared to the slimmer pX, fewer oX molecules are observed in the vertical orientation in the centre of the channel.

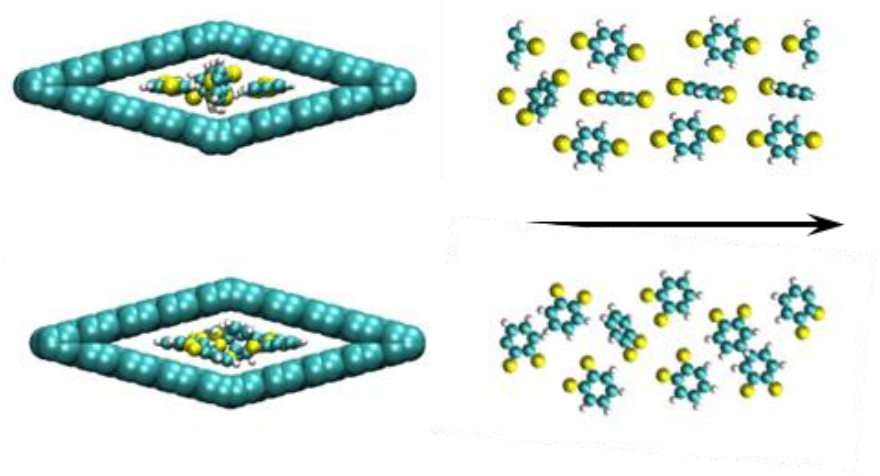

Figure 4.6 – Packing arrangements of pX (top) and oX (bottom) in the D6.1_A30 system looking along the channel (left) and a top-down view of the channel length (right). The framework atoms have been omitted for clarity in the right-hand image. The black arrow indicates the channel direction. Colour scheme: C – cyan; H – white; CH_3 – yellow.

It can be seen that both of these small-pore channels introduce a significant degree of confinement on adsorbed xylene molecules and that the xylenes take up regular packing arrangements which appear to be specific to the individual system. As the selectivity is defined by the packing arrangement rather than an interaction with the pore walls, it is not possible to say that all channels of similar diameters will result in pX selective systems.

In order to evaluate the impact of pore diameter on xylene-xylene interactions, it is useful to consider the ratio of the interaction between pX molecules ($E_{pX\text{-}pX}$) to that between oX molecules ($E_{oX\text{-}oX}$), $\alpha_{pX\text{-}pX/oX\text{-}oX}$:

$$\alpha_{pX-pX/oX-oX} = \frac{E_{pX-pX}}{E_{oX-oX}} \qquad \textbf{Equation 4.2}$$

A number close to unity indicates that there is little difference in the xylene-xylene interaction energies for the two species, while a number less than unity indicates that oX-oX interactions are stronger than pX-pX. While the xylene-xylene interactions initially favour pX, as the channel diameter is increased, the xylene-xylene interactions begin to favour oX over pX (Figure 4.7). Although the optimal value of channel diameter depends strongly on the wall intersection angle, the strongest packing preference for oX is observed in channels of between 7 and 12 Å in diameter.

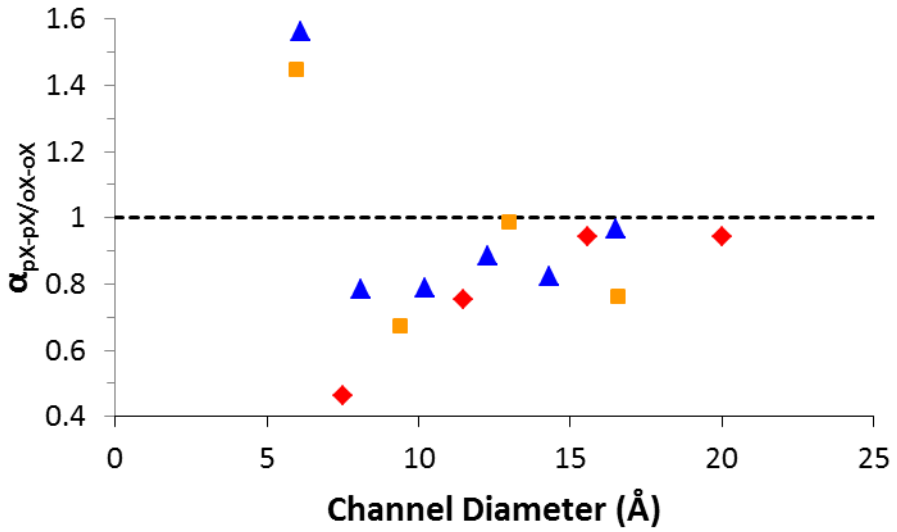

Figure 4.7 – Influence of channel diameter on the ratio of pX-pX to oX-oX interaction energies ($\alpha_{pX\text{-}pX/oX\text{-}oX}$) for model pore systems with wall intersection angles of 30° (blue triangles), 60° (orange squares) and 90° (red diamonds). Error bars are within the symbol size.

The data presented in Figure 4.7 describes a number of different packing regimes. In the largest diameter pores (D20.0_A90 and D16.5_A30), the fractional loading is low enough at 1 Pa that xylenes are only adsorbed in a monolayer near the channel wall. In this case, the difference in packing density and xylene-xylene interactions between pX and oX is limited. As the channel diameter is decreased below ~16 Å, multilayer adsorption is observed, even at low pressure. In some cases (e.g. D15.6_A90), the second layer exhibits a low degree of ordering in the adsorbed xylene molecules and the packing preference for one isomer over the other remains low. For systems where the second and third layers of xylene molecules display a regular packing arrangement (frameworks with channel diameters between 9 and 15 Å), the xylene-xylene interactions favour oX over pX. In these cases the more compact oX molecule is able to make more efficient use of the available pore space and pack more closely together. The asymmetric nature of oX also allows pairs of oX molecules to fit together extremely well with the methyl groups on each molecule directed away from each other (Figure 4.8). As the channel diameter is reduced further, xylene molecules no longer form a monolayer and pairs of xylene molecules become the preferred adsorption regime, resulting in the comparatively low value of $\alpha_{pX\text{-}pX/oX\text{-}oX}$ observed for the D7.5_A90 system.

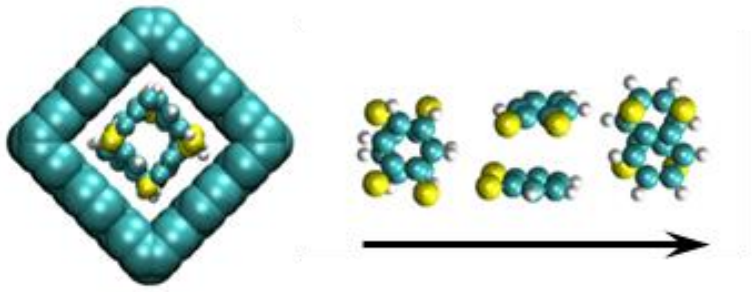

Figure 4.8 – o-xylene packing arrangement in the D7.5_A90 system looking along the channel (left) and a top-down view of the channel length (right). The framework atoms have been omitted for clarity in the right-hand image. The black arrow indicates the channel direction. Colour scheme: C – cyan; H – white; CH_3 – yellow.

Further reduction of the pore diameter forces xylene molecules to adsorb in a single-file manner, as described for the D6.0_A60 and D6.1_A30 systems, which strongly favours pX-pX interactions. The importance of this single-file packing to pX-selectivity is underlined when the selectivity of D6.0_A60 is compared at 1 Pa and 2 kPa. This system was the only one for which an increase in external pressure resulting in a statistically significant change in selectivity (Appendix J). At 1 Pa, xylenes were found to adsorb in a single-file arrangement (Figure 4.5) and the pore was pX-selective as a result. At 2 kPa, both pX and oX were found to form pairs with the faces of their aromatic rings parallel to the pore wall. This change from a 1D to 2D xylene packing arrangement was accompanied by a reversal in selectivity, with the structure found to be oX-selective ($S_{oX\text{-}pX} = 1.4$).

Although the xylene-framework interaction energies for pX and oX in the smallest, pX-selective model pore systems were found to be nearly identical and the selectivity was determined by the xylene-xylene interaction energies, this is not always the case (Figure 4.9). The influence of channel diameter on the xylene-framework interaction energy may be examined through a similar construction to that used for xylene-xylene interactions – the ratio of pX-framework to oX-framework interactions ($\alpha_{pX\text{-}F/oX\text{-}F}$).

In general, the difference in xylene-pore interaction energies for pX and oX is limited in the 60° and 90° pore systems. For these structures, the primary interaction mode is between the aromatic ring of the xylene and the surface of the pore wall, with xylene molecules oriented parallel to the surface. The homogeneous, flat surfaces considered in these pore systems are not capable of taking advantage of the difference in shape between the isomers and the overall interaction energies are very similar.

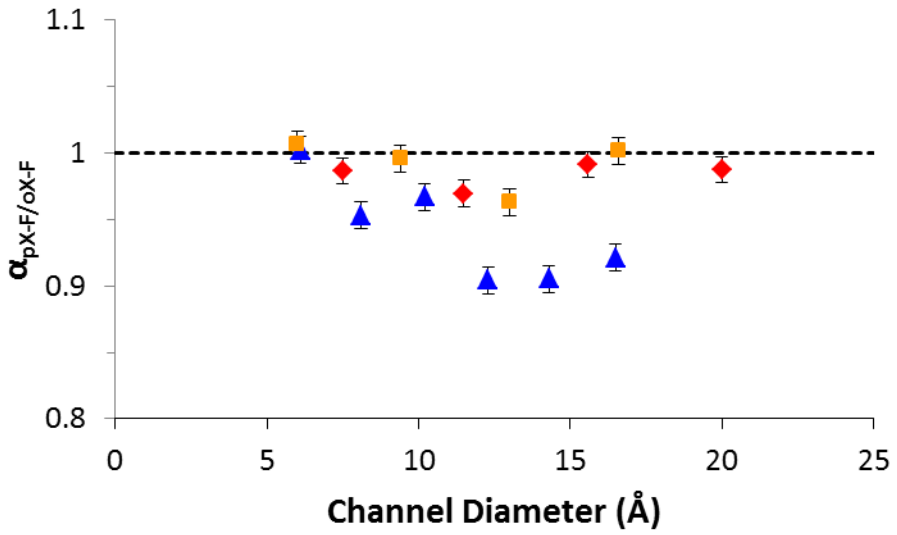

Figure 4.9 - Influence of channel diameter on the ratio of pX-framework to oX-framework interaction energies ($\alpha_{pX\text{-}F/oX\text{-}F}$) for model pore systems with wall intersection angles of 30° (blue triangles), 60° (orange squares) and 90° (red diamonds).

In the 30° systems, however, two distinct interaction modes are present: a higher energy interaction in the acute corners of the pores, where there is a significant overlap in LJ potentials of the two intersecting wall surfaces; and a lower energy interaction with the rest of the pore surface, where the interaction is primarily between the xylene molecule and only one wall. The corners of the pores in the 60° and 90° systems are not sufficiently narrow to induce such an overlap in potentials. The presence of two interaction sites can be seen in the probability histograms of xylene-framework interaction energy observed during GCMC simulations for both pX and oX (Figure 4.10).

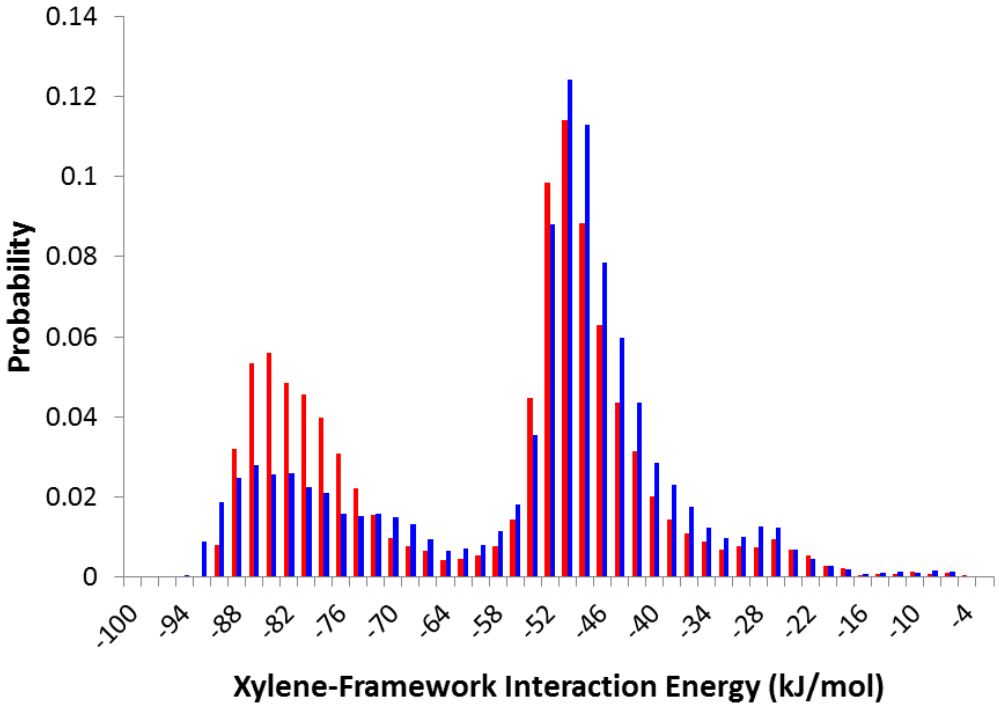

Figure 4.10 – Probability histograms of observed xylene-framework interaction energies for oX (red) and pX (blue), calculated from GCMC simulations of equimolar pX-oX mixtures in D16.5_A30. The peak on the left corresponds to adsorption in the corner of the pore, while the peak on the right represents adsorption near the pore wall but away from the corners. Only xylene molecules which formed the adsorbed monolayer were considered in these calculations.

The presence of two peaks in the histograms of both pX and oX shows that both sites are accessible to both molecules. In addition, both peaks are centred on the same average values for both isomers, suggesting that both pX and oX interact equally strongly with each individual site. It can be seen that the height of the peak corresponding to adsorption in the corner for oX is roughly twice that of pX. Since these histograms were generated based on binary GCMC simulations, this shows that oX is 2-3 times more likely than pX to occupy the corner of the pore (i.e. the Boltzmann factor for oX in this site is 2-3 times greater than that of pX). This is a direct consequence of the methyl groups being too large to fit into the corner of the pore. The preferred orientation for both pX and oX in this site is with the hydrogens of the aromatic ring pointing into the corner of the pore. For pX, this leaves little room for the molecule to rotate in the aromatic plane (Figure 4.11) before the methyl

groups overlap with the pore wall. oX, which has both methyl groups on one side of the aromatic ring, is much more free to rotate around this axis, resulting in an increase in the Boltzmann factor for this site.

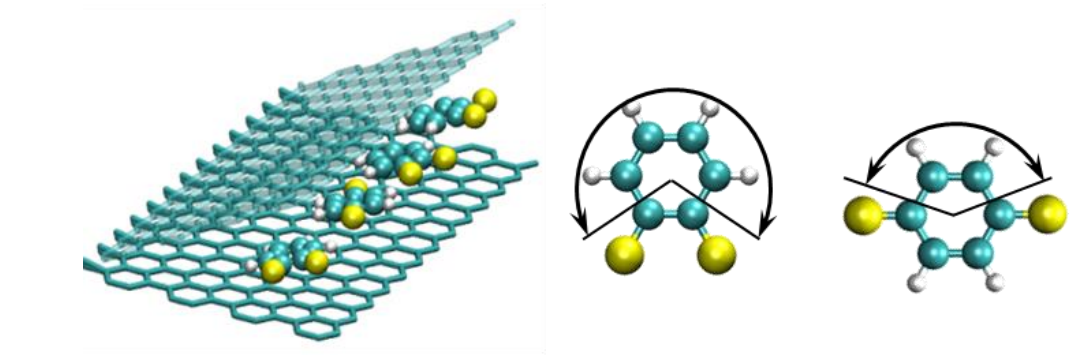

Figure 4.11 – Adsorption of pX and oX in the acute corner of the 30° model pore systems with hydrogen atoms pointing into the corner of the pore (left). The degree of rotational freedom around the axis perpendicular to the aromatic ring experienced by oX (centre) and pX (right) in this orientation is indicated by the black arrows. Colour scheme: C – cyan; H – white; CH_3 – yellow.

Overall, these results suggest that while the initial screening protocol of Moghadam and co-workers can be successfully applied to the competitive adsorption of pX and oX in model rhombic channel systems, a wider range of channel diameters must be considered in the identification of oX-selective structures (6 – 15 Å rather than the 6 - 9 Å range suggested). Similar to the MOFs investigated in this screening protocol, it can be seen that some degree of confinement is required in order to induce a preference for either pX or oX. This preference may be achieved either through the creation of ordered and well-defined packing arrangements of xylene molecules, or through the creation of adsorption sites whose shape is well suited to one isomer over the other. Structures which exhibit neither of these qualities will be unable to separate these components.

4.3.2 Adsorption of Mixtures Containing mX in Model Pores

In the work of Moghadam and co-workers, it was assumed that, due to the lack of mX-selective MOFs observed in either simulation or experiment, only an understanding of pX-oX selectivity was required to develop an effective screening protocol. Here, the competitive adsorption of equimolar binary mixtures containing mX is considered in order to explore the validity of the aforementioned assumption.

The selectivity towards oX from an oX-mX mixture at 1 Pa in each of the model pores is shown in Figure 4.12. It can be seen that none of the structures were found to be mX-selective and that the 30° and 60° systems selectively adsorbed oX over a wide range of channel diameters (6 – 16 Å). In addition, while the highest selectivity towards oX was observed in the D7.5_A90 system, the other structures in this series were found to be non-selective.

The origin of the preference of these structures for oX over mX is very similar to that for the selectivity over pX outlined in Section 4.3.1. Only the 30° series of channels are capable of inducing a preference for oX based on xylene-framework interactions (0) – a result of the higher degree of orientational freedom experienced by oX in the corners of the pores. The rotation of mX around the axis perpendicular to the aromatic ring is less restricted than a similar rotation for pX, however, and the overall ratio of the Boltzmann factors of oX and mX for the corner adsorption site is lower than that of oX to pX. For this reason, the xylene-frameworks energies of oX and mX are much more closely matched when averaged over both adsorption sites and $\alpha_{xyl\text{-}pore}$ for oX-mX is closer to unity than for oX-pX.

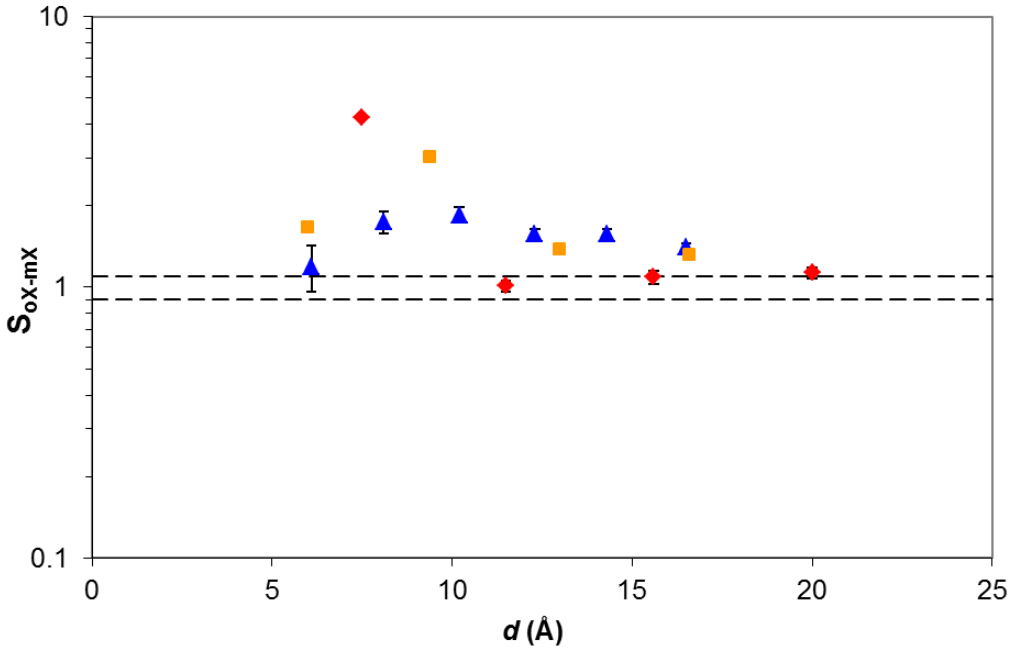

Figure 4.12 – Selectivity towards oX from simulations of adsorption from an equimolar oX-mX mixture at 1 Pa for rhombic model pores with wall intersection angles of 30° (blue triangles), 60° (orange squares) and 90° (red diamonds) as a function of the PSD channel diameter. Where error bars are not visible, the error is within the symbol size. The dashed lines indicate the non-selective region ($0.9 \leq S_{oX\text{-}mX} \leq 1.1$).

As in pX-oX mixtures, xylene-xylene interactions were found to favour oX in channels of less than 15 Å in diameter due to its more efficient use of the available pore volume. Unlike in pX-oX simulations, however, the xylene-xylene interactions in the two smallest pores were also found to favour oX. While these pores were particularly well-suited to pX and resulted in configurations with a high degree of ordering in pX molecules for pX-oX mixtures, neither mX or oX were seen to occupy particularly well-defined orientations. In the absence of a strong driving force towards the other component, the higher general packing efficiency of oX results in the smaller pores remaining oX-selective.

For oX-mX mixtures in rhombic channel systems, therefore, screening based solely on channel diameter appears to be justified. Channels less than 15 Å in diameter may be expected to preferentially adsorb oX over mX, with the highest selectivities likely to be found in channels of less than 10 Å in diameter.

For pX-mX mixtures, however, the case is less clear. The majority of the model pore systems were found to be unable to discriminate between pX and mX at either 1 Pa (Figure 4.1) or 2 kPa (Appendix J) based on binary GCMC simulations.

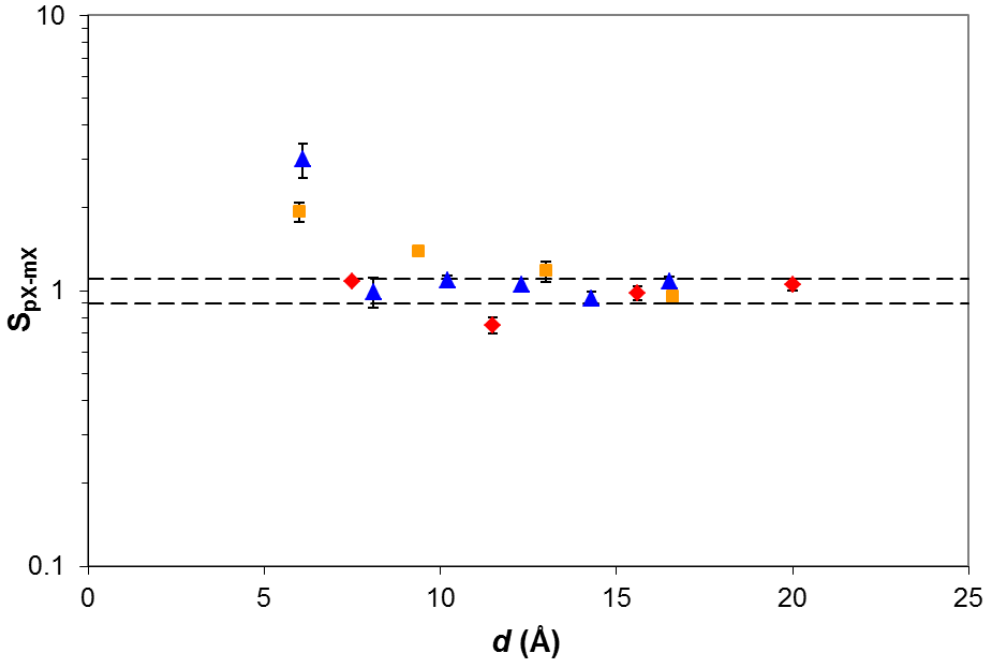

Figure 4.13 – Selectivity towards pX from simulations of adsorption from an equimolar pX/mX mixture at 1 Pa for rhombic model pores with wall intersection angles of 30° (blue triangles), 60° (orange squares) and 90° (red diamonds) as a function of the PSD channel diameter. Where error bars are not visible, the error is within the symbol size. The dashed lines indicate the non-selective region ($0.9 \leq S_{oX\text{-}mX} \leq 1.1$).

As for pX-oX and oX-mX, very little difference in xylene-framework interaction energy was observed for the two isomers (Appendix K). In the 30° series, which was seen to strongly favour oX over the other two isomers ($\alpha_{xyl\text{-}pore} = 0.9 – 0.95$), a slight preference for mX was observed ($\alpha_{xyl\text{-}pore} = 0.95 – 1$), a result of the marginally higher degree of rotational freedom experienced by mX in the corner of the pore. The overall lack of selectivity in the 30° series is a result of this xylene-framework preference for mX being negated by a packing preference for pX, the origin of which will be discussed shortly.

As for pX-oX and oX-mX mixtures, the adsorptive preference is defined primarily by the xylene-xylene interactions, which were found to strongly favour pX for small pores (Figure 4.14). A preference for pX was observed for both the 30° and 60° systems for channel diameters of up to ~13 Å, while the 90° systems were generally unable to discriminate between pX and mX, although a distinct preference for mX was observed in the D11.5_A90 system.

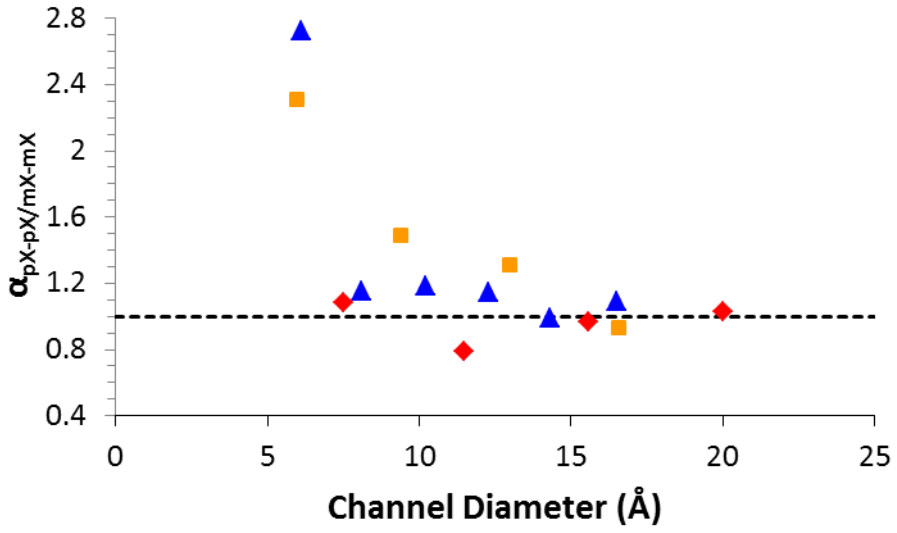

Figure 4.14 - Influence of channel diameter on the ratio of pX-pX to mX-mX interaction energies ($\alpha_{pX\text{-}pX/mX\text{-}mX}$) for model pore systems with wall intersection angles of 30° (blue triangles), 60° (orange squares) and 90° (red diamonds).

For the two smallest systems, the strong packing preference for pX over mX is a result of the same, well-defined arrangement of pX molecules which is responsible for the pX/oX selectivity (Figure 4.5 and Figure 4.6). The restrictive nature of these pores means that pX is the only isomer for which these packing arrangements are accessible. As the pore diameter is increased, similar packing arrangements are favoured by both isomers, resulting in lower differences between pX-pX and mX-mX interactions.

For all three wall intersection angles, larger pores allow the development of a well-defined monolayer with the aromatic rings of the xylene molecules parallel to the pore wall (Figure 4.15). In the 90° systems, the xylene molecules in the monolayer

are primarily packed in a triangular array and neighbouring monolayers are interwoven near the corners of the pore, akin to interlocking fingers. Rhombic packing with no interweaving of neighbouring monolayers is preferred in the 30° systems. In the 60° systems, a mixture of triangular and rhombic packing is observed, along with some interweaving of the monolayers near the corners of the pore.

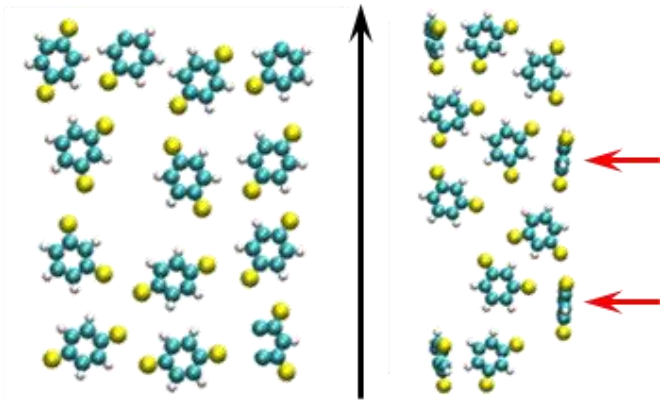

Figure 4.15 – Top-down view of the pX-mX monolayer in the 30° (left) and 90° (right) system. The channel direction is indicated by the black arrow. Interwoven xylenes from a neighbouring monolayer in the 90° system are indicated by red arrows. Colour scheme: C – cyan; H – white; CH_3 – yellow.

The square packing of xylene molecules seen in the 30° systems favours pX as the methyl groups of neighbouring xylene molecules are well-aligned and are able to interact strongly as well as resulting in a higher packing density of pX than mX. On the other hand, a triangular array of xylene molecules enables the methyl groups of neighbouring mX molecules to interact. For pX, a triangular array forces the methyl groups to interact primarily with the aromatic carbon and hydrogen atoms of neighbouring molecules. Monolayers with a triangular array are therefore expected to exhibit a packing preference for mX. This is not the case for either the 60° or 90° channels. We can surmise that the interweaving of monolayers in the corner of the pore observed in these systems favours pX over mX by both disrupting the regular triangular packing arrangement and introducing additional methyl groups between neighbouring xylene molecules, which are able to interact with the previously redundant CH_3 species of pX.

In the 90° systems, the triangular packing (which favours mX) and interweaving (which favours pX) cancel each other out, resulting in a low overall packing preference. In the D11.5_A90 system, which was the structure which showed mX-selectivity, the interweaving tends to result in additional hydrogen atoms being introduced to neighbouring monolayers rather than additional methyl groups, which indicates that it is the introduction of methyl groups to neighbouring monolayers which drives the packing preference for pX seen in other systems with interwoven monolayers. In the 60° channels, the additional pX-preference from interweaving works in conjunction with the existing pX-preference from the observed regions of square packing, resulting in a strong packing preference for pX over mX. In larger diameter channels, the xylene monolayers become much less well-defined, with low levels of order observed near the pore wall, which results in only negligible differences in pX-pX and mX-mX interaction energies and low overall selectivities.

It can be seen that for the rhombic channel systems investigated in this work, the overall suitability of a structure for the separation of xylene isomers cannot necessarily be judged solely on an understanding of the pX-oX system. Structures which selectively adsorb pX over oX appear to also prefer pX over mX, suggesting that the selection of a pX-selective adsorbent based on pore diameter is a reasonable approach for these systems. A high proportion of oX-selective channels, however, are unable to effectively discriminate between pX and mX, making them unsuitable adsorbents for the separation of mixtures of xylene isomers into their individual components.

4.3.3 Comparison of Model Pore Systems with MOFs

So far, it has been shown that the influence of channel diameter on adsorptive preference in these model pore systems is in qualitative agreement with the MOFs studied by Moghadam and co-workers. While a number of these model pore systems are analogous to MOFs in terms of their channel diameter and geometry, it is useful

to consider whether these model systems are indeed directly comparable to similar MOF structures – i.e. whether the relative heterogeneity of the pore walls present in MOFs plays an important role in the competitive adsorption of xylenes.

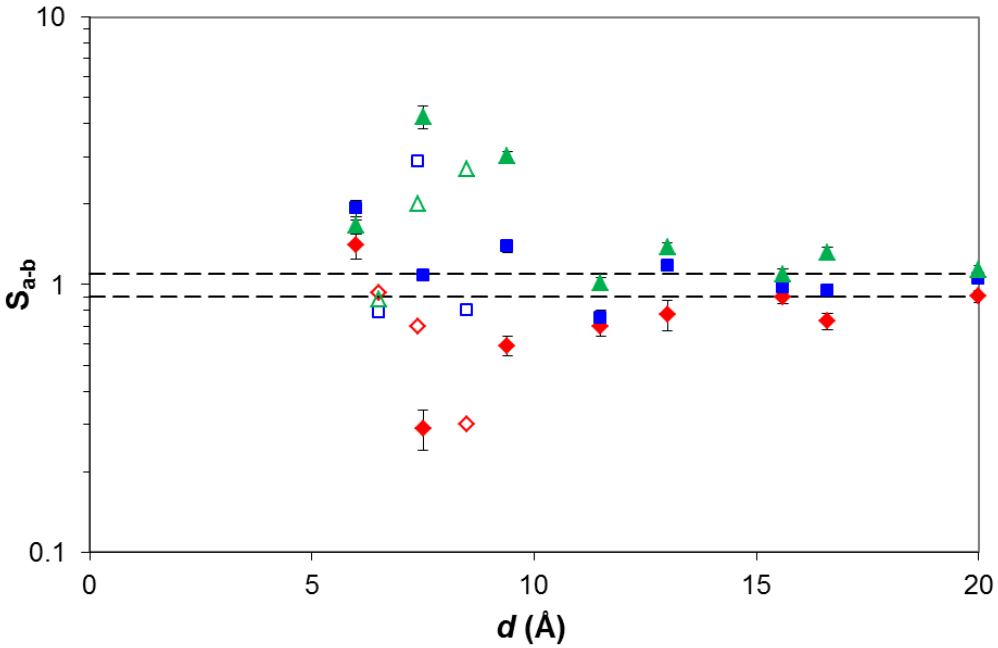

Figure 4.16 – Selectivity towards component *a* from an equimolar *a/b* mixture for 60° and 90° model pores (filled symbols) and MOFs (empty symbols) as a function of the PSD channel diameter for pX-oX (red) pX-mX (blue) and oX-mX (green). Where error bars are not visible, the error is within the symbol size. The dashed lines indicate the non-selective region ($0.9 \leq S_{a-b} \leq 1.1$). Selectivities for MIL-47(V) and MIL-53(Al) were taken from the experimental work of Alaerts *et al* (2008).

Here, competitive xylene adsorption in rhombic model pore systems and in the 1D rhombic channel MOFs CAU-8 (d = 6.5 Å, angle = 89°), MIL-47(V) (d = 7.4 Å, angle = 80°) and MIL-53(Al) (d = 8.5 Å, angle = 80°) is compared. It should be noted that the flexible MIL-53(Al) can exhibit a range of channel diameters depending on temperature and sorbate loading and, following the work of Moghadam, the fully open form of the MOF is considered here. The simulated selectivities of the 60° and 90° model pore series are shown alongside the experimentally-observed selectivities of MIL-47(V) and MIL-53(Al) and the simulated selectivity of CAU-8 in Figure 4.16.

It can be seen that the smallest of the three MOFs, CAU-8, exhibits low overall selectivity. The channel diameter of CAU-8 (6.5 Å) lies very close to the diameter identified both here for model pore systems and by Moghadam as marking the transition between pX-selective and oX-selective. The inability of the MOF to differentiate between oX and pX suggests that an additional 'transition region' should be incorporated into any screening protocol, in which low selectivities for either pX or oX are expected. For rhombic systems, this zone appears to lie between 6 and 7 Å. This transition region is further explored for triangular channel systems in Section 4.4.

As in the model pore systems, no difference in xylene-framework interactions was observed between the three components in CAU-8 and the low selectivities are a result of the similar xylene-xylene interactions experienced by the three isomers. While the pore is small enough to restrict the xylenes to adsorbing in a single-file arrangement (Figure 4.17), similar to that observed in the D6.0_A60 system (Figure 4.5), the molecules have a much greater degree of rotational freedom, which results in all three isomers achieving the same packing density. In the more restrictive D6.0_A60 system, this arrangement was readily available only to pX. The channel of CAU-8 is still too small to allow the formation of xylene pairs, which were responsible for the high oX-selectivity observed in larger model pore systems (e.g. D7.5_A90).

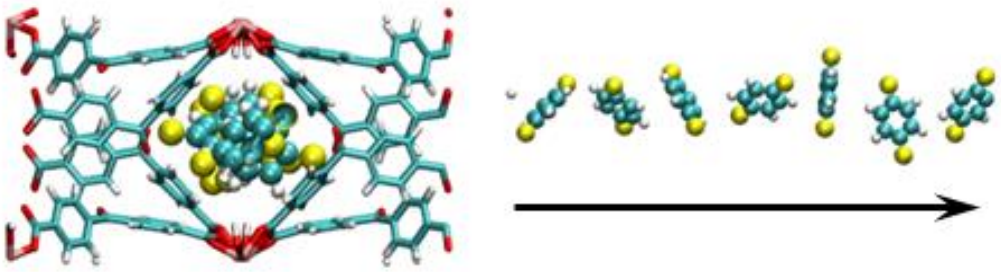

Figure 4.17 - Xylene packing arrangement in CAU-8 looking along the channel (left) and a top-down view of the channel length (right). The framework atoms have been omitted for clarity in the right-hand image. The black arrow indicates the channel direction. Colour scheme: C – cyan; H – white; O – red; Al – pink; CH_3 – yellow.

Both the MIL-47(V) and MIL-53(Al) systems show some deviation from the model pore systems. While the model pore systems appear to be in good numerical agreement with MIL-53(Al) in terms of selectivity, the origin of the selectivity in the two types of structure is not in complete agreement. Experimentally, the enthalpy of adsorption of oX in MIL-53(Al) has been demonstrated to be much higher than that of mX, which in turn has a higher affinity than pX (Duan *et al.*, 2013), which was not the case for the model pore systems. This is most likely to be a result of the breathing of MIL-53(Al). At low xylene loading, the MIL-53(Fe) analogue has been shown to take on the narrow pore form (wall intersection angle ~ 25°), before moving into the large pore form (wall intersection angle ~ 80°) at saturation loading (El Osta *et al.*, 2012). If a similar transition occurs for MIL-53(Al), then the system is better compared to the 30° model pore systems at low loading, in which the order of xylene-framework interaction energies was indeed oX > mX > pX. In the MIL-47(V) structure, for which the narrow pore form is not accessible during xylene adsorption, all three isomers were seen to experience similar enthalpies of adsorption (Alaerts *et al.*, 2008), in agreement with the 60° and 90° model pore systems. The ability of MIL-53(Al) to separate the isomers based on enthalpies of adsorption is thus a result of the pore volume being confined enough to create specific adsorption sites which are well suited to oX, as outlined in Section 4.3.1.

The xylene pairs which were observed in the D7.5_A90 model pore system are prevalent in both MIL-53(Al) and (Fe) and MIL-47(V) (Alaerts *et al.*, 2008; Castillo *et al.*, 2009; El Osta *et al.*, 2012), resulting in a strong preference for oX over both pX and mX. The model pore systems appear to overestimate the selectivity towards oX for both pX-oX and oX-mX mixtures, however, as well as failing to predict the strong preference for pX over mX in MIL-47(V). As the experimental selectivity in MIL-47(V) is determined by packing effects, it seems likely that the introduction of variations in the van der Waals surface of the pore – essentially a molecular-level surface roughness when compared to the homogeneous graphitic model pore (Figure 4.18) – has a strong influence on the packing of each of the three isomers by allowing the molecules slightly more orientational freedom and less strictly enforcing a regular packing arrangement. As has been shown for both MOFs

(Moghadam, 2013) and model pores, a reduction in the ordering of the xylene molecules in the system results in a decrease in selectivity, which may explain the higher selectivities observed in the model pore systems.

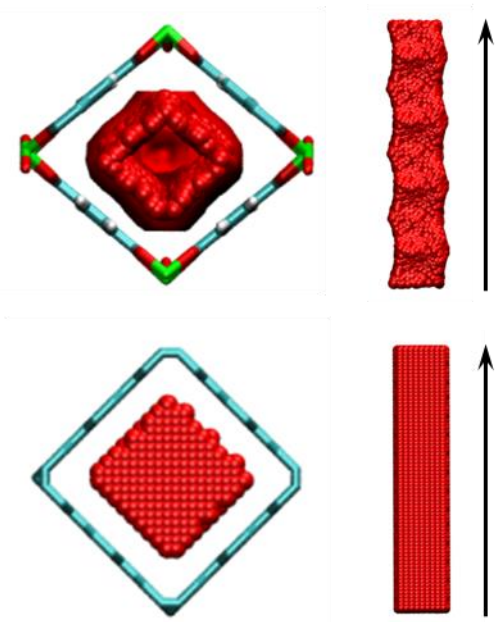

Figure 4.18 – Helium pore volumes (red) of the D7.5_A90 model pore (bottom) and MIL-47(V) (top) viewed along the channel length (left-hand images) and top-down (right-hand images). Colour scheme: C – cyan; H – white; O – red; V – green.

The less homogenous surface of MIL-47(V) appears to have a drastic impact on the adsorption of mX. The simulated maximum uptake of mX was found to be much lower than that of pX and oX in MIL-47(V) (Castillo *et al.*, 2009). This was shown to be a result of the methyl groups of neighbouring mX molecules introducing a steric hindrance not present for pX and oX, which forced mX molecules to be adsorbed much less closely together. In contrast, in the D7.5_A90 model pore system, oX exhibited a higher maximum uptake (17 molec/UC) than pX and mX (both 16 molec/UC). Although the two systems have the same channel diameter and similar wall intersection angles, the surface heterogeneity of the MOF results in a structure which is geometrically much better suited to pX than the model pore and is thus able to separate pX from mX.

Overall, model pore systems appear to be capable of qualitatively predicting the impact of channel geometry and diameter on the strength of xylene-framework interactions. The lack of energetic preference observed in both MIL-47(V) and CAU-8, as well as the order of interaction strength in MIL-53(Al), were in agreement with their analogous model pore systems. The prediction of packing densities and packing arrangements was less successful, however. While similar packing arrangements were observed in MIL-47(V) and the D7.5_A90 systems, the density of these packing schemes and the overall order of preference of the structures were not the same. Even in these relatively simple systems, the spatial variation of pore volume introduced by using individual linkers rather than graphitic sheets to define the pore wall appears to be capable of strongly influencing the adsorption of one isomer over the other.

4.4 Xylene Adsorption in the MIL-140 Series

Having considered adsorption in rhombic channels systems, we now turn our attention to another simple 1D channel geometry – the triangle. The MIL-140 (Guillerm *et al.*, 2012) series of isoreticular MOFs are comprised of infinite 1D zirconium oxide chains connected by linkers of increasing length (1,4-BDC, 2,6-NDC, 4,4'-BPDC and 4,4'-azo-BDC), creating a series of MOFs with 1D triangular channels of diameters ranging from 3.3 Å to 6.6 Å (c.f. Section 3.4.3). These structures provide an excellent opportunity to investigate the impact of pore size on adsorptive preference for xylene isomers in pore diameters where a transition from *para*- (d < 6 Å) to *ortho*-selective (d > 6 Å) appears to occur. As the channels of MIL-140A (Zr-BDC) were found to be too small to allow xylene adsorption to take place, this section focuses on the remaining three structures: MIL-140B (Zr-NDC, d = 4.2 Å), MIL-140C (Zr-BPDC, d = 5.9 Å) and MIL-140D (Zr-azo-BDC, d = 6.6 Å).

Despite the similarities in both pore geometry and diameter between the three structures, each MOF was found to exhibit a very different adsorptive preference to

the other two (Figure 4.19 and Figure 4.20). The smallest diameter MOF – MIL-140B – was found to be highly selective towards pX, particularly at low loading. In contrast, pX was the least preferred component in MIL-140D, while MIL-140C was unable to effectively discriminate between the three isomers except at high pressure, where a slight *meta*-selectivity was observed.

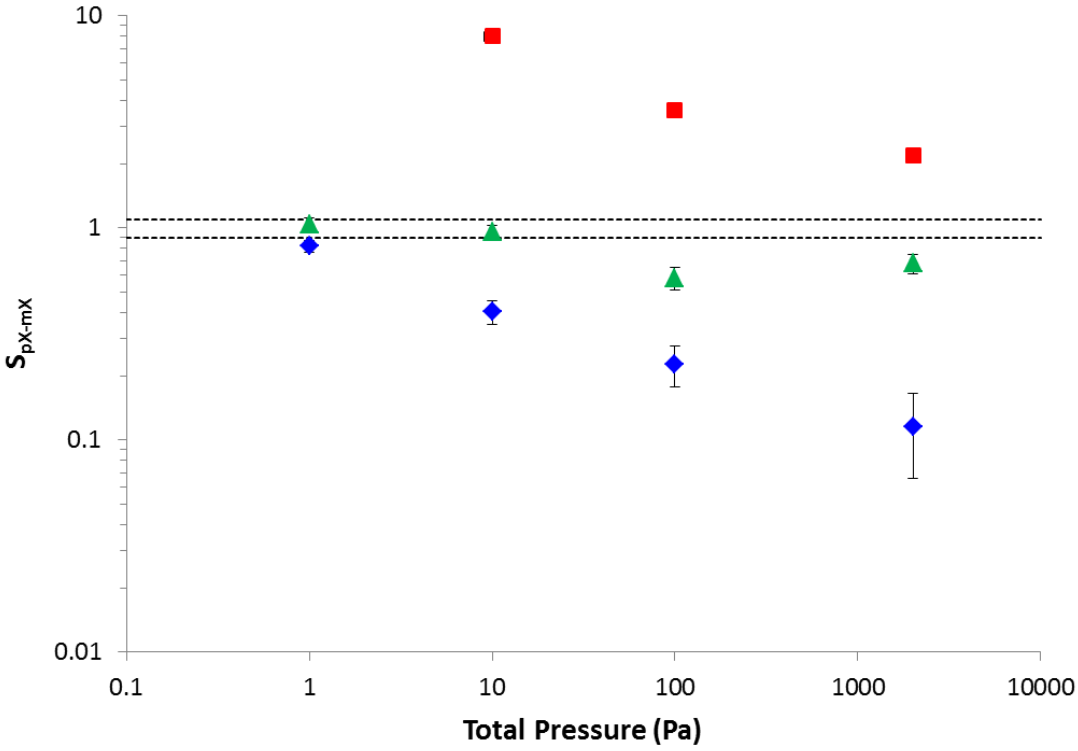

Figure 4.19 – Simulated selectivity as a function of pressure for adsorption from equimolar pX-mX binary mixtures in MIL-140B (red), MIL-140C (green) and MIL-140D (blue). No xylene adsorption was observed at 1 Pa in MIL-140B

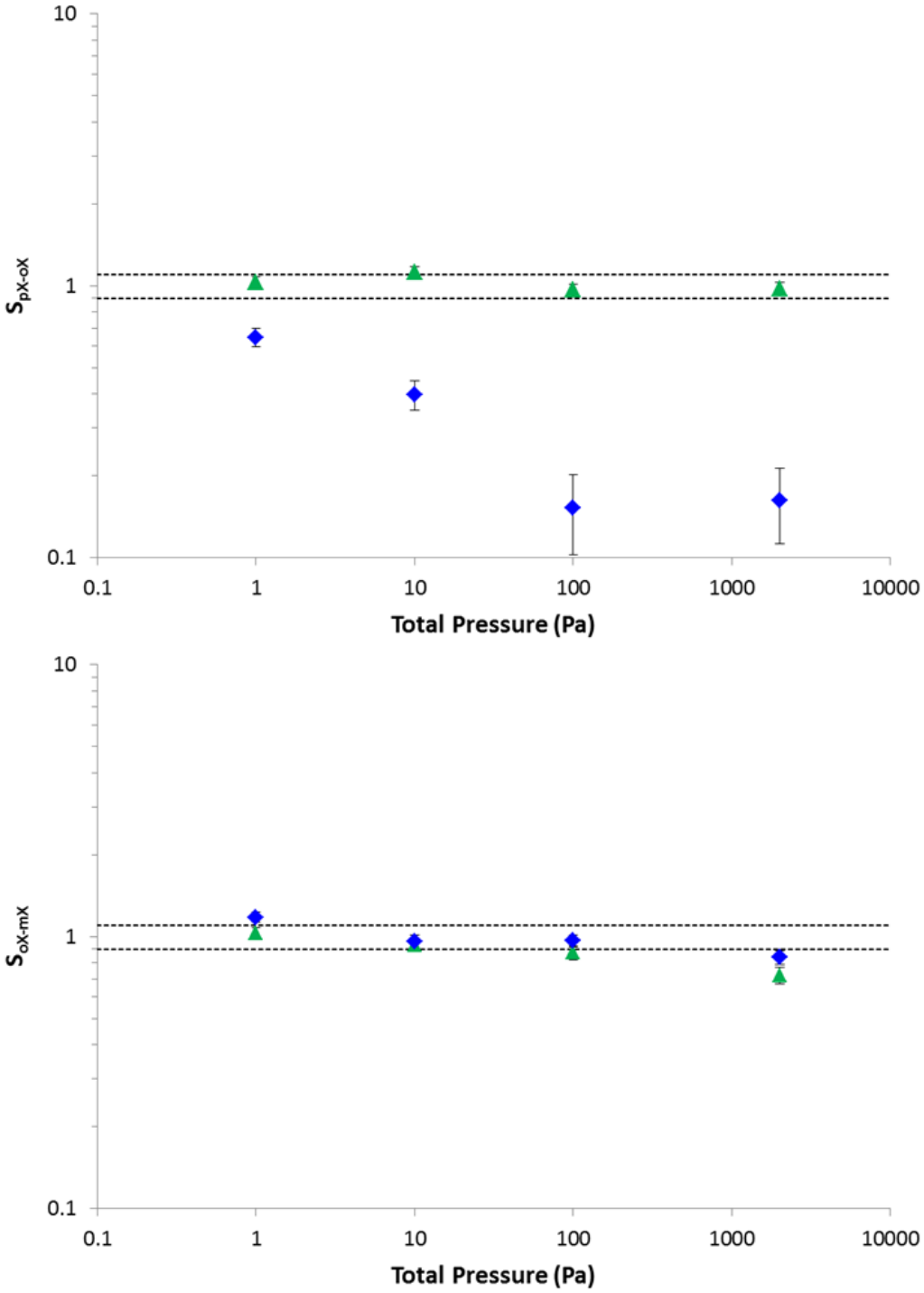

Figure 4.20 – Simulated selectivity as a function of pressure for adsorption from equimolar pX-oX (top) and oX-mX (bottom) binary mixtures in MIL-140C (green) and MIL-140D (blue). Note that oX does not adsorb in MIL-140B and the infinite selectivity towards pX and mX for oX-containing mixtures in this MOF are not shown.

In both single- and binary adsorption simulations, oX was found to be the "wrong" shape to fit into the narrow channels of MIL-140B, resulting in negligible oX uptake and an overall order of preference of pX > mX >> oX. In the case of pX-mX mixtures, the highest selectivity towards pX was observed at low loading ($S_{pX\text{-}mX}$ = 8.0 at 10 Pa), before decreasing as the pressure is increased ($S_{pX\text{-}mX}$ = 2.3 at 2 kPa). This type of behaviour is typically the result of a strong enthalpic preference for one component at low loading being overcome by a strong packing preference for the other component as the loading is increased, as previously described for the majority C_3-MOF systems in Section 3.4.2. In the case of MIL-140B, however, pX and mX exhibit identical xylene-MOF interaction energies (pX: -63.4 ± 1.7 kJ/mol, mX: -63.4 ± 1.9 kJ/mol). The high pX selectivity at low pressure is a result of the much higher number of adsorption sites available to pX, a consequence of a combination of pore and isomer geometry.

While the channel of MIL-140B may be described as generally triangular in cross-section, the periodic protrusion of the pillaring NDC linker into the channel creates variations in channel width along the length of the channel (Figure 3.21). Although the channel diameter from the PSD (i.e. the largest sphere which may be inserted into the channel) is only 4.2 Å, additional pockets of space between the pillaring NDC linkers mean that some sections of the channel have much larger edge-to-edge widths (up to 8.7 Å).

At low loading, both pX and mX are preferentially located in similar high-energy adsorption sites with their respective methyl groups found near the centre of the channel (Figure 4.21). The geometry of the pore is such that the methyl groups (σ = 3.8 Å) are too large to fit into either the corners of the channel or the pockets of space between the NDC linkers (smallest dimension ~3 Å) and so must be located near the centre of the channel. It is this restriction which limits the uptake of oX in the MOF – if both methyl groups are placed in the centre of the channel, the opposite side of the aromatic ring overlaps with the framework. The critical xylene dimension for this system ($d_{crit,M140B}$) is thus the largest distance from an axis running through both methyl groups to the edge of the xylene molecule (Figure 4.22).

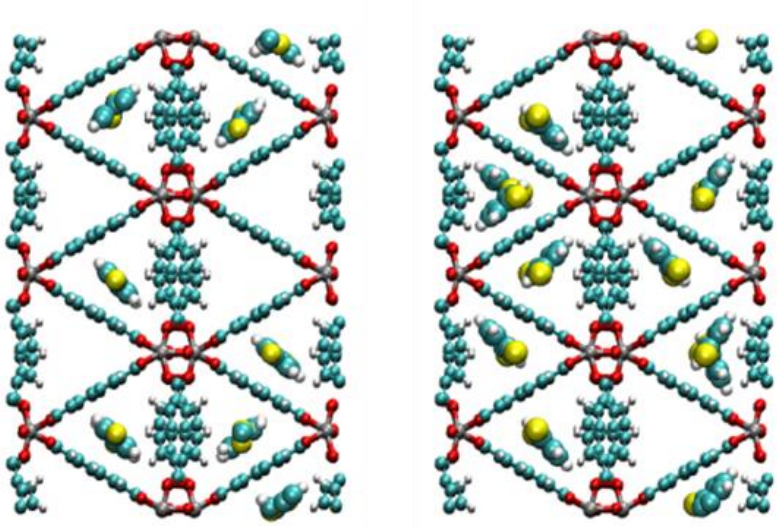

Figure 4.21 – Adsorption locations of pX (left) and mX (right) at low loading in MIL-140B from single-component simulations. The shape of the pore forces both methyl groups (yellow) to be located near the centre of the channel. Colour scheme: Zr – grey; O - red; C – cyan; H – white; CH_3 pseudo-atom – yellow.

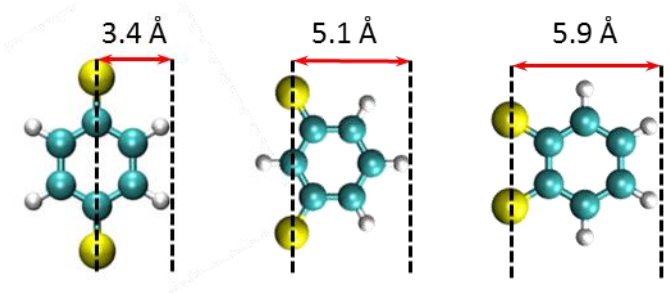

Figure 4.22 – Methyl-to-edge length of pX (left), mX (centre) and oX (right) – the critical xylene dimension for this system ($d_{crit,M140B}$).

Although both mX and pX are adsorbed in similar locations, mX is considerably more restricted in the orientations available to it in this site due to the much larger critical distance. The asymmetric nature of the mX molecule means that when the methyl groups are in the centre of the channel, the opposite hydrogen atom is forced into the extreme corner of the pore, severely limiting the rotational freedom of mX around its long axis. pX, whose methyl groups are coincident with the long axis of

the molecule, enjoys more freedom to rotate around this axis. While the interaction with the framework is the same for both molecules, the Boltzmann factor for pX is much higher than that of mX as a consequence of the greater rotational freedom experienced by pX. This results in a high selectivity towards pX at low loading (Figure 4.19).

As the loading is increased, xylene molecules adsorb in slightly less favourable positions, but always with their methyl groups located in the channel centre and their long axes aligned parallel to the channel length. The limiting factor on xylene packing density along the channel is the length of the individual xylene molecule, evidenced by the slightly higher maximum capacity of the MOF for the slightly shorter mX molecule (1.82 ± 0.09 molecules/UC) compared to pX (1.65 ± 0.06 molecules/UC). The slightly enhanced packing density, coupled with an associated slight increase in xylene-xylene interactions for mX over pX contributes to a loss in selectivity at higher pressure (Figure 4.20).

While MIL-140B remains selective towards pX at saturation, further increases in the selectivity may be achieved through the functionalisation of the NDC linker. The ability of mX to fit in the pore relies on the pockets of space available near the linker and the reduction of this space through the introduction of functional groups to the linker may be expected to result in the exclusion of mX from the structure. This was explored by considering the case of fluorinated NDC, wherein the hydrogen atoms on the 1,5 positions of the NDC linker were replaced with fluorine atoms (Figure 4.23). While the introduction of the fluorine atoms did not reduce the capacity of the MOF for pX in pure component GCMC simulations, mX was found to be completely excluded from the structure, a result replicated in binary pX-mX simulations. This suggests that fluoro-functionalised MIL-140B may be used to separate pX from mX and oX via molecular sieving.

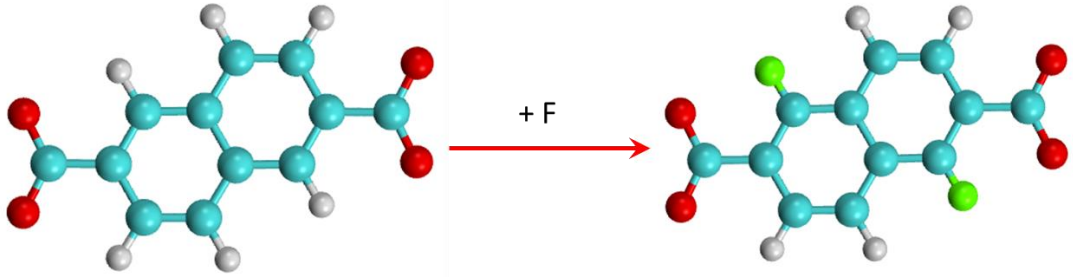

Figure 4.23 – Theoretical functionalisation of the NDC linker of MIL-140B with fluorine atoms on the 1,5 positions.

Replacement of the NDC linker of MIL-140B with BPDC allows the synthesis of MIL-140C, a framework isostrucural to MIL-140B with a slightly larger channel diameter (d = 5.5 Å). The channel is now large enough to allow oX adsorption and all three isomers exhibit slightly higher maximum gravimetric uptakes than in MIL-140B. The less constrictive pore compared to MIL-140B means that all three isomers experience similar and comparatively high levels of orientational freedom. Xylene molecules are still adsorbed in a single-file manner along the channel length but the methyl groups are not restricted to the centre of the channel and it is not necessary for the long axes of the xylene molecules to be completely parallel to the channel axis. As in MIL-140B, all isomers experience very similar interactions with the framework at low loading (pX: -65.4 ± 1.2 kJ/mol; mX: -66.2 ± 1.1 kJ/mol; oX: -65.7 ± 0.9 kJ/mol). In the absence of any orientational restriction for any of the isomers, however, the structure is non-selective at low pressure (Figure 4.20 and Figure 4.19).

At higher pressures, the MOF becomes slightly selective towards mX ($S_{pX\text{-}mX}$ ~ 0.6, $S_{oX\text{-}mX}$ ~ 0.8) but remains unable to discriminate between pX and oX ($S_{pX\text{-}oX}$ ~ 1.0). This is due to an increased packing density for mX compared to the other two isomers, which is also evident in the single-component isotherms (0). It is possible to fit in roughly half a molecule more mX than oX and almost one extra molecule of mX than pX per unit cell at saturation (mX: 4.9 ± 0.1 molec/UC; oX: 4.4 ± 0.1 molec/UC; pX: 4.0 ± 0.1 molec/UC). This difference in packing density is a result of oX and mX having an additional orientation available to them which is unavailable to pX. The longer pX molecule is forced to keep the aromatic

ring roughly parallel with the channel axis (Figure 4.24; left). Both mX and oX, which are more compact than pX, are not restricted in the same manner, with some molecules even being observed with the aromatic ring perpendicular to the channel axis (Figure 4.24; middle and right). Although this results in a less favourable interaction with the framework as the aromatic ring is less able to interact with the pore wall, it does result in an increase in packing density along the channel length as the molecules are much less 'thick' (~ 4 Å) than they are long (~7 to 8 Å). This orientation is much more accessible to mX (for which the fraction of molecules observed in the perpendicular orientation was 0.23 ± 0.05, compared to only 0.03 ± 0.02 for oX), enabling mX to achieve a higher packing density. The low observed frequency of perpendicular oX molecules suggests that the difference between pX and oX is primarily due to the greater length of pX compared to oX.

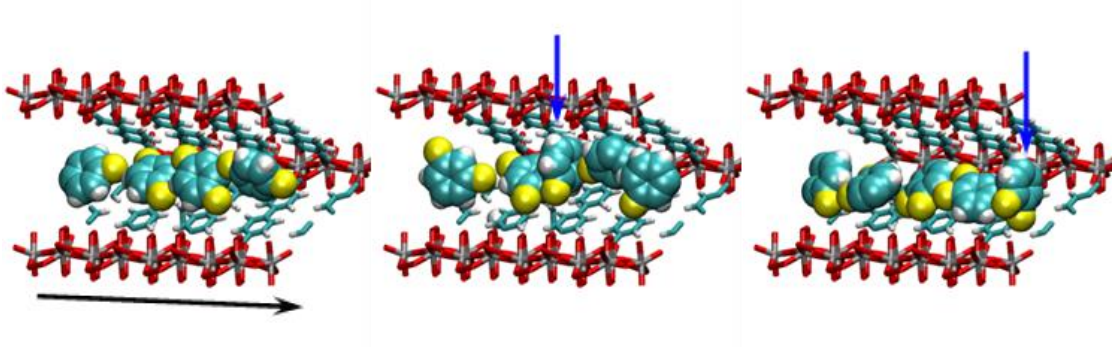

Figure 4.24 – Simulation snapshots of pX (left), mX (centre) and oX (right) in MIL-140C at saturation loading. For clarity, only two walls of the channel are shown. The channel axis is indicated by the black arrow. The blue arrows indicate molecules of mX and oX which are aligned with their aromatic rings perpendicular to the channel axis, an orientation inaccessible to pX. Colour scheme: Zr – grey; O - red; C – cyan; H – white; CH_3 pseudo-atom – yellow.

The use of azo-benzene dicarboxylate as a linker in MIL-140D allows a further increase in pore diameter (d = 6.6 Å). Unlike MIL-140C, MIL-140D is selective even at low loading, with an overall order of preference of oX > mX > pX. The larger pore diameter results in weaker (i.e. less negative) average xylene-MOF interaction energies when compared to MIL-140B and C (pX: -46.1 ± 0.1 kJ/mol; oX: -46.99 ± 0.04 kJ/mol; mX: -46.8 ± 0.1 kJ/mol). Although all three isomers

exhibit similar average interactions with the framework in single-component simulations, the distribution of xylene-MOF interaction energies is quite broad (Figure 4.25) and the selectivity towards oX in competitive simulations is due to the much higher maximum xylene-MOF interaction energy (pX: -52.4 kJ/mol; oX: -56.0 kJ/mol; mX: -54.3 kJ/mol) rather than the slightly higher average value.

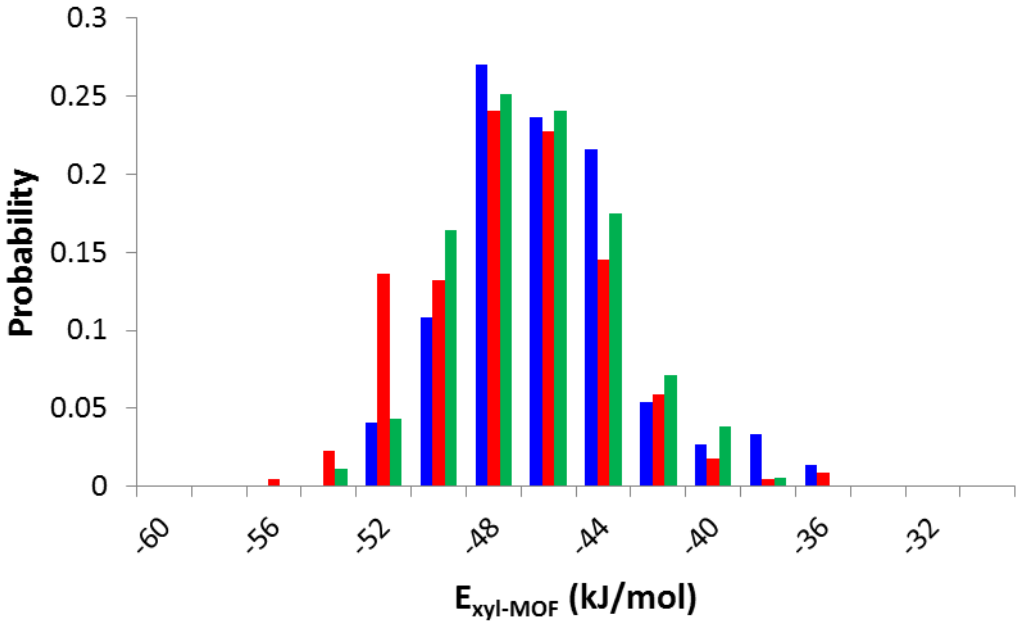

Figure 4.25 – Probability histograms of the observed xylene-MOF interaction energy ($E_{xyl\text{-}MOF}$) for pX (blue), oX (red) and mX (green) in MIL-140D.

While the distribution of xylene-MOF interaction energies for mX and pX are quite similar, displaying a single peak centred around -48 kJ/mol, the distribution for oX is much less symmetric and a second peak appears be present, centred on -52 kJ/mol. The different shape of the oX –MIL-140D interaction energy distribution indicates that an additional orientation is available to oX which is not accessible to the other two isomers. Examination of snapshots from the simulation reveal the slightly larger channels of MIL-140D in comparison to MIL-140B and C provide a good match to the methyl-to-edge distance of oX (5.9 Å; Figure 4.22), allowing the molecule to position both methyl groups in one corner of the pore while retaining a strong interaction between the other edge of the aromatic ring and the opposite pore wall (Figure 4.26). A similar orientation was not observed for either pX or mX.

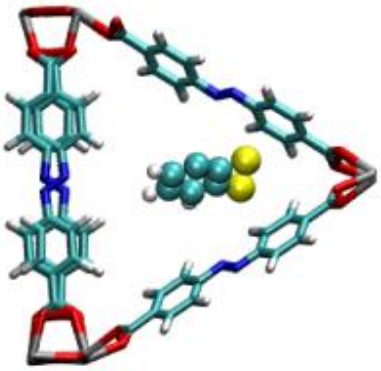

Figure 4.26 – The channel of MIL-140D provides an excellent match to the oX molecule, which is able to position its methyl groups (yellow) in the corner of the pore and still maintain a strong interaction with the opposite pore wall. Colour scheme: C - cyan; H – white; N – blue; O – red; Zr – grey; CH_3 – yellow.

At higher loading, mX and oX are able to pack much more closely together than pX, resulting in much higher maximum capacities for these two isomers in single-component simulations (pX: 2.08 ± 0.12 molec/UC; oX: 2.66 ± 0.13 molec/UC; mX: 2.66 ± 0.09 molec/UC).The comparatively low packing density of pX is a result of the much greater molecule length (Figure 4.1). As in MIL-140C, both oX and mX are able to position themselves so as the aromatic ring is perpendicular to the channel, an orientation still not accessible to pX. In MIL-140C, oX was found to more strongly favour the parallel over this perpendicular orientation when compared to mX. In contrast, the perpendicular orientation is equally accessible to both isomers in the slightly larger channel of MIL-140D and both oX and mX exhibit identical saturation loadings. The greater packing density of oX and mX is responsible for the high selectivity towards these two compounds over pX observed in competitive simulations at high pressure ($S_{mX\text{-}pX} = 8.6 \pm 0.1$; $S_{oX\text{-}pX} = 6.3 \pm 0.1$). The near-identical packing densities and MOF-framework interactions mean that MIL-140D is essentially unable to discriminate between oX and mX at high pressure ($S_{oX\text{-}mX} = 0.84 \pm 0.1$).

Overall, it can be seen that while GCMC simulations of xylene adsorption in the MIL-140 series of MOFs provide some support for the size-selectivity concept and screening protocol outlined in Section 4.1, they also confirm both the presence of a low-selectivity transition region in terms of pore diameter and that the effect of mX on the separation cannot be accurately predicted based solely on a knowledge of the pX-oX system. The smallest pore MOF, MIL-140A (d = 3.3 Å), was found to be too small to allow any xylene adsorption. MIL-140B, which is predicted to be *para*-selective based on pore diameter (d = 4.2 Å), was indeed found to be strongly selective towards pX. Both pX and mX were found to interact equally strongly with the framework and the selectivity is a result of the narrow channel being more accessible to the slimmer pX molecule. While the preference of MIL-140B was well predicted based on pore diameter, this is not the case for MIL-140C. For a pore diameter less than 6 Å (d = 5.9 Å), the MOF is predicted to be pX selective, whereas the overall order of preference in MIL-140C at higher pressure from binary mixture simulations is mX > oX > pX, matching the order of saturation capacities from single-component simulations. At low pressure, the MOF is non-selective. When compared to the *para*-selective model pore systems of similar diameter (D6.0_A60 and D6.1_A30), this suggests that pore diameter is not a reliable indicator of selectivity for pores close to 6 Å in diameter and that the selectivity is more likely to be a function of pore shape for these structures. The preference of the larger MIL-140D for oX over pX matches that predicted based on its pore diameter (d = 6.6 Å). In this case, the MOF exhibits a strong preference of oX and mX over pX at high pressures which is a result of the relatively low packing density of pX compared to the other two isomers. It can be seen that while the longer, slimmer pX molecule is well suited to small pore diameters, its increased length compared to the other isomers becomes a hindrance during adsorption in larger pores, in which the more compact oX and mX molecules have a much greater degree of rotational freedom, allowing them to make more efficient use of the available pore volume.

4.5 Conclusions

In this chapter, the influence of pore diameter on the competitive adsorption of xylene isomers was explored for both rhombic and triangular channel systems. It was shown that for pX-oX and oX-mX mixtures, the adsorptive preference of the structure may be predicted based on the channel diameter. In both rhombic and triangular systems, pores less than 4 Å were too small to allow xylene adsorption, providing a lower limit for pore diameter in the screening of new MOF structures for this application. The most oX-selective structures were found to have channel diameters of 7-12 Å, above which the selectivity gradually diminished. Small-pore structures ($4 < d < 6$ Å) were found to be either non-selective or selective towards pX. The adsorptive preference in these cases is strongly dependent upon the geometry of both the channel and the surface of the pore wall. Flat-walled rhombic model pore systems were found to be strongly pX-selective even for diameters up to 6.1 Å as a result of the pX experiencing a higher degree of orientational freedom than both oX and mX. All three isomers were comparatively unconstrained in the similarly-shaped but slightly larger MOF CAU-8 (d = 6.5 Å) and this structure is unable to effectively discriminate between any of the isomers as a result. For triangular systems, MIL-140C (d = 5.9 Å) was non-selective while MIL-140D (d = 6.6 Å) was strongly oX-selective. This suggests that any screening protocol which is based solely on pore diameter should approach MOFs with channel diameters of 5-6 Å with care or perhaps even discount these structures entirely as potential candidate adsorbents for this separation.

The selectivity in the triangular MIL-140 series is predominantly defined by entropic and packing effects. In MIL-140B (d = 4.2 Å), only pX and mX are able to enter the pore, while oX is completely excluded. The higher degree of rotational freedom experienced by pX in this narrow channel results in high pX-selectivity. This selectivity may be further enhanced by making the pore more restrictive through the functionalisation of the linker with fluorine. The fluorine atoms create a more uniformly-shaped channel, which is now perfectly suited to pX, excluding both mX and oX. While the reasonably high solvothermal stability (Guillerm *et al.*, 2012) of

MIL-140B is attractive from an industrial perspective, the relatively low xylene capacity of both forms of MIL-140B (~0.65 mol/kg of MOF crystal) is likely to preclude the use of this MOF in bulk chemical separations such as SMB operation, although the structure may be of interest in chromatographic or sensing applications where selectivity is the over-riding quality.

The slight increase in channel diameter achieved in MIL-140C (d = 5.9 Å) was shown to be of benefit to mX and oX. While all three isomers are restricted to a single-file arrangement, all three isomers experience approximately equal degrees orientational freedom, resulting in a non-selective structure. In MIL-140D (d = 6.6 Å), the shorter oX and mX isomers are less orientationally constrained than pX, allowing the structure to selectively adsorb oX and mX over pX, particularly at high loading where the reduced packing density of pX is of most importance. The channels of MIL-140D are still too constrictive to allow the MOF to distinguish between oX and mX based on packing effects, however, and a further increase in pore diameter (e.g. through the use of a longer linker such as terphenyl dicarboxylate) is likely to result in a MOF more capable of separating oX from both mX and pX.

In the case of rhombic pore systems, it was found that graphitic model pores are capable of qualitatively predicting the trends in xylene-framework interactions which are observed in analogous MOF structures. The inability of model pores with wall intersection angles of 60° and 90° to discriminate between xylene isomers based on xylene-framework interaction energy is in agreement with the computational observations in the similar CAU-8 structure presented in this work and the computational and experimental studies of the xylene-MIL-47(V) system available in the literature (Alaerts *et al.*, 2008; Castillo *et al.*, 2009). In addition, the enthalpic preference of the narrow pore form of MIL-53(Al) (wall intersection angle ~ 25°) for oX observed in experiment (Duan *et al.*, 2013) is in qualitative agreement with the increased oX-framework interaction energies observed in the 30° model pore systems, which were shown to be a result of the increased rotational freedom of oX compared to pX and mX in these pores. Model pore systems therefore provide a

useful tool to further assess the influence of channel geometry and diameter on xylene-framework interactions in one-dimensional structures, allowing fine control of both pore diameter and pore geometry without introducing variations in composition or surface heterogeneity. Such an approach enables the optimum pore size and geometry for either pX- or oX-selectivity to be established, providing a target structure for future MOF development.

As in the MIL-140 series, the selectivity of the model pore systems was primarily determined by the different packing densities and arrangements accessible to the different isomers. In small channels, the longer and slimmer pX molecule is able to interact more strongly with neighbouring molecules than either mX or oX. In less restrictive pores, all three isomers take up similar packing arrangements but the more compact oX molecule is able to make more efficient use of the available pore volume, resulting in oX-selective structures. It was shown that these packing effects may be heavily influenced by the shape of the surface of the pore wall, however, and that model pore systems are not able to accurately predict these effects in MOFs. The packing density of oX was found to be much higher than that of pX and mX in the D7.5_A90 system, for example, and the order of preference in the structure was oX > mX = pX as a result. In the analogous MIL-47(V) structure, however, the packing densities of oX and pX are reported to be very similar, while that of mX is much lower (Castillo *et al.*, 2009) and the structure shows a strong preference for pX over mX. The spatial variation of the van der Waals surface of the pore along the channel length in MIL-47(V) allows pX to achieve a similar packing arrangement as oX, an arrangement which is not accessible to pX in the flat-walled model pore system. While this indicates that further work is required to fully understand the influence of heterogeneity in the density of wall atoms on xylene packing, it also suggests that the selectivity of a MOF at high loading may be further controlled through the introduction of variations in the pore surface, e.g. by introducing functional groups to the linker or by varying the spacing between linkers in a 1D channel system.

5 Molecular Simulation Studies of Xylene Adsorption and Diffusion in UiO-66(Zr)

In the previous chapter, the adsorption of xylene isomers in comparatively simple, one-dimensional pore systems was discussed. Here, we consider xylene adsorption and diffusion in a much more complex MOF – UiO-66(Zr). This framework has received considerable interest in recent years, the most relevant aspects of which are outlined in Section 5.1. The simulation parameters and inputs are detailed in Section5.2. Single-and multi-component adsorption of *para*-, *ortho*- and *meta*-xylene is explored in Sections 5.3 and 5.4 respectively, while the diffusion of the individual compounds through the framework is discussed in Section 5.5. Finally, Section 5.6 summarises the key findings and further questions emerging from this research.

5.1 Introduction

Since its discovery in 2008, the zirconium-based MOF UiO-66(Zr) (Cavka *et al.*, 2008) has been the subject of a great deal of interest in the scientific community. Comprised of zirconium oxide clusters connected by benzene dicarboxylate (BDC) linkers, the framework demonstrates excellent hydrothermal and mechanical stability (Cavka *et al.*, 2008; Valenzano *et al.*, 2011), making it an attractive proposition for industrial applications. The pore network of UiO-66(Zr) is constructed from larger, octahedral cavities connected by smaller tetrahedral pores (Figure 5.1). In order to diffuse through the framework, a molecule must pass from one type of pore to the other via a window of roughly 4 – 5 Å in diameter.

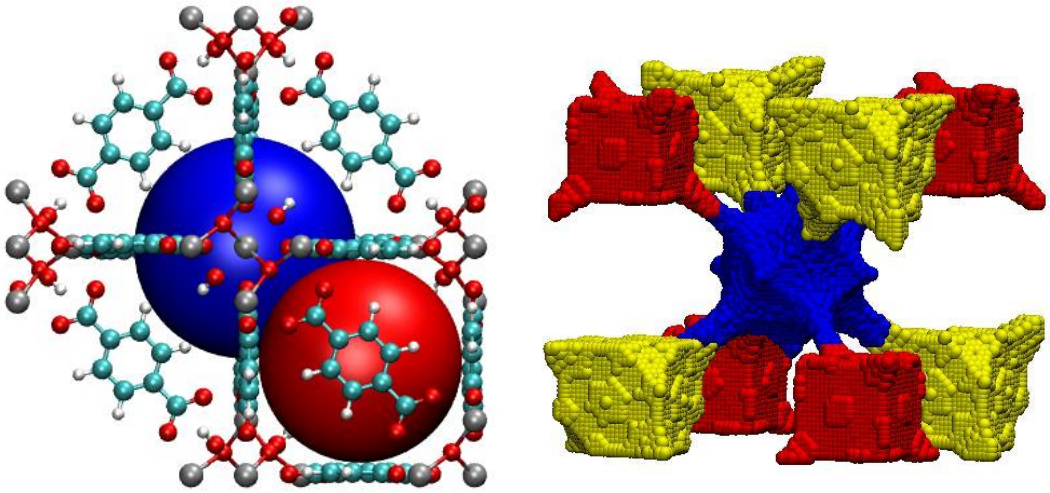

Figure 5.1 - Pore structure of UiO-66(Zr). The relative positions of the octahedral (blue) and tetrahedral (red) pores are common to both the hydroxylated and the dehydroxylated form of the MOF (left). In addition to the central octahedral cavity (blue), hydroxylated UiO-66(Zr) contains two distinct tetrahedral pores (red and yellow in the image on the right). Colour scheme: C – cyan; H – white; O – red; Zr – grey.

As-synthesised UiO-66 is fully hydroxylated, with each metal cluster containing four hydroxyl groups alongside eight-coordinated zirconium atoms [$Zr_6O_4(OH)_4$]. Two of these hydroxyl groups along with the remaining two hydrogen atoms can be driven off under heating above 523 K, producing a de-hydroxylated structure wherein each cluster contains only oxygen and seven-coordinated zirconium atoms [Zr_6O_6] (Cavka *et al.*, 2008). In the case of the hydroxylated UiO-66(Zr), the μ-OH groups forming part of the metal cluster produce a distortion in the linker geometry resulting in two distinct types of tetrahedral cavity. These μ-OH groups are driven off during the de-hydroxylation process, leaving only uniformly sized tetrahedral pores. The different pore types present in the two forms are easily identified in their respective pore size distributions (Figure 5.2). In the case of the de-hydroxylated UiO-66(Zr), two distinct peaks are observed in the PSD - one at 6.6 Å and one at 7.3 Å, corresponding to the tetrahedral and larger octahedral cavities respectively (points A and B in Figure 5.2). Examination of the PSD of the hydroxylated MOF reveals two, much broader, peaks at 6.6 Å and 7.3 Å. In contrast to the de-hydroxylated form, intermediately sized pores of ~7 Å make a considerable contribution to the PSD, evidenced by the smearing of the PSD in this region (point C in Figure 5.2).

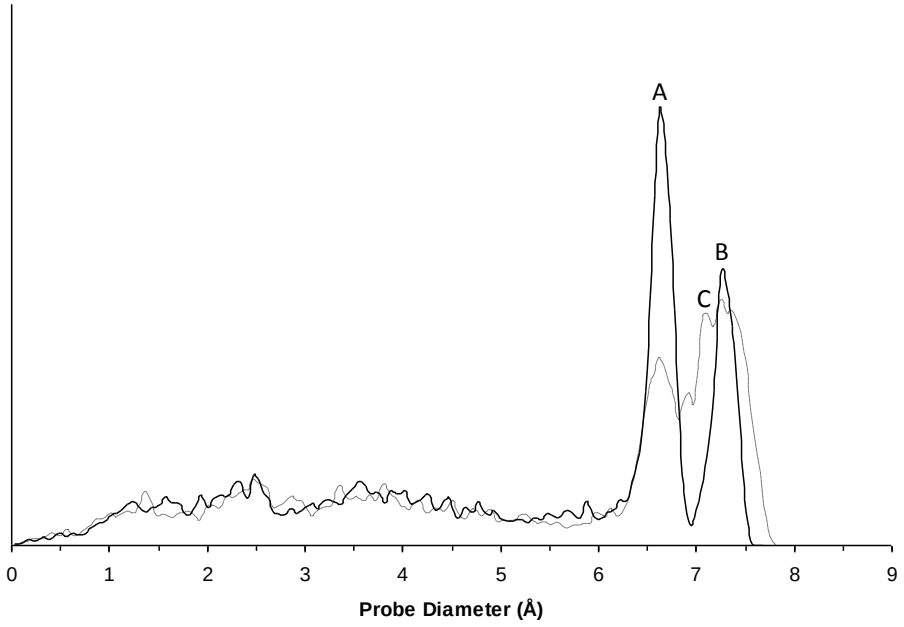

Figure 5.2 - Pore size distribution of hydroxylated (dashed line) and de-hydroxylated (solid line) UiO-66(Zr). Points A and B correspond to the smaller tetrahedral pore and the octahedral cavity, which are present in both forms of UiO-66(Zr). Point C corresponds to the intermediately sized tetrahedral cavity, which is present only in the hydroxylated form.

In classical MOF terminology, UiO-66(Zr) is described as being a rigid structure. Even at elevated temperature (up to 648 K), the X-ray diffraction (XRD) data reveals no significant structural flexibility or breathing effects (Valenzano *et al.*, 2011). Although the MOF does not exhibit any large breathing or swelling effects, such as those observed in the MIL-53 (Serre *et al.*, 2002) or MIL-88 (Serre *et al.*, 2004a) systems, the structure is not completely rigid. The primary mode of structural movement In UiO-66(Zr) and its functionalised analogues is via the rotation or 'flipping' of the BDC linker around its long axis (Devautour-Vinot *et al.*, 2012; Kolokolov *et al.*, 2012). While this linker rotation has little impact on the overall pore size or topology, it has been shown to impact considerably on the diffusion of light gases via modulation of the window size (Yang *et al.*, 2011a; Yang *et al.*, 2011b).

UiO-66 has been shown experimentally to be selective towards oX (Barcia *et al.*, 2011; Moreira *et al.*, 2012a), exhibiting so-called 'inverse shape selectivity' where,

in contrast to more conventionally shape selective MOFs such as MIL-125(Ti), oX is favoured over the slimmer pX. In the initial adsorption breakthrough studies of Barcia *et al* (2011) and Moreira *et al* (2012a), this preference was attributed to the close match between the diameters of the pores within the MOF and the kinetic diameter of oX, a concept previously described in the separation of linear and branched alkanes in the zeolites SAPO-5 (Santilli *et al.*, 1993) and MCM-22 (Denayer *et al.*, 2005). The least rotationally constrained isomer will experience the lowest loss of entropy upon adsorption, resulting in an overall lower Gibbs free energy of adsorption for species with similar adsorption enthalpies. In the UiO-66(Zr) – xylene system, this effect is expected to manifest itself in an entropic preference for the more compact *ortho*- isomer. This entropic driving force has also been held responsible for the experimentally observed preference of UiO-66(Zr) for branched over linear C_6 isomers (Barcia *et al.*, 2011; Duerinck *et al.*, 2013; Bozbiyik *et al.*, 2014). More recently, Chang and Yan (2012) and Duerinck *et al* (2013) have demonstrated experimentally an additional enthalpic preference for *ortho*-xylene, reporting an increased heat of adsorption for oX when compared to mX and pX of 7.5-13.1 kJ/mol, which was suggested to be a result of either favourable interactions between the aromatic rings of oX and the BDC linkers (π-π stacking) or enhanced electrostatic interactions between oX and the μ-OH groups of the MOF.

While the preliminary computational work of Granato *et al* (2014) correctly predicted the ortho-selective nature of the MOF and provided reasonable qualitative agreement to experiment for measured quantities such as maximum capacity and adsorption enthalpy, the adsorption mechanism and origin of the *ortho*-preference remains unclear. This chapter, therefore, addresses the fundamental aspects of xylene adsorption and diffusion in UiO-66(Zr) using a range of computational tools and sets out to identify the factors which drive the experimentally observed *ortho*-selectivity.

5.2 Method

5.2.1 Force Field Details

Both the hydroxylated and de-hydroxylated forms of UiO-66(Zr) were considered in this work. The geometry optimised structures of Yang et al, which have been shown to successfully reproduce light gas adsorption isotherms (Yang *et al.*, 2011a; Yang *et al.*, 2011b), were used. In MC simulations, the MOF structures were considered to be rigid and atoms were kept fixed at their optimised crystallographic positions. Framework LJ parameters and sources of DFT partial charges are listed in Appendix C and Appendix D respectively.

Two types of MD simulations were undertaken – one set in which the MOF was treated as rigid and another in which the MOF atoms were allowed to move. The flexible MOF was described using the force field developed by Yang and co-workers (2011b). In addition to the bonded potentials described in Section 2.2.4 and Appendix B, intra-framework non-bonded interactions between framework atoms were considered in simulation in the flexible MOF. For atoms separated by four or more bonds, both LJ and electrostatic interactions were considered, using the DREIDING (Mayo *et al.*, 1990) or UFF (Rappe *et al.*, 1992) parameters and DFT charges respectively. For atoms separated by three bonds, only the LJ term was included.

Xylene isomers were described using the force fields outlined in Section 4.2.1 – i.e. they were treated as rigid molecules in all simulations, with all atoms defined explicitly with the exception of methyl groups, which were treated as single spheres. All bonded parameters, partial charges and LJ parameters are listed in Table 4.1.

5.2.2 Monte Carlo Simulations

The adsorption of xylene isomers in rigid UiO-66(Zr) was simulated at 300 K via GCMC implemented in the MuSiC software (Gupta *et al.*, 2003) using the

parameters and move types described in Section 2.2.2. Single component adsorption isotherms were allowed at least 8 x 10^6 equilibrium steps, followed by 12 x 10^6 production steps for each pressure point, carefully ensuring that equilibrium was reached before starting the sampling process. Mixture simulations were allowed at least 100 x 10^6 steps to come to equilibrium, followed by a further 150 x 10^6 production steps.

The average interaction energy of the different xylene isomers with the framework in each of the pore types in UiO-66(Zr) was studied through Monte Carlo simulations in the NVT ensemble. Simulations were carried with a total of at least 108 xylene molecules (corresponding to one molecule per cavity of interest) and consisted of at least 8 x 10^6 equilibrium steps, followed by 12 x 10^6 production steps. In these simulations, xylene molecules were subjected to random rotation and displacement moves. The starting positions of the xylene molecules were restricted and any displacement which resulted in the molecule entering a neighbouring pore was rejected so as only one pore type was explored in each run.

5.2.3 Molecular Dynamics Simulations

The diffusion of xylene isomers in de-hydroxylated UiO-66(Zr) was studied through MD simulations using the DL_Poly Classic package (Todorov *et al.*, 2006). Initial simulations were carried out with the framework held rigid and the atoms kept fixed in their optimised crystallographic positions for xylene loadings of 3, 6, 9 and 12 molecules/UC. In order to assess the impact of framework flexibility on diffusion, simulations for a xylene loading of 3 molecules/UC were also carried out where the movement of MOF atoms was described using the force field of Yang and co-workers (Yang *et al.*, 2011a; Yang *et al.*, 2011b). Both sets of simulations were carried out in the NVT ensemble using a timestep of 1 fs. The simulations were allowed at least 0.1 ns to come to equilibrium before a production run of 10 ns. In the rigid MOF, simulations were carried out at both 300 K and 500 K, while in the flexible MOF, simulations were undertaken at 300 K and at temperatures ranging from 500 – 900 K. In both cases, the Berendsen thermostat was used to control the

temperature. The starting positions of the xylene molecules were taken from fully equilibrated GCMC simulations at the appropriate loading.

5.3 Single-Component Xylene Adsorption

The simulated adsorption isotherms of pure pX, mX and oX in hydroxylated UiO-66(Zr) are presented in Figure 5.3. It is immediately apparent that, despite the similarity of the three isomers, their resulting adsorption isotherms are unique. While pX and mX exhibit Type I isotherms, several sub-steps are apparent in the isotherm of oX. The low pressure uptake of oX is considerably enhanced when compared to the other isomers, while the maximum uptake of pX is greater than oX and mX. Whereas the increased low pressure uptake of oX is in qualitative agreement with the work of Moreira *et al* (2012a), there is no experimental evidence to support an enhanced saturation capacity for pX and, as shall be discussed later, this phenomenon is likely to be an artefact of the GCMC simulation.

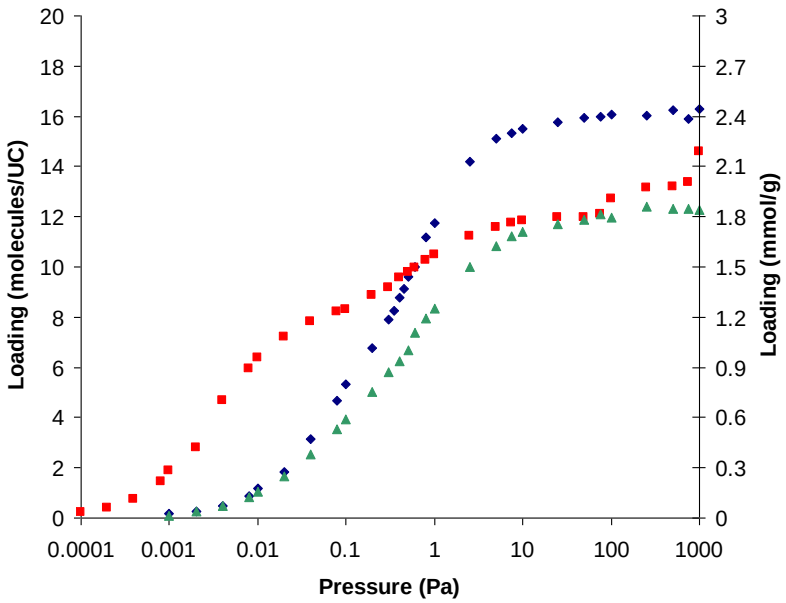

Figure 5.3 - Single-component pX (blue), oX (red) and mX (green) adsorption in hydroxylated UiO-66(Zr) at 300 K.

Stepped adsorption isotherms have been previously reported for the xylene-MIL-53 system, wherein the adsorption steps correspond to a guest-induced structural change in the MOF (Duan *et al.*, 2013). In contrast, the steps present in the oX isotherm in the non-breathing MOF UiO-66(Zr) can be attributed to the presence of preferred adsorption sites within the structure. The average energy of interaction of a single xylene molecule with the framework in each pore type is reported in Figure 5.4.

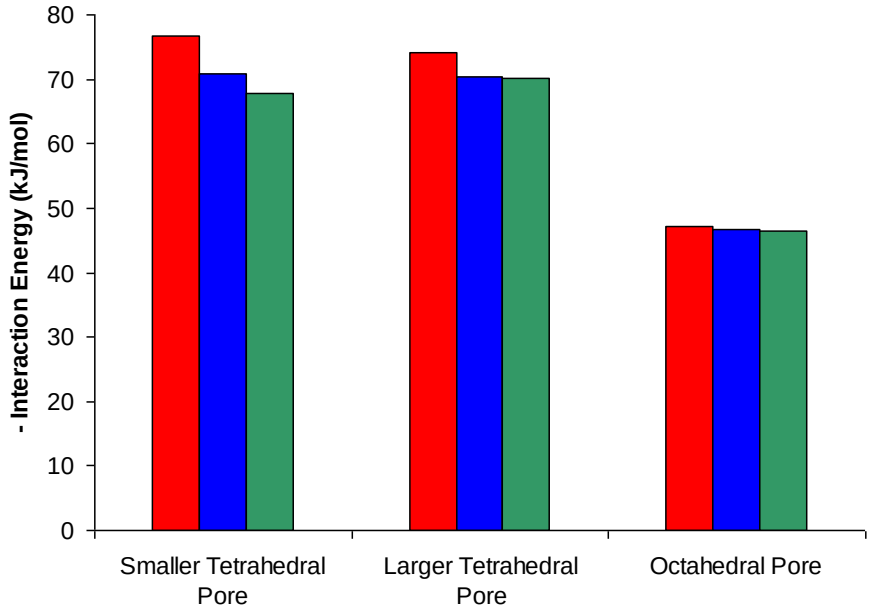

Figure 5.4 - Xylene–framework interaction energies of pX (blue), oX (red) and mX (green) in the different pore types present in hydroxylated UiO-66(Zr)

For each isomer, the octahedral pore presents a less attractive option energetically with the average interaction energies being 20-30 kJ/mol less than those observed in the tetrahedral pores. This difference is due to the different relative orientation of the BDC linkers in the tetrahedral and octahedral cavities. In the tetrahedral cavity, the pore is defined by the flat surface of the BDC linker and a guest molecule is able to interact equally strongly with the entirety of the benzene ring. From the perspective of a guest molecule in an octahedral pore, the linker is rotated 90° and the guest will interact primarily with only half of the benzene ring (c.f. Figure 5.1), resulting in a considerably lower energy of interaction. The same difference in relative linker orientation exists in the two pore types of the de-hydroxylated structure and the

average xylene-MOF interaction energies in the tetrahedral pore are likewise 25-30 kJ/mol stronger than in the octahedral pore (-73.7 kJ/mol and -46.7 kJ/mol respectively, when averaged over the three isomers).

At low loading, xylene molecules are mainly located in the tetrahedral cavities and the enhanced oX-framework interactions (6-7 kJ/mol stronger) calculated in these pore types are in agreement with the higher enthalpy of adsorption reported in literature for oX (Chang and Yan, 2012; Duerinck *et al.*, 2013) and are responsible for the increased uptake of oX at low pressure observed in the simulations. The electrostatic contribution to the xylene-framework interaction in the tetrahedral pore types (the cavity types occupied at low pressure) was found to be slightly repulsive and of a similar magnitude for all isomers (+0.25 to +1.5 kJ/mol) indicating that van der Waals interactions are responsible for the increase in oX-UiO-66(Zr) interaction energy. Examination of simulation snapshots shows that the origin of this enhancement lies in the ability of oX to position both methyl groups relatively centrally in the pore, allowing a strong interaction with the BDC linkers (Figure 5.5). In the case of both pX and mX, one or both of the methyl groups are forced away from the centre of the pore towards the less energetically favourable pore window

It is clear from both the visualisation and methyl group probability distributions presented in Figure 5.5 that the geometry of oX allows both methyl groups to remain closer to the centre of the pore than the other two isomers, allowing them to interact strongly with all of the surrounding BDC linkers and maximising the xylene-MOF van der Waals interaction. The methyl groups of both mX and pX are pushed further away from the centre, towards the pore windows, resulting in a lower overall interaction with the framework. In the case of pX, the two peaks observed in the distribution function in the small tetrahedral pore are a result of the geometry of the pX isomer. In pX, the two methyl groups are diametrically opposite one another on the aromatic ring and separated by ~6 Å. When one methyl group is located near the first peak (i.e. 2.5 Å from the centre of the pore in one direction), the other must be located 6 Å away, but in the opposite direction (i.e. 3.5 Å from the centre). In the intermediate pore, the centre-of-mass of the pX molecule tends to be located much

closer to the centre of the pore and the two peaks are now both centred at the same radial position (3 Å from the centre of the pore).

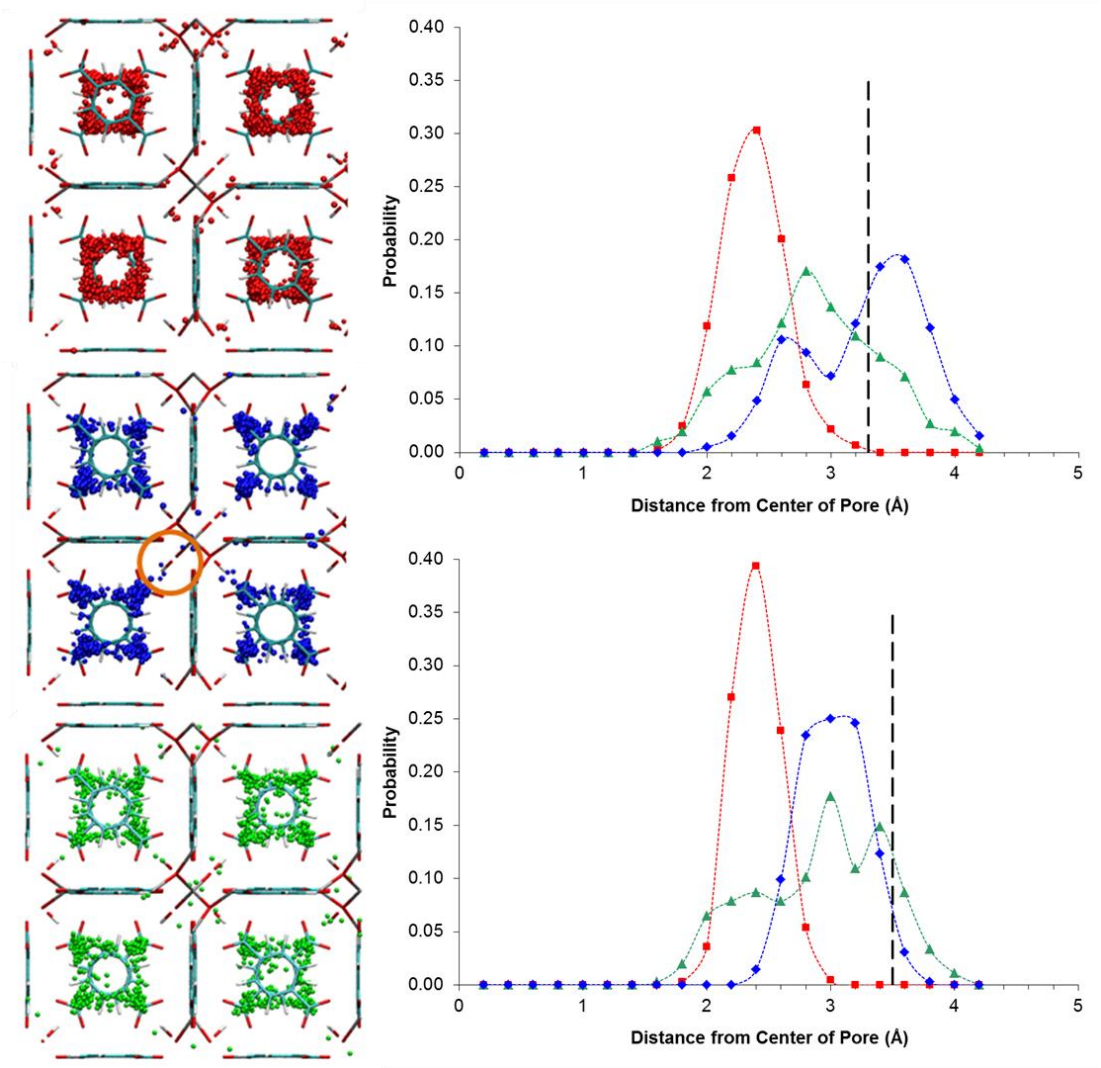

Figure 5.5 – Left: Visual distribution of methyl groups within UiO-66(Zr) in single component adsorption at low pressure of pX (blue), oX (red) and mX (green). The pore windows are located towards the corners of each pore (e.g. the orange circle in the left-centre image).
Right: Corresponding number probability distribution of the methyl groups as a function of radial distance from the pore centre in the small (top) and intermediate (bottom) tetrahedral pores. Lines have been added to guide the eye. Black, dashed lines indicate the radii of the two pores, as determined from their respective PSDs.

None of the snapshots revealed any evidence of xylene molecules taking up a position parallel to one of the BDC linkers, indicating that π-π interactions do not

play a significant role in the low-pressure adsorption properties for any of the isomers. Further investigation using a modified version of the Kh_d toolset (Sarkisov, 2012) showed that while none of the isomers are sterically restricted from accessing orientations which allow π-π interactions with the framework, these orientations are not energetically favourable. In these simulations, the pore space was discretised on a 0.2 Å grid and the interaction of a probe molecule (i.e. one of the three xylene isomers) with the framework at each point on the grid was evaluated and averaged over 1000 trial orientations. The rotational freedom of the probe molecules was restricted so as the aromatic ring of the xylene molecule was kept parallel (± 2.5°) to a plane corresponding to the BDC linkers which define one face of the tetrahedral pore type, mimicking π-π stacking. As the BDC linkers in the tetrahedral pores are arranged along the faces of a cube, all three primary π-π interaction geometries (Figure 5.6, following Martinez and Iverson (2012)) are explored in this manner.

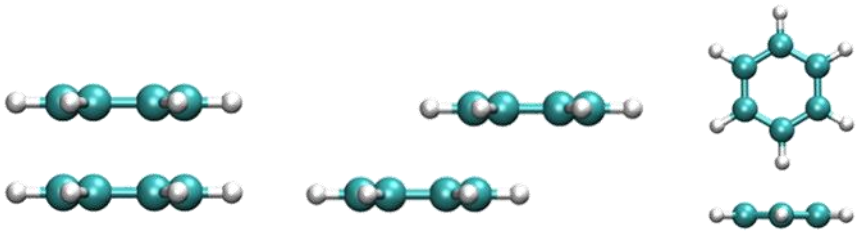

Figure 5.6 – The three primary modes of π-π interactions, demonstrated for benzene molecules: sandwich (left), parallel displaced (centre) and T-shaped (right). Colour scheme: C – cyan; H – white.

While all three isomers are able to take up both sandwich and T-shaped geometries in the tetrahedral cavities, the maximum xylene-MOF interaction energy in these orientations (-38 to -45 kJ/mol) is considerably less than that observed in these pore types in NVT-MC simulations (-68 to -77 kJ/mol) where all possible orientations, including those which do not promote π-π interactions, are allowed. The limited pore space available to xylene molecules does not permit the formation of parallel displaced pairs, while the cubic arrangement of the BDC linkers means that if a molecule takes up an energetically favourable T-shaped arrangement with one linker,

it must also be in an energetically unfavourable sandwich orientation with the neighbouring linkers, resulting in a comparatively low overall xylene-MOF interaction energy.

By tracking the location of adsorbed molecules throughout the simulation, it is possible to decompose an overall single-component isotherm into three site isotherms – one for each pore type present in hydroxylated UiO-66(Zr). From these site isotherms (Figure 5.7), the preference for the tetrahedral pores over the larger octahedra is clear for all isomers. In the case of mX and pX, there is considerable overlap between the filling of the three pore types, resulting in a smooth isotherm. In contrast, oX fills the two types of tetrahedral pore almost concurrently, with the octahedral pores only beginning to fill as the tetrahedral cavities approach saturation.

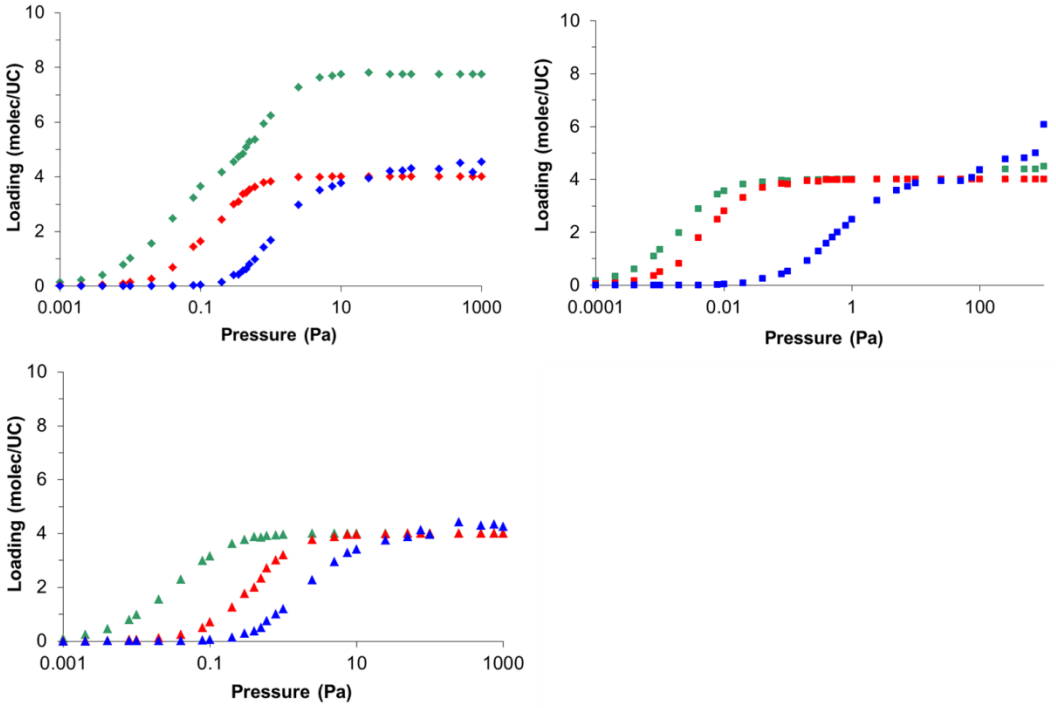

Figure 5.7 - Decomposed single-component isotherms for pX (top-left), oX (top-right) and mX (bottom-left). Adsorption isotherms are per pore type: small tetrahedral (red), intermediate tetrahedral (green) and larger octahedral (blue) pore.

The behaviour of the three isomers in the two types of tetrahedra is more complex. From Figure 5.7, it is clear that the larger of the two tetrahedra is preferred by pX

and mX and, to a lesser extent, oX. This is not reflected in the average interaction energies: oX interacts more strongly with the smaller of the two tetrahedral pores; mX interacts more strongly with the larger of the two tetrahedra; while in the case of pX, the two tetrahedra are energetically indistinguishable. Detailed study of the energetics within the two pore types (Appendix M) did not reveal the presence of any comparatively rare but high-energy adsorption sites within the larger of the two tetrahedra which may have introduced a bias for this pore, indicating that the preference for this pore type is not energy-driven.

The preference for molecules to occupy the intermediate pore can be attributed to the difference in relative accessibility of the two pore types. In the case of the smallest pore, the number of possible locations and orientations available to a xylene molecule is considerably less than in the larger of the two tetrahedral pores. This difference, which may be loosely termed an entropic driving force, was estimated by splitting each pore into a series of small cubes and attempting to insert a xylene molecule in each cube sequentially. It was found that each isomer has at least seven times as many accessible sites to choose from in the intermediate tetrahedral pore than in the small tetrahedral pore (Table 5.1). In the case of mX and pX, this ratio is even higher (mX: 13; pX: 16). The total number of accessible sites within the MOF for each of the isomers was found to be in the order of oX > mX > pX, in agreement with the order of adsorption entropies determined via vapour-phase chromatography experiments (Chang and Yan, 2012).

Table 5.1 - Number of accessible adsorption sites in each of the three pore types present in hydroxylated UiO-66(Zr) for each isomer.

	Number of accessible sites		
	Small Pore	Intermediate Pore	Large Pore
pX	2531	40,409	79,566
mX	2914	38,108	93,746
oX	6932	53,603	115,785

This entropic preference towards the intermediate pore must be considered in conjunction with the energetics of the two types of tetrahedral cavity. For oX, where there is a comparatively low entropic preference for the intermediate pore and also an energetic preference for the smaller of the two tetrahedra, the difference in the pressure at which oX begins to fill the two cavities is small (Figure 5.7). For mX, a large entropic preference for the intermediate pore is coupled with an energetic preference for the same pore. This results in a strong overall preference for the intermediate pore and the small tetrahedral pore does not begin to fill until the intermediate pore approaches saturation. pX lies between these two extremes – while the two pores are energetically equivalent, there is a large entropic preference for the intermediate pore and the difference in entry pressure between the two pore types lies between that experienced by oX and mX. The synergistic nature of these entropic and energetic driving forces for oX, therefore, is responsible for the steps visible in the oX isotherm.

The impact of differing levels of pore accessibility, both in different pores and for different isomers, on xylene adsorption isotherms can be more clearly seen when decoupled from the energetics of the system. To this end, GCMC simulations were performed for pX, mX and oX in hydroxylated UiO-66(Zr) in which xylene-MOF interaction potentials were artificially adjusted so as all three cavities within UiO-66(Zr) were equally attractive for all three isomers. In these artificially adjusted simulations, the repulsive portion of the guest-MOF interactions were described using a standard Lennard-Jones potential, while all attractive interactions were specified as -1.26 kJ/mol, a value chosen to return an average xylene-MOF interaction energy of -62 kJ/mol, comparable to that observed in standard GCMC simulations (i.e. those using non-adjusted LJ parameters; Figure 5.4). The overlap of the xylene molecule with the framework (i.e. number of accessible sites and orientations) is defined by the repulsive portion of the Lennard-Jones potential and is thus unchanged from standard GCMC simulations. The interaction of each isomer with the framework, irrespective of adsorption location, is identical, eliminating any energetic driving force which existed in standard simulations. The isotherms generated through this method are presented in Figure 5.8.

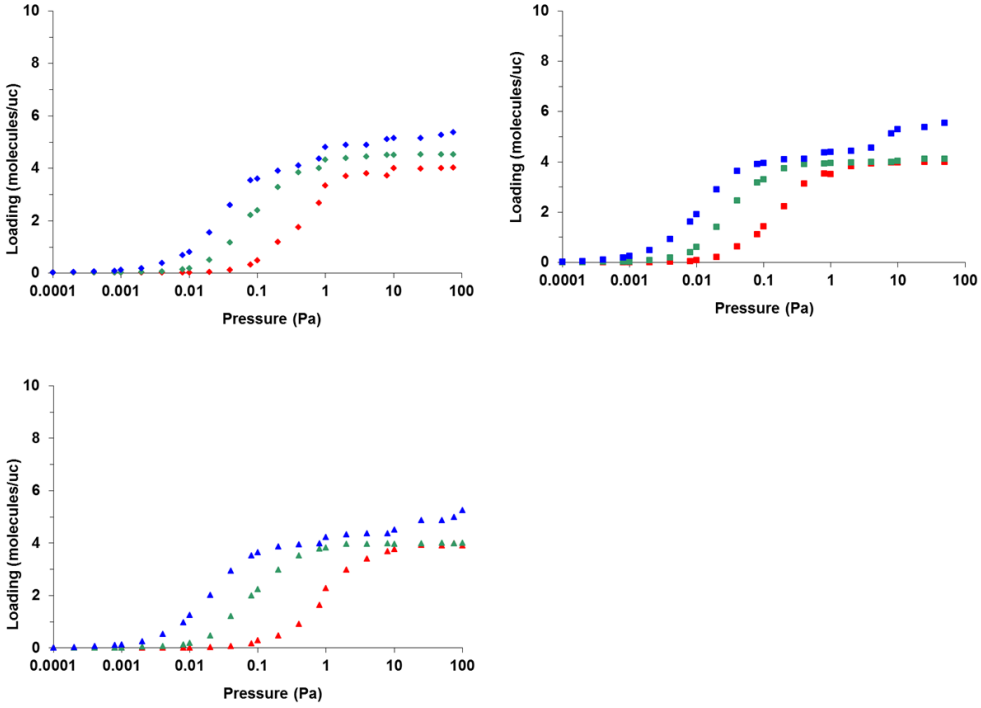

Figure 5.8 – Adsorption site isotherms of pX (top-left), oX (top-right) and mX (bottom-left) in hydroxylated UiO-66(Zr) where xylene-MOF interactions have been adjusted so as the average xylene-MOF interaction in each pore type is identical. Adsorption is shown per cavity type: small tetrahedral pore (red), intermediate tetrahedral pore (green) and octahedral pore (blue).

In the absence of any energetic preference for one pore over the other, all three xylene isomers fill the pores of UiO-66(Zr) by order of pore diameter, with the largest octahedral pore, having the highest number of accessible sites, being filled first and the smallest pore last. The entry pressure in each of the pores for oX is noticeably lower than for the other two isomers, consistent with the increased accessibility of each pore to the more compact *ortho* isomer (Table 5.1). Although the average xylene-MOF interaction energy is the same in each pore type, the Boltzmann factor – which is dependent on the total number of accessible orientations – is highest in the octahedral pore and this pore is filled preferentially by all isomers as a result.

Finally, we turn our attention to the increased uptake of pX observed in the simulated isotherms obtained from standard GCMC simulations in the hydroxylated MOF (Figure 5.3). The site isotherms from standard GCMC simulations (Figure 5.7) show

that the uptake of pX in the intermediate tetrahedral pore is double that of oX and mX. While only one oX or mX molecule is observed per cavity, pX is seen to form pairs in the intermediate tetrahedral pore. This cavity type seems well tailored to pX, allowing the two molecules to take up a cruciform-like arrangement with both methyl groups in the diametrically opposed pore windows (Figure 5.9), an arrangement which is unavailable to mX and oX. While in this particular case it is likely that diffusion limitations would prevent the formation of pX pairs in the experimental system, it is possible that this remarkable match between sorbate and adsorbent geometry may contribute towards the rational design of porous solids which are selective towards either pX or other *para*-isomers.

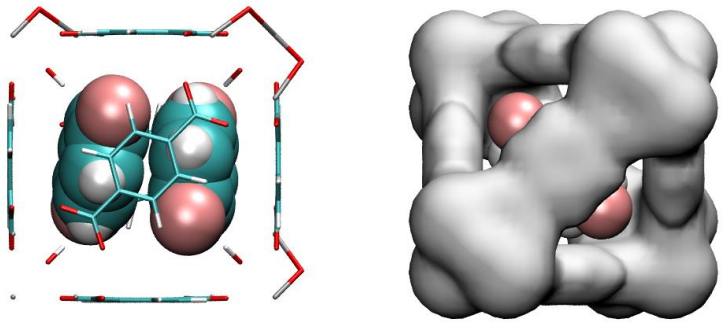

Figure 5.9 - In contrast to the other two isomers, two pX molecules may be adsorbed within the intermediate tetrahedral cavity, taking up a cruciform arrangement with their methyl groups (pink spheres) located within the pore windows. The van der Waals volume of the framework atoms, shown in grey in the right image, allows the location of the methyl groups within the windows to be clearly seen. Colour scheme: C – cyan; H – white; O – red; Zr – grey; CH_3 groups – pink.

The increased saturation uptake of *para*-xylene is only observed in the intermediate tetrahedral cavity, which is only present in the hydroxylated form of UiO-66. In the de-hydroxylated MOF, in which only the smaller of the two tetrahedral pores is present, all three isomers exhibit similar maximum capacities (Figure 5.10). In the case of pX, the isotherms in the two forms of the MOF begin to diverge significantly – with reduced uptake observed in the de-hydroxylated MOF - at pressures above 0.2 Pa, the point at which the first pX-pX pairs are observed in the hydroxylated structure.

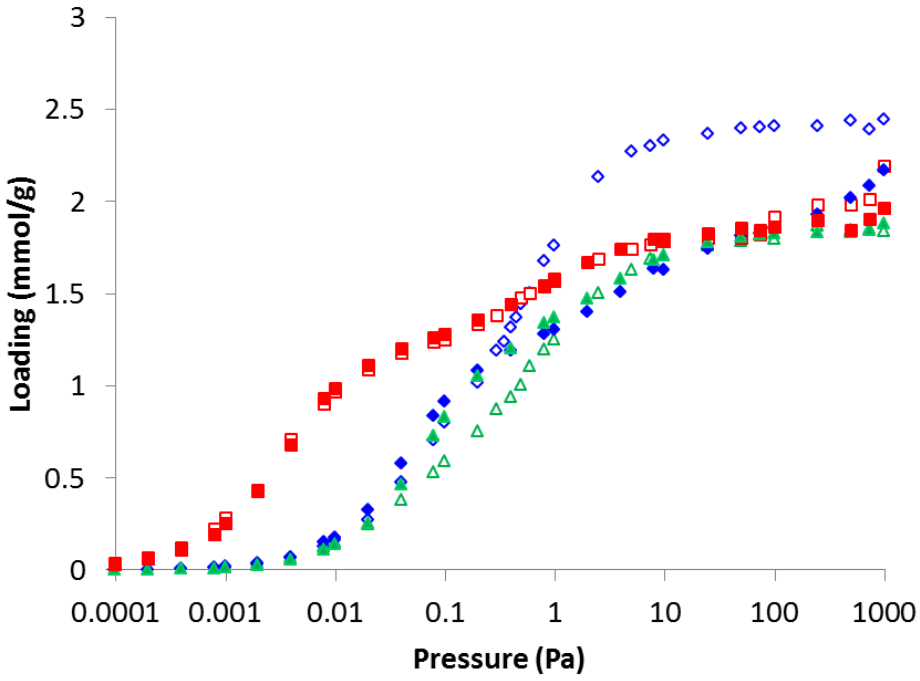

Figure 5.10 – Simulated single-component isotherms of pX (blue), mX (green) and oX (red) in de-hydroxylated UiO-66(Zr) at 300 K (solid symbols). The single-component isotherms in hydroxylated UiO-66(Zr) are shown for comparison (empty symbols). Note that the gravimetric uptake is shown here to allow direct comparison.

In the low pressure region of the isotherms (P < 0.11 Pa), the isotherms in the de-hydroxylated MOF exhibit slightly higher uptakes than those recovered in the hydroxylated form (Figure 5.3), indicating that the hydroxyl groups (which are only present in the hydroxylated MOF) do not present strong interaction sites for xylenes. In fact, the removal of the hydroxyl groups results in a slightly less electrostatically repulsive environment for all isomers, enhancing low-pressure adsorption. The order of pore filling remains the same, with the tetrahedral pores being filled preferentially due to the much higher xylene-MOF interaction energies in this pore. For mX and pX, the absence of the intermediate tetrahedral pore means that there is little overlap in the filling of the tetrahedral and octahedral cavities and slight inflection points become visible in the isotherms as a result - similar to those observed for oX.

The switch to the de-hydroxylated form appears to benefit mX more than the other two isomers, with increased uptake observed in the 0.1 – 1 Pa region compared to the

hydroxylated form. The primary factor in this is the relatively low xylene-MOF interaction experienced by mX in the smaller of the two tetrahedra in the hydroxylated MOF. In hydroxylated UiO-66(Zr), mX initially fills the intermediate tetrahedral cavities ($E_{mX\text{-}MOF}$ = -70.1 ± 0.2 kJ/mol), followed by the smaller tetrahedra ($E_{mX\text{-}MOF}$ = -67.9 ± 0.2 kJ/mol). In the de-hydroxylated structure, both of these cavity types are replaced by a single tetrahedral pore in which the interaction between mX and the framework is -71.8 kJ/mol. The mX-MOF interaction energies in the intermediate tetrahedral pore of the hydroxylated MOF and the tetrahedral pore of the de-hydroxylated MOF are therefore very similar. In the hydroxylated MOF, mX is adsorbed primarily in the intermediate tetrahedra at low pressure and the enhancement in interaction energy in moving to the de-hydroxylated MOF is therefore initially quite low and the isotherms remain very similar. The small tetrahedra in the hydroxylated MOF become more important at higher pressure ($0.1 < P < 1$ Pa) and the relative enhancement provided by the de-hydroxylated tetrahedra is greater ($\Delta E_{mX\text{-}MOF}$ = -3.9 ± 0.4 kJ/mol), resulting in a noticeable increase in mX uptake in this pressure range. For oX, in which the two tetrahedra fill concurrently in the hydroxylated form, the relative enhancement provided by the de-hydroxylated tetrahedra is small (-0.8 ± 0.4 kJ/mol) and little change in the isotherm is observed. For pX, for which the two tetrahedra in the hydroxylated form are energetically equivalent, the relative enhancement is moderate (-2.2 ± 0.4 kJ/mol) and while a small increase in low pressure uptake is observed for $P < 0.1$ Pa, this is later off-set by the elimination of pX-pX pair formation for $P > 0.2$ Pa.

5.4 Competitive Adsorption

Industrially, the ability of UiO-66(Zr) to differentiate between the xylene isomers and selectively adsorb one isomer over the others is more relevant than its uptake of pure xylene. To this end, GCMC simulations of equimolar binary mixtures (oX-pX, oX-mX and pX-mX) were carried out at both low (1 Pa) and high (1000 Pa) pressure. In each case, the reported selectivity ($S_{a\text{-}b}$) is calculated using Equation 4.1.

A selectivity greater than unity indicates a preference for component *a*, while a value less than one indicates a preference for component *b*.

5.4.1 Selectivity Towards ortho-xylene

In line with the single-component isotherms and published experimental data (Barcia *et al.*, 2011; Moreira *et al.*, 2012a) UiO-66(Zr) is selective towards oX in GCMC mixture simulations (Figure 5.11), particularly at low pressure. Adsorption at low pressure is primarily in the tetrahedral cavities and the enhanced oX-MOF interactions (Figure 5.4) act in concert with the entropic preference for oX seen in the number of accessible sites available to each isomer in the tetrahedral pores (Table 5.1). For oX, there are 2.3 or 2.8 times as many sites in the smaller tetrahedral cavity when compared to mX and pX, and 1.3 or 1.4 times as many sites in the intermediate tetrahedral pore. Both the greater number of available configurations and the stronger interaction energy combine to greatly enhance the Boltzmann factor for oX compared to the other isomers, resulting in high selectivities towards *ortho*-xylene in the tetrahedral cavities (Table 5.2).

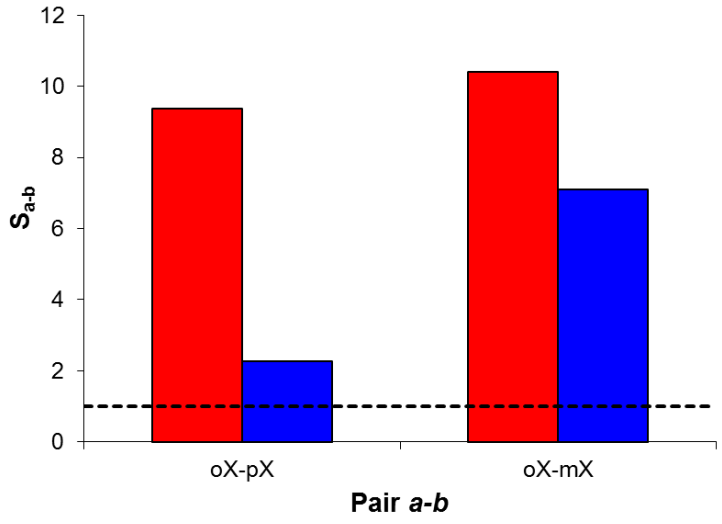

Figure 5.11 - Overall selectivity towards species *a* from pair *a-b* at 1 Pa (red) and 2000 Pa (blue) for equimolar, binary mixtures containing oX in hydroxylated UiO-66(Zr). The dashed line indicates *S* = 1.

Table 5.2 – Selectivity of each pore type in hydroxylated UiO-66(Zr) at low and high pressure.

Mixture	Selectivity					
	Small Tetrahedral Pore		Intermediate Tetrahedral Pore		Octahedral Pore	
	1 Pa	2000 Pa	1 Pa	2000 Pa	1 Pa	2000 Pa
oX-pX	24.4± 0.1	20.8± 0.1	6.2 ± 0.1	0.9 ± 0.2	7.3 ± 0.1	2.9 ± 0.1
oX-mX	80.5± 0.1	59.2± 0.1	12.2 ± 0.1	8.8 ± 0.1	3.0 ± 0.1	3.6 ± 0.1

At higher pressure, adsorption in the octahedral cavity plays a more important role. While a clear energetic preference for oX is seen in the tetrahedral cavities (Figure 5.4), the preference is less distinct in the xylene-MOF interaction energies in the octahedral cavity (oX: -47.3 kJ/mol; pX: -46.6 kJ/mol; mX: -46.5 kJ/mol). The selectivity of the octahedral cavity towards oX is primarily entropic in nature, a consequence of the greater number of accessible sites available to oX (Table 5.1). This relatively limited energetic preference results in a comparatively low selectivity in the octahedral pore (Table 5.2), and a reduced selectivity towards oX overall at high pressure.

The formation of pX-pX pairs in the intermediate pore, which was discussed in Section 5.3, is also observed in binary simulations performed at high pressure and is a major contributor to the considerable reduction in overall oX selectivity in the case of oX-pX mixtures. The drop in selectivity from *ortho*-selective ($S_{oX\text{-}pX} = 6.2$) to non-selective ($S_{oX\text{-}pX} = 0.9$) in the intermediate cavity is a direct result of presence of pX-pX pairs. As discussed earlier, experimental evidence suggests that the formation of pX-pX pairs is an artefact of the GCMC simulation and thus competitive simulations in the de-hydroxylated MOF – where pX-pX pairs were not observed in single-component simulations – can be expected to give a better approximation of the experimental system.

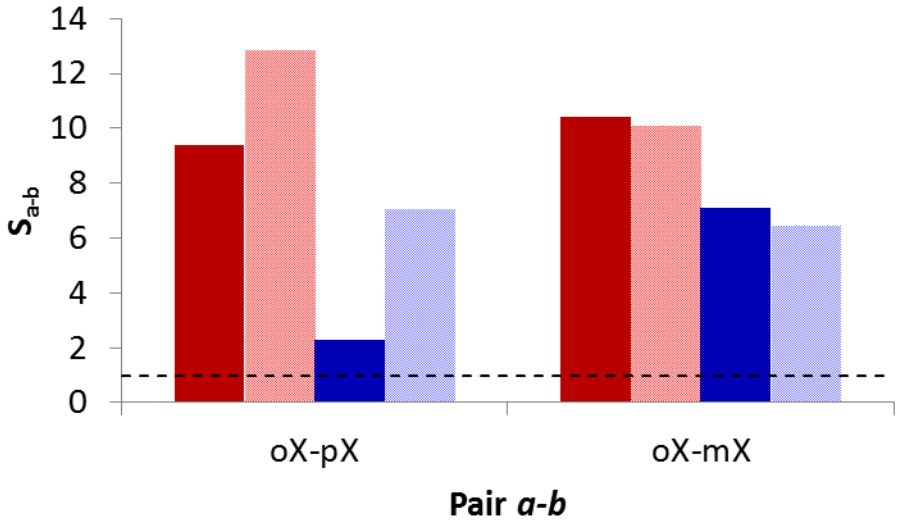

Figure 5.12 - Overall selectivity towards species *a* from pair *a-b* at 1 Pa (red) and 2000 Pa (blue) for binary mixtures containing oX in de-hydroxylated UiO-66(Zr) (light colours). Selectivity in the hydroxylated MOF is shown for comparison (dark colours) The dashed line indicates *S* = 1.

The de-hydroxylation of the MOF has minimal effect on selectivity in the oX-mX mixture (Figure 5.12), with only slight decreases in selectivity observed. As discussed in Section 5.3, de-hydroxylation of the MOF effectively replaces both types of tetrahedral pores present in the hydroxylated MOF with a single cavity type. In competitive oX-mX adsorption, this has the effect of reducing the energetic preference for oX. The difference in average xylene-MOF interaction energies is 7.1 kJ/mol stronger for oX than mX in the hydroxylated MOF but only 5.7 kJ/mol stronger in the de-hydroxylated structure, shifting the selectivity slightly away from oX. In contrast, replacing the intermediate hydroxylated tetrahedra with a slightly smaller type of pore enhances the entropic preference for oX. These two effects act in opposite directions, and the overall effect is small.

In the oX-pX mixture, however, while the energetic preference for oX remains largely unaffected by the de-hydroxylation process, the enhancement in entropic preference for oX still plays a role. Additionally, the elimination of pX-pX pairs was shown to alter the pX isotherm at pressures as low as 0.2 Pa in single-component simulations (Figure 5.10) and can be expected to play a role even in low pressure

competitive simulations, where the partial pressure of pX is 0.5 Pa. The increase in selectivity towards oX at low pressure in de-hydroxylated UiO-66(Zr) is thus a combination of the entropic advantage enjoyed by oX in smaller pores and the elimination of pX-pX pairs. The effect of de-hydroxylation on selectivity at high pressure, where the pairing-up of pX molecules in the intermediate hydroxylated tetrahedra is considerably more prevalent, is even greater and the de-hydroxylated MOF remains strongly selective towards oX ($S_{oX\text{-}pX}$ = 6.4).

5.4.2 Competitive Adsorption of pX/mX Mixtures

A strong preference for *ortho*-xylene is observed in vapour-phase quaternary breakthrough experiments (Barcia *et al.*, 2011) and both liquid-phase binary and ternary breakthrough experiments (Moreira *et al.*, 2012a). In the case of pX-mX mixtures, the situation is less clear. In the vapour-phase work of Barcia *et al* (2011), the MOF was unable to discriminate between mX and pX. In the later work of Moreira *et al* (2012a), UiO-66(Zr) was found to be weakly selective towards mX in both binary pX-mX and ternary pX-oX-mX breakthrough ($S_{pX\text{-}mX}$ = 0.9). It should be noted that the studies of Moreira *et al* (2012a) were carried out in the liquid phase with heptane as a solvent which results in competitive adsorption of heptane and the xylene isomers. A direct comparison with the simulation is therefore difficult). In the quaternary (pX-mX-oX-ethylbenzene) competitive simulations reported by Granato *et al* (2014), the MOF exhibited a slight preference for either pX or mX, depending on which force field was selected to describe the xylene isomers. In the present work, the hydroxylated form of the MOF was found to be selective towards pX, while the de-hydroxylated structure was unable to effectively discriminate between the two isomers (Figure 5.13).

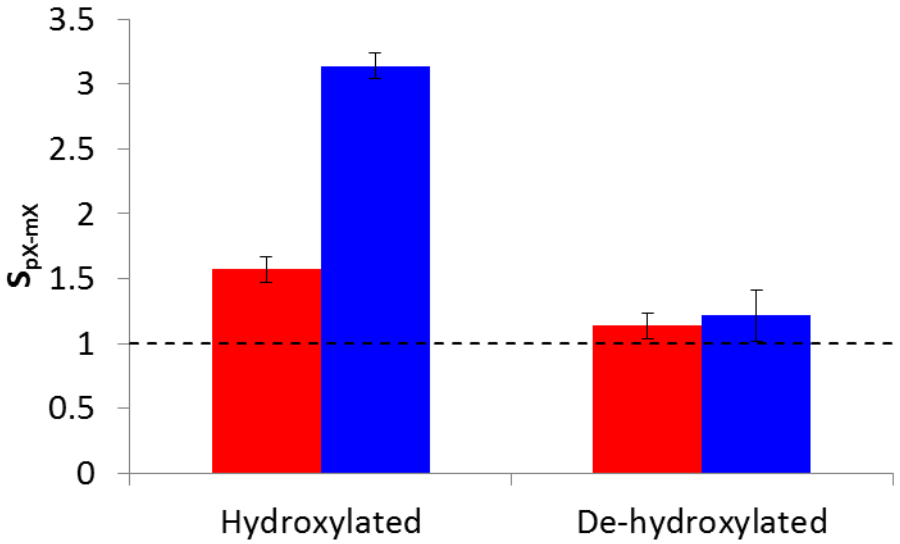

Figure 5.13 – Selectivity towards pX from equimolar pX-mX mixture simulations in the hydroxylated and de-hydroxylated forms of UiO-66(Zr) at 1 Pa (red) and 2000 Pa (blue).

In both forms of the MOF, the selectivity towards pX increases at higher pressure. For the hydroxylated MOF, this increase is primarily a consequence of the increasing prevalence of pX-pX pairs in the intermediate tetrahedral pore, where the selectivity increases from 1.4 at 1 Pa to 13.0 at 2000 Pa (Table 5.3). In the de-hydroxylated MOF, the tetrahedra remains only slightly *para*-selective at higher pressure (S_{pX-mX} = 1.2 ± 0.1 at 1 Pa and 1.3 ± 0.2 at 2000 Pa).

Table 5.3 – Selectivity towards pX for pX-mX mixtures by pore type in the hydroxylated and de-hydroxylated forms of UiO-66(Zr).

Structure	Selectivity					
	Small Pore		Intermediate Pore		Large Pore	
	1 Pa	2000 Pa	1 Pa	2000 Pa	1 Pa	2000 Pa
Hydroxylated	2.9 ± 0.1	3.0 ± 0.1	1.4 ± 0.1	13.0 ± 0.1	0.6 ± 0.1	1.4 ± 0.1
De-hydroxylated	1.2 ± 0.1	1.3 ± 0.2	-	-	0.5 ± 0.1	0.8 ± 0.2

As expected from the single component isotherms (Figure 5.10), it can be seen that the de-hydroxylation of the MOF benefits mX more than pX (Figure 5.13). The low pressure selectivity is primarily determined by adsorption in the tetrahedral pore types. In the hydroxylated MOF, the smaller tetrahedra exhibits a clear preference for

pX which is primarily energetic in nature, with xylene-MOF interactions found to be 2.9 ± 0.3 kJ/mol stronger for pX than mX. The entropic contribution in this pore is negligible (Table 5.1). The intermediate tetrahedra does not exhibit an energetic preference for either isomer ($\Delta E_{xylene\text{-}MOF}$ = 0.2 ± 0.3 kJ/mol towards pX) and the slight *para*-selectivity observed in this pore is also likely to be entropic in nature (Table 5.1). In the de-hydroxylated MOF, the entropic preference for pX in the tetrahedra remains but the energetic preference is removed almost completely ($\Delta E_{xylene\text{-}MOF}$ = 0.4 ± 0.2 kJ/mol towards pX), resulting in a low selectivity overall.

Intriguingly, the large octahedral cavity becomes more attractive to pX as the pressure is increased, in both forms of the MOF. This manifests itself in a decrease in *meta*-selectivity in the de-hydroxylated case and a reversal in selectivity in the hydroxylated MOF (Table 5.3). This phenomenon is a result of the strong interaction between pX molecules in neighbouring pores (Table 5.4), which become increasingly important as the pressure is increased. When competitive adsorption of an equimolar pX-mX mixture was simulated in a system where the tetrahedral pores were artificially blocked – i.e. molecules were only allowed to adsorb in the octahedral pore - the pore remained selective towards mX even at high pressure, confirming that the change in selectivity within the octahedral pore is due to the influence of neighbouring xylene molecules. The low-pressure preference of the octahedral pore for mX over pX exists despite the near-identical xylene-framework interactions of the two species in this pore type in both forms of UiO-66(Zr). This preference is entropic in nature and originates from the increase in relative accessibility of the large pore to the *meta* isomer. In this case, 20% more mX-accessible sites than pX-accessible sites are available (Table 5.1).

Table 5.4 – Average xylene-xylene interaction energies at 2000 Pa from single-component GCMC simulations.

	$E_{xyl\text{-}xyl}$ (kJ/mol)	
	Hydroxylated	De-hydroxylated
pX-pX	-9.4 ± 0.2	-7.6 ± 0.2
mX-mX	-5.0 ± 0.2	-3.7 ± 0.2

Overall, the simulation results indicate that the MOF is unable to effectively discriminate between pX and mX via adsorption equilibrium. The interplay between energetic and steric effects during the competitive adsorption of pX/mX mixtures appears to be strongly dependent on the pore geometry and is likely to be strongly influenced experimentally by sample quality and adsorbent preparation.

5.5 Diffusion of Xylene Isomers in UiO-66(Zr)

The design of an industrial adsorption process relies not only on knowledge of the equilibrium properties of the system, but also on an understanding of the kinetics of the adsorption process. Experimentally, adsorption breakthrough or chromatographic experiments are often used to evaluate the selectivity of a material. In such experiments, the selectivity is determined by the retention time of each component in the material, which represents a combination of adsorption affinity, inter-particle diffusivity (i.e. movement of the component through the void space of the column) and intra-crystalline diffusivity (movement of the component within the adsorbent) (Ruthven, 1984). In order to fully understand the selectivity of UiO-66(Zr) for oX observed in breakthrough experiments (Barcia *et al.*, 2011; Chang and Yan, 2012; Moreira *et al.*, 2012a), it is therefore necessary to assess the adsorption kinetics and diffusivity of the three isomers in the MOF. Additionally, it is clear that based on the crystallographic structure of UiO-66(Zr), the limiting pore window diameter in the static MOF (4-5 Å) should be too small to allow xylene molecules passage and that some degree of structural flexibility is required to enable xylenes to diffuse through the MOF. In order to address these points, molecular dynamics (MD) simulations were undertaken in both rigid and flexible UiO-66(Zr), allowing both the underlying diffusion mechanism to be identified and the relative mobility of the three isomers to be assessed.

The structure of UiO-66(Zr) is such that in order to diffuse through the framework, a sorbate molecule must move from one octahedral pore to the next octahedra via a tetrahedral pore. These two pores are connected by an irregular hexagonal window of

roughly 4-5 Å incircle diameter. In MD simulations where the MOF is kept rigid, none of the xylene isomers were observed moving from one pore to the next, either at 300 K or 500 K. Although self-diffusion coefficients (D_s) may be extracted from the mean square displacement data gathered in the rigid structure simulations (Figure 5.14), these coefficients only represent the localised movement of sorbate molecules around their starting locations and are not representative of the overall diffusion mechanism. As the movement of xylene molecules is limited by the pore diameter in the rigid MOF and each pore can only accommodate one molecule, the calculated diffusion coefficients are unaffected by xylene loading.

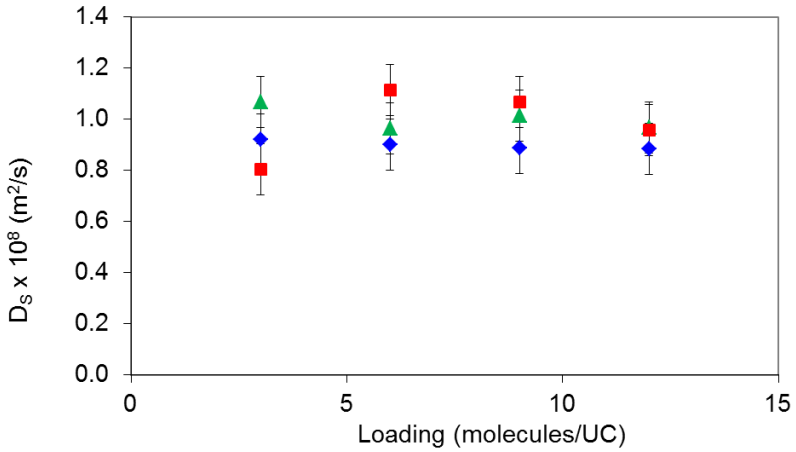

Figure 5.14 – Self-diffusion coefficients for pX (blue), oX (red) and mX (green) at 300 K in rigid UiO-66(Zr).

When the MOF is kept rigid, the window diameter is too small to allow xylene isomers to move through the framework. Even in MD simulations in UiO-66(Zr) using a force field which allows framework flexibility at 300 K, xylene molecules remained localised within the cages and no transitions between cavities were observed. Further MD simulations were undertaken at elevated temperatures of (500 – 1000 K). Above 1000 K, the force field was found to break down as the movement of framework atoms became too extreme to allow calculation of intra-framework bond energies (it should be noted that this exceeds the limit of thermal stability of the MOF, which shows evidence of structural collapse at ~720 K (Cavka *et al.*, 2008)).

In the case of pX and mX, xylene molecules were seen to move between cage types at temperatures of 500 K and above (Figure 5.15). This transition remained extremely rare at 500 K, with each pX molecule undergoing an average of 0.11 transitions per nanosecond. As the temperature was increased, the transition rate increased to 1.13 molec^{-1} ns^{-1} and 1.52 molec^{-1} ns^{-1} at 800 K and 900 K respectively. mX was found to be much less mobile than pX, with an observed transition rate of 0.02 molec^{-1} ns^{-1} at 500 K – a factor of six lower than pX. Surprisingly, oX was found to be the least mobile of the three isomers and transitions were only observed above 800 K. Transition rates for oX could not be reliably calculated as a result of the extremely low number of observed transition events.

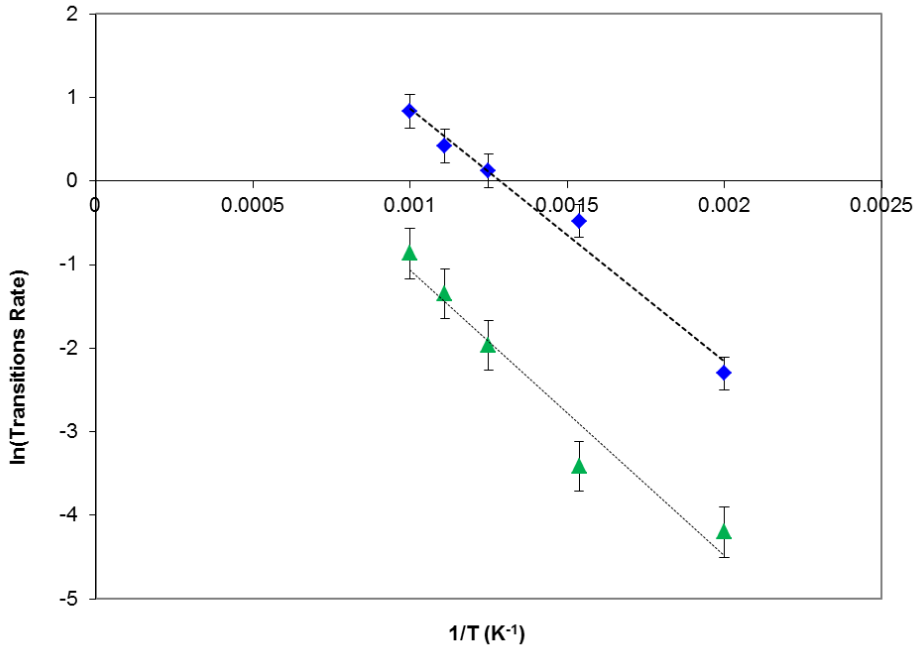

Figure 5.15 - Temperature-dependence of the cage-to-cage transition rate of pX (blue) and mX (green) in flexible UiO-66(Zr). Dotted lines are those of best fit, from which the Arrhenius coefficients in Equation 5.1 were determined.

The increase in the pX and mX transition rate constant with temperature is well described by the standard Arrhenius equation:

$$r_T = r_{T0} e^{\left(\frac{-Ea}{RT}\right)} \qquad \textbf{Equation 5.1}$$

Where r_T indicates the transition rate at temperature T, r_{T0} is the transition attempt frequency, E_a is the activation energy of the transition and R is the universal gas constant.

The activation energy associated with the movement of molecules between cages at low loading was calculated to be 25.2 ± 0.5 kJ/mol for pX and 28.4 ± 1.4 kJ/mol for mX. The lower activation energy for pX compared to mX suggests that the observed selectivity towards mX in breakthrough experiments may be a kinetic rather than equilibrium separation, where the more mobile pX isomer elutes first.

In contrast to pX and mX, the movement of oX from cage to cage remained an extremely rare event even at elevated temperature. For oX, only two transition events were observed per 10 ns simulation run at 800 K, and only three at 900 K. While it is impossible to accurately determine activation energies from this data, the two order of magnitude difference in transition rate between pX and oX suggests that the activation energy for oX is approximately 20 kJ/mol higher. From this data, the transition rate for pX (the most mobile of the isomers) at 300 K, was estimated to be only 0.0001 molec^{-1} ns^{-1} – i.e. for a system at low loading, on average, one transition would be observed every 430 ns (taking approximately 300 days to simulate). As a result, it is clear that while the incorporation of framework flexibility allows the movement of xylene molecules between cages, MD simulations with the currently available force fields are unsuitable for the determination of long-range diffusion coefficients for this system.

The mechanism by which xylene isomers are able to move between neighbouring pores may be elucidated from the MD simulations in flexible UiO-66(Zr). The window connecting adjoining pores is defined by three BDC linkers arranged in a triangular fashion (Figure 5.16; left) which, when held rigid, create a hexagonal window with an incircle diameter of ~4-5 Å. When compared to the kinetic diameter of the slimmest isomer (d_{pX} = 6.7 Å), it is clear that this window is too small to allow xylene molecules to pass through. When the framework is treated as flexible, the

window-defining BDC linkers are able to undergo a rotation around the (OOC)-(COO) axis (the red dashed line in Figure 5.16) and distortion of the aromatic-substituent improper torsion centre (the pink lines in Figure 5.16). The combination of these two motions, induced by interaction between the linkers and adsorbed xylene molecules, causes the window to enlarge and change shape (Figure 5.16; right), allowing the xylene molecule to move from one pore to the next.

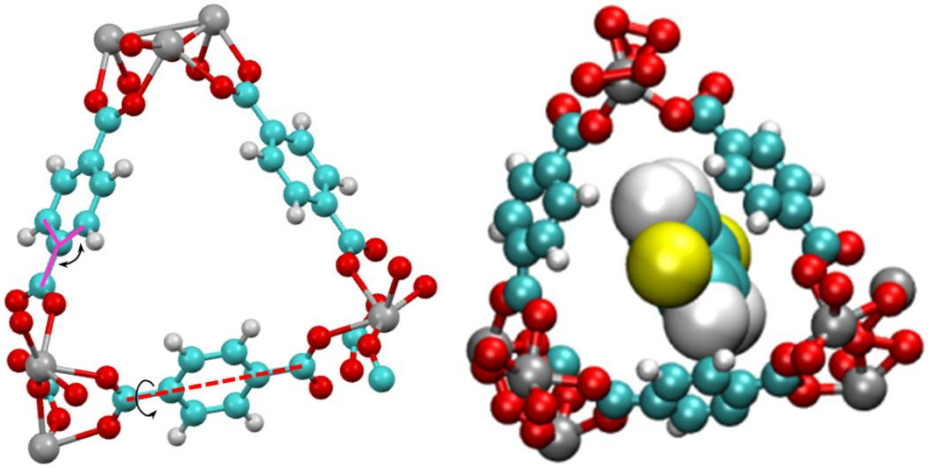

Figure 5.16 - BDC linkers forming the window present in UiO-66(Zr) in the equilibrium atomic positions used in the rigid structure (left) and during deformation of the window in the presence of pX in MD simulations using a flexible force field (right). The important rotation axis (red dashed line) and torsion centres (pink solid lines) are highlighted. Colour scheme: C – cyan; H – white; O – red; Zr – grey; CH_3 group – yellow.

Interestingly, the overall order of mobility observed in MD simulations (pX > mX >> oX) does not correspond to the order of kinetic diameters of the isomers (pX < oX < mX). The reason for this apparent discrepancy lies in the fact that the kinetic diameter does not take into account the rotation of the molecule during the transition event. pX was seen to move through the window with minimal rotation of the isomer – the only observed rotation was around the long (CH_3-CH_3) axis of the molecule (Figure 5.17; top). The required window diameter (critical diameter) for this motion is approximately 6.7 Å. While moving through the pore window, mX follows a different path, experiencing rotation around the centre of the aromatic ring, perpendicular to the long axis of the molecule (Figure 5.17; middle).

As a result of the rotation of the molecule, the critical diameter is much less than the measured kinetic diameter (7.4 Å compared to 7.8 Å). The lower mobility of mX compared to pX is thus primarily a result of the larger critical diameter and the increased distortion of the framework required to allow passage through the window.

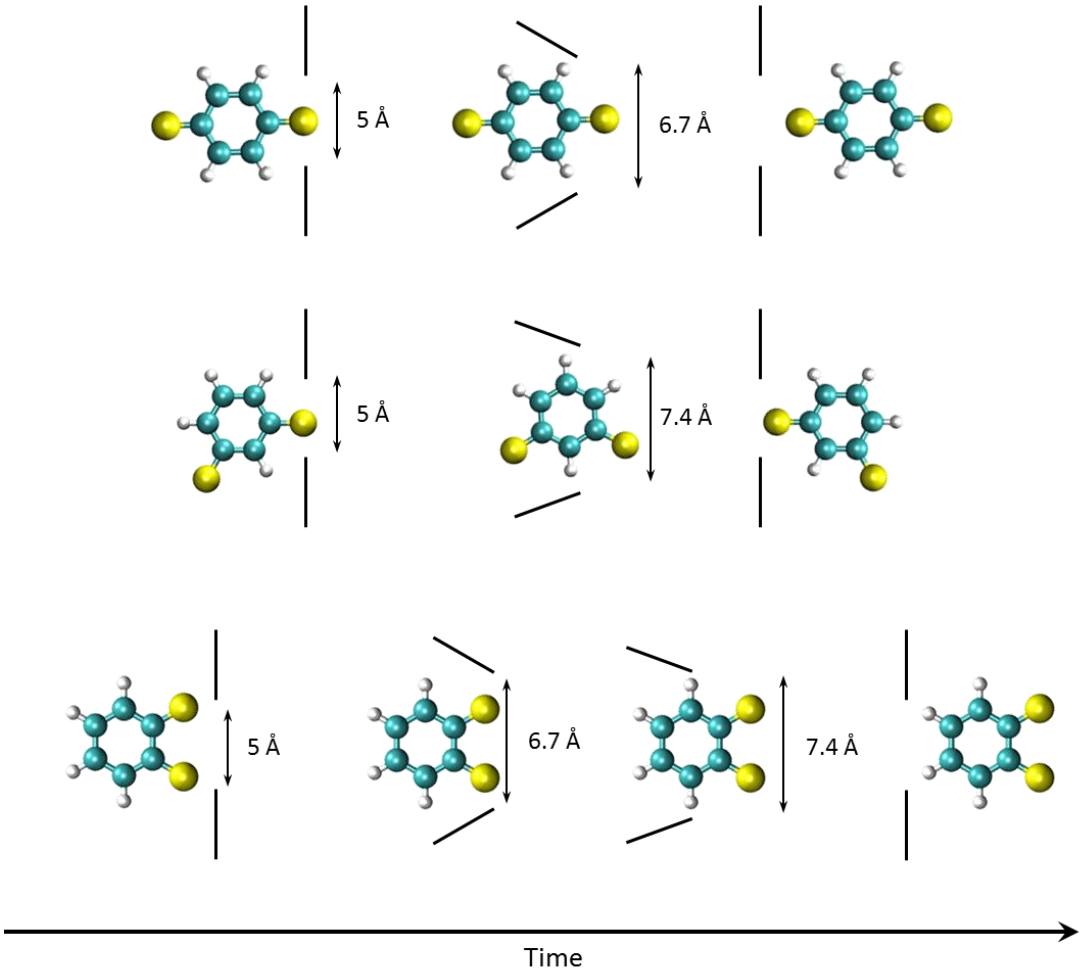

Figure 5.17 – Schematic representation of the movement of of pX (top), mX (middle) and oX (bottom) through the window of UiO-66(Zr). The relative orientation of the linkers is shown by the solid black lines while the minimum window diameter for each of the steps is indicated alongside. Vertical black lines correspond to the equilibrium linker orientation. Colour scheme: C – cyan; H – white; CH_3 group – yellow.

The smallest critical diameter which oX is capable of presenting is also 7.4 Å and, given that the window is capable of admitting mX, the movement of oX should not be restricted from a geometric perspective. The primary difference between oX and the other isomers is that the methyl groups exist as a pair rather than single

protruding entities. The pore window has an equilibrium diameter of roughly 4 - 5 Å, while the single methyl group has a diameter of 3.8 Å in these simulations. It is clear that even without framework distortion the single methyl group is able to enter the pore window. In contrast, the methyl pair on oX has a combined diameter of approximately 6.7 Å – too large to enter into the pore window without prior distortion of the framework (Figure 5.17; bottom).

It seems likely that the single methyl groups present on mX and pX act as a wedge whose presence within the pore window is able to induce further distortion of the framework, enlarging the window and enabling the rest of the molecule to pass through. The low mobility of oX is therefore a result of the molecule being forced to wait for the window to spontaneously enlarge before any portion of the molecule is able to enter the window. The ability of pX and mX to position their methyl groups within the pore windows even when the structure is at equilibrium is supported by the GCMC results presented earlier, wherein both pX and mX were observed to preferentially locate one or both methyl groups in the pore window (Figure 5.5). In GCMC simulations, this had the effect of reducing the adsorption affinity of the MOF for pX and mX compared to oX. The complete encapsulation of the oX molecule within the pore thus enhances the equilibrium selectivity, while simultaneously reducing the mobility of oX within the framework compared to pX and mX, introducing an additional kinetic selectivity to the system.

The breakthrough experiments of Moreira *et al* (2012a) provide some evidence of a considerably lower transition rate of oX compared to the other two isomers. The experimental pure component breakthrough profiles for oX are noticeably more disperse than those of pX and mX for both adsorption and desorption. This is replicated in the pulse breakthrough response curves for the ternary system. This data shows that the movement of oX through the adsorption column is significantly retarded compared to the other two isomers, which may be a result of the difference in transition mechanism for oX outlined above (Figure 5.17). It should be noted, however, that the experimentally observed dispersion may also be influenced by differences in the macropore and/or film diffusivity of oX and that further

experimental work is required to confirm that the observed difference is indeed a result of differences in micropore diffusivity (Ferreira, 2014).

5.6 Conclusions

In this chapter, a detailed computational study of xylene adsorption and diffusion in the metal-organic framework UiO-66(Zr) was presented, augmenting GCMC simulations of adsorption with NVT MC, complementary geometric tools and MD simulations in both rigid and flexible frameworks. The clear preference of the MOF for oX observed in experiment was correctly predicted by simulation and, furthermore, the calculated xylene-framework interactions are in good agreement with the enthalpies of adsorption reported by Chang *et al* (2012) and Deurinck *et al* (2013). It was shown that the enhanced xylene-framework interactions observed for oX in comparison to the other two isomers arises from neither π-π or electrostatic interactions but is a result of the complete encapsulation of the oX molecule within the tetrahedral cavities. Geometric restrictions force the other isomers to take up less energetically favourable positions with one or both methyl groups located in the pore windows. The entropic preference of the MOF for oX was also demonstrated qualitatively through the estimation of the total number of accessible locations available to each isomer. oX was found to have at least 1.3 times as many accessible sites than either mX or pX.

In competitive adsorption simulations, UiO-66 was found to be highly selective towards oX at both low and high pressure, commensurate with published experimental results and calculated xylene-framework interaction energies. When artefacts of the GCMC simulations are excluded, the MOF was found to be unable to differentiate between pX and mX, suggesting that the experimentally observed preference for mX may be of a kinetic rather than enthalpic nature. The adsorption of a pX-mX mixture was demonstrated to be a complex competition between the slight energetic preference for pX in one pore type, combined with cooperative effects between pX molecules in neighbouring pores, and the overall entropic bias towards

mX. It is reasonable to suggest that factors which will further disrupt the interaction between pX molecules - such as the presence of a solvent, as used in many experimental studies - will result in a decrease or inversion in selectivity. In light of this, future work should address the presence of additional species within the system.

While xylene adsorption in UiO-66(Zr) is generally well-predicted when the framework is kept rigid, the flexibility of the MOF and movement of atoms away from their crystallographic positions was found to be crucial in allowing xylene molecules to diffuse through the structure. The movement of xylene molecules from one cage to the next was only observed during simulations using a flexible framework. The ability of the BDC linkers to both rotate and flex in response to interaction with adsorbed xylene molecules was seen to result in an enlargement of the window diameter, enabling xylenes to pass from one pore to the next. This transition was found to be hindered considerably in the case of oX, whose twinned methyl groups are less able to induce the enlargement of the window than the individual methyl groups of pX and mX.

Recently, it has been demonstrated that the UiO-66(Zr) structure typically contains a non-negligible number of linker defects (Wu *et al.*, 2013; Cliffe *et al.*, 2014). In the ideal structure, each metal cluster is coordinated with 12 BDC linkers. Under standard synthesis conditions, however, only 11 of these linkers are present on average, with the vacant coordination site occupied by an alternative terminal group. While it is as yet unclear whether these defects are homogeneously distributed throughout the crystal or if the structure contains large regions of near-perfect crystallinity alternating with regions of meso-porosity, these linker defects introduce the possibility of cooperative adsorption and packing effects as well as enhancing the diffusion of all three isomers through the structure, influencing both the adsorption equilibrium and adsorption kinetics of the system. The incorporation of linker defects into both MD and MC simulations should therefore be a focus of future projects.

6 Summary and Outlook

Over the past decade, MOFs have emerged as possible adsorbents for a range of gas storage and gas- and liquid-phase separations, offering industry the opportunity to shift away from more traditional separation processes such as distillation towards potentially more energy-efficient adsorption processes. The rapid discovery of new MOF structures, however, threatens to out-pace the experimental evaluation of MOFs for adsorption applications. The use of molecular simulation tools, both to complement experimental adsorption studies and to quickly evaluate new structures for particular applications, offers a means to bridge the gap between MOF discovery and industrial application. In the work presented in this thesis, a range of computational approaches have been applied to the structural characterisation of MOFs and the evaluation of their potential as adsorbents in two key industrial separations: the separation of propane from propylene and the separation of xylene isomers.

In the case of propane/propylene separations, this work set out to identify the structural characteristics of the MOF which define the selectivity for one component over the other and, from this, determine whether it is possible to design a MOF which selectively adsorbs propane over propylene at industrially relevant pressure (i.e. $P > 0.1$ bar). It was shown that while it is possible to easily predict the preference of the MOF at low loading for either propane or propylene based solely on pore diameter, a more detailed description of the pore shape is required to predict the selectivity as the loading is increased.

The strength of the electrostatic interaction between propylene and the framework was found to determine the enthalpic preference of the MOF - based solely on van der Waals interactions, all of the MOFs in this study with a pore diameter of less than 9 Å were found to be propane-selective. The minimisation of the electrostatic interactions is thus key to ensuring that propane has a higher enthalpy of adsorption than propylene. It was demonstrated that the electrostatic interaction may be reduced

by initially avoiding polar substituents such as NH_2 or NO_2 on the organic linkers of the MOF, which serves to reduce the magnitude of partial charges on the framework atoms. More intriguingly, it was shown that the magnitude of the electrostatic contribution may be reduced by using small-pore MOFs. In 1D frameworks, this was shown to be due to a mismatch between the preferred van der Waals adsorption sites and the preferred electrostatic adsorption sites. In all cases, the strongest electrostatic interactions were found near the edges of the pore, while the centre of the channel was shown to experience low electrostatic interactions. In small-pore MOFs, the preferred van der Waals adsorption sites are in the centre of the channel, corresponding to regions of low electrostatic interaction, while for larger channels, the preferred adsorption sites are near the linkers and the corners of the pore, corresponding to the ideal electrostatic adsorption sites. Further work, however, is required to more fully understand the link between pore geometry, pore size and electrostatics in a more systematic manner, for example, via the generation of scalable point charge distributions such as those employed by García *et al.* (2014) in the evaluation of CO_2 electrostatic interactions in CPO-27(Ni).

As the C_3 loading is increased, the vast majority of MOFs are propylene-selective as a result of the lower packing density of propane. The MIL-140 series of small-pore MOFs, however, were identified as retaining their selectivity towards propane even at saturation loading. The MIL-140C and D in particular combine some of the highest selectivities towards propane yet reported ($S_{propane\text{-}propylene}$ = 2-3) with reasonable C_3 capacities (MIL-140C: 2.8 mol/kg; MIL-140D: 4 mol/kg), making them attractive candidates for further experimental evaluation. These MOFs contain specific, localised adsorption sites separated by nearby organic linkers which protrude into the channel and disrupt C3 packing along the channel length, eliminating the entropic advantage enjoyed by propylene. This effect may not be predicted based solely on pore diameter, however, and any screening protocol for the evaluation of new structures for this separation requires an effective way of quantifying the shape of the pore and identifying the presence of localised adsorption sites. In this respect, the development of effective tools for the characterisation of

pore shape (e.g. (Sarkisov and Harrison, 2011; First *et al.*, 2013; Garcia *et al.*, 2013)) is of prime importance.

The influence of pore geometry and pore diameter on sorbate-framework and sorbate-sorbate interactions was likewise explored for the separation of *para*-, *meta*- and *ortho*-xylene in both 1D model pores and analogous MOF structures. While this work confirmed that the pore diameter is a useful quantity for identifying non-selective (d > ~12 Å), oX-selective (7 < d < 10 Å) and pX-selective (4 < d < 5.5 Å) structures, it also demonstrated the presence of a transition region in which structures are likely to be non-selective (5.5 < d < 7 Å). In addition, it was shown that rhombic channels are generally unable to differentiate between pX and mX for pore diameters greater than ~5.5 Å. The comparison of xylene selectivity in model pores and analogous MOF structures demonstrated that the effect of pore geometry and pore diameter on adsorptive preference in MOFs may be qualitatively predicted using model pores. As model pores allow fine control of geometry and pore diameter in simulation, this approach may be used to identify ideal topologies (i.e. target MOF structures) for xylene selectivity. It should be noted that the majority of the xylene separations explored in both model pores and in MOFs were primarily entropic in nature – i.e. all three isomers exhibited very similar interaction energies with the framework. The selectivity of these structures is thus determined by the different degrees of confinement experienced by the different isomers and efforts should be made in future to develop methods of predicting or quantifying this confinement effect and its impact on selectivity (e.g. Garcia *et al* (2013)).

Given that the pX preference observed in narrow channels was shown to be a result of the increased rotational freedom of the slimmer pX molecule, it is unlikely that these structures will be able to effectively discriminate between pX and the final C_8 alkylaromatic isomer, ethylbenzene, which has a similar diameter to pX. Future work should therefore address the influence of ethylbenzene on this separation and the development of structure-property relationships which are inclusive of all four isomers. In addition, while high pX-selectivities may be achieved using small-pore MOFs, the low xylene capacity associated with these structures may limit their

usefulness to industry. It has been shown that larger pores which selectively adsorb pX exist (e.g. in the MOF MIL-125 (Vermoortele *et al.*, 2011) and more recently in the zeolitic structure MAF-X8 (Torres-Knoop *et al.*, 2014)) and the exploration of packing effects in more complex, 3D model pore systems may allow the rational design of pX-selective pores with higher capacity.

Finally, the value of molecular simulation in furthering our understanding of adsorption and diffusion processes in MOFs was demonstrated for the xylene-UiO-66(Zr) system. While the system has been extensively studied in the scientific literature, many aspects of the adsorption mechanism remained unclear - in particular whether an enthalpic preference for oX exists and the origin of any energetic preference and the ability of the MOF to separate pX and mX.

Adsorption simulations were able to correctly predict the equilibrium preference of UiO-66(Zr) for oX – a preference which was shown to contain both entropic and enthalpic contributions. The enhancement in oX-MOF interaction energy compared to the other isomers predicted by simulations matched that observed experimentally and was shown to be a result of the complete encapsulation of the oX molecule within the pores of UiO-66(Zr). While both methyl groups of oX were seen to be contained within the pore itself, steric restrictions forced one or both methyl groups of pX and mX to be sited in the pore window, resulting in lower overall interaction energies with the framework for the molecule.

The importance of small-scale framework flexibility was demonstrated during MD simulations of xylene diffusion in UiO-66(Zr). The ability of the organic linkers within the MOF to rotate and flex was found to be fundamental in allowing xylene molecules to move through the windows of the structure. The interaction between xylene molecule and the linkers which define the pore window is able to induce distortion of the linkers and an enlargement of the pore window, allowing the bulky xylene molecules to pass through. The overall order of mobility was found to be pX > mX >> oX and although no equilibrium separation of pX and mX was observed in GCMC simulations, MD simulations suggest that the MOF is able to

separate pX and mX via a kinetic separation. The high mobility of pX and mX is a result of the single methyl groups on these isomers being able to enter the pore window and interacting strongly with the linker atoms, acting as a wedge to distort the window further and allow passage of the rest of the xylene molecule. While the presence of the methyl group in the pore window was seen to reduce the enthalpy of adsorption of these species, it simultaneously enhances diffusion. Further work, however, is required to validate that the flexibility introduced to the framework by the classical force field used in this work is an accurate reflection of the real system, for example, through the use of *ab initio* methods to explore linker movement (e.g.(Chen *et al.*, 2013a; Banu, 2014)).

This work has shown that computational techniques can be used to develop effective screening protocols for the rapid evaluation of new MOF structures for particular applications based on easily measured metrics and, as importantly, is able to explain the mechanisms responsible for these separations. In the case of C_3 separations, the ideal propane-selective MOF uses non-functionalised organic linkers and fully-coordinated metal centres to create a pore of 4-8 Å in diameter. Structures which do not meet these basic requirements are unlikely to be propane-selective. These heuristics are likely to be applicable for the separation of any light gas mixture (i.e. up to C_4 in mass terms) in which the separation of polar from non-polar species is required while minimising the heats of adsorption and adsorbent regeneration costs. As the chain length is increased, the role of diffusion becomes more pronounced and the optimum pore diameter for the optimisation of van der Waals interactions may be expected to increase. For mixtures of xylene isomers, while the 'ideal' characteristics of a MOF for either pX- or oX-selectivity have not been established, it is clear that the pore diameter should certainly be either between 4 Å and 6 Å or between 7 Å and 15 Å. It also seems that while one-dimensional MOFs may show high selectivity for one component, it is unlikely that they will be able to effectively discriminate between all three isomers. Ultimately, these screening protocols – along with others – would be best implemented as a combined computational toolset made available to MOF synthesis groups. Based on only the crystal structure, such a tool would be able to evaluate the structural characteristics of the MOF before comparing these

characteristics against a wide range of screening protocols in order to identify applications for which the MOF may be suitable, thus speeding up the identification of new adsorbents for further in-depth study while also ensuring that MOFs which may be well-suited to a particular application are not overlooked.

While the work presented in this thesis demonstrates the important role that molecular simulation can play in the evaluation of MOFs for adsorption applications, it also highlights some of the challenges facing the simulation community. A number of the systems explored in this work were found to be heavily influenced by comparatively subtle variation in pore size or pore geometry – aspects of the system which are likely to be impacted upon by localised linker movement. The prediction of framework flexibility and its incorporation into the simulation of adsorption equilibria, therefore, must be addressed in future work. Similarly, while great strides have been made in the computational characterisation of pore shape, the impact of, for example, linker libration on these properties should also be considered.

Traditionally – and this work is no exception – molecular simulation has been used to evaluate the potential of well-activated, defect-free structures. Structural defects, such as those observed in UiO-66, can be expected to impact upon both the adsorption and catalytic properties of a structure and the evaluation of the role of defects in these processes via molecular simulation must be addressed in the future. Through the development of more versatile computational tools such as those outlined above, we can ensure that computational approaches are capable of describing and evaluating the more complex varieties of porous solids, including flexible and hierarchical structures, and remain an important component of structure and process development.

Nomenclature and Acronyms

Acronyms and Abbreviations

BDC – benzene dicarboxylate
BET – Brunauer-Emmett-Teller
BPDC – bi-phenyl dicarboxylate
Coul – Coulombic interaction
DFT – Density functional theory
EQeq – Extended charge equilibration
GCMC – grand canonical Monte Carlo
LJ – Lennard-Jones
MC – Monte Carlo
MD – molecular dynamics
MOF – metal-organic framework
mX – meta-xylene
NDC – naphthalene dicarboxylate
oX – ortho-xylene
PET – polyethylene terephthalate
PSD – Pore size distribution
pX – para-xylene
SMB – Simulated moving bed
UC – Unit cell
vdW – van der Waals
XRD – X-Ray diffraction

Latin Symbols

acc() – Probability of accepting an MC move
att() – Probability of attempting an MC move
d – pore diameter
D_s – self-diffusion coefficient (m^2/s)

E – Energy (kJ/mol)

E_a – Activation energy (kJ/mol)

F_i – Force acting on particle i

f – Fugacity

ħ – Planck's constant

k_B – Boltzmann constant

k_L – Bond stretching stiffness constant (kJ mol^{-1} $Å^{-2}$**)**

k_θ – Bond bending stiffness constant (kJ mol^{-1} rad^{-2})

k_φ – Torsion force constant (kJ/mol)

L – Bond length (Å)

L_{eq} – Equilibrium bond length (Å)

M – measured property

m – Mass

N – number of molecules

I – Torsion periodicity

P – Pressure

PV_{He} – Simulated helium pore volume (cm^3/g)

q – Partial charge (e)

R – Universal gas constant (kJ/mol/K)

r_{ij} – Separation distance of particles i and j

r_T – Cage-to-cage transition rate ($molec^{-1}$ ns^{-1})

r_{T0} – Arrhenius pre-exponential factor ($molec^{-1}$ ns^{-1})

S – Selectivity

s – Vector containing the position of a particle

SA_{acc} – Accessible surface area (m^2/g)

SA_{BET} – BET surface area (m^2/g)

SA_{GCMC} – Simulated BET surface area (m^2/g)

T – Temperature (K)

t – time

V – volume

Z – partition function

Greek Symbols

α – ratio of interaction energies

ε – Lennard-Jones well-depth

ε_0 – Permittivity of free space

ε/k_B – Lennard-Jones well-depth (K)

η_i – Probability of observing microstate *i*

θ – Bond angle (°)

θ_{eq} – Equilibrium bond angle (°)

θ_{wall} – Wall intersection angle (°)

Λ – de Broglie wavelength

μ – chemical potential

ν – Vector containing the momentum of a particle

$\pi()$ – Transition probability

$\rho()$ – Probability

σ – Lennard-Jones diameter (Å)

φ – Dihedral angle (°)

φ_{eq} – Equilibrium dihedral angle (°)

References

Ahnfeldt, T., *et al.* (2009). "Al-4(Oh)(2)(Och3)(4)(H2n-Bdc)(3) Center Dot Xh(2)O: A 12-Connected Porous Metal-Organic Framework with an Unprecedented Aluminum-Containing Brick." *Angewandte Chemie-International Edition* **48** (28) 5163-5166

Alaerts, L., *et al.* (2008). "Selective Adsorption and Separation of Ortho-Substituted Alkylaromatics with the Microporous Aluminum Terephthalate Mil-53." *Journal of the American Chemical Society* **130** (43) 14170-14178

Albesa, A. G., *et al.* (2012). "Ethane/Ethylene Adsorption on Carbon Nanotubes: Temperature and Size Effects on Separation Capacity." *Langmuir* **28** (3) 1824-1832

Allen, P. and Tildesley, D. J. (1987). *Computer Simulation of Liquids*, Oxford University Press, Oxford, UK.

Bae, Y. S., *et al.* (2012). "High Propene/Propane Selectivity in Isostructural Metal-Organic Frameworks with High Densities of Open Metal Sites." *Angewandte Chemie-International Edition* **51** (8) 1857-1860

Banu, A.-M. (2014), "Molecular Simulation Studies of Metal Organic Frameworks Focusing on Hydrogen Purification", PhD Thesis, Institute for Materials and Processes, Edinburgh, The University of Edinburgh

Bao, Z. B., *et al.* (2011). "Adsorption of Ethane, Ethylene, Propane, and Propylene on a Magnesium-Based Metal-Organic Framework." *Langmuir* **27** (22) 13554-13562

Barcia, P. S., *et al.* (2011). "Reverse Shape Selectivity in the Adsorption of Hexane and Xylene Isomers in Mof Uio-66." *Microporous and Mesoporous Materials* **139** (1-3) 67-73

Barcia, P. S., *et al.* (2012). "Modeling Adsorption Equilibria of Xylene Isomers in a Microporous Metal-Organic Framework." *Microporous and Mesoporous Materials* **155** 220-226

Barthelet, K., *et al.* (2004). "V-Iii(Oh){O2c-C6h4-Co2}(Center Dot)(Ho2c-C6h4-Co2h)(X)(Dmf)(Y)(H2o)(Z) (or Mil-68), a New Vanadocarboxylate with a Large Pore Hybrid Topology: Reticular Synthesis with Infinite Inorganic Building Blocks?" *Chemical Communications* (5) 520-521

Barthelet, K., *et al.* (2002). "A Breathing Hybrid Organic-Inorganic Solid with Very Large Pores and High Magnetic Characteristics." *Angewandte Chemie - International Edition* **41** (2) 281-284

Batten, S. R., *et al.* (2013). "Terminology of Metal-Organic Frameworks and Coordination Polymers (Iupac Recommendations 2013)." *Pure and Applied Chemistry* **85** (8) 1715-1724

Berendsen, H. J. C., *et al.* (1984). "Molecular Dynamics with Coupling to an External Bath." *The Journal of Chemical Physics* **81** (8) 3684-3690

Biswas, S. and Van Der Voort, P. (2013). "A General Strategy for the Synthesis of Functionalised Uio-66 Frameworks: Characterisation, Stability and Co2 Adsorption Properties." *European Journal of Inorganic Chemistry* **2013** (12) 2154-2160

Bloch, E. D., *et al.* (2012). "Hydrocarbon Separations in a Metal-Organic Framework with Open Iron(Ii) Coordination Sites." *Science* **335** (6076) 1606-1610

Blytas, G. C. (1992). "Separation of Unsaturates by Complexing with Nonaqueous Solutions of Cuprous Salts" in *Separation and Purification Technology*. N. N. Li, Taylor & Francis Ch. 3

Bohme, U., *et al.* (2013). "Ethene/Ethane and Propene/Propane Separation Via the Olefin and Paraffin Selective Metal-Organic Framework Adsorbents Cpo-27 and Zif-8." *Langmuir* **29** (27) 8592-8600

Bojan, M. J., *et al.* (1992a). "Computer-Simulation Studies of the Storage of Methane in Microporous Carbons." *Separation Science and Technology* **27** (14) 1837-1856

Bojan, M. J., *et al.* (1992b). "Simulation Studies of Adsorption in Rough-Walled Cylindrical Pores." *Langmuir* **8** (3) 901-908

Bozbiyik, B., *et al.* (2014). "Adsorption and Separation of N-Hexane and Cyclohexane on the Uio-66 Metal-Organic Framework." *Microporous and Mesoporous Materials* **183** 143-149

Broughton, D. B., *et al.* (1970). "Parex Process for Recovering Paraxylene." *Chemical Engineering Progress* **66** (9) 70-&

Bryan, P. F. (2004). "Removal of Propylene from Fuel-Grade Propane." *Separation and Purification Reviews* **33** (2) 157-182

Cannella, W. J. (2000). "Xylenes and Ethylbenzene" in *Kirk-Othmer Encyclopedia of Chemical Technology*. John Wiley & Sons, Inc. Ch.

Castillo, J. M., *et al.* (2009). "Molecular Simulation Study on the Separation of Xylene Isomers in Mil-47 Metal-Organic Frameworks." *Journal of Physical Chemistry C* **113** (49) 20869-20874

Cavka, J. H., *et al.* (2008). "A New Zirconium Inorganic Building Brick Forming Metal Organic Frameworks with Exceptional Stability." *Journal of the American Chemical Society* **130** (42) 13850-13851

Chang, N. and Yan, X.-P. (2012). "Exploring Reverse Shape Selectivity and Molecular Sieving Effect of Metal-Organic Framework Uio-66 Coated Capillary Column for Gas Chromatographic Separation." *Journal of Chromatography A* **1257** 116-124

Chatt, J. and Duncanson, L. A. (1953). "Olefin Co-Ordination Compounds. Part Iii. Infra-Red Spectra and Structure: Attempted Preparation of Acetylene Complexes." *Journal of the Chemical Society (Resumed)* 2939-2947

Chen, L., *et al.* (2013a). "Elucidating the Breathing of the Metal-Organic Framework Mil-53(Sc) with Ab Initio Molecular Dynamics Simulations and in Situ X-Ray Powder Diffraction Experiments." *Journal of the American Chemical Society* **135** (42) 15763-15773

Chen, L. J., *et al.* (2011). "Accurate Prediction of Methane Adsorption in a Metal-Organic Framework with Unsaturated Metal Sites by Direct Implementation of an Ab Initio Derived Potential Energy Surface in Gcmc Simulation." *Journal of Physical Chemistry C* **115** (46) 23074-23080

Chen, L. Y., *et al.* (1997). "Thermal and Hydrothermal Stability of Framework-Substituted Mcm-41 Mesoporous Materials." *Microporous Materials* **12** (4-6) 323-330

Chen, X. C., *et al.* (2013b). "Cu(I)-Based Ionic Liquids as Potential Absorbents to Separate Propylene and Propane." *Separation Science and Technology* **48** (15) 2317-2323

Cheng, L. S. and Yang, R. T. (1995). "Monolayer Cuprous Chloride Dispersed on Pillared Clays for Olefin Paraffin Separations by Pi-Complexation." *Adsorption-Journal of the International Adsorption Society* **1** (1) 61-75

Choudhary, V. R., *et al.* (1995). "Sorption Isotherms of Methane, Ethane, Ethene and Carbon-Dioxide on Nax, Nay and Na-Mordenite Zeolites." *Journal of the Chemical Society-Faraday Transactions* **91** (17) 2935-2944

Cliffe, M. J., *et al.* (2014). "Correlated Defect Nanoregions in a Metal–Organic Framework." *Nat Commun* **5**

Cohen, S. M. (2012). "Postsynthetic Methods for the Functionalization of Metal-Organic Frameworks." *Chemical Reviews* **112** (2) 970-1000

Cracknell, R. F., *et al.* (1993). "A Grand-Canonical Monte-Carlo Study of Lennard-Jones Mixtures in Slit Shaped Pores." *Molecular Physics* **80** (4) 885-897

Cruz, F., *et al.* (2010). "A Molecular Simulation Study of Propane and Propylene Adsorption onto Single-Walled Carbon Nanotube Bundles." *Journal of Nanoscience and Nanotechnology* **10** (4) 2537-2546

Curbelo, S. and Muller, E. A. (2005). "Modelling of Ethane/Ethylene Separation Using Microporous Carbon." *Adsorption Science & Technology* **23** (10) 855-865

Da Silva, F. A. and Rodrigues, A. E. (2001). "Vacuum Swing Adsorption for Propylene/Propane Separation with 4a Zeolite." *Industrial & Engineering Chemistry Research* **40** (24) 5758-5774

Dan-Hardi, M., *et al.* (2009). "A New Photoactive Crystalline Highly Porous Titanium(Iv) Dicarboxylate." *Journal of the American Chemical Society* **131** (31) 10857-+

Dau, P. V., *et al.* (2012). "Functional Group Effects on Metal-Organic Framework Topology." *Chemical Communications* **48** (75) 9370-9372

De Malsche, W., *et al.* (2012). "Unusual Pressure-Temperature Dependency in the Capillary Liquid Chromatographic Separation of C8 Alkylaromatics on the Mil-53(Al) Metal-Organic Framework." *Microporous and Mesoporous Materials* **162** 1-5

Denayer, J. F. M., *et al.* (2005). "Rotational Entropy Driven Separation of Alkane/Isoalkane Mixtures in Zeolite Cages." *Angewandte Chemie International Edition* **44** (3) 400-403

Devautour-Vinot, S., *et al.* (2012). "Structure and Dynamics of the Functionalized Mof Type Uio-66(Zr): Nmr and Dielectric Relaxation Spectroscopies Coupled with Dft Calculations." *Chemistry of Materials* **24** (11) 2168-2177

Devic, T., *et al.* (2009). "Functionalization in Flexible Porous Solids: Effects on the Pore Opening and the Host-Guest Interactions." *Journal of the American Chemical Society* **132** (3) 1127-1136

Dewar, J. S. (1951). "A Review of the Pi-Complex Theory." *Bulletin De La Societe Chimique De France* **18** (3-4) C71-C79

Dill, K. A. and Bromberg, S. (2003). *Molecular Driving Forces: Statistical Thermodynamics in Chemistry and Biology*, Garland Science, New York, USA.

Do, D. D. (1998). *Adsorption Analysis: Equilibria and Kinetics*, Imperial College Press, London, UK.

Do, D. D. and Do, H. D. (2005). "Cooperative and Competitive Adsorption of Ethylene, Ethane, Nitrogen and Argon on Graphitized Carbon Black and in

Slit Pores." *Adsorption-Journal of the International Adsorption Society* **11** (1) 35-50

Duan, L. H., *et al.* (2013). "Adsorption and Diffusion Properties of Xylene Isomers and Ethylbenzene in Metal-Organic Framework Mil-53(Al)." *Journal of Porous Materials* **20** (2) 431-440

Duerinck, T., *et al.* (2013). "Understanding Hydrocarbon Adsorption in the Uio-66 Metal-Organic Framework: Separation of (Un)Saturated Linear, Branched, Cyclic Adsorbates, Including Stereoisomers." *Journal of Physical Chemistry C* **117** (24) 12567-12578

Duren, T., *et al.* (2009). "Using Molecular Simulation to Characterise Metal-Organic Frameworks for Adsorption Applications." *Chemical Society Reviews* **38** (5) 1237-1247

Duren, T., *et al.* (2007). "Calculating Geometric Surface Areas as a Characterization Tool for Metalâˆ’Organic Frameworks." *The Journal of Physical Chemistry C* **111** (42) 15350-15356

Eddaoudi, M., *et al.* (2002). "Systematic Design of Pore Size and Functionality in Isoreticular Mofs and Their Application in Methane Storage." *Science* **295** (5554) 469-472

El Osta, R., *et al.* (2012). "Liquid-Phase Adsorption and Separation of Xylene Isomers by the Flexible Porous Metal-Organic Framework Mil-53(Fe)." *Chemistry of Materials* **24** (14) 2781-2791

Eldridge, R. B. (1993). "Olefin Paraffin Separation Technology - a Review." *Industrial & Engineering Chemistry Research* **32** (10) 2208-2212

Engerer, L. K. and Hanusa, T. P. (2011). "Geometric Effects in Olefinic Cation-Pi Interactions with Alkali Metals: A Computational Study." *Journal of Organic Chemistry* **76** (1) 42-49

Everett, D. H. and Powl, J. C. (1976). "Adsorption in Slit-Like and Cylindrical Micropores in Henrys Law Region - Model for Microporosity of Carbons." *Journal of the Chemical Society-Faraday Transactions I* **72** 619-636

Ewald, P. P. (1921). "The Calculation of Optical and Electrostatic Grid Potential." *Annalen Der Physik* **64** (3) 253-287

Fabri, J., *et al.* (2000). "Xylenes" in *Ullmann's Encyclopedia of Industrial Chemistry*. Wiley-VCH Verlag GmbH & Co. KGaA Ch.

Fairen-Jimenez, D., *et al.* (2012). "Flexibility and Swing Effect on the Adsorption of Energy-Related Gases on Zif-8: Combined Experimental and Simulation Study." *Dalton Transactions* **41** (35) 10752-10762

Faiz, R., *et al.* (2013). "Separation of Olefin/Paraffin Gas Mixtures Using Ceramic Hollow Fiber Membrane Contactors." *Industrial & Engineering Chemistry Research* **52** (23) 7918-7929

Faiz, R. and Li, K. (2012). "Olefin/Paraffin Separation Using Membrane Based Facilitated Transport/Chemical Absorption Techniques." *Chemical Engineering Science* **73** 261-284

Farha, O. K., *et al.* (2012). "Metal–Organic Framework Materials with Ultrahigh Surface Areas: Is the Sky the Limit?" *Journal of the American Chemical Society* **134** (36) 15016-15021

Farrusseng, D. (2011). *Metal-Organic Frameworks: Applications from Catalysis to Gas Storage*, Wiley, Weinheim, Germany.

Farrusseng, D., *et al.* (2009). "Heats of Adsorption for Seven Gases in Three Metal-Organic Frameworks: Systematic Comparison of Experiment and Simulation." *Langmuir* **25** (13) 7383-7388

Ferey, G., *et al.* (2007). "Mixed-Valence Li/Fe-Based Metal-Organic Frameworks with Both Reversible Redox and Sorption Properties." *Angewandte Chemie-International Edition* **46** (18) 3259-3263

Ferey, G., *et al.* (2004). "A Hybrid Solid with Giant Pores Prepared by a Combination of Targeted Chemistry, Simulation, and Powder Diffraction." *Angewandte Chemie-International Edition* **43** (46) 6296-6301

Ferreira, A. F. P., (2014), *Personal Communication*

Ferreira, A. F. P., *et al.* (2011). "Suitability of Cu-Btc Extrudates for Propane-Propylene Separation by Adsorption Processes." *Chemical Engineering Journal* **167** (1) 1-12

Finsy, V., *et al.* (2009). "Low-Coverage Adsorption Properties of the Metal-Organic Framework Mil-47 Studied by Pulse Chromatography and Monte Carlo Simulations." *Physical Chemistry Chemical Physics* **11** (18) 3515-3521

First, E. L., *et al.* (2013). "Predictive Framework for Shape-Selective Separations in Three-Dimensional Zeolites and Metal-Organic Frameworks." *Langmuir* **29** (18) 5599-5608

Fischer, M., *et al.* (2012). "Modeling Adsorption in Metal-Organic Frameworks with Open Metal Sites: Propane/Propylene Separations." *Langmuir* **28** (22) 8537-8549

Freeman, B. and Yampolskii, Y. (2010). *Membrane Gas Separation*, Wiley, Weinheim, Germany.

Frenkel, D., Smit, B. (1996). *Understanding Molecular Simulation: From Algorithms to Applications*, Academic Press, San Diego.

Garcia, E. J., *et al.* (2013). "Quantification of the Confinement Effect in Microporous Materials." *Physical Chemistry Chemical Physics* **15** (15) 5648-5657

García, E. J., *et al.* (2014). "How to Optimize the Electrostatic Interaction between a Solid Adsorbent and Co2." *The Journal of Physical Chemistry C* **118** (18) 9458-9467

Gelb, L. D. and Gubbins, K. E. (1998). "Characterization of Porous Glasses: Simulation Models, Adsorption Isotherms, and the Brunauer-Emmett-Teller Analysis Method." *Langmuir* **14** (8) 2097-2111

Gladden, L. F., *et al.* (1997). "Adsorption and Transport of Ethane and Ethene in Zeolite Naa: H-2 Nmr and Monte Carlo Lattice Dynamics Studies." *Journal of Physical Chemistry B* **101** (48) 10121-10127

Gomes, P. S., *et al.* (2009). "Design of a Gas Phase Simulated Moving Bed for Propane/Propylene Separation." *Chemical Engineering Science* **64** (6) 1336-1357

Granato, M. A., *et al.* (2014). "Adsorption of Xylene Isomers in Mof Uio-66 by Molecular Simulation." *Microporous and Mesoporous Materials* **190** 165-170

Grande, C. A., *et al.* (2004). "New Pi-Complexation Adsorbents for Propane-Propylene Separation." *Langmuir* **20** (13) 5291-5297

Grande, C. A., *et al.* (2006). "Adsorption of Propane and Propylene in Zeolite 4a Honeycomb Monolith." *Chemical Engineering Science* **61** (10) 3053-3067

Grande, C. A., *et al.* (2010). "Propane/Propylene Separation with Li-Exchanged Zeolite 13x." *Chemical Engineering Journal* **160** (1) 207-214

Greathouse, J. A., *et al.* (2010). "Computational Screening of Metal-Organic Frameworks for Large-Molecule Chemical Sensing." *Physical Chemistry Chemical Physics* **12** (39) 12621-12629

Gu, Z.-Y., *et al.* (2009). "Adsorption and Separation of Xylene Isomers and Ethylbenzene on Two Zn−Terephthalate Metal−Organic Frameworks." *The Journal of Physical Chemistry C* **114** (1) 311-316

Gucuyener, C., *et al.* (2010). "Ethane/Ethene Separation Turned on Its Head: Selective Ethane Adsorption on the Metal-Organic Framework Zif-7 through a Gate-Opening Mechanism." *Journal of the American Chemical Society* **132** (50) 17704-17706

Guillerm, V., *et al.* (2012). "A Series of Isoreticular, Highly Stable, Porous Zirconium Oxide Based Metal-Organic Frameworks." *Angewandte Chemie-International Edition* **51** (37) 9267-9271

Gupta, A., *et al.* (2003). "Object-Oriented Programming Paradigms for Molecular Modeling." *Molecular Simulation* **29** (1) 29-46

Gutierrez-Sevillano, J. J., *et al.* (2010). "Analysis of the Itq-12 Zeolite Performance in Propane-Propylene Separations Using a Combination of Experiments and Molecular Simulations." *Journal of Physical Chemistry C* **114** (35) 14907-14914

Hampson, J. A. and Rees, L. V. C. (1994). "Adsorption of Lower Hydrocarbons in Zeolite Nay and Theta-1 - Comparison of Low and High-Pressure Isotherm Data" in *Zeolites and Microporous Crystals*. T. Hattori and T. Yashima, Elsevier Science Bv Ch.

Hara, N., *et al.* (2014). "Diffusive Separation of Propylene/Propane with Zif-8 Membranes." *Journal of Membrane Science* **450** 215-223

Hartmann, M., *et al.* (2008). "Adsorptive Separation of Isobutene and Isobutane on Cu(3)(Btc)(2)." *Langmuir* **24** (16) 8634-8642

Hayashi, J., *et al.* (1996). "Separation of Ethane/Ethylene and Propane/Propylene Systems with a Carbonized Bpda-Pp'oda Polyimide Membrane." *Industrial & Engineering Chemistry Research* **35** (11) 4176-4181

Herdes, C., *et al.* (2007). "Selective Adsorption of Volatile Organic Compounds in Micropore Aluminum Methylphosphonate-Alpha: A Combined Molecular Simulation-Experimental Approach." *Langmuir* **23** (13) 7299-7305

Hill, T. L. (1956). *Statistical Mechanics: Principles and Selected Applications*, McGraw-Hill, New York, USA.

Hinks, N. J., *et al.* (2010). "Metal Organic Frameworks as No Delivery Materials for Biological Applications." *Microporous and Mesoporous Materials* **129** (3) 330-334

Hirai, H., *et al.* (1985). "Polystyrene-Supported Aluminum Silver-Chloride as Selective Ethylene Adsorbent." *Angewandte Makromolekulare Chemie* **130** (MAR) 207-212

Hirschfelder, J. O., *et al.* (1954). *Molecular Theory of Gases and Liquids*, Wiley, New York, USA.

Huang, L. and Cao, D. P. (2013). "Selective Adsorption of Olefin-Paraffin on Diamond-Like Frameworks: Diamondyne and Paf-302." *Journal of Materials Chemistry A* **1** (33) 9433-9439

Hunt, L. B. (1984). "The First Organo-Metallic Compounds." *Platinum Metals Review* **28** (2) 76-83

Jakobtorweihen, S., *et al.* (2005). "Molecular Simulation of Alkene Adsorption in Zeolites." *Molecular Physics* **103** (4) 471-489

Jarvelin, H. and Fair, J. R. (1993). "Adsorptive Separation of Propylene Propane Mixtures." *Industrial & Engineering Chemistry Research* **32** (10) 2201-2207

Jorge, M., *et al.* (2010). "Molecular Simulation of Propane/Propylene Separation on the Metal-Organic Framework Cubtc." *Colloids and Surfaces a-Physicochemical and Engineering Aspects* **357** (1-3) 27-34

Jorgensen, W. L., *et al.* (1993). "Monte-Carlo Simulations of Pure Liquid Substituted Benzenes with Opls Potential Functions." *Journal of Computational Chemistry* **14** (2) 206-215

Ke, F., *et al.* (2011). "Facile Fabrication of Magnetic Metal-Organic Framework Nanocomposites for Potential Targeted Drug Delivery." *Journal of Materials Chemistry* **21** (11) 3843-3848

Keller, G. E., *et al.* (1992). "Olefin Recovery and Purification Via Silver Complexation" in *Separation Purification and Technology*. N. N. Li, Taylor & Francis Ch. 2

Kim, J., *et al.* (2012a). "Large-Scale Computational Screening of Zeolites for Ethane/Ethene Separation." *Langmuir* **28** (32) 11923-11928

Kim, M., *et al.* (2012b). "Postsynthetic Ligand and Cation Exchange in Robust Metal-Organic Frameworks." *Journal of the American Chemical Society* **134** (43) 18082-18088

Kirk, R. E., *et al.* (1991). *Kirk-Othmer Encyclopedia of Chemical Technology*, Wiley, New York.

Klein, N., *et al.* (2010). "Monitoring Adsorption-Induced Switching by Xe-129 Nmr Spectroscopy in a New Metal-Organic Framework Ni-2(2,6-Ndc)(2)(Dabco)." *Physical Chemistry Chemical Physics* **12** (37) 11778-11784

Klomkliang, N., *et al.* (2012). "Affinity and Packing of Benzene, Toluene, and P-Xylene Adsorption on a Graphitic Surface and in Pores." *Industrial & Engineering Chemistry Research* **51** (14) 5320-5329

Kolokolov, D. I., *et al.* (2012). "Probing the Dynamics of the Porous Zr Terephthalate Uio-66 Framework Using H-2 Nmr and Neutron Scattering." *Journal of Physical Chemistry C* **116** (22) 12131-12136

Kroon, M. C. and Vega, L. F. (2009). "Selective Paraffin Removal from Ethane/Ethylene Mixtures by Adsorption into Aluminum Methylphosphonate-Alpha: A Molecular Simulation Study." *Langmuir* **25** (4) 2148-2152

Kumar, R., *et al.* (1972). "Process Design Considerations for Extractive Distillation - Separation of Propylene-Propane." *Advances in Chemistry Series* (115) 16-34

Kurup, A. S., *et al.* (2005). "Optimal Operation of an Industrial-Scale Parex Process for the Recovery of P-Xylene from a Mixture of C-8 Aromatics." *Industrial & Engineering Chemistry Research* **44** (15) 5703-5714

Kwasniewski, V. J., *et al.*, (1999). "Unsaturated Hydrocarbon Separation and Recovery Process", U. S. Patent 5,863,420

Lamia, N., *et al.* (2009). "Adsorption of Propane, Propylene and Isobutane on a Metal-Organic Framework: Molecular Simulation and Experiment." *Chemical Engineering Science* **64** (14) 3246-3259

Lee, J., *et al.* (2009). "Metal-Organic Framework Materials as Catalysts." *Chemical Society Reviews* **38** (5) 1450-1459

Lemmon, E. W., *et al.* (2014). "Thermophysical Properties of Fluid Systems" in *NIST Chemistry WebBook, NIST Standard Reference Database Number 69*. P. J. Linstrom and W. G. Mallard, National Institute of Standards and Technology, http://webbook.nist.gov, Retrieved April 23 2014

Li, J. R., *et al.* (2009a). "Selective Gas Adsorption and Separation in Metal-Organic Frameworks." *Chemical Society Reviews* **38** (5) 1477-1504

Li, K. H., *et al.* (2009b). "Zeolitic Imidazolate Frameworks for Kinetic Separation of Propane and Propene." *Journal of the American Chemical Society* **131** (30) 10368-+

Liu, D. F., *et al.* (2014). "Gas Transport Properties and Propylene/Propane Separation Characteristics of Zif-8 Membranes." *Journal of Membrane Science* **451** 85-93

Low, J. J., *et al.* (2009). "Virtual High Throughput Screening Confirmed Experimentally: Porous Coordination Polymer Hydration." *Journal of the American Chemical Society* **131** (43) 15834-15842

Ma, X. L., *et al.* (2013). "Gamma-Alumina Supported Carbon Molecular Sieve Membrane for Propylene/Propane Separation." *Industrial & Engineering Chemistry Research* **52** (11) 4297-4305

Maginn, E. J., *et al.* (1996). "Dynamics of Long N-Alkanes in Silicalite: A Hierarchical Simulation Approach." *J. Phys. Chem.* **100** 7155-7173

Martinez, C. R. and Iverson, B. L. (2012). "Rethinking the Term "Pi-Stacking"." *Chemical Science* **3** (7) 2191-2201

Mayo, S. L., *et al.* (1990). "Dreiding - a Generic Force-Field for Molecular Simulations." *Journal of Physical Chemistry* **94** (26) 8897-8909

Metropolis, N., *et al.* (1953). "Equation of State Calculations by Fast Computing Machines." *Journal of Chemical Physics* **21** (6) 1087-1092

Minceva, M. and Rodrigues, A. E. (2004). "Adsorption of Xylenes on Faujasite-Type Zeolite - Equilibrium and Kinetics in Batch Adsorber." *Chemical Engineering Research & Design* **82** (A5) 667-681

Moghadam, P. Z. (2013), "Molecular Simulation Studies of Gas Adsorption and Separation in Metal-Organic Frameworks", PhD Thesis, Institute for Materials and Processes, Edinburgh, University of Edinburgh

Moreira, M. A., *et al.* (2012a). "Reverse Shape Selectivity in the Liquid-Phase Adsorption of Xylene Isomers in Zirconium Terephthalate Mof Uio-66." *Langmuir* **28** (13) 5715-5723

Moreira, M. A., *et al.* (2012b). "Effect of Ethylbenzene in P-Xylene Selectivity of the Porous Titanium Amino Terephthalate Mil-125(Ti)_Nh2." *Microporous and Mesoporous Materials* **158** 229-234

Moreira, M. A., *et al.* (2012c). "Toward Understanding the Influence of Ethylbenzene in P-Xylene Selectivity of the Porous Titanium Amino Terephthalate Mil-125(Ti): Adsorption Equilibrium and Separation of Xylene Isomers." *Langmuir* **28** (7) 3494-3502

Myers, A. L. and Monson, P. A. (2002). "Adsorption in Porous Materials at High Pressure: Theory and Experiment." *Langmuir* **18** (26) 10261-10273

Olson, D. H., *et al.* (2004). "Light Hydrocarbon Sorption Properties of Pure Silica Si-Cha and Itq-3 and High Silica Zsm-58." *Microporous and Mesoporous Materials* **67** (1) 27-33

Padin, J. and Yang, R. T. (2000). "New Sorbents for Olefin/Paraffin Separations by Adsorption Via Pi-Complexation: Synthesis and Effects of Substrates." *Chemical Engineering Science* **55** (14) 2607-2616

Pantu, P., *et al.* (2007). "The Adsorption of Saturated and Unsaturated Hydrocarbons on Nanostructured Zeolites (H-Mor and H-Fau): An Oniom Study." *Journal of Molecular Catalysis a-Chemical* **277** (1-2) 171-179

Peng, D. and Robinson, D. B. (1976). "New 2-Constant Equation of State." *Industrial & Engineering Chemistry Fundamentals* **15** (1) 59-64

Peralta, D., *et al.* (2012). "Adsorption and Separation of Xylene Isomers: Cpo-27-Ni Vs Hkust-1 Vs Nay." *Journal of Physical Chemistry C* **116** (41) 21844-21855

Porter, M. C. (1990). *Handbook of Industrial Membrane Technology*, Noyes Publications, New Jersey, USA.

Potoff, J. J. and Siepmann, J. I. (2001). "Vapor-Liquid Equilibria of Mixtures Containing Alkanes, Carbon Dioxide, and Nitrogen." *Aiche Journal* **47** (7) 1676-1682

Rabago, R., *et al.* (1996). "Evidence for Parallel Pathways in the Facilitated Transport of Alkenes through Ag+-Exchanged Nafion Films." *Industrial & Engineering Chemistry Research* **35** (4) 1090-1096

Rappe, A. K., *et al.* (1992). "Uff, a Full Periodic-Table Force-Field for Molecular Mechanics and Molecular-Dynamics Simulations." *Journal of the American Chemical Society* **114** (25) 10024-10035

Ravanchi, M. T., *et al.* (2010). "Supported Liquid Membrane Separation of Propylene-Propane Mixtures Using a Metal Ion Carrier." *Desalination* **250** (1) 130-135

Rawat, D. S. and Migone, A. D. (2011). "Ethylene Films Adsorbed onto Purified Hipco Single Walled Carbon Nanotubes: A Comparison with Ethane and Longer Alkanes." *Adsorption Science & Technology* **29** (8) 723-731

Rege, S. U., *et al.* (1998). "Olefin/Paraffin Separations by Adsorption: Pi-Complexation Vs. Kinetic Separation." *Aiche Journal* **44** (4) 799-809

Reid, R. C., *et al.* (1977). *The Properties of Gases and Liquids*, McGraw-Hill, New York, USA.

Reinsch, H., *et al.* (2013a). "First Keto-Functionalized Microporous Al-Based Metal-Organic Framework: Al(Oh)(O2c-C6h4-Co-C6h4-Co2)." *Inorganic Chemistry* **52** (4) 1854-1859

Reinsch, H., *et al.* (2013b). "Structures, Sorption Characteristics, and Nonlinear Optical Properties of a New Series of Highly Stable Aluminum Mofs." *Chemistry of Materials* **25** (1) 17-26

Ren, T., *et al.* (2006). "Olefins from Conventional and Heavy Feedstocks: Energy Use in Steam Cracking and Alternative Processes." *Energy* **31** (4) 425-451

Rouquerol, F., *et al.* (1999). *Adsorption by Powders and Porous Solids: Principles, Methodology and Applications*, Academic Press, London, UK.

Rouquerol, J., *et al.* (2006). "Is the Bet Equation Applicable to Microporous Adsorbents?" in *Characterization of Porous Solids Vii - Proceedings of the*

7th International Symposium on the Characterization of Porous Solids. P. L. Llewellyn, F. Rodriquez Reinoso, J. Rouqerol and N. Seaton, Elsevier Science Bv Ch.

Rowsell, J. L. C. and Yaghi, O. M. (2004). "Metal-Organic Frameworks: A New Class of Porous Materials." *Microporous and Mesoporous Materials* **73** (1-2) 3-14

Ruthven, D. M. (1984). *Principles of Adsorption and Adsorption Processes*, Wiley, New York, USA.

Sanchez, L. M. G., *et al.* (2009). "Potential of Silver-Based Room-Temperature Ionic Liquids for Ethylene/Ethane Separation." *Industrial & Engineering Chemistry Research* **48** (23) 10650-10656

Santilli, D. S., *et al.* (1993). "Inverse Shape Selectivity in Molecular Sieves: Observations, Modelling, and Predictions." *Microporous Materials* **1** (5) 329-341

Sarkisov, L. (2012). "Toward Rational Design of Metal-Organic Frameworks for Sensing Applications: Efficient Calculation of Adsorption Characteristics in Zero Loading Regime." *Journal of Physical Chemistry C* **116** (4) 3025-3033

Sarkisov, L. and Harrison, A. (2011). "Computational Structure Characterisation Tools in Application to Ordered and Disordered Porous Materials." *Molecular Simulation* **37** (15) 1248-1257

Serre, C., *et al.* (2006). "Synthesis, Structure and Properties of Related Microporous N,N '-Piperazinebismethylenephosphonates of Aluminum and Titanium." *Chemistry of Materials* **18** (6) 1451-1457

Serre, C., *et al.* (2004a). "A Route to the Synthesis of Trivalent Transition-Metal Porous Carboxylates with Trimeric Secondary Building Units." *Angewandte Chemie International Edition* **43** (46) 6285-6289

Serre, C., *et al.* (2004b). "Synthesis, Characterisation and Luminescent Properties of a New Three-Dimensional Lanthanide Trimesate: M((C6h3)-(Co2)(3)) (M = Y, Ln) or Mil-78." *Journal of Materials Chemistry* **14** (10) 1540-1543

Serre, C., *et al.* (2002). "Very Large Breathing Effect in the First Nanoporous Chromium(Iii)-Based Solids: Mil-53 or Cr-Iii(Oh)Center Dot{O2c-C6h4-Co2}Center Dot{Ho2c-C6h4-Co2h}(X)Center Dot H2oy." *Journal of the American Chemical Society* **124** (45) 13519-13526

Shu, C. M., *et al.* (1990). "Experimental and Computational Studies on Propane-Propylene Separation by Adsorption and Variable-Temperature Stepwise Desorption." *Separations Technology* **1** (1) 18-28

Silva, M. S. P., *et al.* (2012). "Adsorbent Evaluation Based on Experimental Breakthrough Curves: Separation of P-Xylene from C8 Isomers." *Chemical Engineering & Technology* **35** (10) 1777-1785

Sing, K. S. W., *et al.* (1985). "Reporting Physisorption Data for Gas Solid Systems with Special Reference to the Determination of Surface-Area and Porosity (Recommendations 1984)." *Pure and Applied Chemistry* **57** (4) 603-619

Snurr, R. Q., *et al.* (1993). "Prediction of Adsorption of Aromatic-Hydrocarbons in Silicalite from Grand-Canonical Monte-Carlo Simulations with Biased Insertions." *Journal of Physical Chemistry* **97** (51) 13742-13752

Tanaka, K., *et al.* (1996). "Permeation and Separation Properties of Polyimide Membranes to Olefins and Paraffins." *Journal of Membrane Science* **121** (2) 197-207

Todorov, I. T., *et al.* (2006). "Dl_Poly_3: New Dimensions in Molecular Dynamics Simulations Via Massive Parallelism." *Journal of Materials Chemistry* **16** (20) 1911-1918

Torres-Knoop, A., *et al.* (2014). "Separating Xylene Isomers by Commensurate Stacking of P-Xylene within Channels of Maf-X8." *Angewandte Chemie-International Edition* **53** (30) 7774-7778

Torrisi, A., *et al.* (2010). "Impact of Ligands on Co2 Adsorption in Metal-Organic Frameworks: First Principles Study of the Interaction of Co2 with Functionalized Benzenes. Ii. Effect of Polar and Acidic Substituents." *Journal of Chemical Physics* **132** (4)

Trens, P., *et al.* (2014). "Adsorption and Separation of Xylene Isomers Vapors onto the Chromium Terephthalate-Based Porous Material Mil-101(Cr): An Experimental and Computational Study." *Microporous and Mesoporous Materials* **183** 17-22

Tuel, A. (1999). "Modification of Mesoporous Silicas by Incorporation of Heteroelements in the Framework." *Microporous and Mesoporous Materials* **27** (2-3) 151-169

Valenzano, L., *et al.* (2011). "Disclosing the Complex Structure of Uio-66 Metal Organic Framework: A Synergic Combination of Experiment and Theory." *Chemistry of Materials* **23** (7) 1700-1718

van den Bergh, J., *et al.* (2011). "Understanding the Anomalous Alkane Selectivity of Zif-7 in the Separation of Light Alkane/Alkene Mixtures." *Chemistry-a European Journal* **17** (32) 8832-8840

van Miltenburg, A., *et al.* (2008). "Propylene/Propane Mixture Adsorption on Faujasite Sorbents." *Adsorption-Journal of the International Adsorption Society* **14** (2-3) 309-321

Vermoortele, F., *et al.* (2011). "P-Xylene-Selective Metal-Organic Frameworks: A Case of Topology-Directed Selectivity." *Journal of the American Chemical Society* **133** (46) 18526-18529

Walton, K. S. and Snurr, R. Q. (2007). "Applicability of the Bet Method for Determining Surface Areas of Microporous Metal-Organic Frameworks." *Journal of the American Chemical Society* **129** (27) 8552-8556

Walton, R. I. and Munn, A. S., (2013), *Personal Communication*

Wang, M. S., *et al.* (2009). "A Direct White-Light-Emitting Metal-Organic Framework with Tunable Yellow-to-White Photoluminescence by Variation of Excitation Light." *Journal of the American Chemical Society* **131** (38) 13572-+

Weissermel, K. and Arpe, H.-J. (2007). "Aromatics — Production and Conversion" in *Industrial Organic Chemistry*. Wiley-VCH Verlag GmbH Ch.

Wilmer, C. E., *et al.* (2012a). "An Extended Charge Equilibration Method." *The Journal of Physical Chemistry Letters* **3** (17) 2506-2511

Wilmer, C. E., *et al.* (2012b). "Large-Scale Screening of Hypothetical Metal-Organic Frameworks." *Nature Chemistry* **4** (2) 83-89

Wolf, D., *et al.* (1999). "Exact Method for the Simulation of Coulombic Systems by Spherically Truncated, Pairwise R(-1) Summation." *Journal of Chemical Physics* **110** (17) 8254-8282

Wood, P. (2013). "Highly Holey: Mofs with Record-Breaking Surface Areas." Retrieved 20/06/2014, from http://www.ccdc.cam.ac.uk/Community/Blog/pages/BlogPost.aspx?bpid=21.

Wu, H., *et al.* (2013). "Unusual and Highly Tunable Missing-Linker Defects in Zirconium Metal–Organic Framework Uio-66 and Their Important Effects on Gas Adsorption." *Journal of the American Chemical Society* **135** (28) 10525-10532

Xie, S.-M., *et al.* (2011). "Chiral Metal-Organic Frameworks for High-Resolution Gas Chromatographic Separations." *Journal of the American Chemical Society* **133** (31) 11892-11895

Xu, L. R., *et al.* (2012). "Olefins-Selective Asymmetric Carbon Molecular Sieve Hollow Fiber Membranes for Hybrid Membrane-Distillation Processes for Olefin/Paraffin Separations." *Journal of Membrane Science* **423** 314-323

Yaghi, O. M., *et al.* (1995). "Selective Binding and Removal of Guests in a Microporous Metal-Organic Framework." *Nature* **378** (6558) 703-706

Yaghi, O. M. and Li, H. L. (1995). "Hydrothermal Synthesis of a Metal-Organic Framework Containing Large Rectangular Channels." *Journal of the American Chemical Society* **117** (41) 10401-10402

Yaghi, O. M., *et al.* (2003). "Reticular Synthesis and the Design of New Materials." *Nature* **423** (6941) 705-714

Yang, Q., *et al.* (2011a). "Probing the Dynamics of Co2 and Ch4 within the Porous Zirconium Terephthalate Uio-66(Zr): A Synergic Combination of Neutron Scattering Measurements and Molecular Simulations." *Chemistry-a European Journal* **17** (32) 8882-8889

Yang, Q., *et al.* (2013). "Development of Computational Methodologies for Metal–Organic Frameworks and Their Application in Gas Separations." *Chemical Reviews*

Yang, Q. and Maurin, G., (2010), *Personal Communication*

Yang, Q., *et al.* (2008). "Computational Study of Co2 Storage in Metal-Organic Frameworks." *Journal of Physical Chemistry C* **112** (5) 1562-1569

Yang, Q. Y., *et al.* (2011b). "Understanding the Thermodynamic and Kinetic Behavior of the Co2/Ch4 Gas Mixture within the Porous Zirconium Terephthalate Uio-66(Zr): A Joint Experimental and Modeling Approach." *Journal of Physical Chemistry C* **115** (28) 13768-13774

Yang, Q. Y., *et al.* (2011c). "Functionalizing Porous Zirconium Terephthalate Uio-66(Zr) for Natural Gas Upgrading: A Computational Exploration." *Chemical Communications* **47** (34) 9603-9605

Yang, R. T. (1997). *Gas Separation by Adsorption Processes*, Imperial College Press, Stoneham, USA.

Yang, R. T. and Kikkinides, E. S. (1995). "New Sorbents for Olefin Paraffin Separations by Adsorption Via Pi-Complexation." *Aiche Journal* **41** (3) 509-517

Yazaydin, A. O., *et al.* (2009). "Screening of Metal-Organic Frameworks for Carbon Dioxide Capture from Flue Gas Using a Combined Experimental and Modeling Approach." *Journal of the American Chemical Society* **131** (51) 18198-+

Yoon, J. W., *et al.* (2010). "Controlled Reducibility of a Metal-Organic Framework with Coordinatively Unsaturated Sites for Preferential Gas Sorption." *Angewandte Chemie-International Edition* **49** (34) 5949-5952

Zhu, W., *et al.* (2000). "Shape Selectivity in Adsorption on the All-Silica Dd3r." *Langmuir* **16** (7) 3322-3329

Zimmermann, H. (2011). "Propene" in *Ullmann's Encyclopedia of Industrial Chemistry*. B. Elvers and G. Bellussi, Wiley-VCH Verlag GmbH & Co. KGaA Ch.

Zwillinger, D. (2002). *Crc Standard Mathematical Tables and Formulae, 31st Edition*, Taylor & Francis, Boca Raton, USA.

Appendix A: MOFs Studied in the Present Work

Table A.1 - Common name, composition and dimensionality of the pore system for the 21 MOFs investigated in this work. The references given refer to published synthesis routes, with the exception Co-DPNO, whose structure has yet to be published.

MOF	Metal	Linker	Pore Network	Reference
CAU-1(NH_2)	Al	2-amino-terephthalate	3D	(Ahnfeldt *et al.*, 2009)
CAU-1(NHMe)	Al	2-methylamino-terephthalate	3D	(Ahnfeldt *et al.*, 2009)
CAU-8	Al	4,4'-benzophenone dicarboxylate	1D	(Reinsch *et al.*, 2013a)
CAU-10	Al	isophthalate	1D	(Reinsch *et al.*, 2013b)
Co-DPNO	Co	terephthalate + 2,2'-dipyridyl-N-oxide	2D	(Walton and Munn, 2013)
IRMOF-1	Zn	benzene dicarboxylate	3D	(Eddaoudi *et al.*, 2002)
IRMOF-3	Zn	2-amino-terephthalate	3D	(Eddaoudi *et al.*, 2002)
IRMOF-7	Zn	1,4-napthalene dicarboxylate	3D	(Eddaoudi *et al.*, 2002)
IRMOF-10	Zn	4,4'-biphenyl dicarboxylate	3D	(Eddaoudi *et al.*, 2002)
IRMOF-14	Zn	2,7-pyrene dicarboxylate	3D	(Eddaoudi *et al.*, 2002)
MIL-47	V	benzene dicarboxylate	1D	(Barthelet *et al.*, 2002)
MIL-68	V	benzene dicarboxylate	1D	(Barthelet *et al.*, 2004)
MIL-125	Ti	benzene dicarboxylate	3D	(Dan-Hardi *et al.*, 2009)

MOF	Metal	Linker	Pore Network	Reference
MIL-125(NH_2)	Ti	2-amino-terephthalate	3D	(Dan-Hardi *et al.*, 2009)
MIL-140B	Zr	2,6-napthalenedicarboxylate	1D	(Guillerm et al., 2012)
MIL-140C	Zr	4,4'-biphenyl dicarboxylate	1D	(Guillerm *et al.*, 2012)
MIL-140D	Zr	4,4'-azobenzenedicarboxylate	1D	(Guillerm et al., 2012)
UiO-66	Zr	benzene dicarboxylate	3D	(Cavka et al., 2008)
UiO-66(Br)	Zr	2-bromo-terephthalate	3D	(Biswas and Van Der Voort, 2013)
UiO-66(NH_2)	Zr	2-amino-terephthalate	3D	(Biswas and Van Der Voort, 2013)
UiO-66(NO_2)	Zr	2-nitro-terephthalate	3D	(Biswas and Van Der Voort, 2013)

Appendix B: Force Field Parameters Used to Describe Flexible UiO-66(Zr)

All force field parameters were taken from the work of Yang et al (2011a; 2011b) and the reader is directed towards these papers for discussion of the development and parameterisation of the force field. The non-bonded LJ parameters are listed in 0.

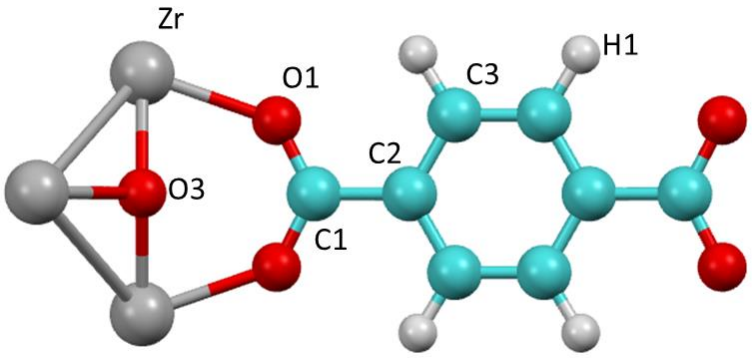

Figure B.1 – Assignment of atomic types used in the force field parameters for flexible UiO-66(Zr). Colour scheme: C – cyan; H – white; O – red; Zr: grey.

Table B.1 – Partial charges used in this force field. The same partial charges were used in simulations of rigid de-hydroxylated UiO-66(Zr).

Atomic Type	Zr	C1	C2	C3	O1	O3	H1
Charge (e)	+1.968	+0.630	-0.082	-0.065	-0.586	-0.992	+0.133

Table B.2 – Bonded parameters used to constrain the movement of framework atoms in simulations of flexible UiO-66(Zr).

Interacting Atoms	**Bond Stretching**	
	L_{eq} (Å)	**k_L (kJ mol^{-1} Å^2)**
Zr-O3	2.098	1077.338
Zr-O1	2.232	2872.902
C1-O1	1.273	4518.720
C1-C2	1.487	2939.283

C2-C3	1.393	4016.641
C3-C3	1.393	4016.640
C3-H1	1.080	3041.068
Interacting Atoms	**Bond Bending**	
	θ_{eq} (º)	**k_θ (kJ mol^{-1} rad^2)**
O3-Zr-O3	71.1	115.776
O3-Zr-O3	700.4	115.776
O1-Zr-O1	76.0	115.776
O1-Zr-O1	81.9	115.776
O1-Zr-O1	69.8	115.776
O1-Zr-O1	74.4	115.776
O1-Zr-O3	85.7	115.776
O1-Zr-O3	124.3	115.776
O1-Zr-O3	127.6	115.776
O1-Zr-O3	143.5	115.776
O1-Zr-O3	150.5	115.776
Zr-O1-C1	135.8	231.637
O1-C1-O1	125.0	1213.360
O1-C1-C2	117.3	456.013
C1-C2-C3	120.0	290.201
C3-C3-C2	120.0	753.120
C2-C3-C3	1200	53.120
C2-C3-H1	120.0	309.616
C3-C3-H1	120.0	309.616
Interacting Atoms	**Torsions**	
	φ_{eq} (º)	**k_φ (kJ mol^{-1})**
Zr-O1-C1-C2	180.0	86.837
O1-C1-C2-C3	180.0	10.460
C1-C2-C3-C3	180.0	12.552
C1-C2-C3-H1	180.0	12.552
C2-C3-C3-H1	180.0	12.552

C3-C3-C2-C3	180.0	12.552
H1-C3-C2-C3	180.0	12.552
H1-C3-C3-H1	180.0	12.552
Interacting Atoms	**Improper Torsions**	
	θ_{eq} (º)	**k_θ (kJ mol^{-1})**
C2-C1-O1-O1	180.0	41.840
C1-C2-C3-C3	180.0	41.840
C2-C3-C3-H1	180.0	1.548

Appendix C: Framework Atom van der Waals Parameters

Table C.1 – van der Waals parameters used to describe MOF atoms in this work. Parameters are taken from either the UFF (Rappe *et al.*, 1992) or DREIDING force fields (Mayo *et al.*, 1990), as indicated.

Element	σ (Å)	ε/k_B (K)	Source
Aluminium	3.91	156.00	DREIDING
Cobalt	2.56	7.05	UFF
Titanium	2.83	8.55	UFF
Vanadium	3.53	7.05	UFF
Zinc	2.46	62.40	UFF
Zirconium	2.78	34.72	UFF
Bromine	3.52	186.19	DREIDING
Carbon	3.47	47.86	DREIDING
Fluorine	3.09	36.48	DREIDING
Hydrogen	2.85	7.65	DREIDING
Nitrogen	3.26	38.95	DREIDING
Oxygen	3.03	48.19	DREIDING

Appendix D: Sources of MOF Partial Charges

Table D.1 – Sources of partial charges for each of the MOFs studied in this work

MOF	Calculation Method	Reference
CAU-1(NH_2)	EQeq	-
CAU-1(NHMe)	EQeq	-
CAU-8	EQeq	-
CAU-10	EQeq	-
Co-DPNO	EQeq	-
IRMOF-1	DFT (Literature)	(Farrusseng *et al.*, 2009)
IRMOF-3	DFT (Literature)	(Yang *et al.*, 2008)
IRMOF-7	DFT (Literature)	(Yang *et al.*, 2008)
IRMOF-10	DFT (Literature)	(Yang *et al.*, 2008)
IRMOF-14	DFT (Literature)	(Yang *et al.*, 2008)
MIL-47	DFT (Literature)	(Yazaydin *et al.*, 2009)
MIL-68	EQeq	-
MIL-125	DFT(Project Partner)	(Yang and Maurin, 2010)
MIL-125(NH_2)	DFT(Project Partner)	(Yang and Maurin, 2010)
MIL-140B	EQeq	-
MIL-140C	EQeq	-
MIL-140D	EQeq	-
UiO-66 (hydroxylated)	DFT (Project Partner)	(Yang and Maurin, 2010)
UiO-66 (de-hydroxylated)	DFT (Literature)	(Yang *et al.*, 2011c)
UiO-66(Br)	DFT (Literature)	(Yang *et al.*, 2011c)
UiO-66(NH_2)	DFT (Literature)	(Yang *et al.*, 2011c)
UiO-66(NO_2)	DFT (Literature)	(Yang *et al.*, 2011c)

Appendix E: MOF Structural Characteristics

Table E.1 – Computationally-determined structural characteristics – nitrogen accessible surface area (SA_{acc}), helium pore volume at 298 K (PV_{He}) and PSD-determined pore diameters – of the MOFs in this work.

MOF	SA_{acc} (m^2/g)	PV_{He} (cm^3/g)	Pore Diameters (Å)
CAU-1(NH_2)	975	0.50	3.9, 9.7
CAU-1(NHMe)	787	0.40	8.86
CAU-8	977	0.52	6.5
CAU-10	300	0.30	5.7
Co-DPNO	525	0.28	6.7
IRMOF-1	3280	1.39	11.1, 14.3
IRMOF-3	3057	1.28	9.5, 14.3
IRMOF-7	2568	1.06	10.0
IRMOF-10	4840	2.72	16.8, 20.0
IRMOF-14	4749	2.39	14.9, 20.1
MIL-47	1503	0.40	7.4
MIL-68	1442	0.60	13.7
MIL-125	1939	0.70	5.5, 11.8
MIL-125(NH_2)	1581	0.60	4.2, 10.5
MIL-140B	731	0.46	4.2
MIL-140C	659	0.37	5.9
MIL-140D	711	0.63	6.6
UiO-66	859	0.40	7.0, 7.7
UiO-66(Br)	687	0.26	6.4, 7.3
UiO-66(NH_2)	529	0.30	6.0, 6.8
UiO-66(NO_2)	399	0.28	5.5, 6.5, 6.9

Appendix F: Pressure Dependence of Propylene-MOF Electrostatic Interactions in 1D MOFs

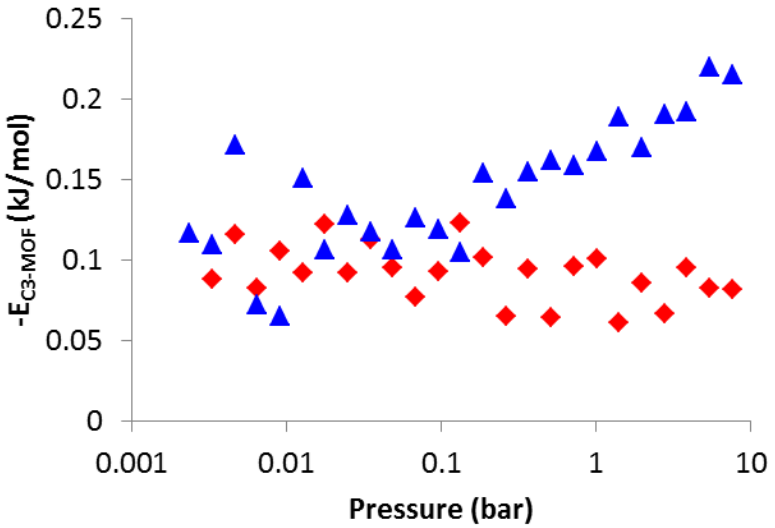

Figure F.1 – Average propylene-MOF electrostatic interaction as a function of pressure in MIL-140B (red) and MIL-140D (blue).

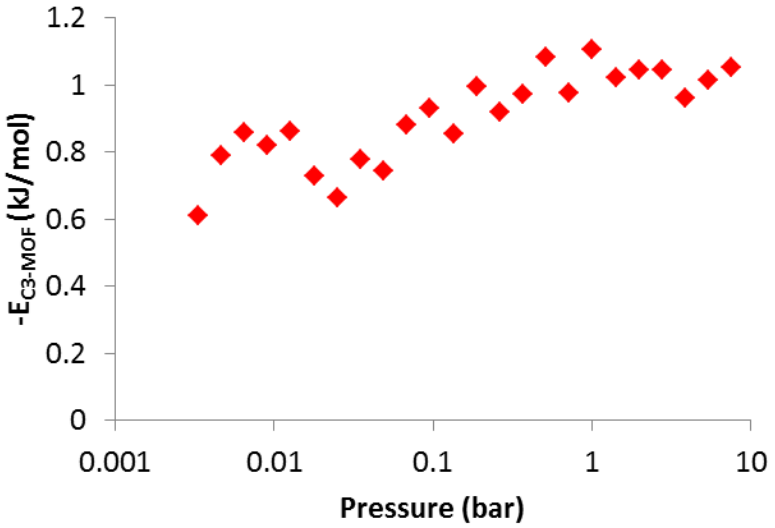

Figure F.2 - Average propylene-MOF electrostatic interaction as a function of pressure in MIL-47(V).

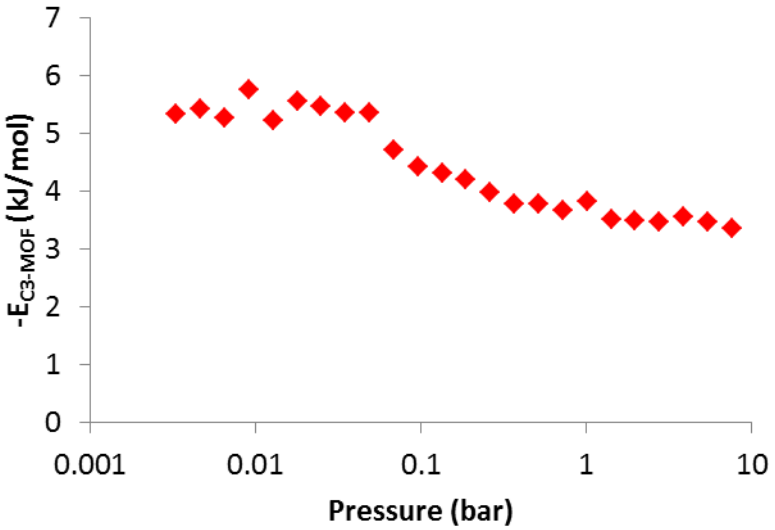

Figure F.3 – Average propylene-MOF electrostatic interaction as a function of pressure in MIL-68(V).

Appendix G: Effect of Mixture Composition on Propylene Selectivity

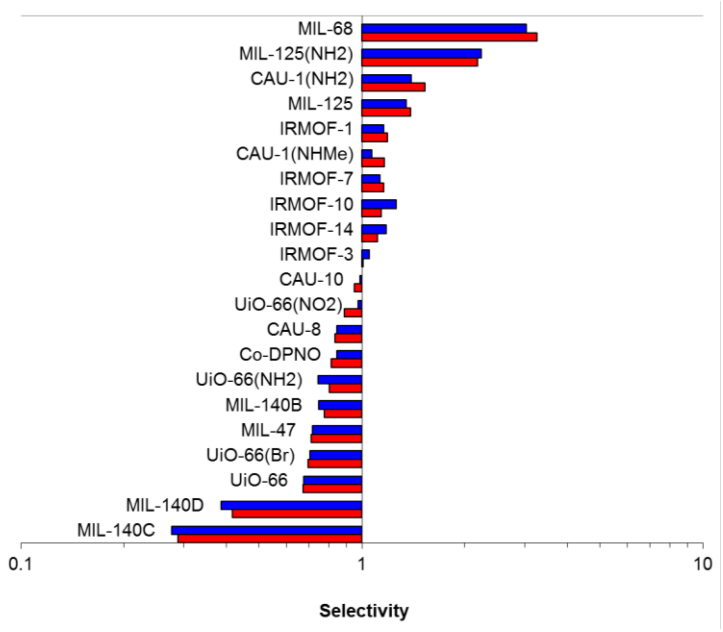

Figure G.1 - Selectivity towards propylene at low pressure for adsorption from an equimolar (red) and propylene-rich (0.7 mol fraction propylene; blue) binary mixture.

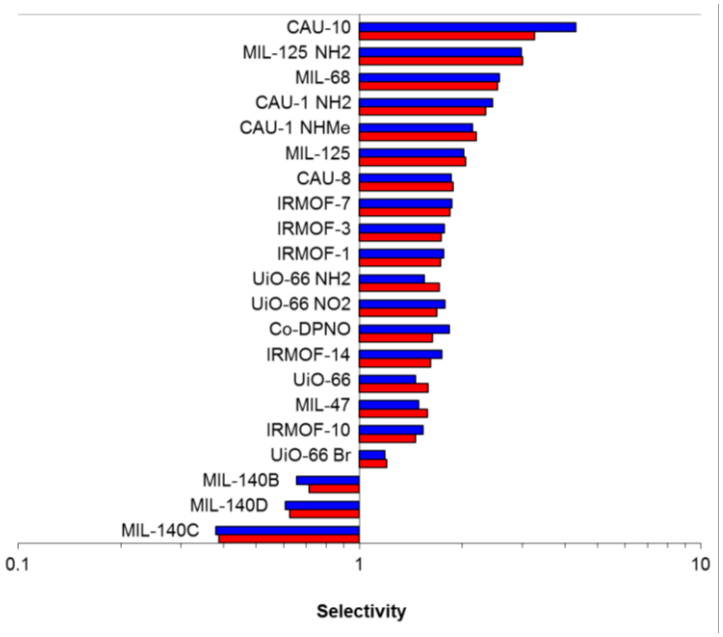

Figure G.2 – Selectivity towards propylene at high pressure for adsorption from an equimolar (red) and propylene-rich (0.7 mol fraction propylene; blue) binary mixture.

Appendix H: C_3 Single-Component Isotherms

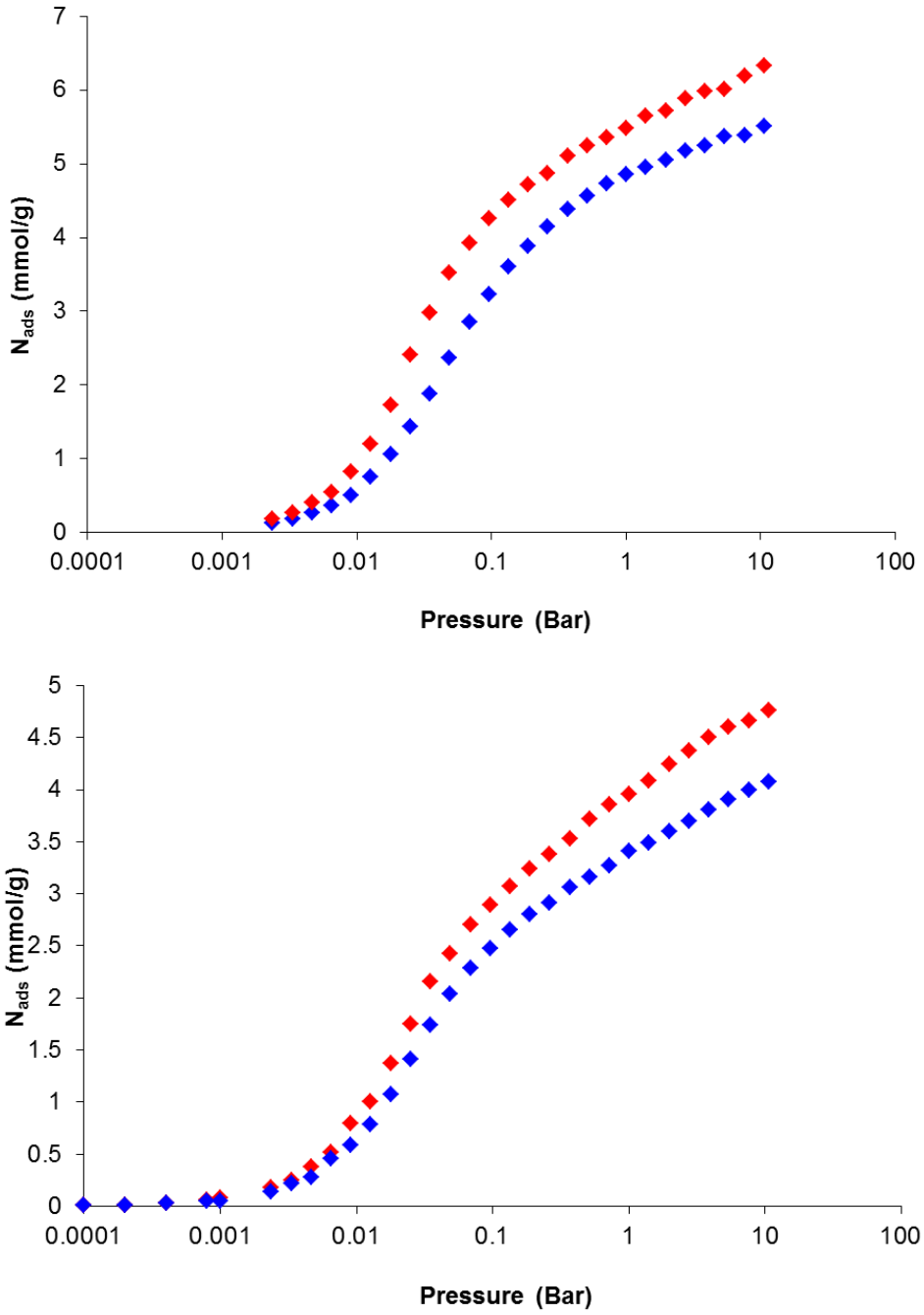

Figure H.1 – Simulated single component adsorption isotherms for propane (blue) and propylene (red) at 303 K in CAU-1(NH_2) (top) and CAU-1(NHMe) (bottom).

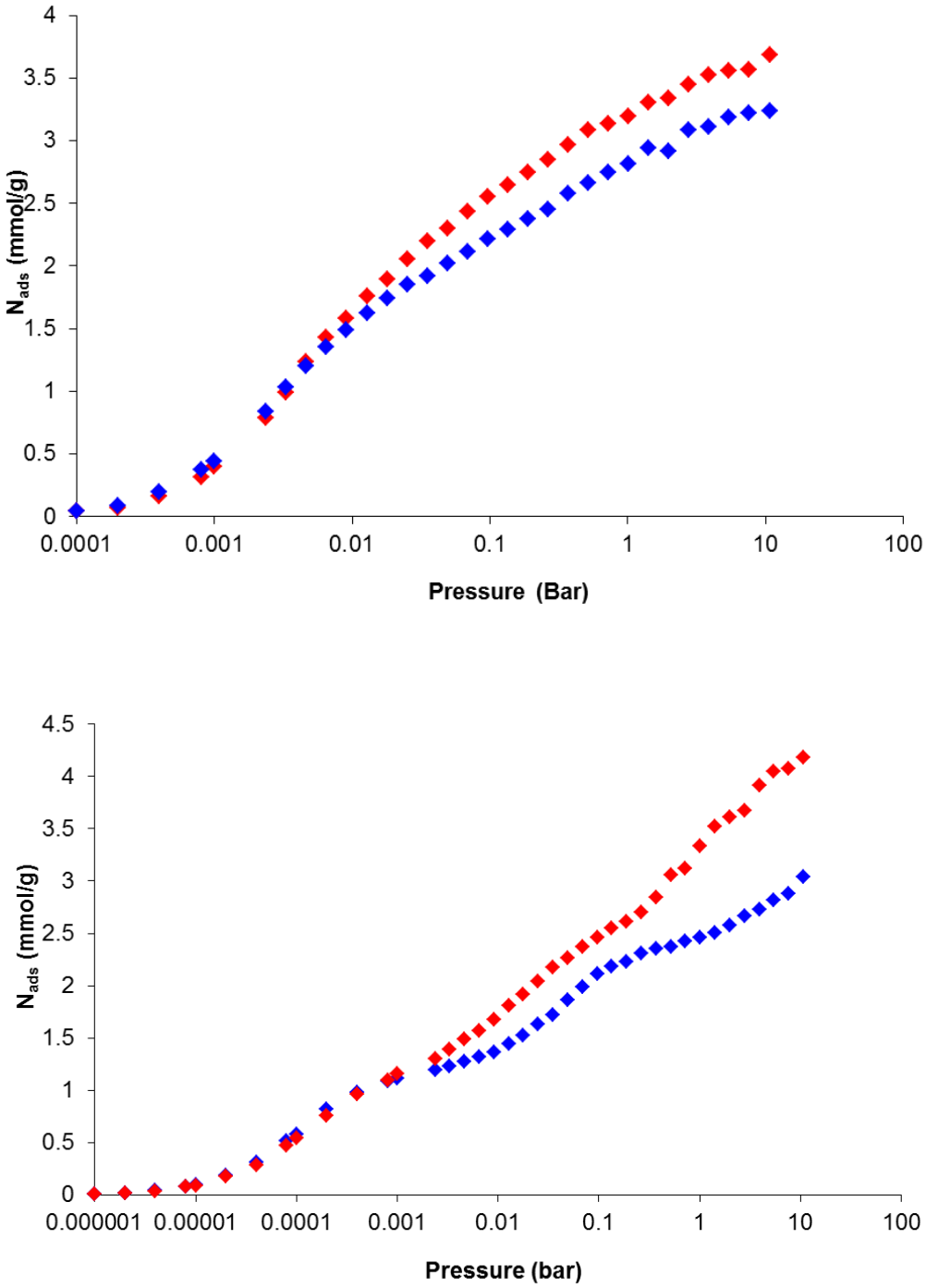

Figure H.2– Simulated single component adsorption isotherms for propane (blue) and propylene (red) at 303 K in CAU-8 (top) and CAU-10 (bottom).

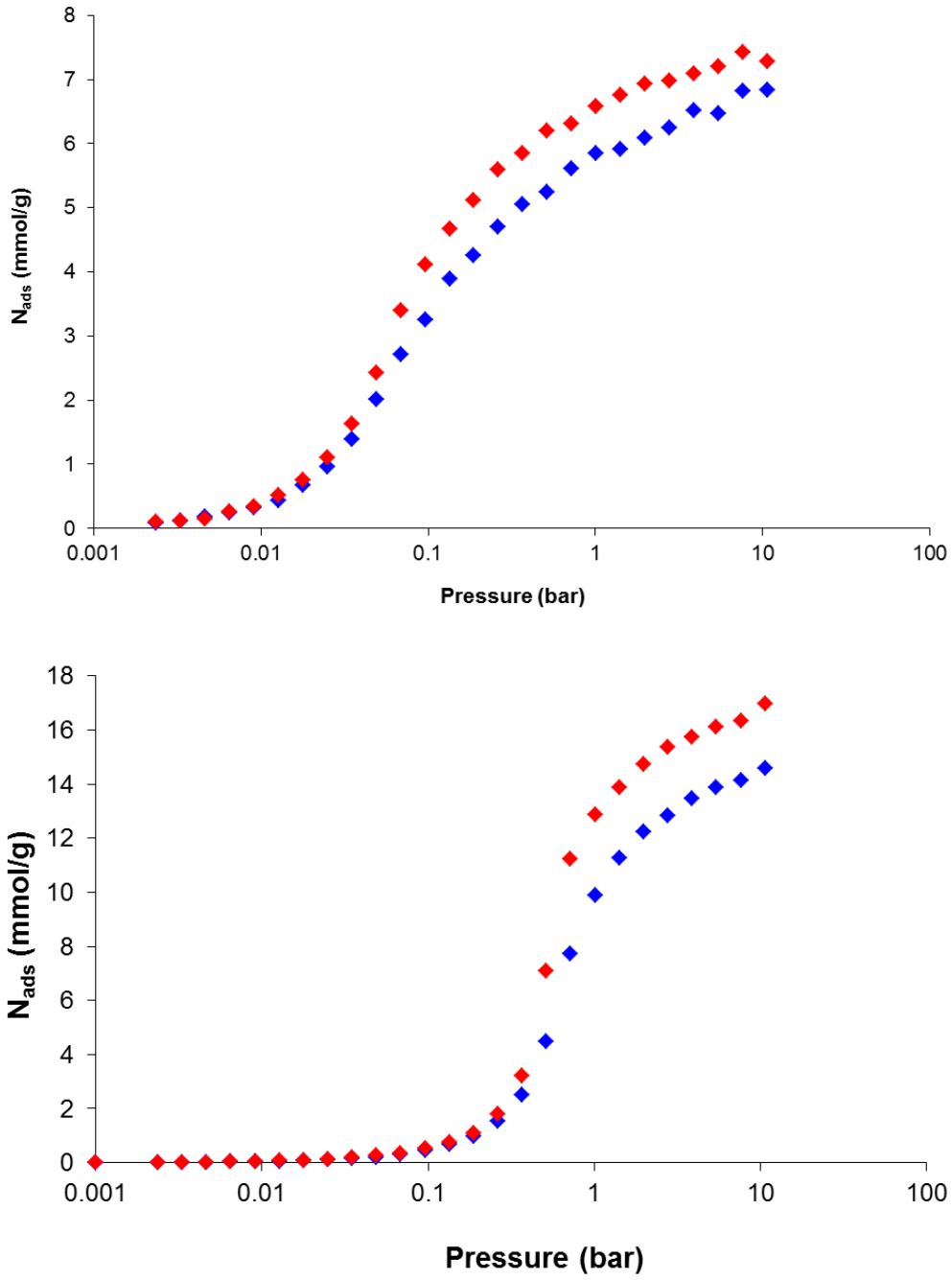

Figure H.3 – Simulated single component adsorption isotherms for propane (blue) and propylene (red) at 303 K in Co-DPNO (top) and IRMOF-1 (bottom).

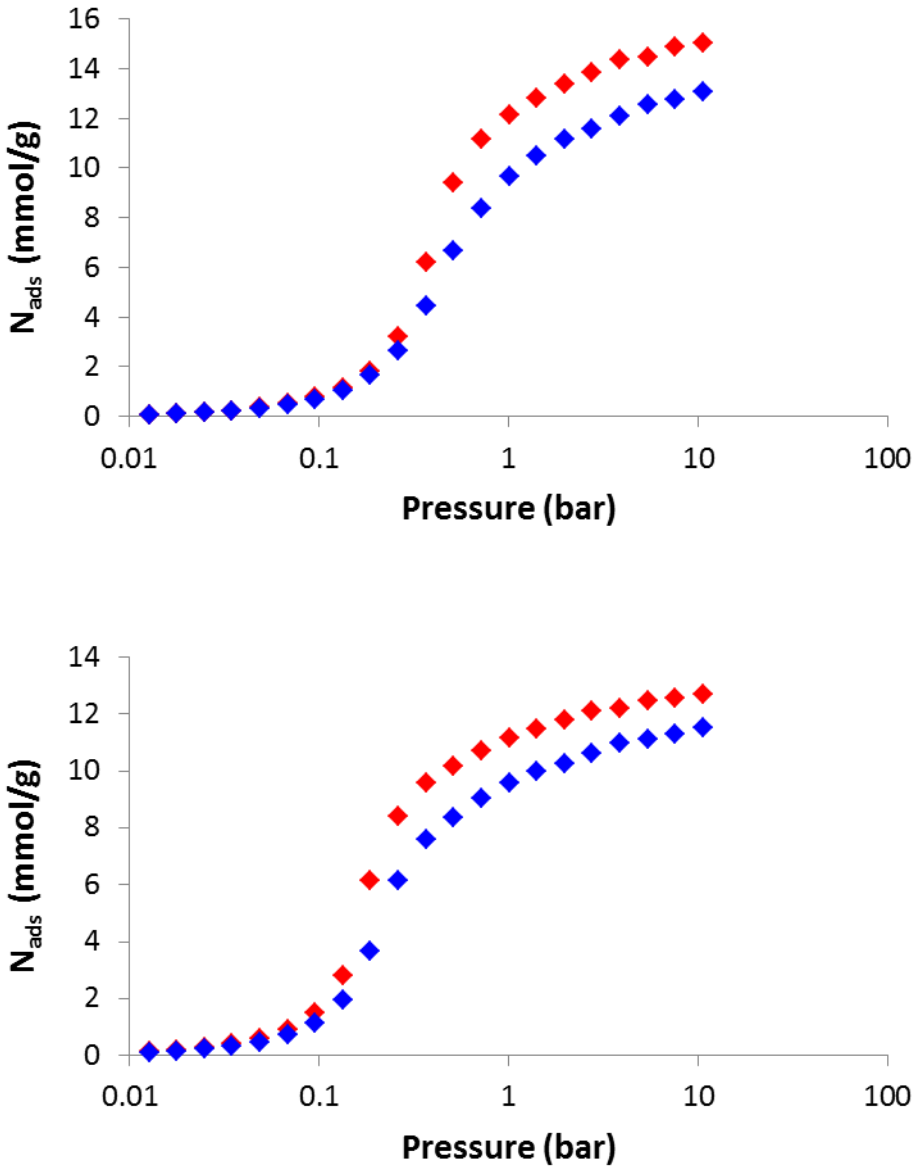

Figure H.4 – Simulated single component adsorption isotherms for propane (blue) and propylene (red) at 303 K in IRMOF-3 (top) and IRMOF-7 (bottom).

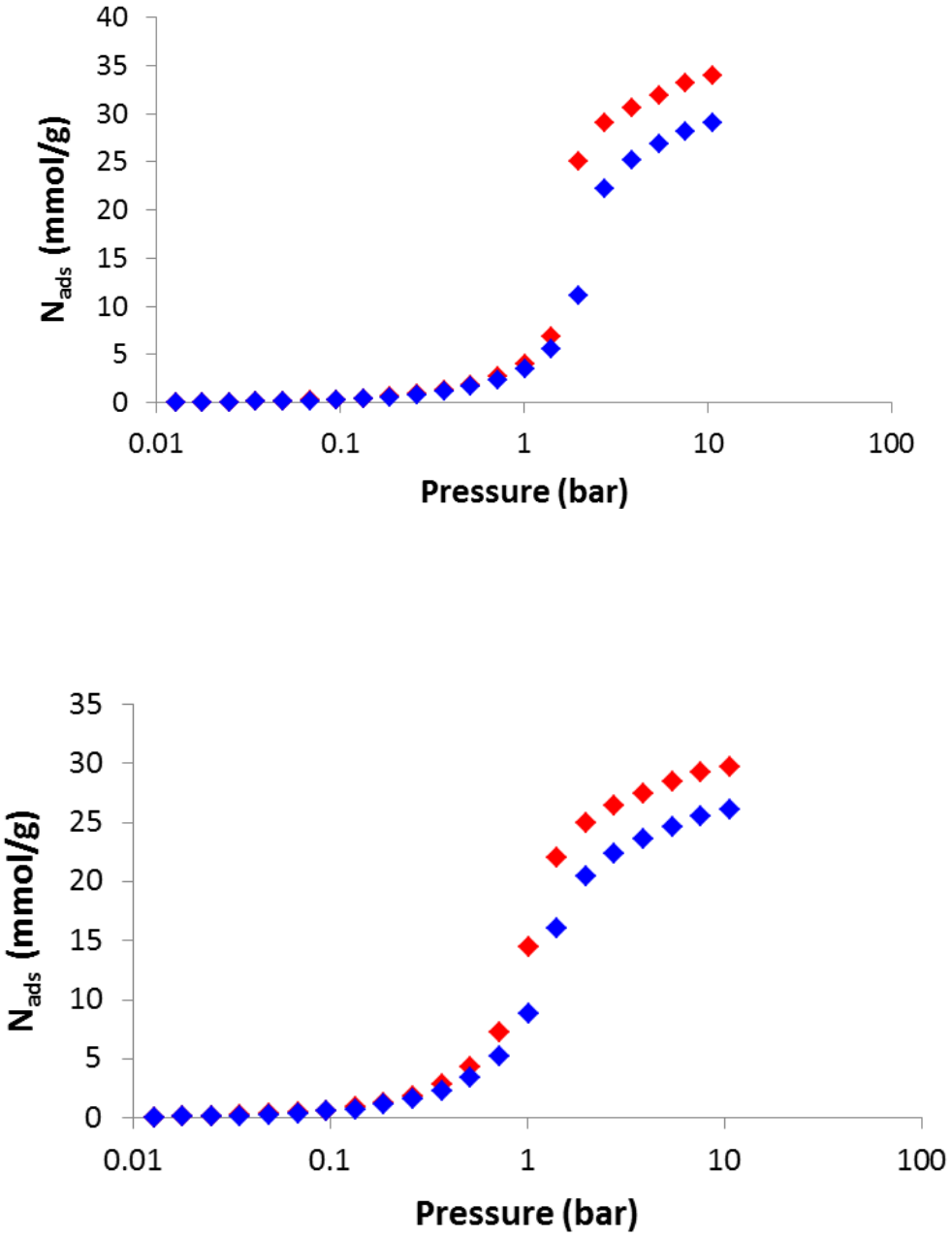

Figure H.5 – Simulated single component adsorption isotherms for propane (blue) and propylene (red) at 303 K in IRMOF-10 (top) and IRMOF-14 (bottom).

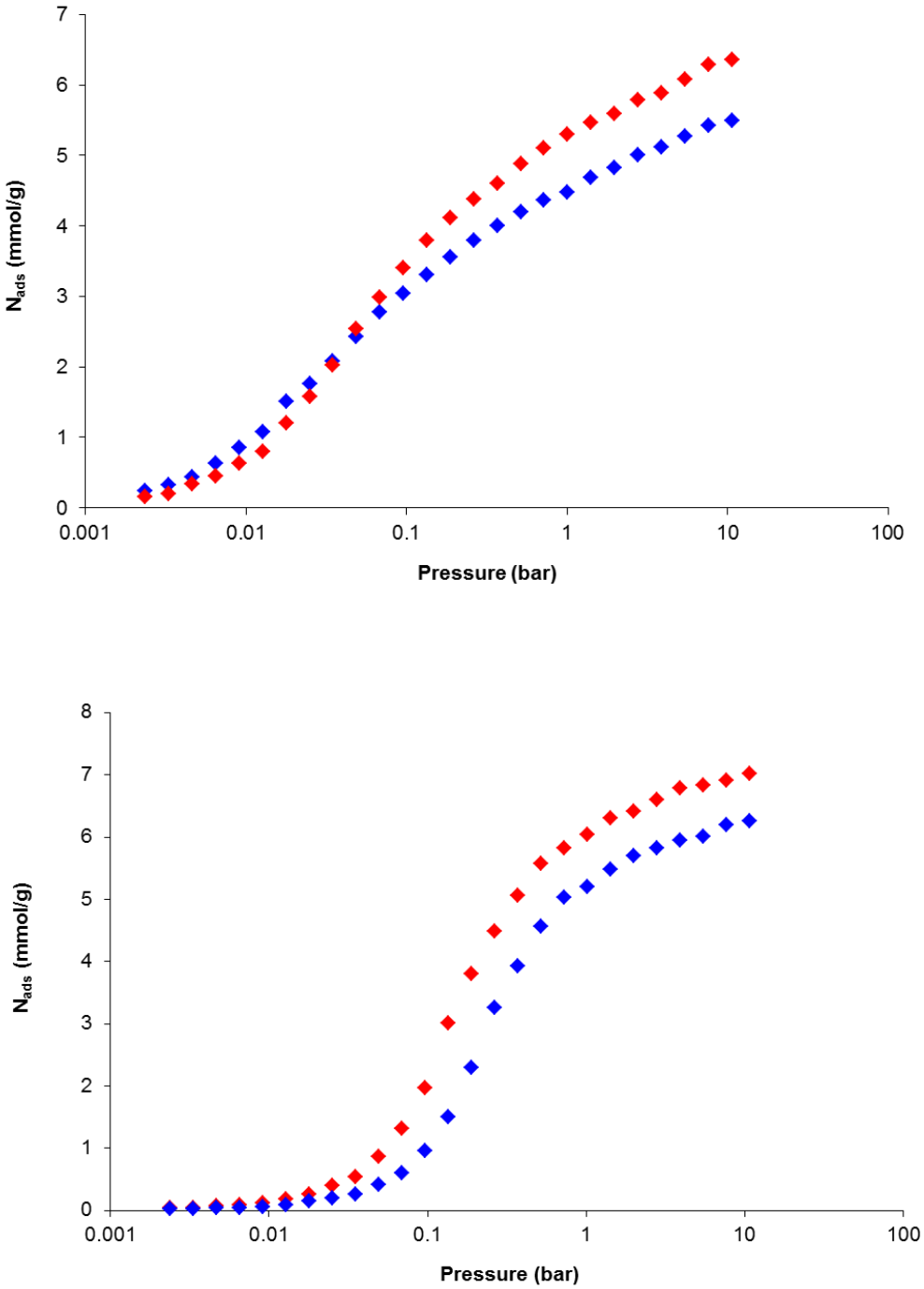

Figure H.6 – Simulated single component adsorption isotherms for propane (blue) and propylene (red) at 303 K in MIL-47 (top) and MIL-68 (bottom).

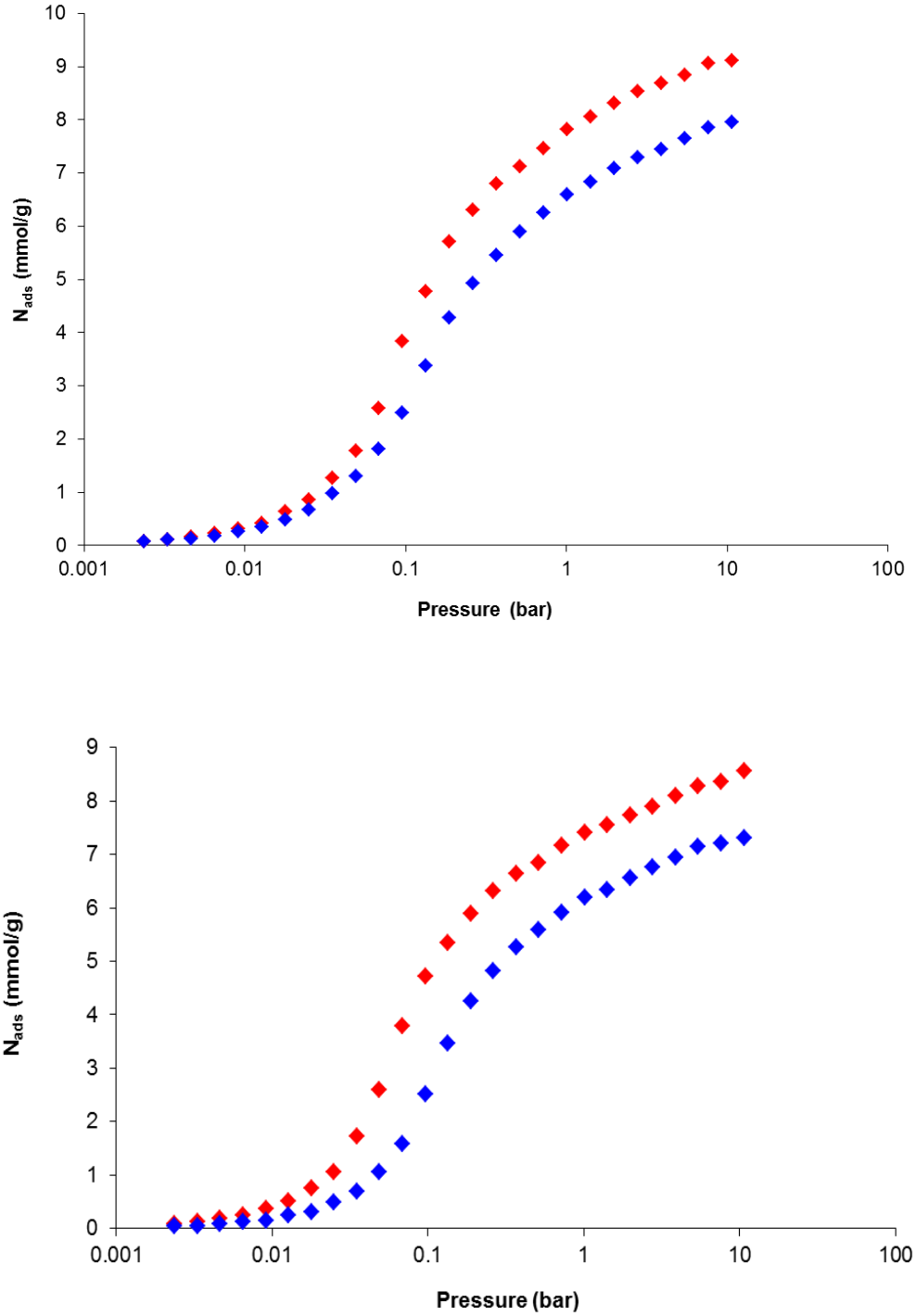

Figure H.7 – Simulated single component adsorption isotherms for propane (blue) and propylene (red) at 303 K in MIL-125 (top) and MIL-125(NH_2) (bottom).

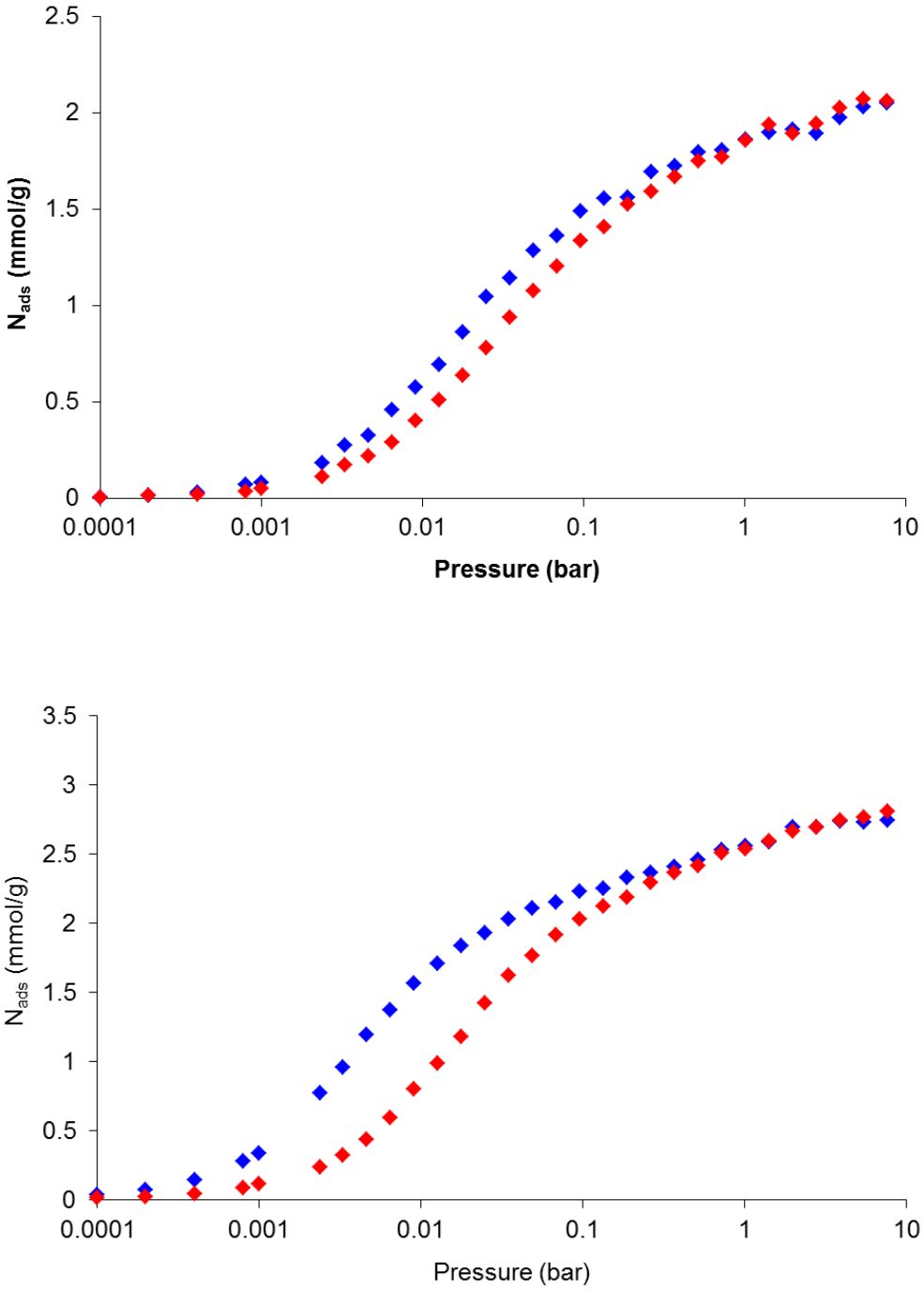

Figure H.8– Simulated single component adsorption isotherms for propane (blue) and propylene (red) at 303 K in MIL-140B (top) and MIL-140C (bottom).

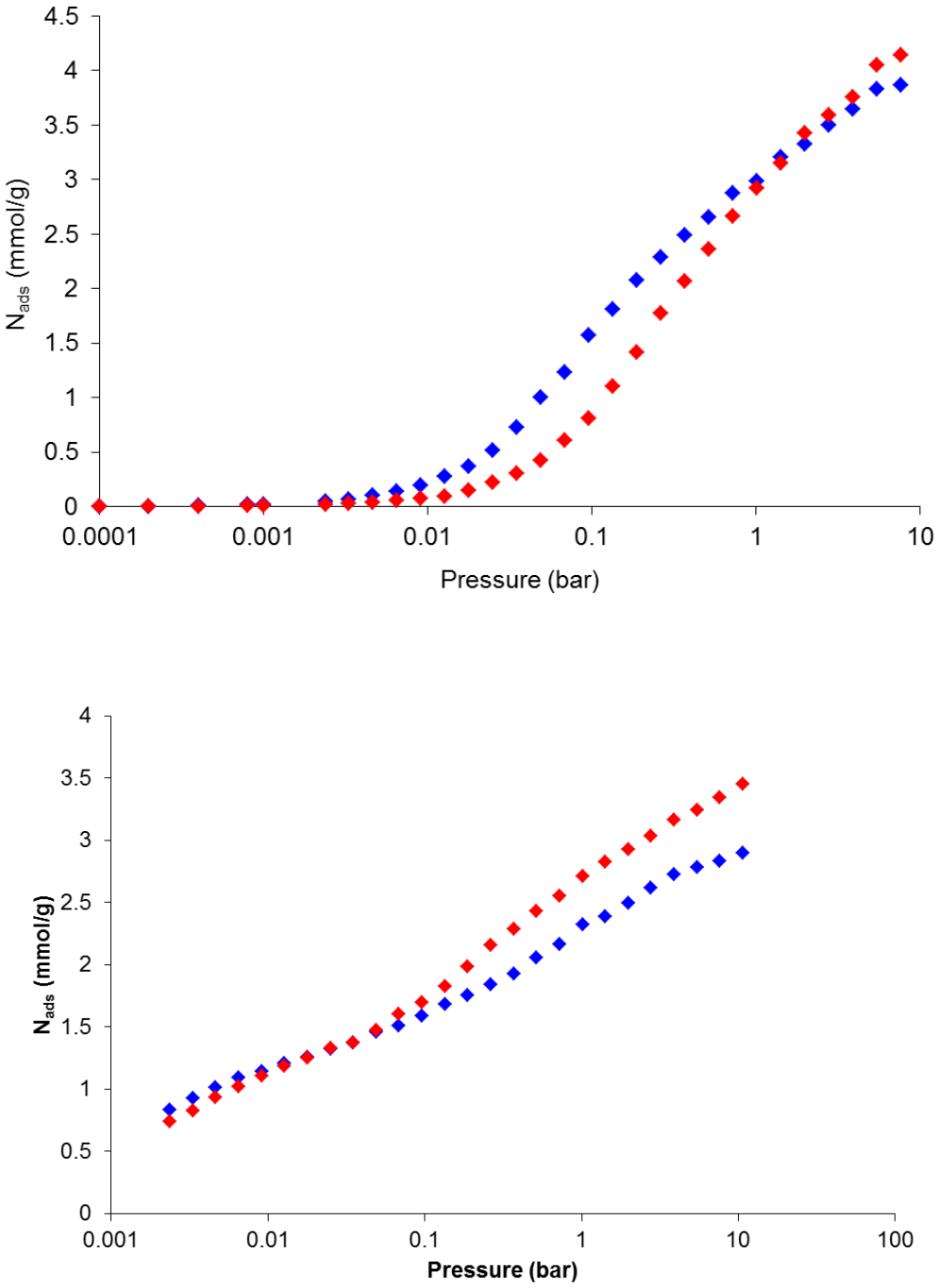

Figure H.9 – Simulated single component adsorption isotherms for propane (blue) and propylene (red) at 303 K in MIL-140D (top) and UiO-66 (bottom).

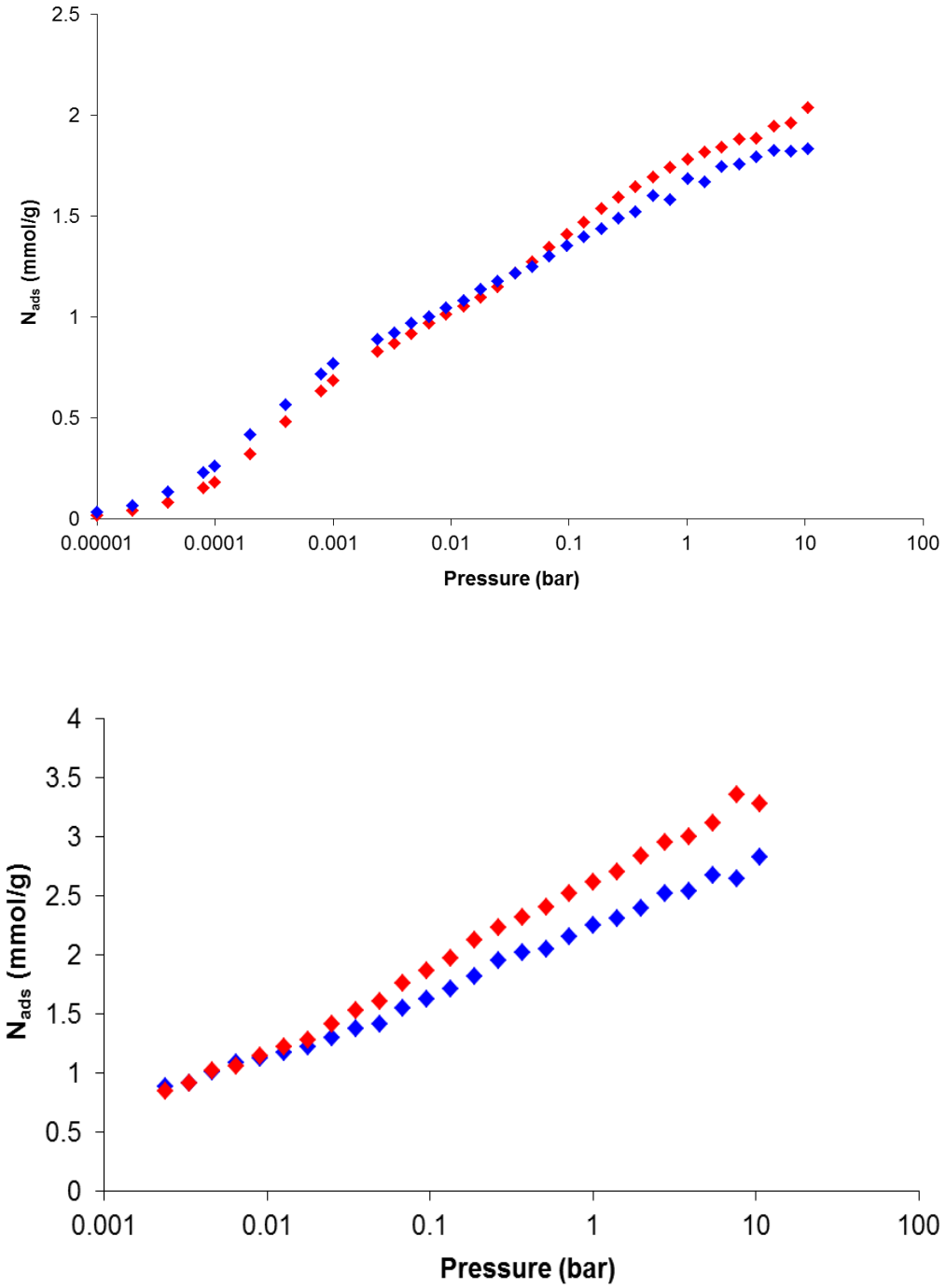

Figure H.10 – Simulated single component adsorption isotherms for propane (blue) and propylene (red) at 303 K in UiO-66(Br) (top) and UiO-66(NH_2) (bottom).

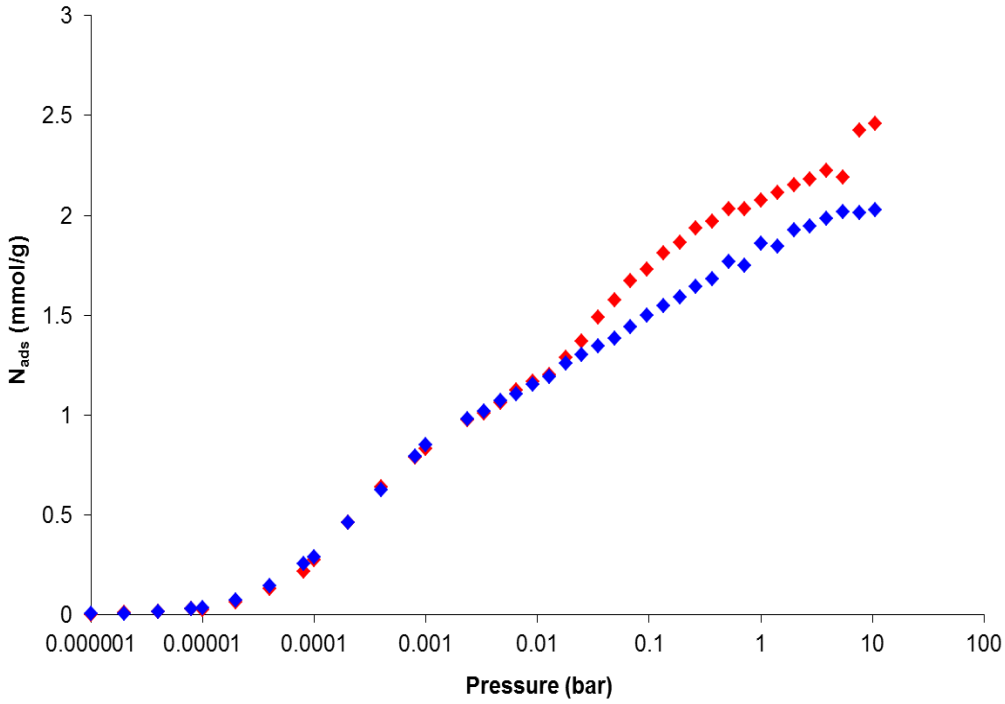

Figure H.11 – Simulated single component adsorption isotherms for propane (blue) and propylene (red) at 303 K in UiO-66(NO_2).

Appendix I: V_d as a Function of Wall Intersection Angle for Rhombic Model Pore Systems

For model pore systems, in which the cross-sectional area of the pore is invariant with distance along the channel length, the fraction of the pore not described by the PSD (V_d) as a function of the wall intersection angle (θ_{wall}) may be determined analytically based on the cross-sectional areas of the circle which describes the PSD diameter and the actual channel cross-sectional area.

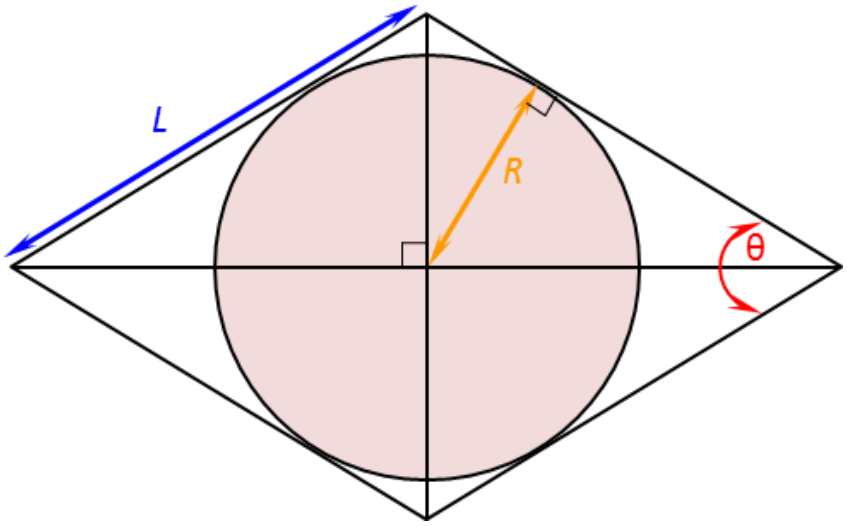

Figure I.1 – Schematic of cross-sectional area of a rhombic model pore with the wall intersection angle (θ_{wall}, red), inradius (R, orange) and edge length (L, blue) indicated. Note that for this simple system, the inradius is equivalent to the channel radius determined from the PSD method of Gelb and Gubbins (1998). The shaded circle thus represents the area of the channel described by the PSD.

The inradius of a rhombus may be calculated from the edge length (L) and the internal angle (θ_{wall}) (Zwillinger, 2002):

$$R = \frac{L}{2}\sin\theta_{wall} \qquad \textbf{Equation I.1}$$

The total cross-sectional area of the pore (A_{pore}) and the area described by the PSD (A_{PSD}) are simply the areas of a rhombus and a circle respectively:

$$A_{pore} = L^2 \sin\theta_{wall} \quad \textbf{Equation I.2}$$

$$A_{PSD} = \frac{\pi L^2}{4}(\sin\theta)^2 \quad \textbf{Equation I.3}$$

The area not described by the PSD is thus:

$$V_d = \frac{A_{pore} - A_{PSD}}{A_{pore}} \quad \textbf{Equation I.4}$$

$$= 1 - \frac{A_{PSD}}{A_{pore}} \quad \textbf{Equation I.5}$$

$$= 1 - \left\{\left[\frac{\pi L^2}{4}(\sin\theta)^2\right] \cdot \left[\frac{1}{L^2 \sin\theta_{wall}}\right]\right\} \quad \textbf{Equation I.6}$$

$$V_d = 1 - \frac{\pi}{4}\sin\theta_{wall} \quad \textbf{Equation I.7}$$

The evolution of with θ_{wall} is shown in Figure 4.4.

Appendix J: Selectivity at 2 kPa for Xylene Adsorption in Model Rhombic Pores

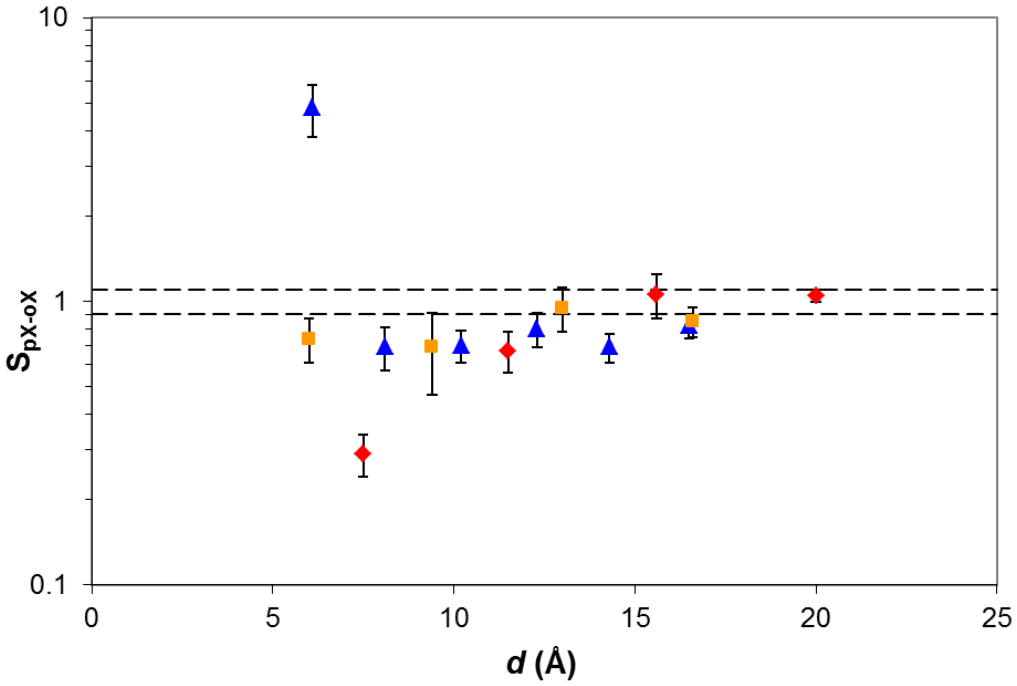

Figure J.1 – Selectivity towards pX for equimolar pX-oX mixture at 2 kPa for rhombic model pores with wall intersection angles of 30° (blue triangles), 60° (orange squares) and 90° (red diamonds) as a function of the PSD channel diameter. Where error bars are not visible, the error is within the symbol size. The dashed lines indicate the non-selective region ($0.9 \leq S_{pX\text{-}oX} \leq 1.1$).

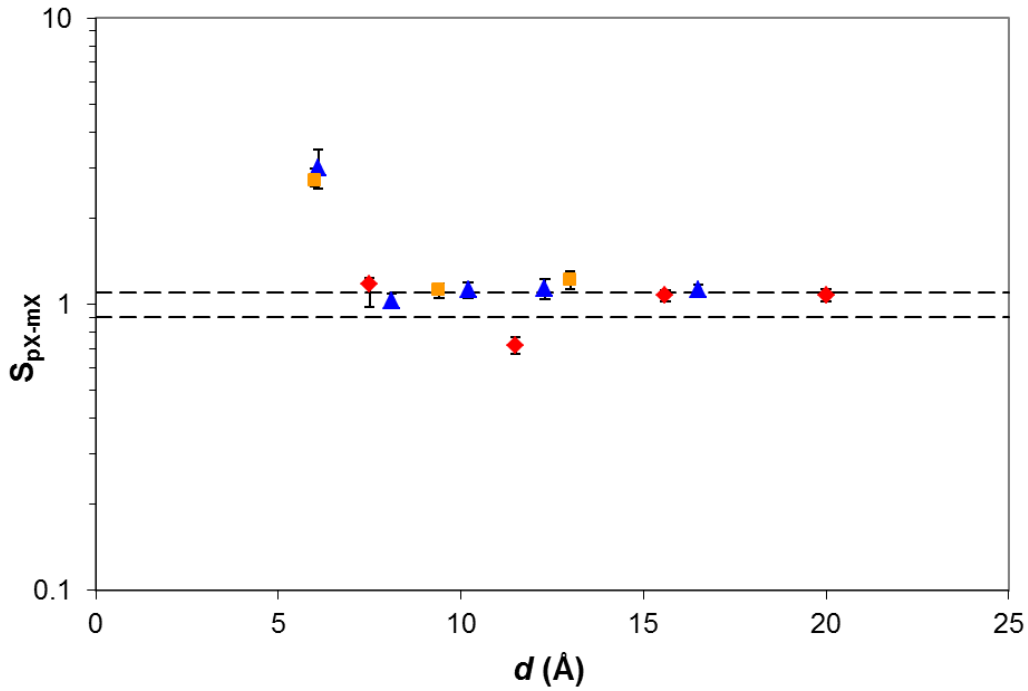

Figure J.2 – Selectivity towards pX for equimolar pX-mX mixture at 2 kPa for rhombic model pores with wall intersection angles of 30° (blue triangles), 60° (orange squares) and 90° (red diamonds) as a function of the PSD channel diameter. Where error bars are not visible, the error is within the symbol size. The dashed lines indicate the non-selective region ($0.9 \leq S_{pX\text{-}mX} \leq 1.1$).

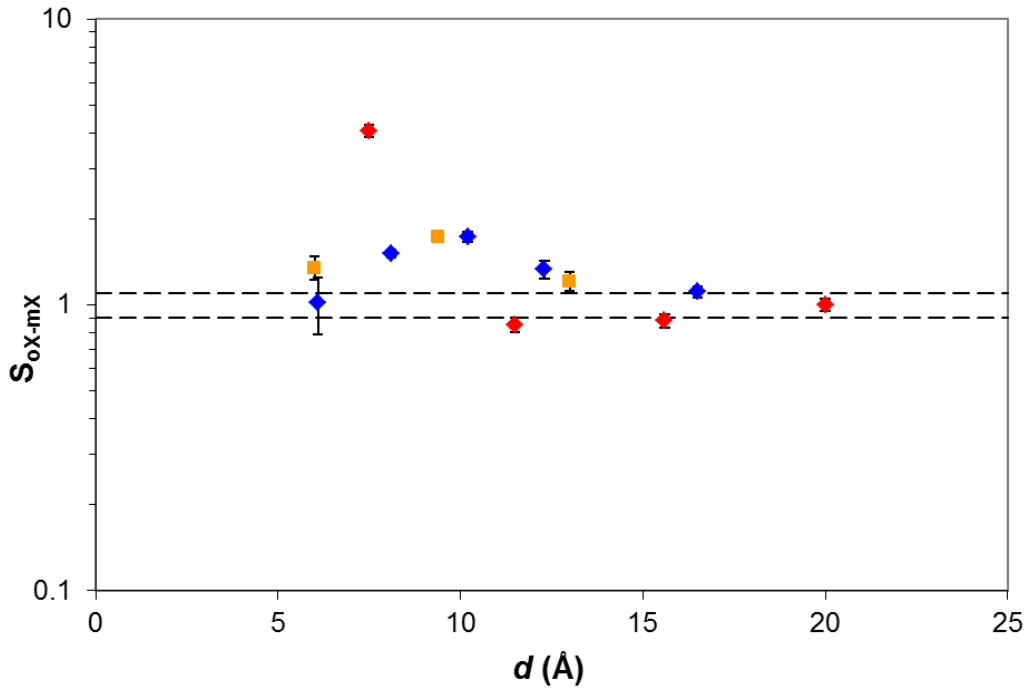

Figure J.3 – Selectivity towards oX for equimolar oX-mX mixture at 2 kPa for rhombic model pores with wall intersection angles of 30° (blue triangles), 60° (orange squares) and 90° (red diamonds) as a function of the PSD channel diameter. Where error bars are not visible, the error is within the symbol size. The dashed lines indicate the non-selective region ($0.9 \leq S_{oX\text{-}mX} \leq 1.1$).

Appendix K: Xylene-Framework and Xylene-Xylene Interactions in Rhombic Model Pores for oX-mX and pX-mX Mixtures

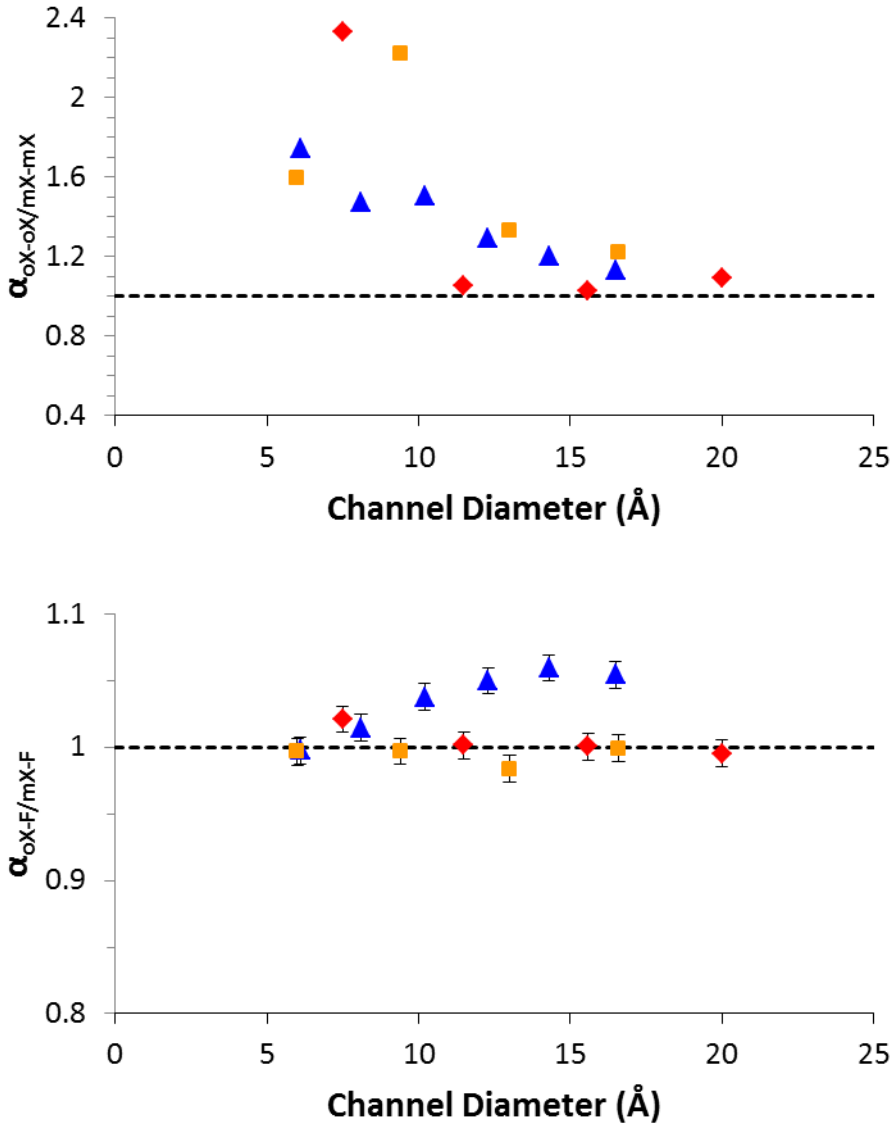

Figure K.1 – Influence of channel diameter on the ratio of oX-oX to mX-mX interaction energies ($\alpha_{oX\text{-}oX/mX\text{-}mX}$) (top) and oX-framework to mX-framework interactions energies ($\alpha_{oX\text{-}F/mX\text{-}F}$) (bottom) for model pore systems with wall intersection angles of 30° (blue triangles), 60° (orange squares) and 90° (red diamonds).

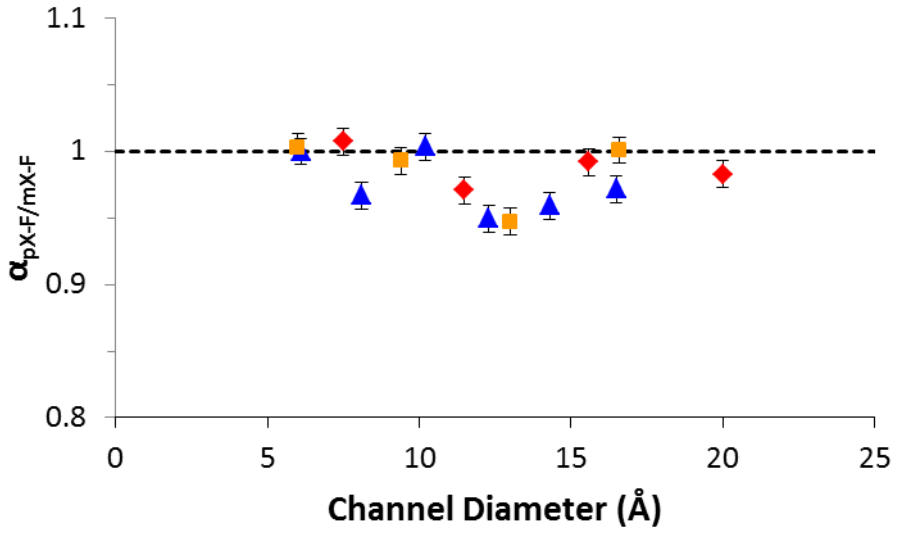

Figure K.2 – Influence of channel diameter on the ratio of pX-framework to mX-framework interaction energies ($\alpha_{pX\text{-}F/mX\text{-}F}$) for model pore systems with wall intersection angles of 30° (blue triangles), 60° (orange squares) and 90° (red diamonds).

Appendix L: Single-Component Xylene Isotherms in the MIL-140 Series

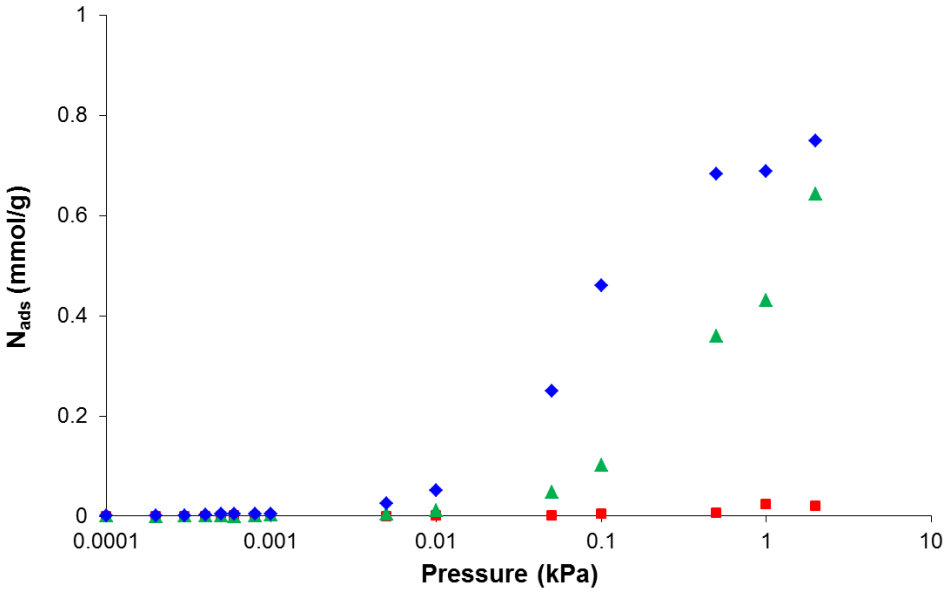

Figure L.1 – Single-component xylene isotherms at 300 K in MIL-140B for pX (blue), mX (green) and oX (red).

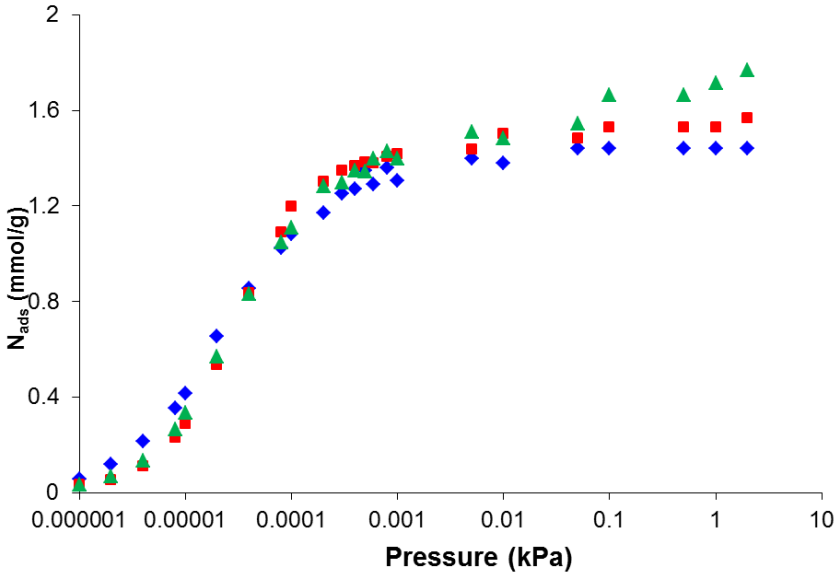

Figure L.2 – Single-component xylene isotherms at 300 K in MIL-140C for pX (blue), mX (green) and oX (red).

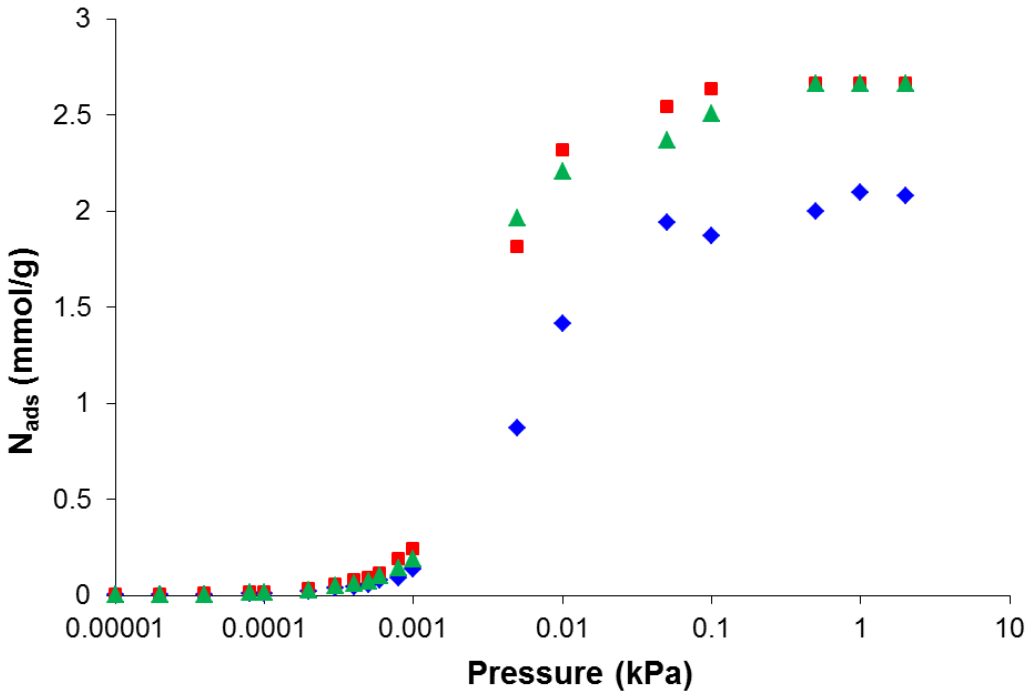

Figure L.3– Single-component xylene isotherms at 300 K in MIL-140D for pX (blue), mX (green) and oX (red).

Appendix M: Xylene-Framework Interaction Energies in the Intermediate Tetrahedral Pore of Hydroxylated UiO-66(Zr)

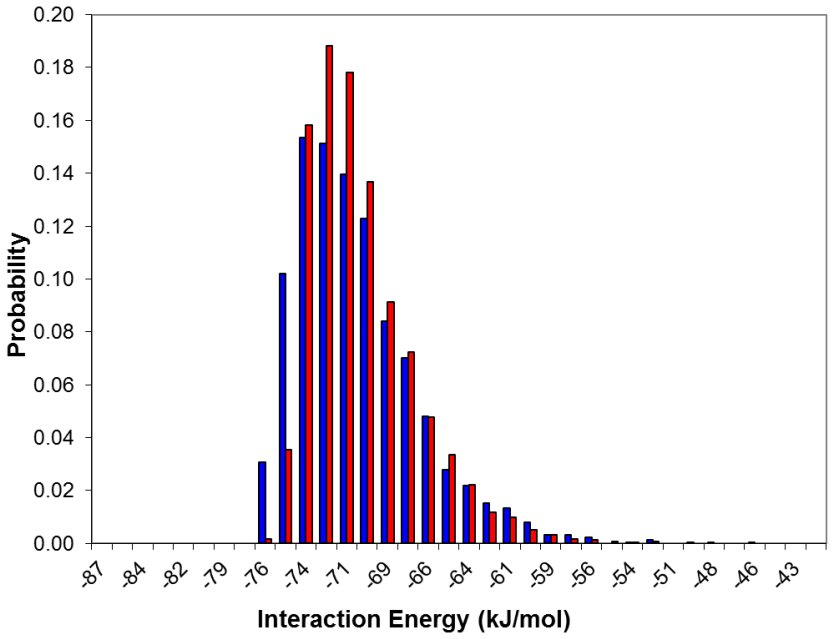

Figure M.1 – Probability histograms of pX-UiO-66(Zr) interaction energies in the small (blue) and intermediate (red) tetrahedral pores at 303 K.

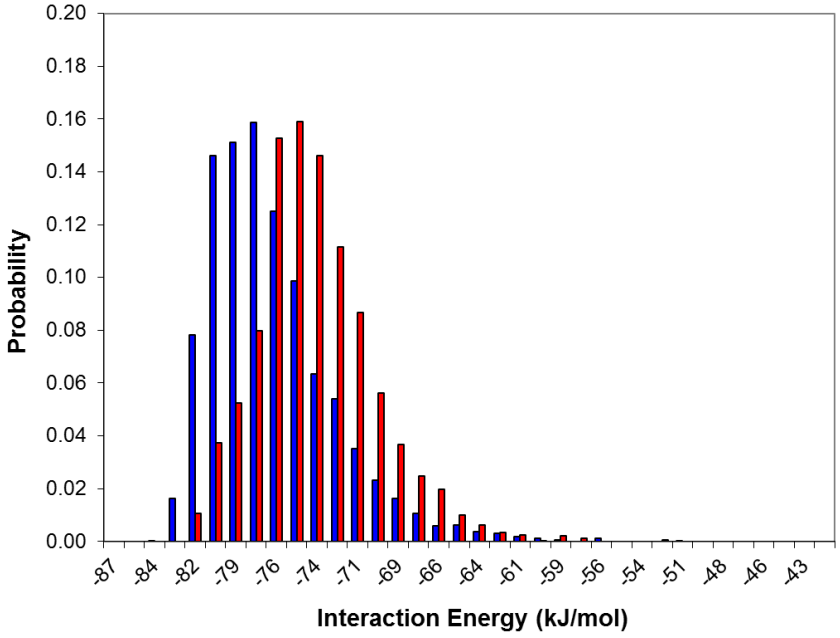

Figure M.2 – Probability histograms of oX-UiO-66(Zr) interaction energies in the small (blue) and intermediate (red) tetrahedral pores at 303 K.

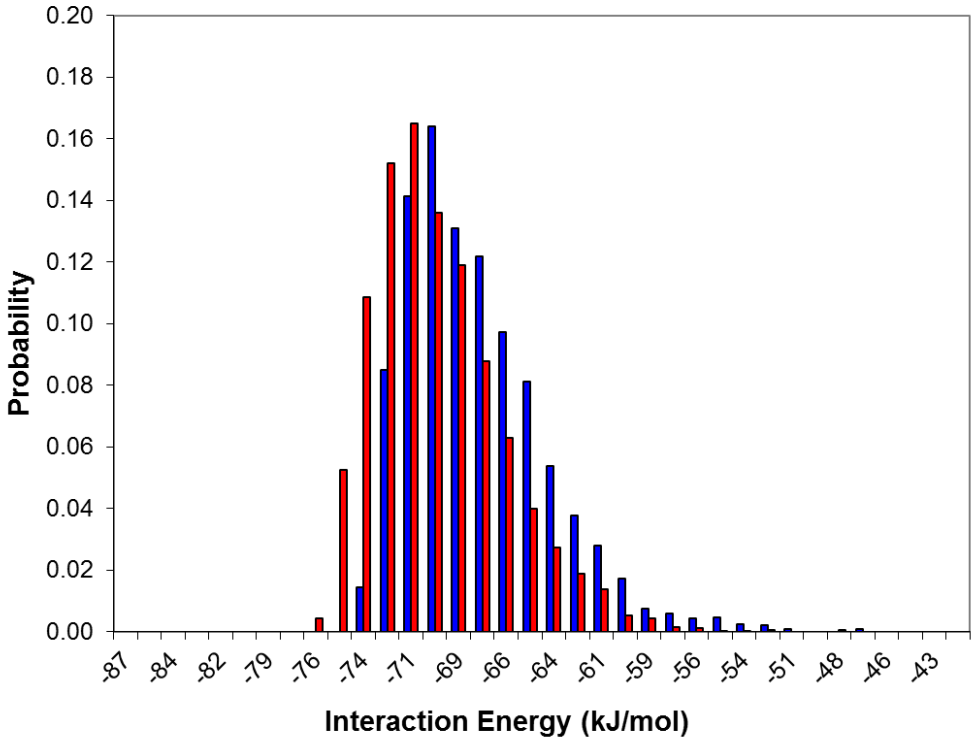

Figure M.3 – Probability histograms of mX-UiO-66(Zr) interaction energies in the small (blue) and intermediate (red) tetrahedral pores at 303 K.

And, of course, for my colleagues in IMP: always last – even in this thesis.